Investigation of Drug Aerosol Size, Delivery, and Deposition in the Mouth-Throat Airway Using a Soft Mist Inhaler (SMI): An Experimental and Numerical Study

By

Taha Sadeghi
M.Sc., Iran Polymer and Petrochemical Institute, Tehran, Iran, 2018

A Thesis Submitted to
the Faculty of Graduate Studies of
Lakehead University

in partial fulfillment of requirements of the degree of
Doctor of Philosophy, Biotechnology

November 2024

To the love of my life, Sadaf, who stood by my side
every step of this journey,
and to my mom, dad, and sis, for their unwavering
encouragement and unconditional support.

Author’s Declaration

I, Taha Sadeghi, do hereby declare that I am the sole composer of this document and that this document has not been submitted, in whole or in part, in any previous application for a degree or professional qualification. This document has been authored solely by myself and is comprised of my own work, except where otherwise stated by reference or acknowledgement.

I authorize Lakehead University to lend this document to other institutions and/or other individuals for the purpose of academic and/or scholarly research. I further authorize Lakehead University to reproduce this document, in whole or in part, via photocopying and/or digital scanning at the request of other institutions and/or individuals for the purpose of academic and/or scholarly research.

I authorize Lakehead University to make this document available electronically to the public.

Taha Sadeghi

Abstract

Investigation of Drug Aerosol Size, Delivery, and Deposition in the Mouth-Throat Airway Using a Soft Mist Inhaler (SMI): An Experimental and Numerical Study

Taha Sadeghi

Respiratory drug delivery has been a key area of research for several decades, driven by the high prevalence of pulmonary diseases and the superior treatment efficiency offered by this approach. However, despite its significant advantages, respiratory drug delivery faces major challenges, particularly low delivery efficiency and substantial drug deposition in undesired areas like the soft mist inhaler (SMI) mouthpiece, oral cavity, and throat wall. This study aimed to enhance the performance of inhalation therapy devices by leveraging insights and findings derived from experimental *in-vitro* and computational fluid dynamic (CFD) simulations.

This study examines the size distribution of drug aerosols and their deposition efficiency in the mouth-throat airway using an SMI. The SMI is known for its high drug delivery rates, ranging from 40% to 60%, and employs a unique atomization process through the Uniblock system to create fine particles that are ideal for lung deposition. To facilitate the research, the geometry of the mouth-throat region was constructed using three-dimensional (3D) printing technology with Ultimaker S3 and S5 printers, utilizing tough poly lactic acid (PLA) for precise and durable models. These printed geometries were then attached to a next-generation impactor (NGI) for experimental analysis. The NGI, which evaluates particle deposition and size distribution, was used to capture aerosolized particles at various stages according to their size. To quantify the deposition of the active pharmaceutical ingredient (API), high-performance liquid chromatography (HPLC) was employed at each stage and collection cup of the NGI, providing accurate measurements of drug deposition. Additionally, CFD simulations were conducted to model aerosol transport and deposition, offering valuable insights into airflow patterns, droplet size distribution, and the effects of geometric and physiological variations within the respiratory tract.

In the first part of the study, SMI performance was analyzed in two simplified mouth geometries: an idealized mouth (IM) and a standard mouth (SM). The effects of nozzle positions (along with the centerline), angles, and a fixed flow rate of 30 l/min were investigated to assess their impact on aerosol deposition and size distribution. The results indicated that SMI positioning and flow rate play a dominant role in determining deposition efficiency and size distribution, with higher flow rates reducing deposition within the mouth cavity. Recirculation regions and backward flows were identified as key contributors to increased particle residence time and deposition on mouth walls. Moving the SMI nozzle forward enhanced particle velocity at the outlet and reduced deposition, particularly in the SM geometry. These findings offer a foundation for developing innovative add-on devices, such as sensors or smart mouthpieces, to guide patients—especially children and the elderly—in optimizing inhalation techniques and improving drug delivery.

The second part of the study examined the combined effects of nasal and oral inhalation on aerosol deposition and size distribution in a modified induction port (MIP) simulating the upper airway. Six oral-to-nasal flow rate ratios were tested at a total inhalation flow rate of 30 l/min, with airflow and droplet behavior analyzed using a shear stress transport (SST) k-ω viscous model. Results revealed that moderate oral/nasal flow ratios (O/N = 1) produced fewer vortices and reduced turbulent kinetic energy, minimizing deposition losses within the MIP. Additionally, the highest drug delivery efficiency to the lower respiratory tract was observed at this ratio, with smaller droplets (0.1–2 µm) exhibiting a significant response to changes in relative humidity (RH). The study emphasizes the importance of combined oral and nasal inhalation strategies to improve aerosol drug delivery and provides recommendations for optimizing flow profiles in clinical settings.

In the third part, the effect of tongue position and inhalation profiles was studied within a realistic pediatric mouth-throat geometry. Utilizing Large Eddy Simulation (LES), this study analyzed the interplay between tongue positioning, fixed flow rates, and realistic chronic obstructive pulmonary disease (COPD) and pulsatile inhalation patterns. Results showed that pediatric airways experience significantly higher deposition compared to adults, with tongue position and flow rates strongly influencing deposition efficiency. Correlations were developed to predict mouth deposition percentages, providing a framework for improving inhalation techniques tailored to pediatric populations. Additionally, pulsatile inhalation profiles reduced deposition within the mouth while enhancing delivery to the lower airways, potentially reducing side effects and variability in pediatric drug delivery.

Acknowledgements

I would like to express my deepest gratitude to my supervisor, Dr. Leila Pakzad, for her unwavering encouragement, patient guidance, and invaluable support throughout every stage of my research. Her profound influence in shaping my research mindset and approach cannot be overstated. I am grateful to my co-supervisor, Dr. Pedram Fatehi, for his insightful advice and steadfast support. His technical expertise and editorial guidance were instrumental in the successful completion of this research.

I extend my heartfelt appreciation to my committee members, Dr. Baoqiang Liao and Dr. Francisco Ramos Pallares, and my external examiner Dr. Lyes Kadem for their time, valuable feedback, and thorough evaluation of this work. Their input has significantly enhanced the quality of this research. I also express my gratitude to Dr. Brenda Magajna, the program facilitator, and Dr. Wensheng Qin, the session chair, for their efforts in organizing and facilitating the defense session.

I would also like to express my appreciation to all my lab mates, Farnia Dastoorian, Mahsa Jahed, and Mona Mohammadkhani. It has been a joy to work alongside you, and I am deeply grateful for all your help and support throughout this journey.

I would like to acknowledge Lakehead University for providing access to LUHPCC, as well as the Narval cluster (narval.alliancecan.ca) and the Digital Research Alliance of Canada (alliancecan.ca) for their high-performance virtual computing platforms, which greatly accelerated the progress of this study. This research would not have been possible without the financial support from the Natural Sciences and Engineering Research Council of Canada, for which I am sincerely thankful. I am also grateful to Boehringer Ingelheim for donating the placebo Respimat SMIs used in this study. My thanks also go to the Ingenuity Centre at Lakehead University and Confederation College for supplying a 3D printer and to the Department of Chemistry at Lakehead University for providing access to the HPLC instrument.

Lastly, and most importantly, I would like to express my heartfelt gratitude to my wife, Sadaf, whose unwavering love, compassion, and sacrifices have made this journey possible. Her steadfast support has been my greatest strength throughout this endeavor.

I am deeply grateful to my beloved parents and sister for their unwavering encouragement and boundless love. Words cannot fully convey the depth of my gratitude or the pride I feel in being

their son and brother. I love them with all my heart and will forever be indebted to them for their steadfast support and belief in me.

Contents

Table of Figures

Table of Tables

Chapter 1 – Introduction

1.1 Introduction

Inhalation therapy is the primary treatment for debilitating respiratory diseases such as asthma, chronic obstructive pulmonary disease (COPD), and cystic fibrosis, which adversely affect the quality of life and account for a large proportion of hospitalizations and mortalities [1]. Inhalation therapy, administered through oral and nasal routes, is the most prevalent treatment for these conditions. The transport and deposition of particles in the human respiratory tract (HRT) are influenced by several factors, including the type of inhaler device, breathing patterns and environmental conditions (such as temperature and relative humidity), and the geometry of the airways based on the 'patient's race, gender, and age [2–5].

Standard techniques for administering aerosol medications to patients involve the use of inhaler devices, including pressurized metered-dose inhalers (pMDIs), dry powder inhalers (DPIs), nebulizers and soft mist inhalers (SMIs) [6]. It is essential to fine-tune the deposition site of the drug-aerosol within the human lower respiratory tract to achieve targeted delivery and minimize unwanted systemic side effects. Depositing the drug in the mouth-throat region results in medication wastage, reducing its effectiveness and increasing intersubjective variability and side effects [7–10]. Pharmaceutical aerosol delivery to human lungs is often inefficient, with around 40% of the drug being lost in the extrathoracic region and approximately 22-27% in the device mouthpiece (MP). The amount of loss varies depending on the inhaler device used [11–13].

SMIs have been developed to address these issues. These devices represent a new generation of inhalation devices, achieving an approximate 40-60% drug delivery rate to the lungs [8]. This can be attributed to their improved usability, being propellant-free, and reducing the dependency on the patient's inhalation effort [14]. Drug delivery to the lung, termed lung deposition efficiency, is generally assessed by comparing the amount of medication that reaches the intended lung site to the total dose emitted from the inhaler device [15–17]. A higher lung deposition efficiency means that a greater percentage of the medication is successfully delivered to the lungs, which is ideal.

The main objective of this study is to examine the drug-aerosol size distribution and deposition efficiency in the mouth-throat airway using an SMI through both experimental and numerical approaches.

1.2 Thesis Structure

This thesis is organized into seven chapters. *Chapter 1* briefly introduces methods to improve inhalation therapy, and discusses the parameters affecting drug delivery efficiency with different inhaler types. It is followed by an outline of the thesis structure.

Chapter 2 delivers an insightful review of the scientific literature surrounding drug delivery to the lungs via inhalers, with a special focus on SMIs. This review effectively examines critical areas, including (i) the efficiency of different inhaler devices, (ii) inhalation profiles and flow patterns within the human respiratory tract, (iii) the geometric characteristics of inhalers, and (iv) influential studies leveraging computational fluid dynamics (CFD) to model pharmaceutical aerosols. By addressing these key topics, we aim to uncover research gaps and articulate our research objectives, ultimately advancing the understanding and effectiveness of lung drug delivery systems.

Chapter 3 details the research methodology, including the theoretical background and experimental techniques, such as next-generation impactor (NGI) and high-performance liquid chromatography (HPLC). It also discusses the role of 3-Dimentional (3D) printing in creating custom models for simulations and outlines the process of submitting simulation jobs on clusters to leverage high-performance computing resources.

Chapter 4 discusses the application of CFD to analyze fluid flow and particle transport in human airways, using the Navier-Stokes equations as the foundational governing principles. It explains how turbulence models like the Reynolds Averaged Navier-Stokes (RANS) with the k-ω model and Large Eddy Simulation (LES) capture complex airflow behaviors. The chapter introduces the Discrete Phase Model (DPM) for simulating particle motion in aerosols, utilizing statistical distributions such as Rosin-Rammler and log-normal to represent polydisperse particle sizes. Additionally, it outlines the numerical methods and solver settings used in the CFD simulations.

In *Chapter 5*, the performance of SMIs is analyzed using CFD modeling, focusing on aerosol velocity profiles, flow patterns, size distribution, and deposition. Two simplified geometries—the idealized mouth and standard mouth—were modeled. This chapter considers three nozzle orifice locations along the centerline of the mouth cavity and two nozzle angles for the idealized mouth geometry. The impact of a 30 l/min flow rate on aerosol velocity, deposition, and size distribution is examined, concluding that flow rate has a greater influence on particle deposition than nozzle position. Findings suggest potential for designing an add-on device, such as a sensor or MP, to help patients (particularly children or the elderly) correctly use SMI inhalers. This study has been published in "Biomechanical Engineering" in 2023.

Chapter 6 evaluates the combined effects of nasal and oral inhalation on drug particle deposition and size distribution in the human upper airway with an SMI. A modified induction port was used to simulate nasal inhalation in the human respiratory tract. Six different oral/nasal flow rate ratios were applied, totalling a flow rate of 30 l/min. Findings show that combined inhalation significantly influences the flow field, altering droplet deposition and size distribution in the modified induction port, with medium oral/nasal ratios showing less intense vortices and lower turbulent kinetic energy. This study was published in the "Annals of Biomedical Engineering" in 2023.

Chapter 7 investigates the effects of tongue position on droplet deposition, size distribution, and airflow patterns within a realistic pediatric mouth-throat geometry using an SMI. Various fixed flow rates, realistic COPD inhalation, and 2-step pulsatile inhalation profiles were considered. Large eddy simulation was used to analyze how airflow, tongue positioning, and drug droplet properties affect deposition efficiency and size distribution. A correlation was developed to predict mouth deposition (%) across different flow rates, and overall deposition in the pediatric mouth-throat was found to be more than double that in adult mouth-throat geometries.

Lastly, *Chapter 8* provides an overall conclusion for the thesis and presents suggestions for future research in this area.

1.3 Nomenclature

COPD	Chronic Obstructive Pulmonary Disease
CFD	Computational Fluid Dynamics
DPI	Dry Powder Inhaler
DPM	Discrete Phase Model
HPLC	High-Performance Liquid Chromatography
HRT	Human Respiratory tract
LES	Large Eddy Simulation
MP	Mouthpiece
NGI	Next Generation Impactor
pMDI	Pressurized Metered Dose Inhaler
RANS	Reynolds Averaged Navier-Stokes
SMI	Soft Mist Inhaler
3D	3-Dimensional

1.4 References

[1] Z. Xu, A.J. Hickey, The physics of aerosol droplet and particle generation from inhalers, in: S. H.D.C., H. A.J. (Eds.), Controlled Pulmonary Drug Delivery, 1st ed., Springer, New York, 2011: pp. 75–100.

[2] A. Arsalanloo, M. Abbasalizadeh, M. Khalilian, Y. Saniee, A. Ramezanpour, M.S. Islam, A computational approach to understand the breathing dynamics and pharmaceutical aerosol transport in a realistic airways, Advanced Powder Technology 33 (2022). https://doi.org/10.1016/j.apt.2022.103635.

[3] M. Talaat, X. Si, J. Xi, Effect of MDI Actuation Timing on Inhalation Dosimetry in a Human Respiratory Tract Model, Pharmaceuticals 15 (2022). https://doi.org/10.3390/ph15010061.

[4] A. Baloira, A. Abad, A. Fuster, J.L.G. Rivero, P. García-Sidro, E. Márquez-Martín, M. Palop, N. Soler, J.L. Velasco, F. González-Torralba, Lung deposition and inspiratory flow rate in patients with chronic obstructive pulmonary disease using different inhalation devices: A systematic literature review and expert opinion, International Journal of COPD 16 (2021) 1021–1033. https://doi.org/10.2147/COPD.S297980.

[5] Y. Zhou, J. Sun, Y.S. Cheng, Comparison of deposition in the USP and physical mouth-throat models with solid and liquid particles, J Aerosol Med Pulm Drug Deliv 24 (2011) 277–284. https://doi.org/10.1089/jamp.2011.0882.

[6] S. Smith, J. Bernstein, Inhalation Aerosols, Therapeutic uses of lung aerosols, Marcel Dekker, New York, 1996.

[7] P.G. Koullapis, L. Nicolaou, S.C. Kassinos, In silico assessment of mouth-throat effects on regional deposition in the upper tracheobronchial airways, J Aerosol Sci 117 (2018) 164–188. https://doi.org/10.1016/j.jaerosci.2017.12.001.

[8] R. Dalby, M. Spallek, T. Voshaar, A review of the development of Respimat® Soft MistTM Inhaler, Int J Pharm 283 (2004) 1–9. https://doi.org/10.1016/j.ijpharm.2004.06.018.

[9] P.W. Longest, M. Hindle, Condensational growth of combination drug-excipient submicrometer particles for targeted high efficiency pulmonary delivery: Comparison of CFD predictions with experimental results, Pharm Res 29 (2012) 707–721. https://doi.org/10.1007/s11095-011-0596-1.

[10] S.P. Newman, K.P. Steed, S.J. Reader, D. Pavia, A.K. Sohal, An in vitro study to assess facial and ocular deposition from Respimat® Soft MistTM inhaler, Journal of Aerosol Medicine: Deposition, Clearance, and Effects in the Lung 20 (2007) 7–12. https://doi.org/10.1089/jam.2006.0563.

[11] A. Alatrash, R. Mehri, N. Ogrodnik, E. Matida, F. Fiorenza, Experimental Study of Spiriva Respimat Soft Mist Inhaler Spray Characterization: Size Distributions and Velocity, J Aerosol Med Pulm Drug Deliv 32 (2019) 293–302. https://doi.org/10.1089/jamp.2018.1501.

[12] P. Worth Longest, M. Hindle, Evaluation of the respimat soft mist inhaler using a concurrent cfd and in vitro approach, J Aerosol Med Pulm Drug Deliv 22 (2009) 99–112. https://doi.org/10.1089/jamp.2008.0708.

[13] P.W. Longest, G. Tian, X. Li, Y.J. Son, M. Hindle, Performance of combination drug and hygroscopic excipient submicrometer particles from a softmist inhaler in a characteristic model of the airways., Ann Biomed Eng 40 (2012) 2596–2610. https://doi.org/10.1007/s10439-012-0616-2.

[14] T. Iwanaga, Y. Tohda, S. Nakamura, Y. Suga, The Respimat® Soft Mist Inhaler: Implications of Drug Delivery Characteristics for Patients, Clin Drug Investig 39 (2019) 1021–1030. https://doi.org/10.1007/s40261-019-00835-z.

[15] R. Mehri, K.L. Slew, A. Alatrash, E. Matida, F. Fiorenza, Aerosol Deposition Measurements with ODAPT Mask Adapter, 13 (2018) 10–14.

[16] P. Worth Longest, M. Hindle, Evaluation of the respimat soft mist inhaler using a concurrent cfd and in vitro approach, J Aerosol Med Pulm Drug Deliv 22 (2009) 99–112. https://doi.org/10.1089/jamp.2008.0708.

[17] R. Dalby, M. Spallek, T. Voshaar, A review of the development of Respimat® Soft MistTM Inhaler, Int J Pharm 283 (2004) 1–9. https://doi.org/10.1016/j.ijpharm.2004.06.018.

Chapter 2 – Literature Review

2.1 Literature Review

One of the most reliable and efficient ways to address respiratory diseases is inhalation therapy, which can be done through oral or nasal inhalation. Inhaler devices have been introduced to deliver a specific amount of drug to the lower human respiratory tract (HRT) and the site of action. These devices include pressurized metered dose inhalers (pMDIs), dry powder inhalers (DPIs), nebulizers and soft mist inhalers (SMIs) [1] and are shown in **Fig 2.1.**

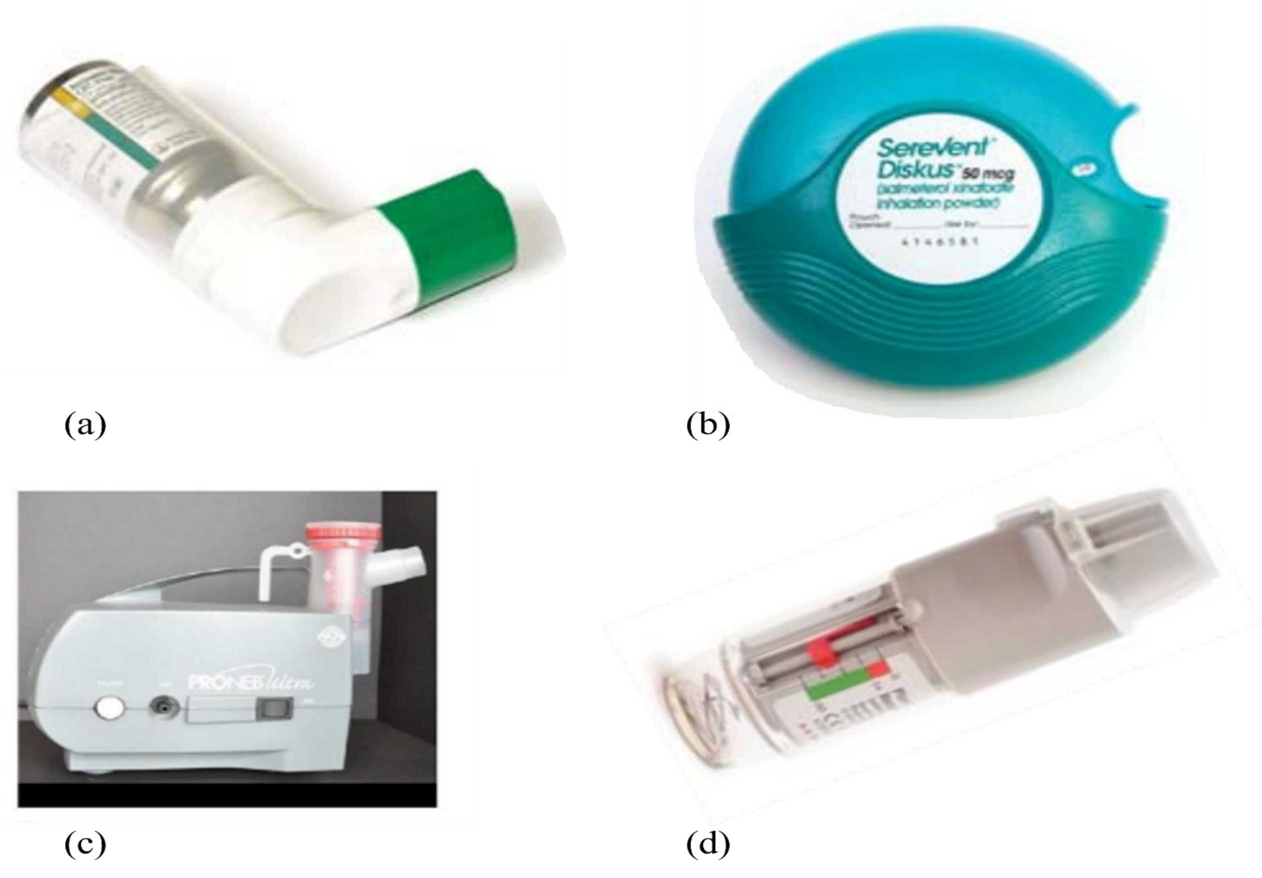

Fig 2.1 Inhaler devices for drug delivery: **(a)** pMDI, **(b)** DPI, **(c)** Nebulizer, and **(d)** SMI [2].

PMDIs (refer to **Fig 2.1(a)**) are the most frequently prescribed inhalers, delivering medication droplets using liquid propellant pressure, with a lung deposition rate of around 10-20% [3]. However, they require priming and shaking before each use, and the rapid aerosol plume makes it difficult for patients to synchronize inhalation with device actuation [4]. Furthermore, the propellants create a cold, freon-like sensation at the back of the throat after actuation, which can be uncomfortable for patients [5]. The droplets' high velocity and large particle size often lead to deposition in the oropharynx, causing side effects and limiting therapeutic effectiveness [6].

DPIs (**Fig 2.1(b)**) rely on the user's inhalation strength to disperse the drug powder into fine aerosol particles for delivery to the target site. These devices are compact, portable, and can be used with one or two puffs over a few seconds. To effectively disperse the medication, a minimum inhalation flow rate of 30 l/min is needed, creating a fine mist [7]. However, like pMDIs, DPIs result in significant oropharyngeal deposition and are generally moisture-sensitive. Due to these requirements, DPIs are less suitable for elderly individuals, children, or those with reduced respiratory capacity, as they may struggle to achieve the necessary inhalation flow rates [8].

Nebulizers (**Fig 2.1(c)**) produce a fine mist for medication administration over an extended period of up to 20 minutes and have long been used to treat chronic obstructive pulmonary disease (COPD). Unlike other inhalers, they do not require priming, hand–breath coordination, or breath holding, and they effectively aerosolize medication that the patient can inhale with regular tidal breathing. This makes nebulizers particularly beneficial for young children, elderly patients, or individuals with limited lung capacity, as they can receive the medication at a comfortable breathing rate without complex technique requirements. However, nebulizers are less portable and often require power sources or regular maintenance, making them less convenient than other inhaler devices [9].

When selecting an inhalation device for patients, healthcare professionals take into account various factors, including the patient's inspiratory flow capacity, ability to coordinate hand movements with breathing, cognitive and motor abilities, as well as the preferences and financial considerations of the patient or caregiver. Effective treatment relies heavily on the correct usage of these devices; improper use can hinder medication delivery, increase the likelihood of exacerbations, and result in greater healthcare expenses and a higher risk of early mortality [10]. To address these issues, SMIs have been introduced, which will be explained in detail in the following sections.

2.1.1 Soft Mist Inhalers (SMIs)

Commercially approved in 2003, these devices are a new generation of inhalation devices, achieving an approximate 40-60% drug delivery rate to the lungs. This can be attributed to their improved usability, being propellant-free, and reducing the dependency on the patient's inhalation effort [11]. **Fig 2.2** shows the design of an SMI that consists of a unique small chip called the Uniblock, which is crucial for atomization [12].

The Uniblock features two micronozzle channels that direct two jets to collide at approximately a 90° angle, just 25 µm from the nozzle outlet. This jet interaction generates significant shear forces that break the liquid's surface tension, resulting in the formation of micro-sized aerosol spray [13]. In the original prototype of the Respimat® SMI, the nozzle openings consisted of small holes drilled into a stainless-steel disk; however, this design proved inadequate for large-scale manufacturing [14]. The issue was addressed through the creation of a miniature sandwich design known as the Uniblock, which consists of a structured silicon wafer attached to a small borosilicate glass plate (2 mm × 2.5 mm). Inlet, outlet, and filter channels, designed to prevent nozzle blockage, are etched into the silicon wafer using microchip fabrication technology, allowing for large-scale production with high precision and accuracy [12].

To actuate the device, the patient must twist the base of the inhaler by 180 degrees. This action meters out a specific amount of dose and compresses the spring inside the base, providing the energy needed to deliver the medication. To administer the dose, the patient must press the dose release button located at the top of the inhaler. This action forces the drug solution through two converging micro-channels (located in the section called Uniblock), typically around 10 µm, generating two laminar micro-liquid jets that collide obliquely downstream of the nozzles, forming a slow-speed spray cloud [15]. Each actuation delivers 2.5 micrograms of tiotropium bromide monohydrate, the active ingredient in the Spiriva Respimat inhaler [16].

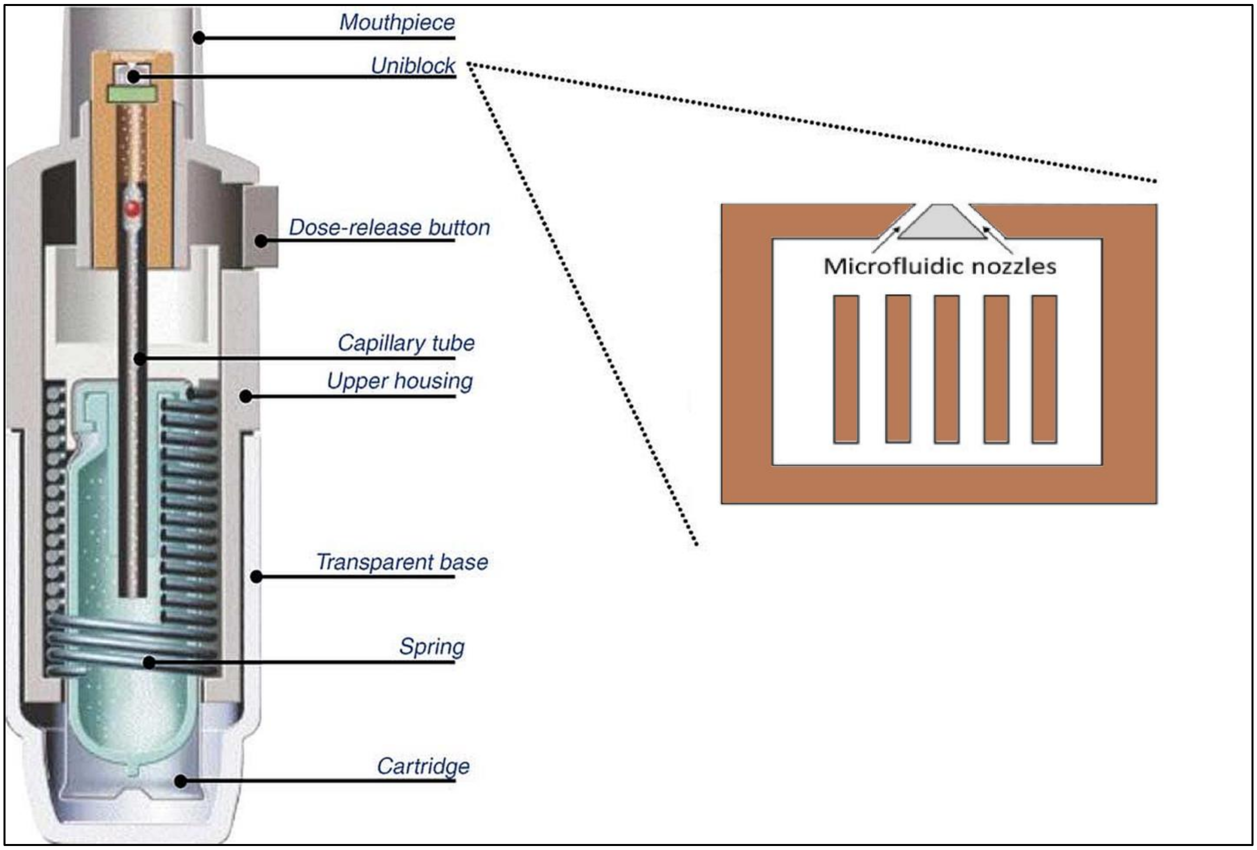

Fig 2.2 The latest design of Respimat® soft mist inhaler [17].

Furthermore, the prolonged, slow-moving aerosol plume produced by an SMI contains a high proportion of fine particles (<5 µm), which enhances drug delivery efficiency to the lungs. These particles are dispensed at a comparatively slow plume velocity of 17.5 m/s, which is significantly lower than the 100 m/s velocity typical of pMDIs. SMIs can generate fine particles distribution in a range of 0.1 to 60 µm with a mass median diameter (MMD) of 5.3 µm, as shown in **Fig 2.3** [18]. Generally, droplets within the 2–5 µm diameter range are more likely to reach and deposit in the lungs. Conversely, larger droplets (over 5 µm) tend to settle in the oropharynx and upper tracheobronchial region before reaching the trachea, while smaller droplets (under 2 µm) are more likely to be exhaled [19,20]. Although SMI achieves a higher lung delivery rate compared with other inhaler devices (i.e. pMDIS, DPIs, and nebulizers), studies have shown that SMIs can lead to a significant loss of medication through the mouthpiece (MP) and oral cavity, estimated at around 30%. Consequently, it is essential to thoroughly understand and optimize the atomization process [18].

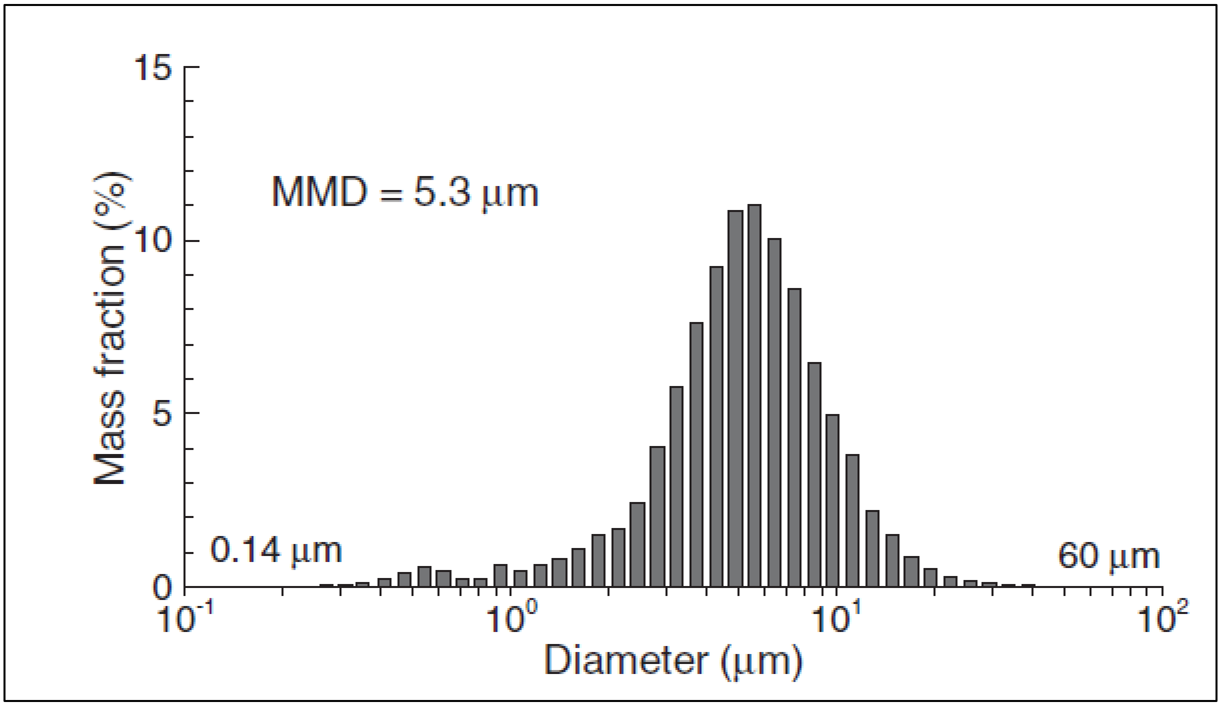

Fig 2.3 The size distribution of the polydisperse Respimat aerosol near the spray nozzle unit [18].

2.1.2 Experimental, Numerical, and Clinical Studies of the SMI

Despite its significant implications and therapeutic effects, there is a lack of extensive research on the spray-generation mechanism of SMIs. Additionally, the actual spray produced by an SMI must be accurately characterized before conducting any clinical, experimental or numerical simulations. This section aims to investigate the parameters that affect the drug delivery of inhalers, especially SMIs, to the lungs.

One of the first studies that was conducted to characterize SMI aerosol was the study of Hochrainer *et al.* in 2005 [21]. They examined the velocity and spray duration of aerosol clouds produced by the Respimat® SMI and compared the findings to those from various chlorofluorocarbon and hydrofluoroalkane pMDIs. A video recording technique was used to measure aerosol *velocity* and compare the spray duration of the Respimat® SMI with other inhalers. The soft mist generated by the SMI demonstrated a markedly slower movement and a longer duration compared to the aerosol clouds from pMDIs. At a distance of 10 cm from the nozzle, the average velocity for the Respimat® SMI was measured at 0.8 m/s, while the velocities for pMDIs varied between 2.0 and 8.4 m/s. The average duration for the Respimat® SMI was 1.5 seconds, in contrast to the 0.15 to 0.36 seconds observed for pMDIs. These characteristics are anticipated to enhance lung deposition and decrease oropharyngeal deposition, likely making it easier to coordinate inhaler actuation with inhalation compared to pMDIs [21].

The droplet size distribution and velocity of SMI aerosols were further investigated by Alatrash *et al.* in 2019 [22]. In this study, phase Doppler anemometry was employed to assess the size and velocity of droplets at four positions along the centerline of the Spiriva Respimat inhaler, as well as at three cross-sections in a free-spray configuration. Additionally, measurements were taken at a single cross-section in confined spray configurations using two distinct idealized mouth cavities. The investigation aimed to explore the impact of sampling distance on particle velocity and size. As shown in **Fig 2.4**, measurements along the centerline of the aerosol mist produced by the Spiriva Respimat inhaler, taken at distances of 6.5, 25, 100, and 125 mm downstream from the nozzle orifice, indicated that droplets at the mouthpiece (MP) had the highest velocity of 10.95 m/s, which decreased to 1.33 m/s at the 125 mm mark. The mean diameter values varied from 3.97 µm at 6.5 mm to 3.67 µm at 125 mm [22].

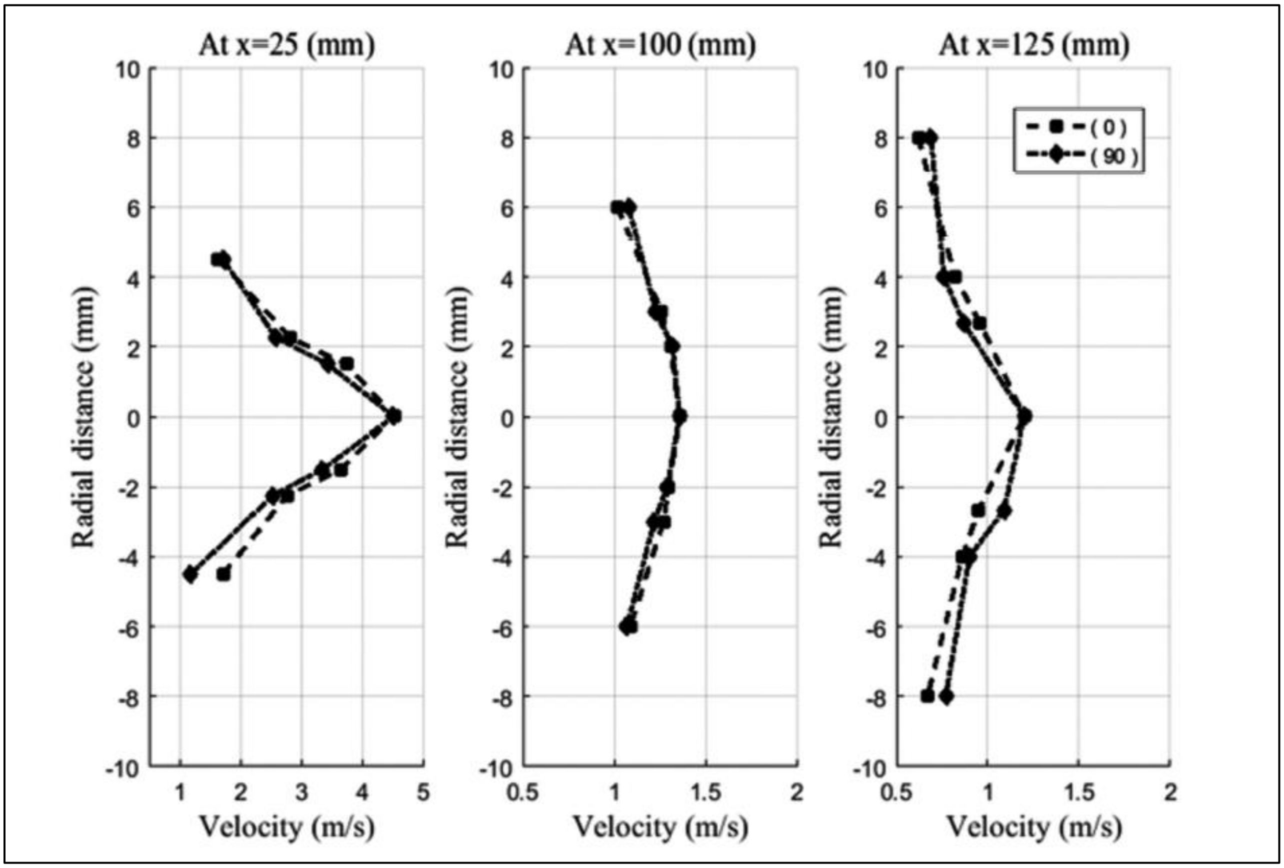

Fig 2.4 Axial mean particle velocity for the Spiriva Respimat inhaler at various longitudinal positions [22].

Breathing pattern and condition are some of the most critical parameters significantly affecting drug delivery efficiency. The inhaled route has recently emerged as a promising method for systemic drug administration due to the lungs' favorable absorption characteristics [23]. The human airway facilitates gas exchange between the lungs and the ambient air and plays a crucial role in the delivery and distribution of inhaled drug particles. Investigating airflow characteristics, flow patterns, and turbulence in the respiratory tract offers valuable insights into the transportation of inhaled particles during respiration. The application of CFD to model airflow and the transport and deposition of aerosols in the extrathoracic airway plays a crucial role in predicting the behavior and response of the system under investigation.

Zhang and Kleinstreuer [24] examined how airflow rate affects nanoparticle deposition within a combined nasal–oral–tracheobronchial airway model. They focused on spherical nanoparticles with mean diameters ranging from 1 to 100 nm and assessed various breathing routes at 30 and 60 l/min flow rates. The study revealed that changing the breathing route from nasal to oral significantly impacts nanoparticle deposition in the nasal and oral cavities, as well as in the nasopharynx and oropharynx. Segmental deposition fraction did not change significantly when switching from 30 l/min to 60 l/min. Moreover, it also affects deposition from the pharynx to the bronchial airways for very small nanoparticles (≤5 nm). Specifically, when transitioning from nasal to oral breathing at a flow rate of 30 l/min, the total deposition fraction in the upper airway model decreased from 77% to 55% for 1 nm particles and from 4.3% to 2.7% for 10 nm particles, attributable to the nasal cavity's larger surface area and more complex geometric structure compared to the oral cavity as shown in **Figs 2.5 (a)** and **(b)**.

In a separate study, Wang *et al.* [25] performed a numerical analysis to investigate the transport and deposition of spray produced by an impinging-jet inhaler in the human respiratory tract at various inhalation flow rates. They implemented an injection model for their simulations, incorporating spray spreading angles in two directions based on experimental data, and adjusted the model parameters to correspond with the mean droplet size determined in previous experiments. To better simulate actual inhaler usage, they applied a flow rate (see **Fig 2.6**). The findings revealed that the inhalation airflow rate has a significant impact on the transport and deposition of the spray within the respiratory tract. Notably, both excessively high and low inhalation flow rates resulted in increased deposition in the mouth-throat area, whereas a moderate flow rate minimized throat deposition and optimized lung deposition. Additionally, the study indicated that higher inhalation flow rates accelerated the delivery of droplets to the lungs, while lower flow rates allowed for more uniform deposition over time. This research underscored a consistent pattern of deposition across various lung lobes and offered valuable insights for optimizing inhalation flow rates in clinical applications of impinging-jet inhalers.

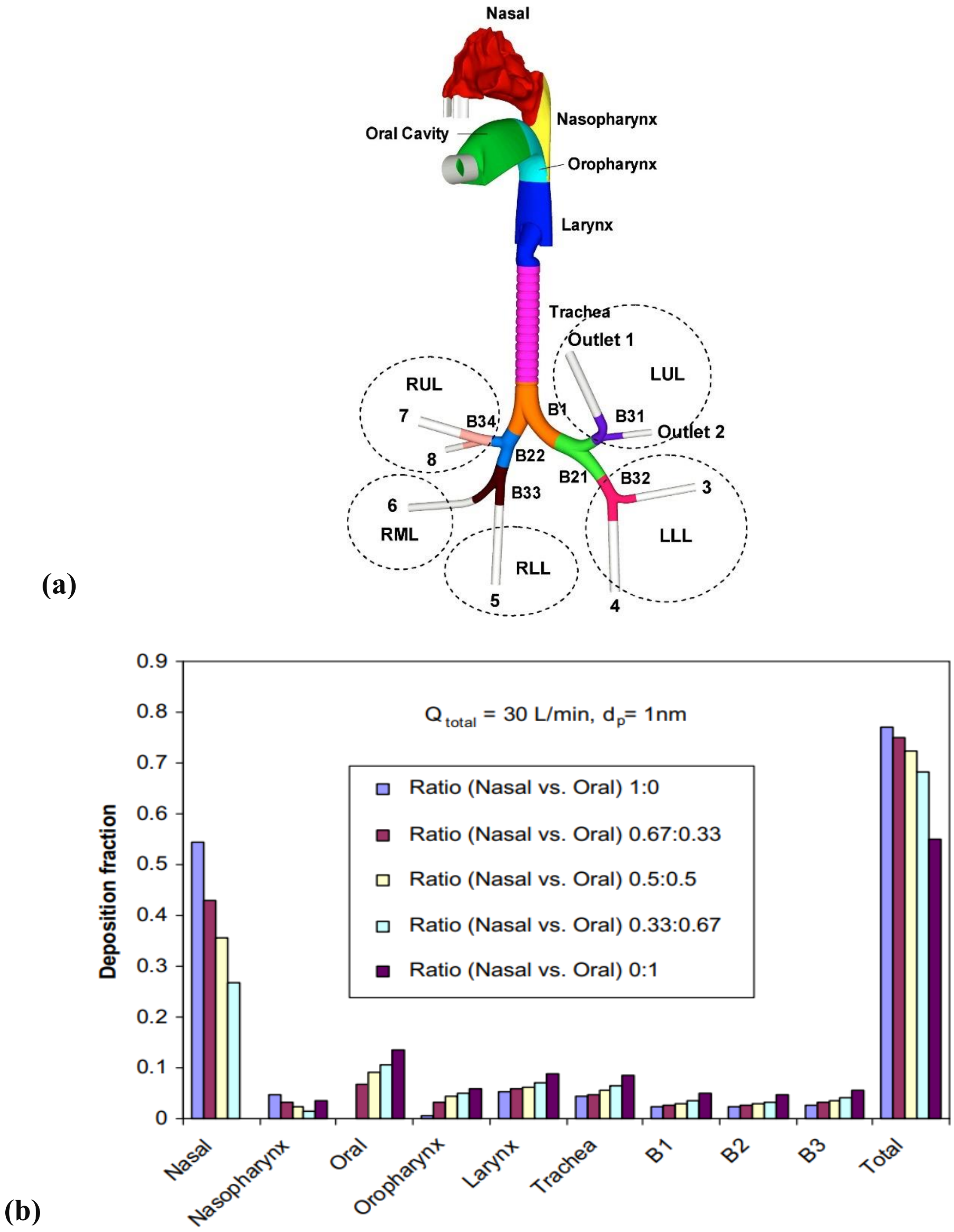

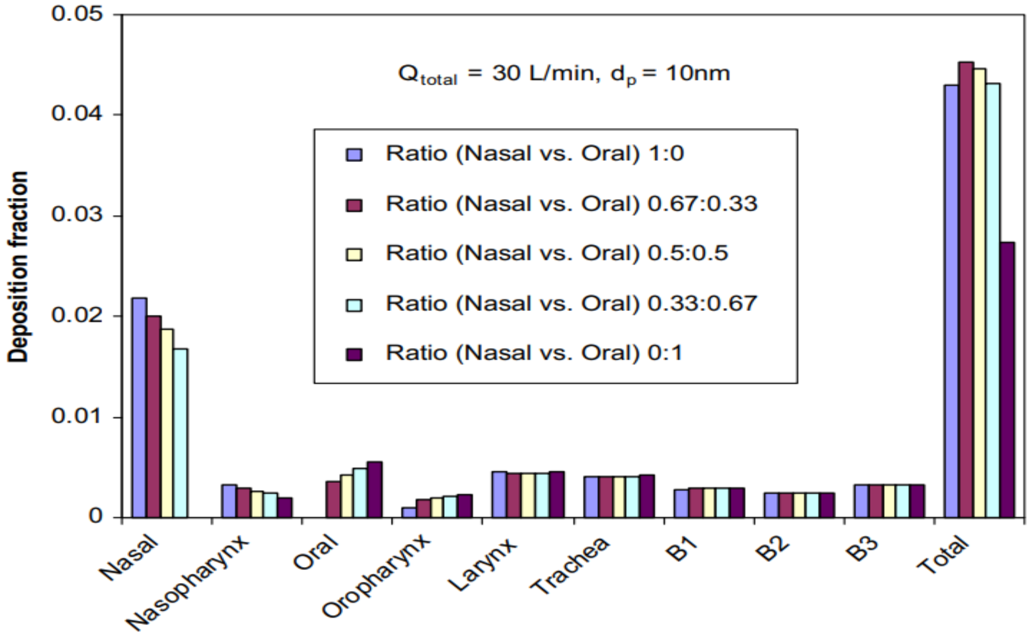

(c)

Fig 2.5 (a) Configuration of representative human upper airway model and influence of breathing routes on local deposition fractions for **(b)** 1 nm particles, and **(c)** 10 nm particles, with a total inspiratory flow rate of 30 l/min in all scenarios [24].

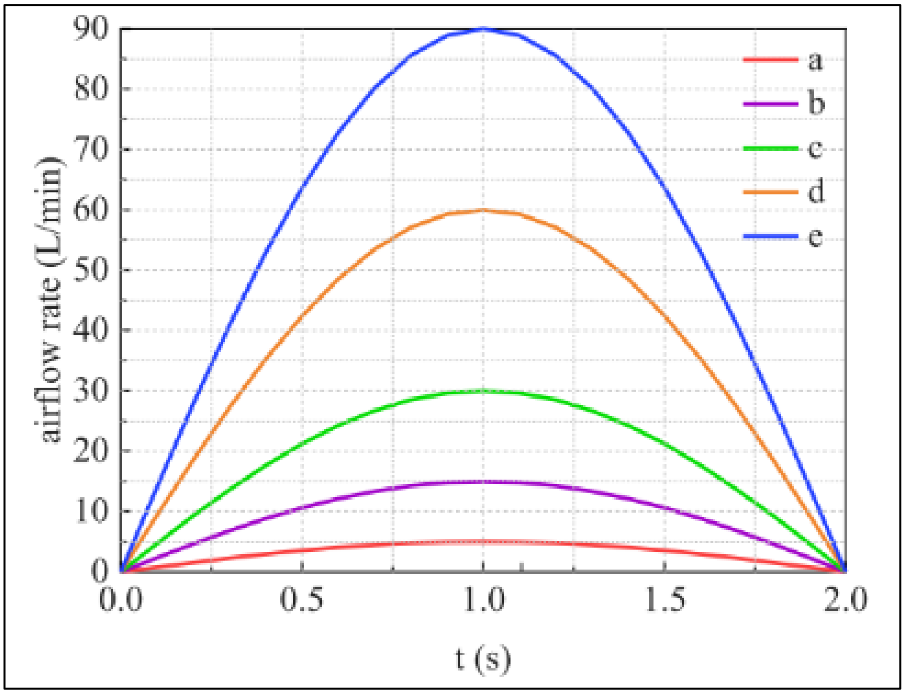

Fig 2.6 Sinusoidal variation in the inhalation flow rate over time for varying flow rates corresponding to **(a)** 5 l/min, **(b)** 15 l/min, **(c)** 30 l/min, **(d)** 60 l/min, and **(e)** 90 l/min [25].

The geometry of the airway can also significantly affect drug delivery and deposition inside the human lungs. Accurate models of nasal, mouth-throat, and lung structures are essential for producing reliable correlations between in vivo data and those obtained through in vitro or in silico methods. However, due to the limited availability of Computed Tomography (CT)/Magnetic Resonance Imaging (MRI) scans and the need to reduce computational costs in numerical studies, simplified oropharyngeal geometries are often used [26]. These simplified models, while useful, can lack the intricacies and variability of actual human airways, leading to potential discrepancies in drug deposition predictions. For instance, the Standard Induction Port (IP) is commonly used for sampling pharmaceutical aerosols and serves as a standard reference geometry, but it may not capture all the nuances of individual patient anatomy, leading to variability in drug delivery efficiency [27].

In the study conducted by Longest and Hindle [18], the deposition of the Respimat aerosol was assessed in the inhaler MP, an IP, and a more realistic mouth-throat geometry (illustrated in **Fig 2.7**) at an inhalation flow rate of 30 L/min. Both experimental methods and a CFD model were utilized to quantify drug deposition in the Respimat inhaler. Laser diffraction experiments were conducted to establish the initial polydisperse aerosol size distribution. The computational predictions of deposition fractions closely matched the experimental results, showing an error margin of within 20% for the IP geometry and within 10% for the MT geometry. Experimental findings revealed that the drug deposition fraction in the mouthpiece ranged from 27% to 29%, which constituted the majority of the total drug loss. According to the CFD analysis, the high deposition in the mouthpiece was attributed to a recirculating flow pattern around the aerosol spray that entrained a significant number of small droplets. In contrast, deposition of the Respimat aerosol was relatively low in both the IP (4.2%) and MT (7.4%) geometries.

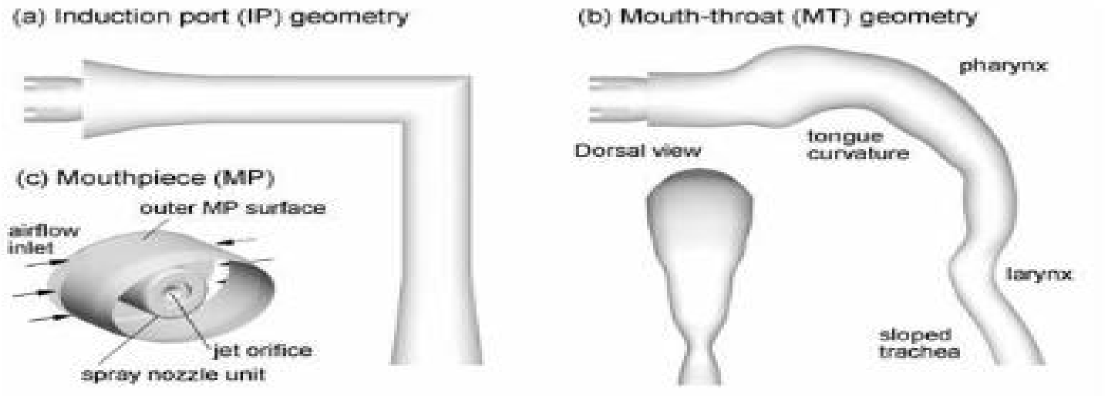

Fig 2.7 Schematics of **(a)** induction port (IP), **(b)** a more realistic mouth-throat, and **(c)** the mouthpiece (MP) geometries [18].

In another study, Xi *et al.* [28] evaluated the relative significance of geometrical factors on deposition within the MT region using a coupled image-CFD approach. This assessment included factors such as the oral cavity volume, glottis area, airway curvature, and the overall volume of the MT airway. Four existing MT models with varying complexities were utilized, and HyperWorks software was employed to modify the dimensions of these geometrical factors. Each factor was studied across five variants in each airway model. A well-validated fluid-particle transport model was implemented to simulate airflow and particle deposition. The variations in deposition induced by the geometrical factors were analyzed using a one-way analysis of variance to ascertain the relative influence of each factor on particle deposition within the MT airway. The more realistic airway models had a significant impact on MT deposition, with the IP model underestimating the realistic model's deposition by as much as 55%, as shown in **Fig 2.8**. The study identified the glottis area and total airway volume as the two most critical factors influencing deposition. Notably, substituting the IP 90° elbow with curved bends resulted in a significant reduction in deposition, whereas the curvature of the MT airway in the other three models showed negligible effects. Additionally, the oral cavity volume was determined to have an insignificant impact. Medium-sized particles (6–12 µm) were found to be more responsive to variations in geometrical factors, with changes in the glottis area causing the largest fluctuations in MT deposition.

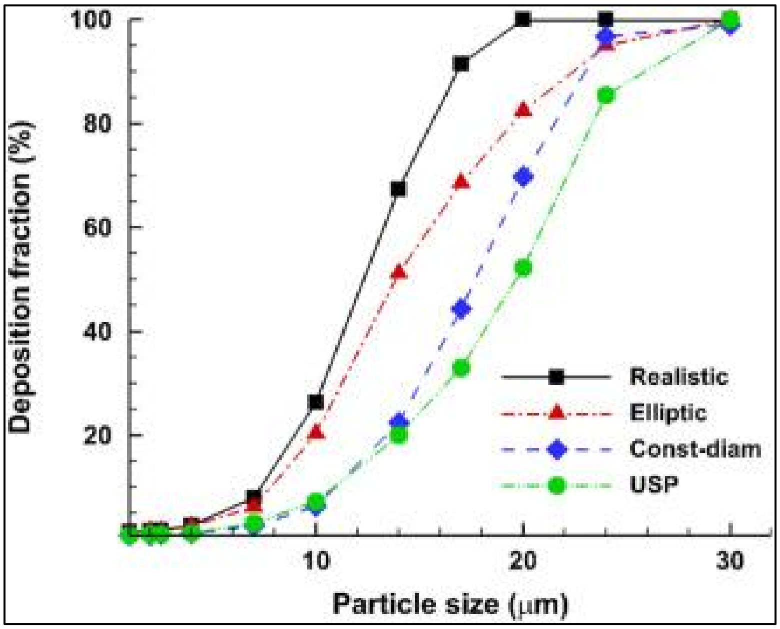

Fig 2.8 A comparison of deposition fractions across the four MT models as a function of particle size at 30 L/min showed higher deposition rates in the more complex models, whereas the USP IP model exhibited the lowest deposition [28].

Xi and Longest [29] also examined four different upper airway models (**Fig 2.9**) to assess the impact of geometry on the airflow field and particle deposition. They compared a realistic model created from CT-scan data with three simplified geometrical models featuring elliptical, variable, and constant circular cross-sections. Their findings revealed that the regional deposition for all four models, when plotted against the Stokes number, was roughly within one standard deviation of the available experimental data. However, when the deposition curve was analyzed as a function of particle diameter, the realistic geometry demonstrated the greatest alignment with the experimental results.

Realistic airway geometries provide a more detailed and accurate representation of the human respiratory tract, allowing for better assessment of how drug particles behave and deposit within the airways. These models help in understanding the regional deposition of aerosols, which is crucial for optimizing drug dosing and enhancing therapeutic efficacy [30]. By integrating realistic airway geometries into computational models, researchers can improve the precision of drug delivery simulations, leading to better-targeted therapies and reduced systemic side effects. This approach is especially important for patients with unique anatomical features or those suffering from respiratory conditions that alter airway geometry [31].

Current characteristic upper airway tracheobronchial models either omit realistic aspects for the sake of simplicity and general applicability or are highly realistic but do not account for intersubject variability and, therefore, have limited scope. Therefore, there is a need to address this limitation through the construction of a patient-specific model that matches certain average geometric characteristics and may be used for computational or experimental analysis.

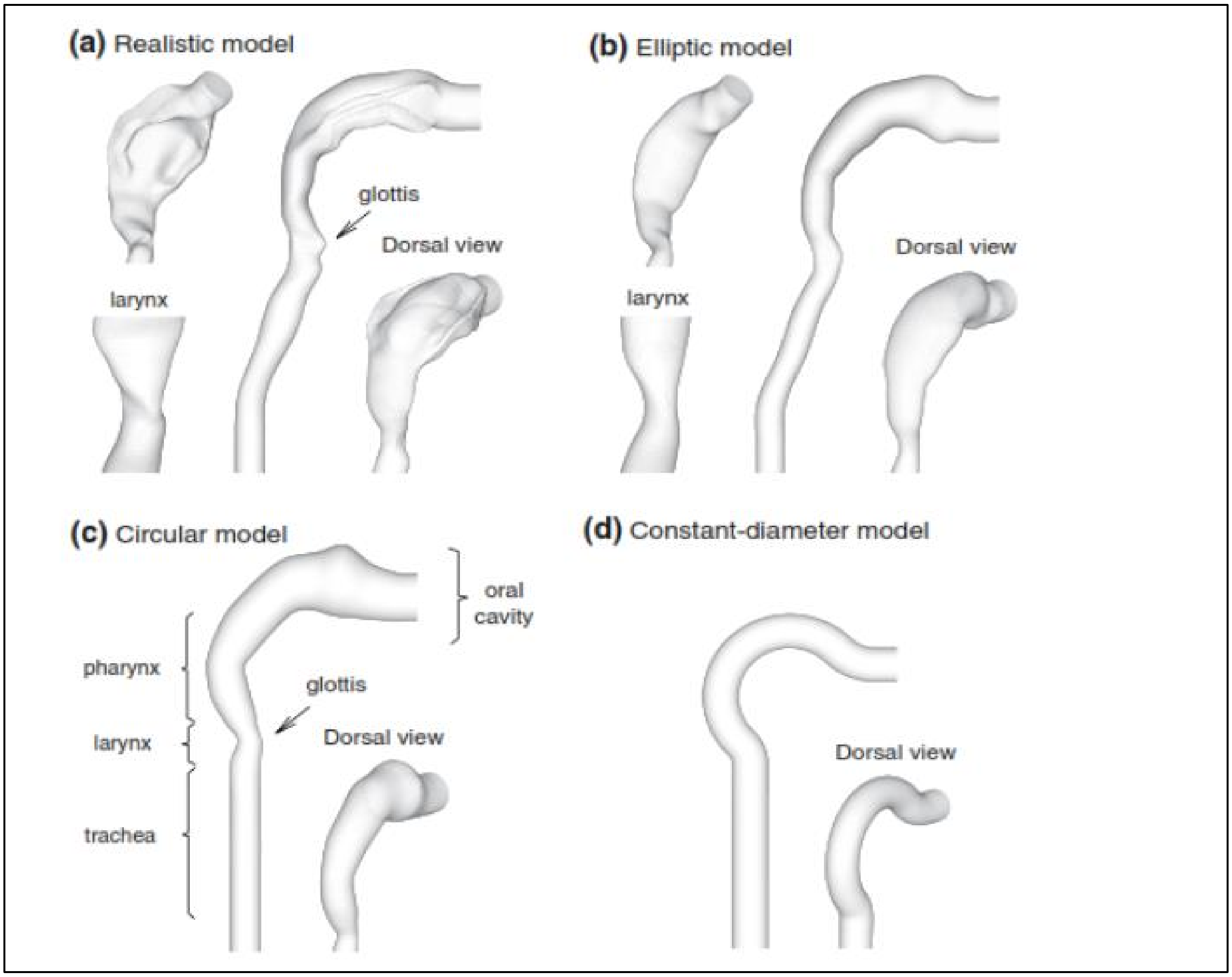

Fig 2.9 Geometric surface models of the extrathoracic oral airway, including the **(a)** realistic, **(b)** elliptic, **(c)** circular, and **(d)** constant-diameter models [29].

The efficacy of drug delivery is partly dependent on the deposition site within the airways, making quantifying regional deposition crucial for assessing and optimizing systemic delivery of drugs with limited lung bioavailability and for topical treatments targeting specific lung sites. CFD models can complement clinical and experimental tests, providing detailed information on regional deposition patterns. These models allow for repeated numerical experiments to isolate the effects of specific variables, which is challenging to achieve experimentally or clinically [32]. The airflow in the respiratory tract can be turbulent, transitional between laminar and turbulent, or purely laminar, depending on the inlet flow rate and the branching generation of the airways.

When simulating turbulent flows, several modeling approaches are available, each with its own advantages and limitations. Direct Numerical Simulation (DNS) is considered the gold standard for turbulence modeling, as it resolves all scales of turbulence without any approximations.

However, this level of detail comes at an immense computational cost, making it impractical for most real-world applications, especially those involving complex geometries or high Reynolds numbers. In contrast, Reynolds-Averaged Navier-Stokes (RANS) models offer a computationally efficient solution by averaging the Navier-Stokes equations over time. While RANS turbulence models such as k-ω and k-ε are widely used in engineering applications and can handle intricate flow scenarios, it often lacks the ability to capture transient behaviors and the detailed turbulence structures present in unsteady flows. The reliance on turbulence closure models in RANS can also introduce inaccuracies, particularly in highly turbulent environments. Large Eddy Simulation (LES) emerges as a favorable middle ground, resolving the larger turbulent structures directly while modeling, the smaller scales using a subgrid-scale model. This approach allows for a more accurate representation of significant flow features and is less computationally demanding than DNS. LES provides a detailed understanding of large-scale turbulence dynamics, making it particularly useful for applications requiring insight into transient behavior and complex interactions within the flow. Thus, many researchers regard LES as a suitable and reliable method for simulating airflow within this complex geometry [33,34].

In a research study, Cui and Gutheil [35] examined the impact of LES on the unsteady flow field in an idealized human MT model. They compared the average gas velocity in a constricted tube against experimental and numerical data derived from RANS equations, specifically utilizing low Reynolds number (LRN) k-ω and shear stress transport k-ω models. Their findings indicated notable improvements, particularly within the transitional regime of laminar to turbulent flow. Additionally, as shown in **Fig 2.10**, they discovered that accounting for the unsteady state of the flow field significantly influences particle movement in the upper respiratory tract, which is critical for drug delivery.

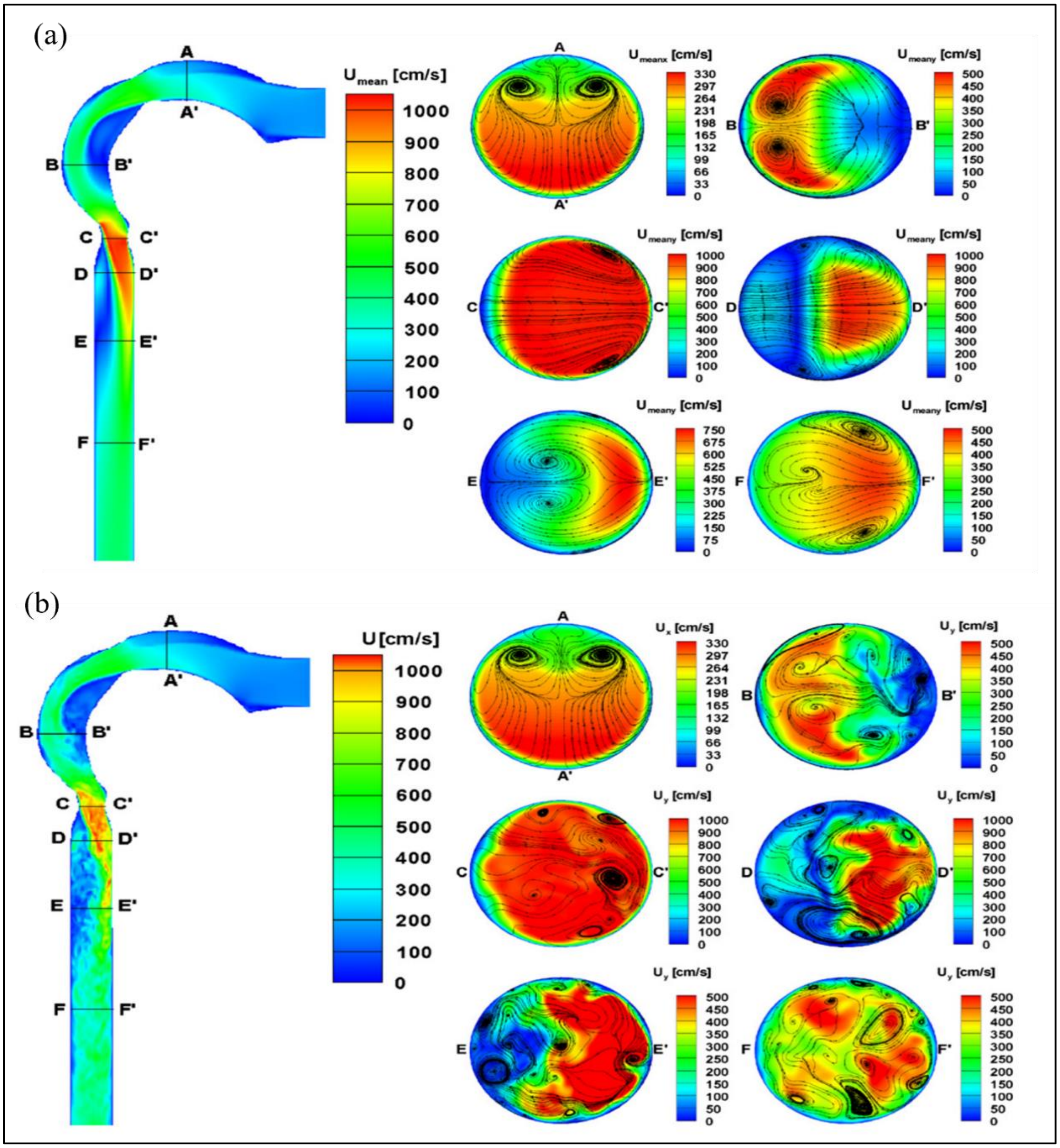

Fig 2.10 velocity contours at mid-plane (left), and axial velocity contour and secondary streams at cross-sections (right) of **(a)** steady, and **(b)** unsteady flow field [35].

In another study, Jayaraju *et al.* [36] compared the performance of RANS k-ω (without near-wall corrections), Detached Eddy Simulation (DES), and LES methods in predicting particle deposition in a human MT. They assessed MT deposition for particle diameters of 2, 4, 6, 8, and 10 μm at a standard flow rate of 30 L/min. Both LES and DES demonstrated significant improvements over the RANS k-ω model in predicting deposition for particles smaller than 5 μm, as shown in **Fig 2.11**. For larger particles, the predictions were comparable between RANS k-ω and the LES/DES approaches. The study concluded that for simulating medication aerosols inhaled at a steady flow rate of 30 L/min, LES and DES yield more accurate results than the RANS k-ω model.

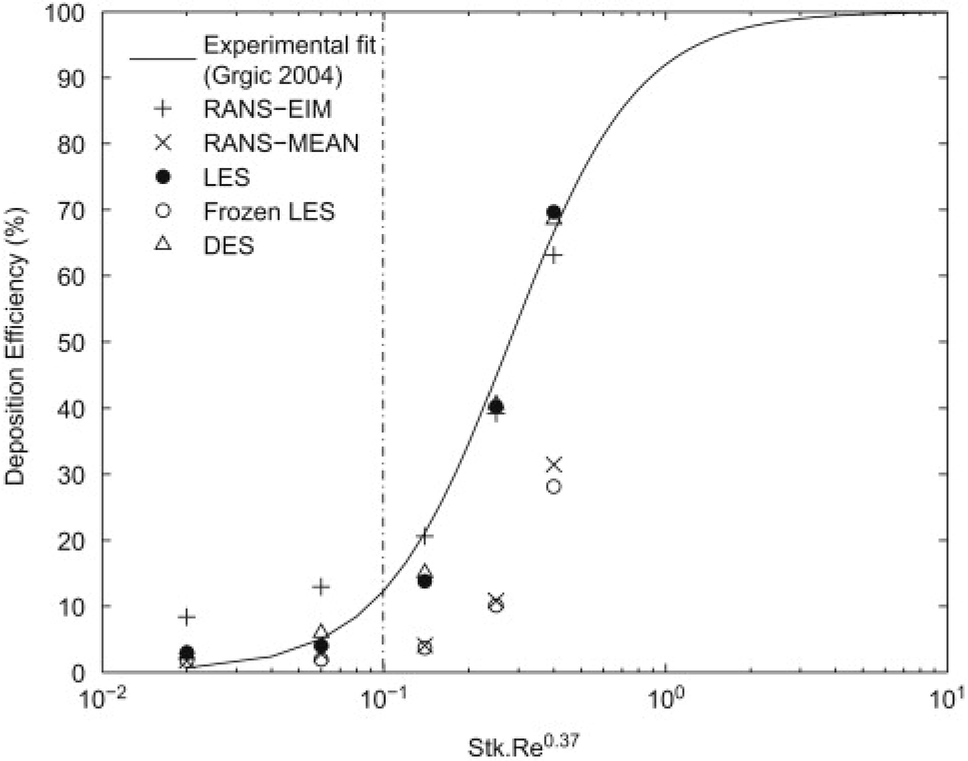

Fig 2.11 The simulated total deposition, expressed as a percentage of particles entering the model, was analyzed as a function of the Stokes and Reynolds numbers [36].

2.2 Research Gaps

A thorough review of the literature has revealed the following research gaps:

- While SMIs are effective for delivering medication to the lungs, there is a noticeable lack of extensive experimental and computational studies on SMIs when compared to traditional inhalation devices such as pMDIs and DPIs.
  - The existing *in-vitro* setups do not accurately mimic real-world SMI usage, which is necessary to validate computational models effectively.
  - CFD studies on aerosol behavior lack robust validation through *in-vitro* experiments, which is necessary to ensure accurate predictions of flow behavior and particle size distributions.

- The impact of the SMI device design, particularly its nozzle design and specifications, on aerosol deposition in the airway, has not been thoroughly studied, especially concerning improper SMI usage.
- The influence of factors such as inhalation profile, mucus layer, airway movement, nasal inhalation, and tongue position and movement during medication delivery using SMI devices has been largely neglected in both experimental and numerical studies.
- The accuracy of numerical methods used in simulating aerosol behavior in the respiratory tract is often limited. Mesh modification is necessary to improve the resolution and capture finer details of particle dynamics, while also balancing computational efficiency and costs. More advanced numerical techniques are needed to ensure greater accuracy without significantly increasing computational time and resources.
- The effect of plume or airflow temperature on aerosol particle deposition and size distribution remains underexplored. Temperature variations, particularly within the inhalation plume, can influence the viscosity and behavior of the aerosolized particles, potentially affecting deposition patterns and lung delivery efficiency.
- There is insufficient research on the optimization of SMI formulations, including the use of excipients and additives, to enhance particle formation and deposition within the lungs, particularly under varying inhalation conditions.
- Research has primarily focused on adult airway structures, neglecting the unique anatomical features of pediatric airways that affect aerosol distribution and deposition.

2.3 Research Objectives

The focus of this study is to improve the efficiency of drug delivery to the lungs using an SMI device. This will be achieved through a combination of experimental investigations and numerical simulations. Experimental validation is crucial for ensuring the accuracy of the numerical simulations. One of the key aspects of this study involved building a three-dimensional (3D)-printed mouth-throat geometry that includes realistic anatomical features for more accurate and localized deposition measurements. The printed geometries were attached to the next-generation impactor (NGI) for experimental analysis. The NGI, which evaluates particle deposition and size distribution, was used to capture aerosolized particles based on their size at various stages. To minimize the risk of evaporation, the NGI cooling box was employed, ensuring that volatile components in the aerosol do not evaporate during the experiments. This can be beneficial when the evaporation factor is not considered in the numerical model. The high-performance liquid chromatography (HPLC) was also used to quantify the Active Pharmaceutical Ingredient (API) deposited at each stage and collection cup of the NGI, ensuring the reliability of the simulation predictions. The research is structured around three distinct objectives, each addressing a specific aspect of drug delivery efficiency to the lungs. The main goal is to accurately predict drug deposition to better understand SMI drug behavior within the human respiratory tract (HRT), leading to more effective pulmonary drug delivery and a reduction in potential side effects. These objectives are outlined below:

Objective 1: **Effective Use of SMI: Essential for Minimizing Drug Loss in the Mouth**

The first objective of this study is to model drug aerosol dynamics, size distribution, and deposition of an SMI using the k-ω viscous model along with DPM to track aerosol trajectories inside both idealized and standard mouth geometries. This initial phase aims to develop a model that accurately predicts the behavior of the SMI aerosol plume at the onset of actuation and within the mouth, where most drug loss occurs. To investigate the effects of misusing the SMI inside the mouth, three nozzle orifice locations along the centerline of the mouth cavity and two nozzle angles for the idealized mouth were considered. The impact of inhalation flow rates within both mouth cavities was determined. Aerosol droplet behavior and its effect on flow patterns, aerosol deposition, and size distribution were compared between standard and idealized mouths.

Objective 2: **Impact of Nasal and Oral Breathing on SMI Aerosol Drug Delivery**

The second objective is to determine the effect of combined oral and nasal inhalation on airflow patterns, aerosol deposition, and size distribution inside a human mouth-throat geometry using an SMI. An available induction port was modified to include a nasal cavity atop the induction port to mimic nasal airflow. To address a wide range of oral/nasal combined flow rates, six different flow rate ratios were applied with a total flow rate of 30 L/min. Since the interaction between oral and nasal flows significantly impacts the fate of aerosols within the geometry, a shear stress transport (SST) k-ω viscous model was employed to improve accuracy. Turbulent kinetic energy and vortex structures were additional parameters examined in our model.

Objective 3: **Pediatric Airflow Patterns and SMI Drug Delivery: Effects of Tongue Position with Varied Inhalation Profiles**

To investigate the effects of tongue position on droplet deposition, size distribution, and airflow patterns within a realistic pediatric mouth-throat geometry using an SMI. Specifically, the study aims to analyze how varying tongue positions, different fixed flow rates, realistic COPD inhalation profiles, and two-step pulsatile inhalation patterns influence deposition efficiency and droplet size distribution. Utilizing LES, the study seeks to understand the interplay between airflow dynamics, tongue positioning, and drug droplet properties. Additionally, the study endeavors to develop a correlation to predict mouth deposition percentages across different flow rates and to quantify how overall deposition in pediatric geometries compares to that in adult mouth-throat structures.

2.4 Nomenclature

Abbreviation

API	Active pharmaceutical Ingredient
COPD	Chronic Obstructive Pulmonary Disease
CFD	Computational Fluid Dynamics
CT	Computed Tomography
DES	Detached Eddy Simulation
DNS	Direct Numerical Simulation
DPM	Discrete Phase Model
HPLC	High Performance Liquid Chromatography
HRT	Human Respiratory Tract
IP	Standard Induction Port
LES	Large eddy Simulation
LRN	Low Reynolds Number
MP	Mouthpiece
MMD	Mass Median Diameter
MRI	Magnetic Resonance Imaging
NGI	Next Generation Impactor
pMDI	Pressurized Metered Dose Inhaler
RANS	Reynolds Averaged Navier Stokes

SMI	Soft Mist Inhaler
SST	Shear Stress Transport
3D	Three dimensional

Notations

d_p	particle diameter, μm
ω	turbulent kinetic energy, m^2/s^2
ε	turbulent dissipation rate, 1/s

2.5 References

[1] S. Smith, J. Bernstein, Inhalation Aerosols, Therapeutic uses of lung aerosols, Marcel Dekker, New York, 1996.

[2] R.N. Dalby, J. Eicher, B. Zierenberg, Development of Respimat® soft mist^{TM} inhaler and its clinical utility in respiratory disorders, Medical Devices: Evidence and Research 4 (2011). https://doi.org/10.2147/MDER.S7409.

[3] F. Dastoorian, L. Pakzad, J. Kozinski, E. Behzadfar, A CFD Investigation on the Aerosol Drug Delivery in the Mouth–Throat Airway Using a Pressurized Metered-Dose Inhaler Device, Processes 10 (2022). https://doi.org/10.3390/pr10071230.

[4] M.G. Cochrane, M. V. Bala, K.E. Downs, J. Mauskopf, R.H. Ben-Joseph, Inhaled corticosteroids for asthma therapy: Patient compliance, devices, and inhalation technique, Chest 117 (2000) 542–550. https://doi.org/10.1378/chest.117.2.542.

[5] P. Rogliani, L. Calzetta, A. Coppola, F. Cavalli, J. Ora, E. Puxeddu, M.G. Matera, M. Cazzola, Optimizing drug delivery in COPD: The role of inhaler devices, Respir Med 124 (2017) 6–14. https://doi.org/10.1016/j.rmed.2017.01.006.

[6] M. Molimard, C. Raherison, S. Lignot, F. Depont, A. Abouelfath, N. Moore, Assessment of Handling of Inhaler Devices in Real Life: An Observational Study in 3811 Patients in Primary Care, 2003. www.liebertpub.com.

[7] W. Kamin, T. Genz, S. Roeder, G. Scheuch, T. Trammer, R. Juenemann, R. Cloes, Mass Output and Particle Size Distribution of Glucocorticosteroids Emitted from Different Inhalation Devices Depending on Various Inspiratory Parameters, 2002. www.liebertpub.com.

[8] L. Agertoft, S. Pedersen, K. Nikander, Drug Delivery from the Turbuhaler and Nebuhaler Pressurized Metered Dose Inhaler to Various Age Groups of Children with Asthma, Mary Ann Liebert, Inc. Pp, 1999. www.liebertpub.com.

[9] H. Dean R, Nebulizers: Principles and Performance, Respir Care 45 (2000) 609–622.

[10] V. Komalla, C.Y.J. Wong, I. Sibum, B. Muellinger, W. Nijdam, V. Chaugule, J. Soria, H.X. Ong, N.A. Buchmann, D. Traini, Advances in soft mist inhalers, Expert Opin Drug Deliv 20 (2023) 1055–1070. https://doi.org/10.1080/17425247.2023.2231850.

[11] T. Iwanaga, Y. Tohda, S. Nakamura, Y. Suga, The Respimat® Soft Mist Inhaler: Implications of Drug Delivery Characteristics for Patients, Clin Drug Investig 39 (2019) 1021–1030. https://doi.org/10.1007/s40261-019-00835-z.

[12] B. Zierenberg, Optimizing the in Vitro Performance of Respimat, Mary Ann Liebert, Inc. Pp. S, 1999. www.liebertpub.com.

[13] H. Wachtel, S. Kattenbeck, S. Dunne, B. Disse, The Respimat® Development Story: Patient-Centered Innovation, Pulm Ther 3 (2017) 19–30. https://doi.org/10.1007/s41030-017-0040-8.

[14] M. Spallek, D. Hochrainer, H. Wachtel, M. Spallek, Optimizing nozzles for soft mist inhalers, Respiratory Drug Delivery VIII (2002).

[15] M. Saeedipour, Atomization of two colliding micro liquid jets in a respiratory inhaler: A computational study, ILASS–Europe 2019, 29th Conference on Liquid Atomization and Spray Systems, 2-4 September 2019, Paris, France (2019).

[16] P. Worth Longest, M. Hindle, Evaluation of the respimat soft mist inhaler using a concurrent cfd and in vitro approach, J Aerosol Med Pulm Drug Deliv 22 (2009) 99–112. https://doi.org/10.1089/jamp.2008.0708.

[17] H. Wachtel, S. Kattenbeck, S. Dunne, The Respimat Ò Development Story : Patient-Centered Innovation, Pulm Ther 3 (2017) 19–30. https://doi.org/10.1007/s41030-017-0040-8.

[18] P. Worth Longest, M. Hindle, Evaluation of the respimat soft mist inhaler using a concurrent cfd and in vitro approach, J Aerosol Med Pulm Drug Deliv 22 (2009) 99–112. https://doi.org/10.1089/jamp.2008.0708.

[19] W. Kamin, M. Frank, S. Kattenbeck, P. Moroni-Zentgraf, H. Wachtel, S. Zielen, A Handling Study to Assess Use of the Respimat® Soft Mist^{TM} Inhaler in Children under 5 Years Old, J Aerosol Med Pulm Drug Deliv 28 (2015) 372–381. https://doi.org/10.1089/jamp.2014.1159.

[20] W.R. Ke, W.J. Wang, T.H. Lin, C.L. Wu, S.H. Huang, H.D. Wu, C.C. Chen, In vitro evaluation of aerosol performance and delivery efficiency during mechanical ventilation between soft mist inhaler and pressurized metered-dose inhaler, Respir Care 65 (2020) 1001–1010. https://doi.org/10.4187/respcare.06993.

[21] D. Hochrainer, H. Hölz, C. Kreher, L. Scaffidi, M. Spallek, H. Wachtel, Comparison of the Aerosol Velocity and Spray Duration of Respimat ® Soft Mist^{TM} Inhaler and Pressurized Metered Dose Inhalers, 2005. www.liebertpub.com.

[22] A. Alatrash, R. Mehri, N. Ogrodnik, E. Matida, F. Fiorenza, Experimental Study of Spiriva Respimat Soft Mist Inhaler Spray Characterization: Size Distributions and Velocity, J Aerosol Med Pulm Drug Deliv 32 (2019) 293–302. https://doi.org/10.1089/jamp.2018.1501.

[23] Z. Xu, A.J. Hickey, The Physics of Aerosol Droplet and Particle Generation from Inhalers, in: S. H.D.C., H. A.J. (Eds.), Controlled Pulmonary Drug Delivery, 1st ed., Springer New York, New York, NY, 2011: pp. 75–100. https://doi.org/10.1007/978-1-4419-9745-6_4.

[24] Z. Zhang, C. Kleinstreuer, Computational analysis of airflow and nanoparticle deposition in a combined nasal-oral-tracheobronchial airway model, J Aerosol Sci 42 (2011) 174–194. https://doi.org/10.1016/j.jaerosci.2011.01.001.

[25] B. Wang, Z. Peng, Q. Liu, X. Chen, Effect of airflow rate on droplet deposition of an impinging-jet inhaler in the human respiratory tract, Int J Pharm 661 (2024). https://doi.org/10.1016/j.ijpharm.2024.124408.

[26] P.R. Byron, M. Hindle, C.F. Lange, P.W. Longest, D. McRobbie, M.J. Oldham, B. Olsson, C.G. Thiel, H. Wachtel, W.H. Finlay, In vivo-in vitro correlations: Predicting pulmonary drug deposition from pharmaceutical aerosols, J Aerosol Med Pulm Drug Deliv 23 (2010). https://doi.org/10.1089/jamp.2010.0846.

[27] M.J. LeBelle, S.J. Graham, E.D. Ormsby, R.M. Duhaime, R.C. Lawrence, R.K. Pike, Metered-dose inhalers. II. Particle size measurement variation, Int J Pharm 151 (1997) 209–221. https://doi.org/10.1016/S0378-5173(97)04905-3.

[28] J. Xi, J.E. Yuan, M. Yang, X. Si, Y. Zhou, Y.S. Cheng, Parametric study on mouth–throat geometrical factors on deposition of orally inhaled aerosols, J Aerosol Sci 99 (2016) 94–106. https://doi.org/10.1016/j.jaerosci.2016.01.014.

[29] J. Xi, P.W. Longest, Transport and deposition of micro-aerosols in realistic and simplified models of the oral airway, Ann Biomed Eng 35 (2007) 560–581. https://doi.org/10.1007/s10439-006-9245-y.

[30] F. Lizal, J. Elcner, J. Jedelsky, M. Maly, M. Jicha, Á. Farkas, M. Belka, Z. Rehak, J. Adam, A. Brinek, J. Laznovsky, T. Zikmund, J. Kaiser, The effect of oral and nasal breathing on the deposition of inhaled particles in upper and tracheobronchial airways, J Aerosol Sci 150 (2020). https://doi.org/10.1016/j.jaerosci.2020.105649.

[31] J. Xi, J.E. Yuan, M. Yang, X. Si, Y. Zhou, Y.S. Cheng, Parametric study on mouth–throat geometrical factors on deposition of orally inhaled aerosols, J Aerosol Sci 99 (2016) 94–106. https://doi.org/10.1016/j.jaerosci.2016.01.014.

[32] P. Koullapis, S.C. Kassinos, J. Muela, C. Perez-Segarra, J. Rigola, O. Lehmkuhl, Y. Cui, M. Sommerfeld, J. Elcner, M. Jicha, I. Saveljic, N. Filipovic, F. Lizal, L. Nicolaou, Regional aerosol deposition in the human airways: The SimInhale benchmark case and a critical assessment of in silico methods, European Journal of Pharmaceutical Sciences 113 (2018) 77–94. https://doi.org/10.1016/j.ejps.2017.09.003.

[33] C. Kleinstreuer, Z. Zhang, Airflow and particle transport in the human respiratory system, Annu Rev Fluid Mech 42 (2010) 301–334. https://doi.org/10.1146/annurev-fluid-121108-145453.

[34] C.G. Ball, M. Uddin, A. Pollard, High resolution turbulence modelling of airflow in an idealised human extra-thoracic airway, Comput Fluids 37 (2008) 943–964. https://doi.org/10.1016/j.compfluid.2007.07.021.

[35] X.G. Cui, E. Gutheil, Large eddy simulation of the unsteady flow-field in an idealized human mouth-throat configuration, J Biomech 44 (2011) 2768–2774. https://doi.org/10.1016/j.jbiomech.2011.08.019.

[36] S.T. Jayaraju, M. Brouns, C. Lacor, B. Belkassem, S. Verbanck, Large eddy and detached eddy simulations of fluid flow and particle deposition in a human mouth-throat, J Aerosol Sci 39 (2008) 862–875. https://doi.org/10.1016/j.jaerosci.2008.06.002.

Chapter 3 – Experimental Methodology

3.1 Experimental Setup

3.1.1 Deposition of Particles in the Respiratory Tract

As discussed in the introduction and literature review, drug deposition is the most important parameter that determines the efficiency of drug delivery to the lungs. When aerosol particles emitted from soft mist inhalers (SMIs) enter the human respiratory tract (HRT), they deposit in different regions based on factors such as lung geometry, breathing patterns, aerosol morphology, particle size, and density [1]. The aerodynamic size of particles is a critical factor in determining the regional deposition of aerosolized particles within the respiratory tract, as it influences how aerosols distribute following inhalation [2]. The aerodynamic diameter of a particle is the diameter of a theoretical spherical particle with a unit density ($\rho = 1.00$ g/cm^3) that would settle at the same velocity as the actual particle. Particles larger than 5-6 μm tend to deposit in the mouth, throat, and at branching points in the upper airways, a process known as oropharyngeal deposition. Smaller particles, typically in the 2-5 μm range, are more likely to reach and settle in the deeper regions of the lungs. Those smaller than 2 μm may either deposit in the lungs due to random Brownian motion or remain suspended in the airflow and be exhaled. The optimal particle size for effective deposition in the human lung is approximately 2-5 μm [3].

Cascade impactors are widely used instruments for in vitro evaluation of delivery efficiency in both inhalers and nebulizers, as they have the capability to directly classify inhaled particles and droplets based on their aerodynamic diameters. Unlike methods that sample only a portion of the dose, these impactors measure the particle size distribution of the entire drug dose delivered. This allows for simultaneous quantification of the mass of the active ingredient across different size ranges within the formulation, independent of any non-drug substances present in the sample [4]. In addition to examining the deposition patterns of aerosolized powders, an impactor allows for the calculation of key aerodynamic parameters of aerosols that determine where particles deposit within the respiratory tract. These include the Mass Median Aerodynamic Diameter (MMAD), the Geometric Standard Deviation (GSD), the Fine Particle Dose (FPD), and the Fine Particle Fraction (FPF) [1].

The MMAD signifies the aerodynamic diameter at which half of the aerosolized drug mass comprises particles smaller than that size, as identified from the cumulative distribution curve at the 50% point. An MMAD of 5 µm or less is desirable to ensure predominant deposition in the smaller airways, as particles with larger MMADs tend to settle in the upper regions of the respiratory tract.

The GSD measures the variability of particle sizes within the aerosol. It is calculated by dividing the particle diameter at the 84.1% point on the cumulative distribution curve by the MMAD. A larger GSD indicates a wider range of particle sizes, resulting in aerosol deposition at multiple sites throughout the respiratory system. Ideally, aerosols should have a ($GSD < 2$) to achieve near-monodispersity, meaning the particles are more uniform in size. This uniformity enhances deposition at the targeted site within the respiratory tract, thereby increasing the efficacy of the treatment.

FPD refers to the portion of a prescribed medication dose that consists of particles small enough—typically 5 µm in diameter or less—to penetrate the lungs during inhalation. The FPF is the FPD expressed as a percentage of the total dose delivered to the patient [5].

The deposition of aerosol particles at various stages within an impactor can generally be linked to how drugs deposit in different lung regions. By observing these patterns, the in vivo deposition can be predicted within the human lungs: larger particles tend to deposit on stages that correspond to the upper airways, while smaller particles settle on stages representing the deeper lung areas. Although impactors are useful for anticipating the deposition patterns of inhaled drugs in the respiratory tract, they are not exact replicas of the lung environment. This is due to differences in geometry at the point where particles impact, the hardness and coating of collection surfaces, and the constant flow rate used during operation, which contrasts with the variable flow rates in human lungs. It is also important to note that the stages of an impactor do not directly match specific deposition sites within the lung [6].

The primary mechanisms contributing to particle deposition within the respiratory tract, as shown in **Fig 3.1,** are inertial impaction, gravitational sedimentation, Brownian diffusion, and, to a lesser extent, interception and electrostatic precipitation [7].

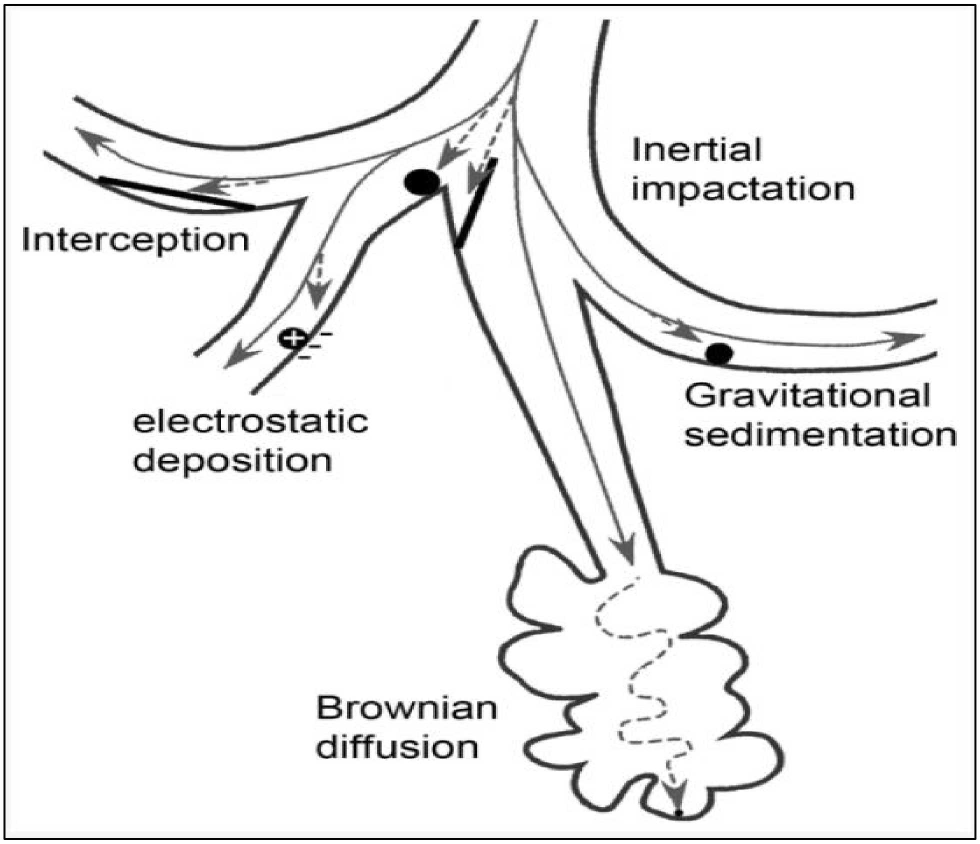

Fig 3.1 Mechanisms of particle deposition in the human airway [7].

Inertial impaction is the primary mechanism of particle deposition in the respiratory tract. Inertia refers to a particle's tendency to resist changes in its motion. Inertial impaction occurs at the bifurcations of the respiratory tract, where the airflow direction changes. In this process, particles in the airstream continue along their original path rather than aligning with the altered airflow. Stokes (St) number (Eq. 3.1, [8]) is a dimensionless quantity used to predict deposition caused by impaction for a particle traveling through an airway.

$$\mathrm{St} = \frac{\rho_d \, d_d^2 \vec{u}}{18\mu R} \tag{3.1}$$

Here, ρ_d represents the droplet density, d_p is the particle diameter, $\vec{u}$ is the air velocity, μ is the air viscosity, and R is the airway radius. The St number indicates that the likelihood of a particle depositing due to inertial impaction is directly proportional to the particle density, the square of the particle diameter, and the air velocity, while being inversely proportional to the airway radius. Inertial impaction is a velocity-dependent mechanism, which causes most particles larger than 5 μm, particularly those greater than 10 μm, to deposit in the upper respiratory tract and large conducting airways [8].

The second mechanism of particle deposition is gravitational sedimentation (Eq. 3.2, [9]), which refers to the process by which particles settle under the influence of gravity. The terminal settling velocity ($\vec{u}_t$) of particles falling due to gravity is described by Stokes law.

$$\vec{u}_t = \frac{(\rho_d - \rho) d_d^2 \vec{g}}{18 \mu R} \tag{3.2}$$

Here, ρ represents the air density, and $\vec{g}$ is the gravitational constant. According to Eq 3.2, the gravitational sedimentation of a respirable particle depends on its size and density. This is a time-dependent process, with deposition increasing as the residence time of a particle in the airways and alveoli lengthens, such as during slow, steady breathing or breath-holding. Gravitational sedimentation is a key mechanism for particle deposition in the size range of 0.5-2 µm, particularly in the small airways and alveoli [9].

Another deposition mechanism is Brownian diffusion which occurs due to the random motion of particles, which results from their collisions with gas molecules. This motion causes particles to move from regions of high to low concentration, leading to their transfer from the aerosol cloud to the walls of the airways. The rate of Brownian diffusion (D) is described by the Stokes-Einstein equation (Eq. 3.3, [9]), which is shown as:

$$D = \frac{K_B T}{3 \pi \mu d_d} \tag{3.3}$$

where K_B is the Boltzmann constant, and T is the absolute temperature. Unlike inertial impaction and gravitational sedimentation, which increase with particle size (Eqs. (3.1) and (3.2)), Brownian diffusion deposition is inversely proportional to particle diameter. This means that as particle size decreases, deposition by Brownian diffusion increases, becoming the dominant mechanism for particles, especially particles smaller than 1 µm in the deep lungs (**Fig 3.2**) [9].

Interception happens when the distal end of a particle encounters the airway wall, even though its center of mass remains within the gas phase streamlines. While this mechanism has little impact on spherical particles, it becomes significant for the deposition of elongated particles with small aerodynamic diameters.

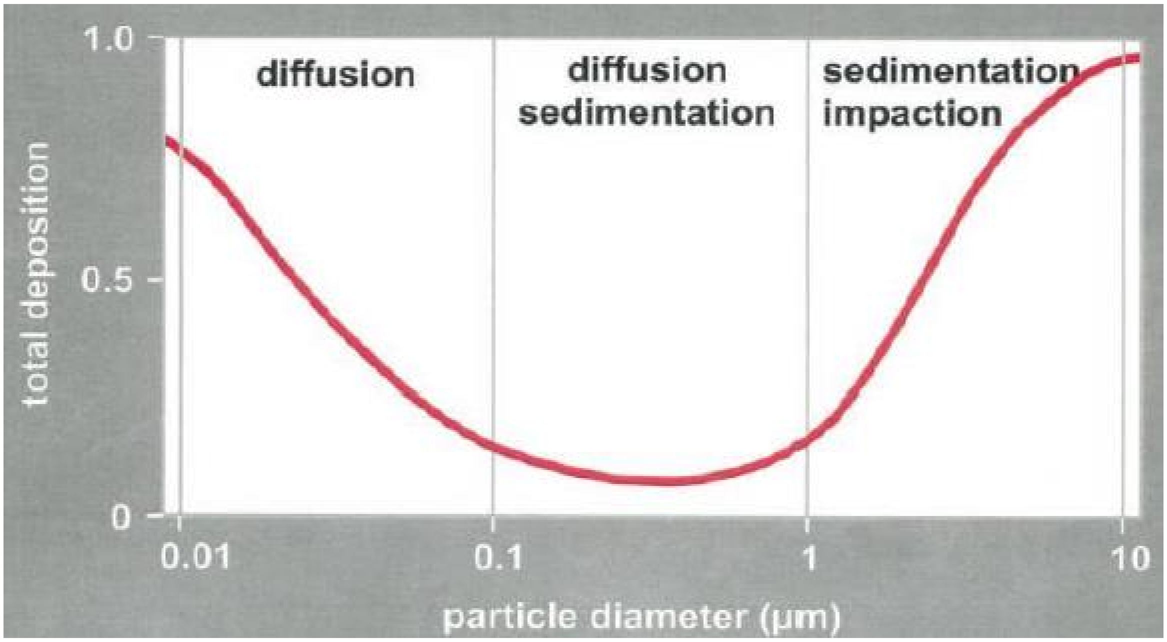

Fig 3.2 Total deposition of unit-density spheres inhaled orally at rest in the human respiratory tract [10].

Finally, during aerosolization, particles can become electrostatically charged. Deposition of charged particles through electrostatic precipitation may occur either by inducing an opposing charge on the airway surfaces, leading to electrostatic attraction, or through repulsion between similarly charged particles, which directs them towards the airway walls [11].

The Cascade impactor’s function is based on the principle of inertial impaction, where aerosolized particles are separated according to their inertia, which depends on their mass and velocity. By maintaining a constant particle velocity, the aerodynamic particle size can be determined. Aerosol droplets or particles are drawn through the impactor at a constant airflow rate and are separated by size across different stages. Larger and heavier particles with higher inertia settle in the initial stages, while smaller and lighter particles with lower inertia are collected in the later stages [12]. The cut-off diameters for each stage of a cascade impactor depend on the airflow rate through the device. They are defined as the particle sizes with a collection efficiency of 50%, while the collection efficiency is determined using the St number [13]. Particles larger than the cut-off size are collected in the cup at that stage, while smaller particles are carried to the next stage by the airstream. Various impactors approved by the USP include the Andersen Cascade Impactor (ACI), Multi-Stage Liquid Impinger (MSLI), and the Next Generation Impactor (NGI) [14].

3.1.2 Next Generation Impactor

The Next Generation Impactor (NGI) was used in our experiments (**Fig 3.3(a)**). Unlike the Andersen Cascade Impactor (ACI) (**Fig 3.3(b)**) and Multi-Stage Liquid Impinger (MSLI) (**Fig 3. 3(c)**), the NGI is arranged horizontally rather than stacked vertically. The use of collection cups as impaction surfaces simplifies handling and allows for easier design modifications [20]. The NGI has been found to be operable across a broad range of flow rates, making it especially suitable for the analysis of aerosolized dry powders [4,13].

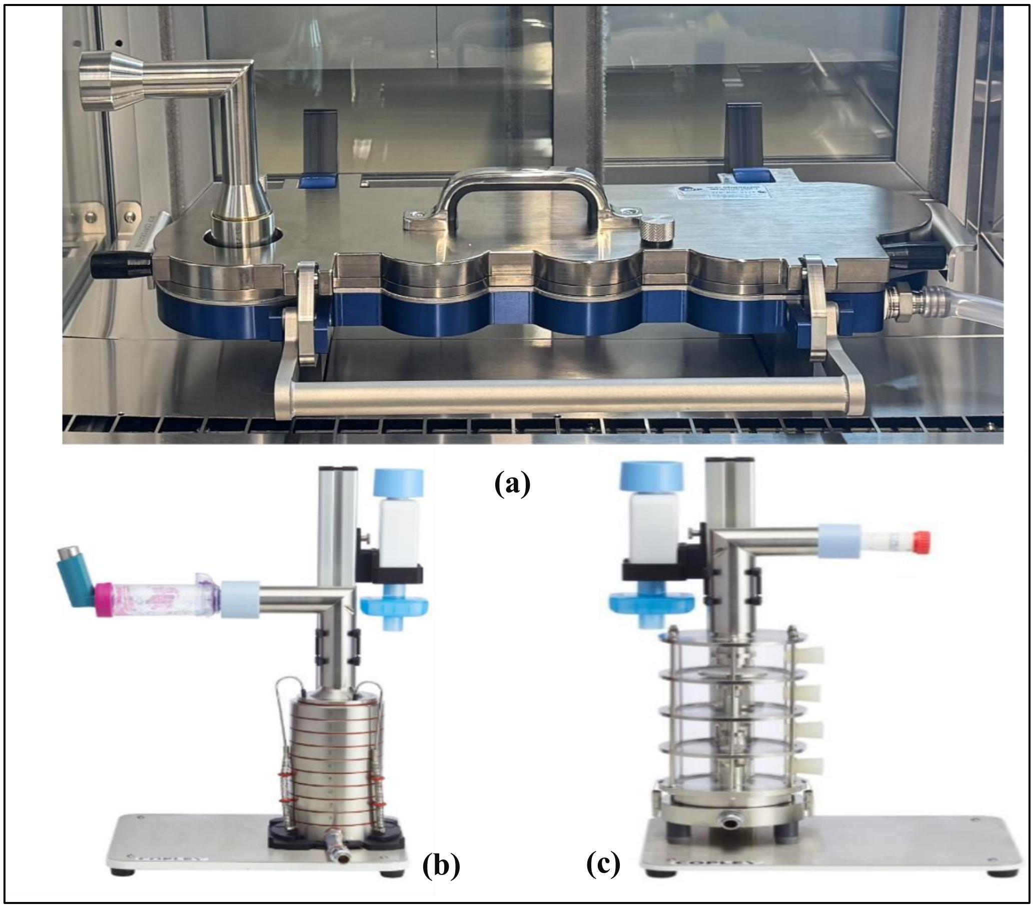

Fig 3.3 (a) Next-generation impactor (NGI), **(b)** Andersen cascade impactor (Copley Instruments Ltd, UK), and **(c)** multi-stage liquid impinger (Copley Instruments Ltd, UK).

The NGI is a planar impactor with seven stages, also known as collection cups or impaction surfaces. These removable cups are arranged horizontally, with a micro-orifice collector (MOC) at the end (**Fig 3.4**). The NGI consists of a base that supports a frame holding the collection cups, and a lid that secures the seal body containing eight nozzle pieces. The lid also includes inter-stage passageways. The lid is attached to the seal body with two limited torque screws. Each eight nozzle piece corresponds to one of the seven stages and the MOC. The nozzle pieces are designed with specific numbers and holes of different sizes according to the stage they correspond to, with the exception of the first stage. O-rings surrounding the nozzle pieces ensure a proper seal to prevent leakage during aerosol testing. The collection cups are tear-shaped, with the larger end positioned directly beneath the nozzle for particle impaction. Airflow moves from this larger impaction region towards the smaller end, where it is drawn upward through a cavity in the lid and directed into the next stage.

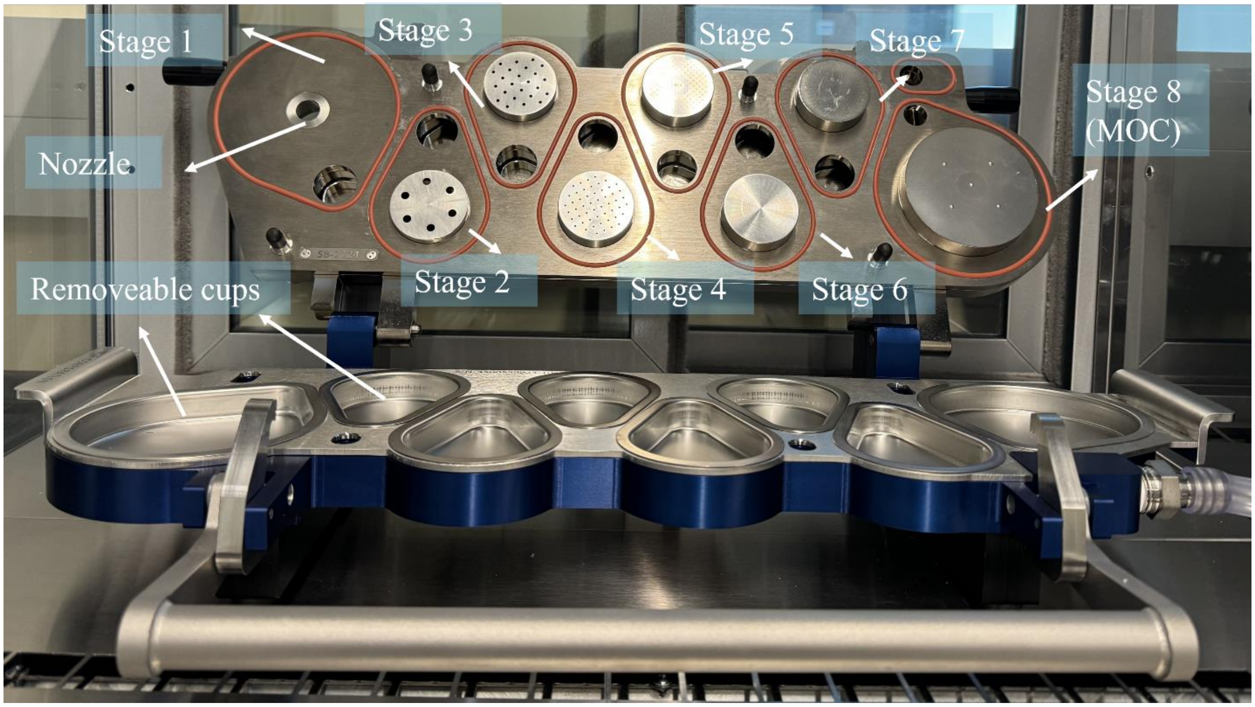

Fig 3.4 NGI in open configuration.

The collection cups for stage 1, and the MOC are larger than those for the other stages to minimize secondary impaction, which occurs when particles impact the walls of the cup. The smaller size of the other stages helps avoid secondary impaction, as the particles deposited there are smaller. The MOC primarily captures the smaller particles that pass through the previous seven stages without being collected. An external filter holder, attached downstream of the MOC, contains a glass fiber insert to collect any remaining smaller particles that the MOC did not capture. The NGI is sealed by locking the lid onto the bottom frame using a past-center cam lock handle mechanism at the front of the device. The cut-off diameters for the relevant stages at volumetric flow rates of 15, 30, 60, and 100 L/min are provided in **Table 3.1**.

Table 3.1 NGI cut-off-sizes at different flow rates [12].

Stage	15 L/min	30 L/min	60 L/min	100 L/min
Stage 1	14.10	11.72	8.06	6.12
Stage 2	8.61	6.40	4.46	3.42
Stage 3	5.39	3.99	2.82	2.18
Stage 4	3.30	2.30	1.66	1.31
Stage 5	2.08	1.36	0.94	0.72
Stage 6	1.36	0.83	0.55	0.40
Stage 7	0.98	0.54	0.34	0.24
Stage 8	0.70	0.36	0.14	0.07

The induction port (IP) is a key component of the NGI, serving as the entry point for the aerosolized drug. It is an L-shaped stainless-steel tube, with one end inserted into the seal body above stage 1 and the other end connecting to the inhalation device, such as an SMI or pMDI. The IP ensures proper alignment of the inhaler mouthpiece, creating an airtight seal between the port and the device. This alignment maintains the mouthpiece in a fixed horizontal orientation relative to the NGI station, ensuring consistent aerosol sampling. The IP is also designed to simulate the human oropharyngeal region in aerosol deposition studies. Its dimensions, particularly the internal diameter, are carefully designed according to USP specifications to regulate the amount of drug entering the impactor.

Other additional equipment which are necessary to be included in the NGI experimental setup (shown in **Fig 3.5**) are as follows:

- A vacuum pump draws air through the system at the designated volumetric flow rate, which creates a sonic flow.
- The mouthpiece adapter (MP) connects the inhaler to the IP or mouth-throat airway and avoids leaking drugs or air.
- The NGI Cooling box is designed to improve the performance of the NGI when evaluating formulations containing volatile components, such as certain propellants or solvents. Its primary function is to maintain the NGI at a lower, controlled temperature during testing

to reduce the evaporation of these volatile substances. This ensures more precise and reliable measurements of the drug particles.

- Critical Flow Controller that generates a standardized breath profile (constant flow rate), which depends on the available respiratory volume, ensuring consistent and reliable testing of SMIs.
- A flowmeter accurately measures the flow rate, ensuring precise airflow monitoring.

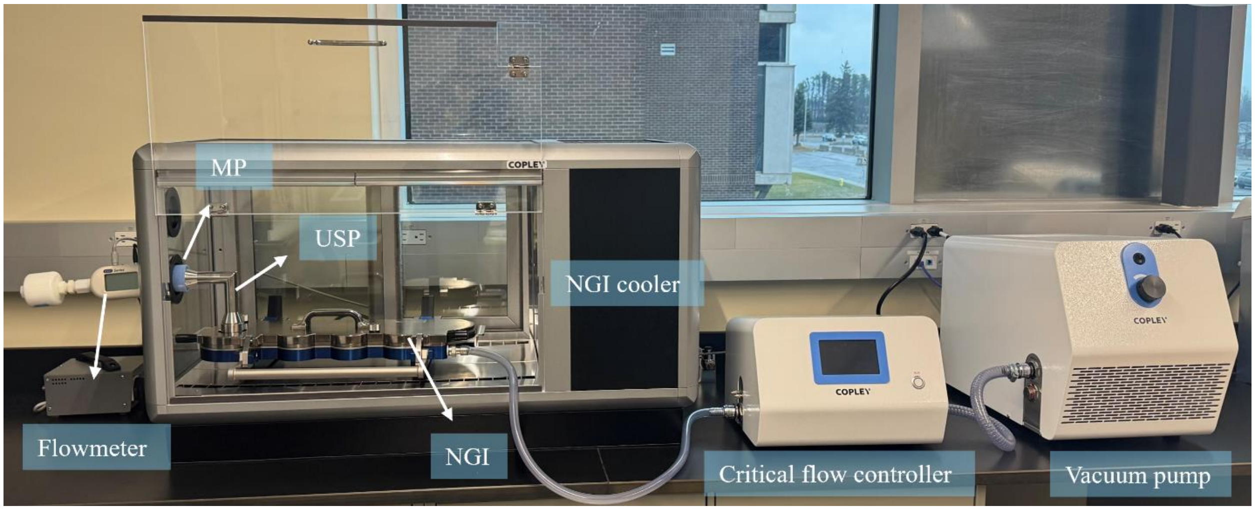

Fig 3.5 The experimental setup used for the evaluation of drug deposition.

A leakage test is performed before each experiment to verify the integrity of the NGI experimental setup by detecting potential leaks. During this test, the NGI is fully assembled with all stages, seals, and connections, and the critical flow controller applies a controlled pressure or vacuum to the system. The outlet of the NGI is sealed to create a closed environment. The critical flow controller then monitors the pressure over a predetermined period, identifying any significant drops that would indicate a leak. If the pressure remains stable within the acceptable range, the system is deemed leak-free. However, if a pressure drop is detected, the setup is inspected for loose connections, damaged seals, or misaligned components, which are then addressed before re-running the test to confirm system integrity.

3.1.3 High-Performance Liquid Chromatography (HPLC)

To achieve the primary objectives of the NGI method, it is essential to utilize a High-Performance Liquid Chromatography (HPLC) technique capable of quantifying the Active Pharmaceutical Ingredient (API) present at the various stages and components.

Liquid chromatography is the science of separating chemical compounds dissolved in a solvent within a sample. HPLC enhances this process by using high pressure to push the solvent through a column packed with small-diameter porous particles. The separation of each chemical entity is based on its unique affinity toward the stationary phase (the adsorbent material in the column) or the mobile phase (the solvent). This difference in affinity causes the various constituents to travel at different velocities, leading to their separation. Advances in HPLC technology have improved resolution, speed, and sensitivity, making it indispensable for pharmaceutical analyses [15].

During an HPLC run, a pump delivers the mobile phase, which can have a constant composition (isocratic elution) or a varying composition (gradient elution). Gradient elution is particularly useful for separating complex mixtures, as it changes the mobile phase properties over time to improve separation efficiency (**Fig 3.6**). After injection, the analytes are transported through the column by the mobile phase and detected by a suitable detector, such as a UV-visible spectrophotometer or a mass spectrometer. The detector sends signals to the HPLC software, generating a chromatogram (see **Fig 3.7** for details). The chromatogram displays peaks corresponding to different analytes, allowing for their identification and quantification based on retention times and peak areas [16].

Among the various separation modes used in chromatography, reversed-phase chromatography is the most common due to its versatility and broad applicability. In this mode, the column packing is non-polar—often functionalized with hydrophobic alkyl chains like C18—while the mobile phase is relatively polar, typically consisting of water mixed with organic solvents like methanol or acetonitrile. This setup causes non-polar compounds to interact more strongly with the stationary phase and thus be retained longer on the column, while polar compounds elute more quickly. Reversed-phase HPLC is particularly effective for analyzing a wide range of pharmaceutical compounds, including active pharmaceutical ingredients (API), due to its ability to handle molecules of varying polarities [16].

Additionally, method development in HPLC involves optimizing several parameters to achieve optimal separation and detection of analytes. These parameters include the choice of mobile phase solvents, pH, flow rate, temperature, and the use of additives like buffers or ion-pairing agents. Fine-tuning these conditions enhances the selectivity and sensitivity of the method, ensuring accurate quantification of the API across different stages of the NGI.

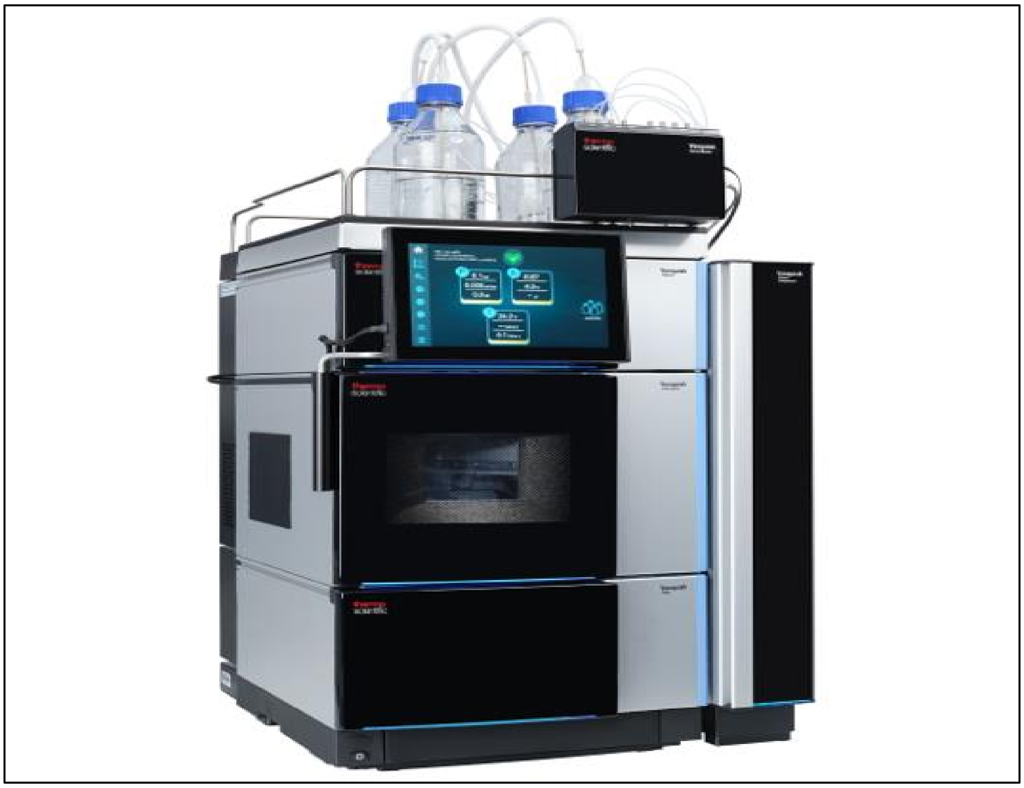

Fig 3.6 High-performance liquid chromatography [17].

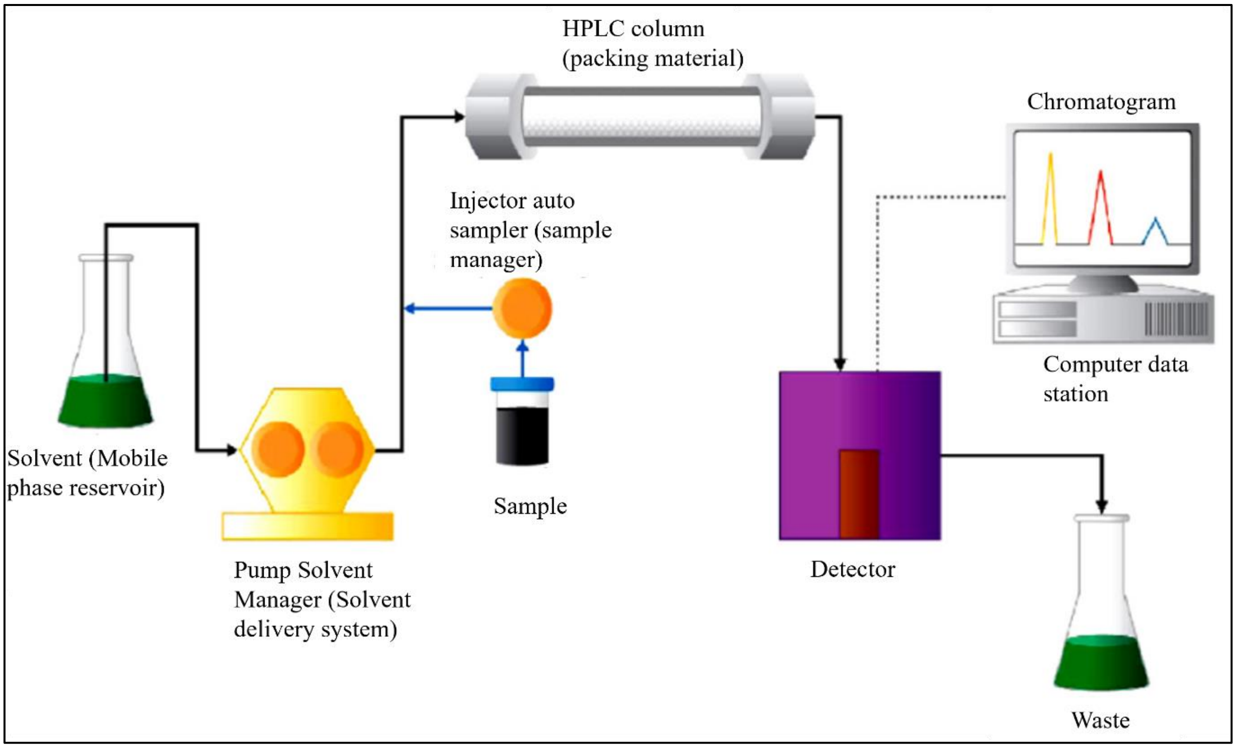

Fig 3.7 Workflow of an HPLC isocratic system [18].

3.1.4 Three-Dimensional (3D) Printing

For the creation of the pediatric mouth-throat geometry and standard induction port, the Ultimaker S3 and Ultimaker S5 3D printers were utilized, as shown in **Fig 3.8**. These printers are well-regarded for their precision, reliability, and versatility in producing high-quality prototypes, making them ideal for complex geometries required in aerosol deposition studies. The Ultimaker S3 and S5 are equipped with advanced features such as a precise print head, a heated bed, and a robust extruder system, which enable the production of detailed and accurate models with smooth finishes. These features allow for consistent printing with a wide variety of materials and ensure that the models printed for this research maintain high fidelity to the intended designs.

The Ultimaker S3 and S5 (Ultimaker S3, Lakehead University and Ultimaker S5, Confederation College) offer excellent compatibility with various materials, and in this case, tough poly lactic acid (PLA) was selected for its combination of ease of use, mechanical strength, and printability. Tough PLA is an enhanced version of standard PLA that provides better durability, impact resistance, and layer adhesion. Compared to standard PLA, which can be brittle, tough PLA offers greater toughness, making it less prone to cracking or breaking during handling or experimental testing. This added strength is particularly important for creating anatomical models that need to withstand mechanical stress, such as during airflow simulations and repeated handling.

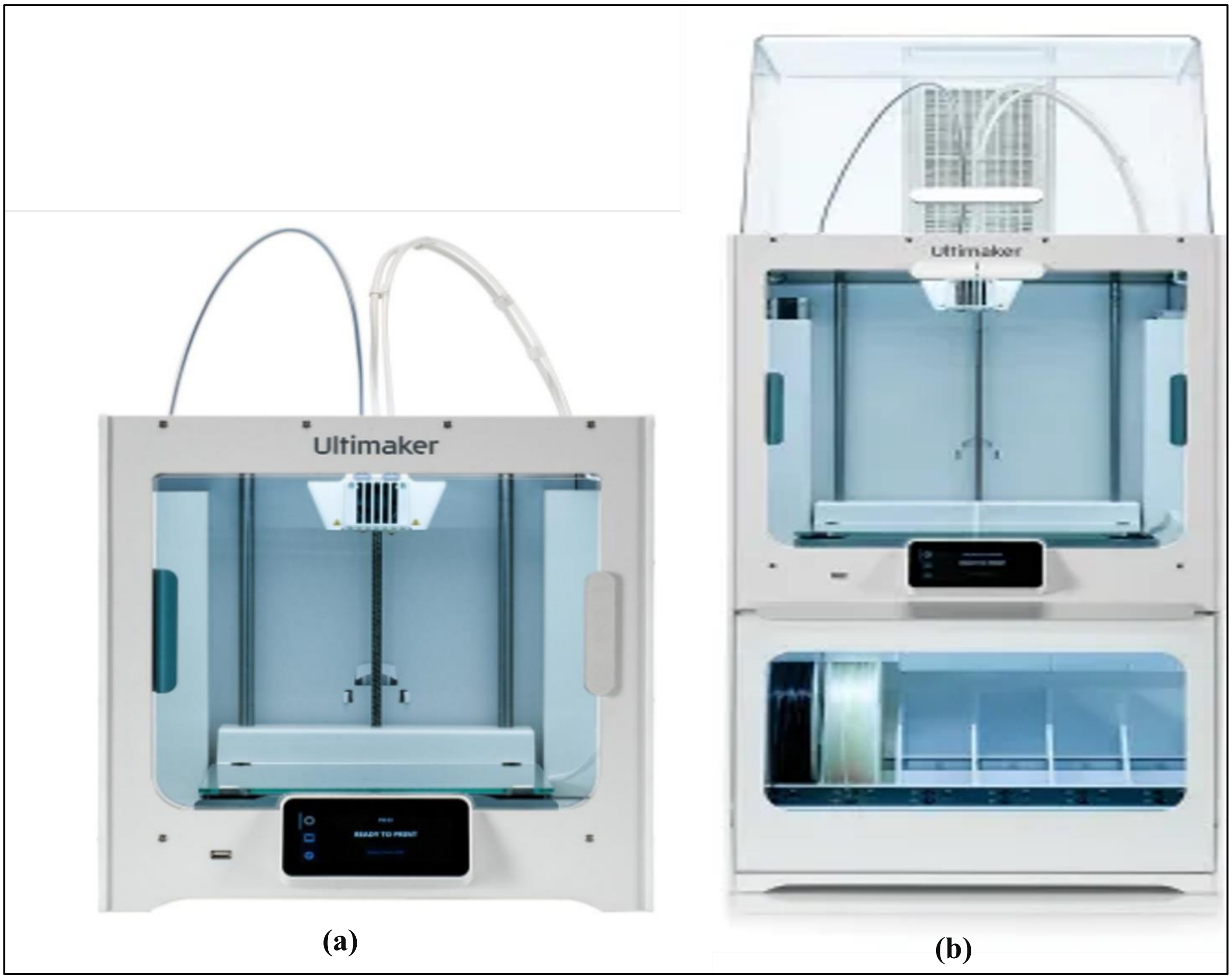

(a) **(b)**

Fig 3.8 (a) Ultimaker S3 (Lakehead University), and **(b)** Ultimaker S5 (Confederation College).

In addition to its superior strength, tough PLA is easy to post-process. One of the major advantages of this material is its ability to be easily polished and smoothed after printing. Unlike other 3D printing materials, such as acrylonitrile butadiene styrene (ABS) or Nylon, which require more intensive post-processing (such as high-temperature curing or solvent treatments), tough PLA can be easily sanded and polished to achieve a smooth surface finish. This property is especially beneficial when working with precise geometries, as it ensures the printed models maintain their accuracy for computational fluid dynamics (CFD) simulations, without introducing surface imperfections that could affect experimental results [19].

Key parameters in the 3D printing process, such as print resolution, layer height, and print speed, were carefully optimized [20]. The resolution, typically set at 0.1 to 0.2 mm, was chosen to capture the fine anatomical details of the mouth-throat geometries. The print speed was adjusted to balance precision with efficiency, ensuring the models were produced in a timely manner without sacrificing quality. Temperature settings for the heated bed and extruder were also fine-tuned to prevent warping and ensure good layer adhesion, further enhancing the accuracy of the printed geometries. The combination of the Ultimaker S3 and S5 printers, along with tough PLA, allowed for the efficient and accurate production of the mouth-throat geometries used in my research. These 3D printed models provided a strong, durable, and highly detailed foundation for studying aerosol deposition and airflow patterns in the pediatric respiratory tract.

3.2 Nomenclature

Abbreviations

ABS	Acrylonitrile Butadiene Styrene
ACI	Andersen Cascade Impactor
API	Active pharmaceutical ingredient
CFD	Computational Fluid Dynamics
FPD	Fine Particle Dose
FPF	Fine Particle Fraction
GSD	Geometric Standard Deviation
HRT	Human Respiratory Tract
HPLC	High-Performance Liquid Chromatography
IP	Standard Induction Port
MP	Mouthpiece
MMAD	Mass Median Aerodynamic Diameter
MSLI	Multi-Stage Liquid Impinger
MOC	Micro-Orifice Collector
PLA	Poly Lactic Acid
SMI	Soft Mist Inhaler
NGI	Next Generation Impactor
3D	3-Dimension

Notations

St	Stokes number, (-)
ρ_d	density of droplet, kg/m^3
ρ	density of air, kg/m^3
$\vec{u}$	air flow velocity, m/s
μ	air dynamic viscosity, kg/ms
R	airway radius, m
$\vec{u}_t$	settling velocity, m/s
d_d	diameter of droplets, m
$\vec{g}$	gravitational acceleration, m/s^2
D	rate of Brownian diffusion, m^2/s
K_B	Boltzmann constant, J/k
T	Absolute temperature, k

3.3 References

[1] M. Taki, C. Marriott, X.M. Zeng, G.P. Martin, Aerodynamic deposition of combination dry powder inhaler formulations in vitro: A comparison of three impactors, Int J Pharm 388 (2010) 40–51. https://doi.org/10.1016/j.ijpharm.2009.12.031.

[2] D. Ganderton, General factors influencing drug delivery to the lung, Respir Med 91 (1997) 13–16. https://doi.org/10.1016/S0954-6111(97)90099-8.

[3] Environments for drug absorption in the lung, n.d.

[4] J.P. Mitchell, M.W. Nagel, Cascade Impactors for the Size Characterization of Aerosols from Medical Inhalers: Their Uses and Limitations, 2003. www.liebertpub.com.

[5] Paolo. Colombo, Daniela. Traini, Francesca. Buttini, Inhalation drug delivery : techniques and products, Wiley-Blackwell, 2013.

[6] marple-et-al-2004-next-generation-pharmaceutical-impactor-(a-new-impactor-for-pharmaceutical-inhaler-testing)-part-i, (n.d.).

[7] E. Fröhlich, S. Salar-Behzadi, Toxicological assessment of inhaled nanoparticles: Role of in vivo, ex vivo, in vitro, and in Silico Studies, Int J Mol Sci 15 (2014) 4795–4822. https://doi.org/10.3390/ijms15034795.

[8] B. Asgharian, S. Anjilvel, A Monte Carlo calculation of the deposition efficiency of inhaled particles in lower airways, J Aerosol Sci 25 (1994) 711–721. https://doi.org/10.1016/0021-8502(94)90012-4.

[9] N.R. Labiris, M.B. Dolovich, Pulmonary drug delivery. Part II: The role of inhalant delivery devices and drug formulations in therapeutic effectiveness of aerosolized medications, Br J Clin Pharmacol 56 (2003) 600–612. https://doi.org/10.1046/j.1365-2125.2003.01893.x.

[10] J. Heyder, Deposition of inhaled particles in the human respiratory tract and consequences for regional targeting in respiratory drug delivery., Proc Am Thorac Soc 1 (2004) 315–320. https://doi.org/10.1513/pats.200409-046TA.

[11] C. Melandri, G. Tarroni, V. Prodi, T. De Zaiacomo, M. Formignani, C.C. Lombardi, Deposition of charged particles in the human airways, J Aerosol Sci 14 (1983) 657–669. https://doi.org/10.1016/0021-8502(83)90070-8.

[12] V.A. Marple, D.L. Roberts, F.J. Romay, N.C. Miller, K.G. Truman, M. Van Oort, B. Olsson, M.J. Holroyd, J.P. Mitchell, D. Hochrainer, Next Generation Pharmaceutical Impactor (A New Impactor for Pharmaceutical Inhaler Testing). Part I: Design, Journal of Aerosol Medicine 16 (2003) 283–299. https://doi.org/10.1089/089426803769017659.

[13] C. Dunbar, J. Mitchell, Analysis of Cascade Impactor Mass Distributions, Journal of Aerosol Medicine 18 (2005) 439–451. https://doi.org/10.1089/jam.2005.18.439.

[14] A.H. De Boer, D. Gjaltema, P. Hagedoorn, H.W. Frijlink, Characterization of inhalation aerosols: a critical evaluation of cascade impactor analysis and laser diffraction technique, n.d. www.elsevier.com/locate/ijpharm.

[15] P.K. Sahu, N.R. Ramisetti, T. Cecchi, S. Swain, C.S. Patro, J. Panda, An overview of experimental designs in HPLC method development and validation, J Pharm Biomed Anal 147 (2018) 590–611. https://doi.org/10.1016/j.jpba.2017.05.006.

[16] R. Peraman, K. Bhadraya, Y.P. Reddy, C.S. Reddy, T. Lokesh, Analytical Quality by Design Approach in RP-HPLC Method Development for the Assay of Etofenamate in Dosage Forms., Indian J Pharm Sci 77 (2015) 751–7. https://doi.org/10.4103/0250-474x.174971.

[17] M. Valizadeh, M. Sohrabi, Z. Ameri Braki, R. Rashidi, M. Pezeshkpur, Investigation of spectrophotometric simultaneous absorption of Salmeterol and Fluticasone in Seroflo spray by continuous wavelet transform and radial basis function neural network methods, Spectrochim Acta A Mol Biomol Spectrosc 263 (2021). https://doi.org/10.1016/j.saa.2021.120192.

[18] N. Srivastava, A. Singh, P. Kumari, J.H. Nishad, V.S. Gautam, M. Yadav, R. Bharti, D. Kumar, R.N. Kharwar, Advances in extraction technologies: isolation and purification of bioactive compounds from biological materials, in: Natural Bioactive Compounds, Elsevier, 2021: pp. 409–433. https://doi.org/10.1016/B978-0-12-820655-3.00021-5.

[19] X. Zhao, H. Hu, X. Wang, X. Yu, W. Zhou, S. Peng, Super tough poly(lactic acid) blends: A comprehensive review, RSC Adv 10 (2020) 13316–13368. https://doi.org/10.1039/d0ra01801e.

[20] S.F. Iftekar, A. Aabid, A. Amir, M. Baig, Advancements and Limitations in 3D Printing Materials and Technologies: A Critical Review, Polymers (Basel) 15 (2023). https://doi.org/10.3390/polym15112519.

Chapter 4 – CFD Model Development

Over the past few decades, Computational Fluid Dynamics (CFD) has emerged as a powerful tool for analyzing fluid flow and particle transport characteristics across various fields, including chemical and environmental engineering, as well as within human airways. CFD is fundamentally based on the governing equations of fluid dynamics, which are mathematical expressions of the conservation laws of physics [1]. This computational approach offers advantages over traditional experimental methods by enabling researchers to explore intricate details of fluid systems that are challenging or costly to measure experimentally. Such details include comprehensive insights into flow turbulence and turbulence development, velocity profiles [2], breathing patterns [3], the influence of discrete particles on a continuous phase [4], and the inertial and gravitational effects on particles [5].

In situations where experimental data are limited, a validated CFD model can be developed to investigate additional aspects of the system under study, thereby eliminating the need for further physical experiments and reducing costs. Moreover, CFD facilitates the analysis of volatile or hazardous systems—such as those involving toxic substances like acrylamide—without exposing investigators to potential risks associated with direct contact or extreme conditions. Another benefit is the ease with which significant modifications to human respiratory tract (HRT) geometries can be implemented and tested without the necessity for physical fabrication [6].

To simplify complex phenomena, CFD models rely on certain assumptions. These include treating fluids as continuous substances, assuming incompressibility and steady-state flow, and choosing between laminar and turbulent flow based on Reynolds numbers. The Navier-Stokes equations, fundamental to fluid dynamics, can be rearranged and simplified into various forms to suit different physical phenomena and scenarios. While these assumptions aid in mathematical simplification, their applicability depends on specific contexts and the required levels of accuracy, necessitating careful consideration when interpreting CFD results.

4.1 The Navier-Stokes Equations

Fundamental principles of fluid flow involve the conservation of mass and momentum [7]. The equation that represents mass conservation is commonly known as the continuity equation, while the equation for momentum conservation is an expression of Newton's generalized law governing fluid motion. In the context of viscous fluids, these equations are referred to as the Navier-Stokes equations [8]. These equations are used to characterize both transient (time-dependent) and steady-state flow phenomena.

The continuity equation, also called the conservation of mass equation, is derived by considering the mass balance within a differential volume element ($\Delta x\ \Delta y\ \Delta z$) through which the fluid flows. It can be expressed as follows [9]:

$$\frac{\partial \rho}{\partial t} = -\left(\frac{\partial}{\partial x}\rho u_x + \frac{\partial}{\partial y}\rho u_y + \frac{\partial}{\partial z}\rho u_z\right) \tag{4.1}$$

where ρ is the fluid density, and u is fluid velocity. The continuity equation describes how the density of a fluid changes over time at a specific point in space. It can be expressed using vector notation as follows [9]:

$$\frac{\partial \rho}{\partial t} = -(\nabla . \rho \vec{u}) \tag{4.2}$$

In this context, the rate at which the density changes over time is represented by $\frac{\partial \rho}{\partial t}$, is associated with the mass flux vector ρu. The divergence of this vector indicates how mass flows into and out of the control volume (**Fig 4.1**).

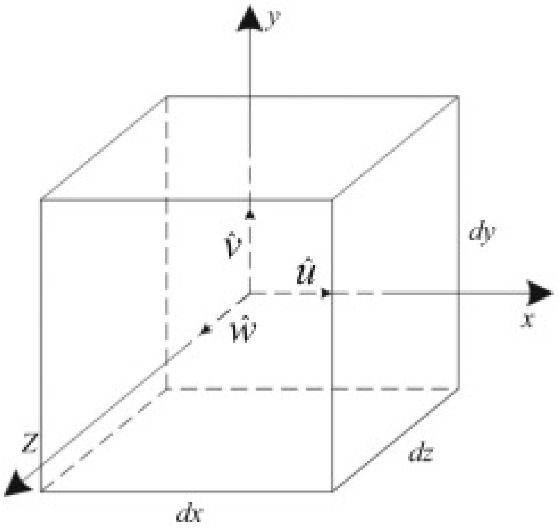

Fig 4.1 Control volume.

4.2 The Reynolds Averaged Navier-Stokes (RANS) Equations

4.2.1 k-ω Turbulence Model

The k-ω turbulence model with low-Reynolds number (LRN) corrections has effectively predicted the average velocity profiles, pressure drop, and shear stresses in the complex flow field within human airways.

The RANS equations are derived by decomposing the variables in the Navier-Stokes equations into their averaged and fluctuating components. These equations, which govern the conservation of mass and momentum in both incompressible laminar and turbulent fluid flows, are expressed in the following equations [10]:

$$\frac{\partial \bar{u}_i}{\partial x_i} = 0 \tag{4.3}$$

$$\frac{\partial \bar{u}_i}{\partial t} + \bar{u}_j \frac{\partial \bar{u}_i}{\partial x_j} = -\frac{1}{\rho}\frac{\partial \bar{P}}{\partial x_i} + \frac{\partial}{\partial x_j}\left[(\upsilon + \upsilon_T)\left(\frac{\partial \bar{u}_i}{\partial x_j} + \frac{\partial \bar{u}_j}{\partial x_i}\right)\right] + \vec{F} \tag{4.4}$$

where $\bar{u}_i$ is the mean air velocity component in three Cartesian coordinate directions, i.e., $i = 1, 2$ and 3, $\bar{P}$ is the pressure, υ is the air kinematic viscosity, and υ_T is the kinematic turbulent (eddy) viscosity, $\vec{F}$ represents body forces acting on the flow, including the gravitational force. The turbulent kinematic viscosity, υ_T, is given by Eq. (4.5, [11]):

$$\upsilon_T = c_\mu f_\mu \frac{k}{\omega} \tag{4.5}$$

where c_μ is a constant with a commonly accepted value of 0.09, and f_μ is a function of $Re_T = \frac{k}{\upsilon\omega}$, as defined in the following equation [11]:

$$f_\mu = exp\left[-\frac{3.4}{(1 + \frac{Re_T}{50})^2}\right] \tag{4.6}$$

In *k-ω* the turbulence model, two parameters are defined to represent the turbulent characteristics of the flow field: the turbulence kinetic energy, k, and ω is the turbulent dissipation rate. These parameters describe the kinetic energy associated with turbulent velocity fluctuations and the rate of viscous dissipation due to turbulent shear stresses, respectively. The equations governing the transport of these turbulence parameters are given in the following equations [11].

$$\frac{\partial k}{\partial t} + \bar{u}_j \frac{\partial k}{\partial x_j} = \mathrm{T}_{ij} \frac{\partial \bar{u}_i}{\partial x_j} - \beta^* k\omega + \frac{\partial}{\partial x_j}\left[(\upsilon + \sigma_k \upsilon_T)\frac{\partial k}{\partial x_j}\right] \tag{4.7}$$

$$\frac{\partial \omega}{\partial t} + \bar{u}_j \frac{\partial \omega}{\partial x_j} = \alpha \frac{\omega}{k} \mathrm{T}_{ij} \frac{\partial \bar{u}_i}{\partial x_j} - \beta\omega^2 + \frac{\partial}{\partial x_j}\left[(\upsilon + \sigma_k \upsilon_T)\frac{\partial \omega}{\partial x_j}\right] \tag{4.8}$$

In this context, T_{ij} represents the Reynolds stress tensor, while β^*, σ_k, α, and β are constants assigned the commonly accepted values of 1.0, 0.5, 0.555, 0.8333, and 0.5, respectively. The initial boundary conditions for the parameters, k and ω, are typically established using empirical correlations, two examples of which are provided in the following equations [11].

$$k = 1.5(I \times \vec{u}_{in}) \tag{4.9}$$

$$\omega = \frac{k^{1.5}}{0.6D} \tag{4.10}$$

where I, $\vec{u}_{in}$, and D denote the upstream turbulence intensity, the average velocity magnitude at the specified boundary, and the hydraulic radius of the boundary, respectively.

4.2.2 Large Eddy Simulation (LES)

Large Eddy Simulation (LES) is a modern alternative to RANS turbulence models, offering a novel methodology. It utilizes filtered versions of the exact Navier-Stokes equations as its governing framework. This approach separates the velocity field into resolved and subgrid-scale components.

This method explicitly resolves the larger, energy-dominant eddies while using an algebraic model to approximate the smaller, dissipative eddies within the computational grid. The underlying principle is that the larger eddies are strongly affected by boundary conditions, making it impractical to create a universally applicable model for them. In contrast, the smaller subgrid eddies tend to behave more isotopically, enabling the development of a generalized model to accurately represent their effects. The filtered Navier-Stokes equations derived from this approach are expressed as follows [12].

$$\frac{\partial \bar{u}_i}{\partial x_i} = 0 \tag{4.11}$$

$$\frac{\partial \bar{u}_i}{\partial t} + \frac{\partial}{\partial x_j}\left(\bar{u}_i \bar{u}_j\right) = -\frac{1}{\rho}\frac{\partial \overline{P}}{\partial x_i} - \frac{\partial}{\partial x_j}\tau_{ij}^{sgs} + \frac{\partial}{\partial x_j}(2\upsilon \bar{S}_{ij}) + \vec{F} \tag{4.12}$$

Here $\bar{u}_i(x_i, t)$ represents the resolved velocity field in the three Cartesian coordinate directions, i.e., i =1, 2 and 3, ρ denotes the air density, $\overline{P}$ is the pressure, υ is the air kinematic viscosity, and $\bar{S}_{ij}$ is the resolved rate of strain tensor. To model the subgrid-scale turbulent stresses, the following equation is used [12]:

$$\tau_{ij}^{sgs} = \overline{u_i u_j} - \bar{u}_i \bar{u}_j \tag{4.13}$$

The resolved rate of strain tensor, $\bar{S}_{ij}$, is computed as:

$$\bar{S}_{ij} = \frac{1}{2}\left(\frac{\partial \bar{u}_i}{\partial x_j} + \frac{\partial \bar{u}_j}{\partial x_i}\right) \tag{4.14}$$

The subgrid-scale (SGS) turbulent stress, generated by the filtering operation in Eq. (4.13) is unknown and requires a closure model. This is typically addressed using the eddy-viscosity assumption, which provides:

$$\tau_{ij} = \frac{2}{3}k_{sgs}\delta_{ij} - 2\upsilon_t \bar{S}_{ij} \tag{4.15}$$

Here, δ_{ij} denotes the Kronecker delta, $\upsilon_t(= C_k k_{sgs}^{1/2}\overline{\Delta})$ represents the subgrid-scale viscosity, and $\bar{S}_{ij}$ is the isotropic eddy-viscosity model calculates the SGS kinetic energy using the transport equation, expressed as:

$$\frac{\partial k_{sgs}}{\partial t} + \frac{\partial}{\partial x_j}\left(k_{sgs}\bar{u}_j\right) = \frac{\partial}{\partial x_j}\left(\frac{\upsilon_t}{\sigma_k}\frac{\partial k_{sgs}}{\partial x_j}\right) - C_\varepsilon \frac{k_{sgs}^{3/2}}{\overline{\Delta}} - \frac{\partial \bar{u}_i}{\partial x_j}\tau_{ij} \tag{4.16}$$

Here, C_k , σ_k, and C_ε are model constants that establish the relationships between turbulent kinetic energy, eddy viscosity, and energy dissipation. $\overline{\Delta}$ represents the subgrid characteristic length scale. The three terms on the right-hand side of Eq. (4.16) correspond to the transport rate of k_{sgs}, the dissipation and production rates, respectively [13].

4.3 Discrete Phase Model (DPM)

An aerosol composed of particles of identical size is referred to as a monodisperse aerosol, while one with particles of varying sizes is called a polydisperse aerosol. Ambient aerosols are typically polydisperse, whereas monodisperse aerosols can be carefully generated in laboratory settings. The particle sizes in a polydisperse aerosol can span two or more orders of magnitude, necessitating the use of statistical methods to describe their size distribution.

Aerosol sampling devices generally measure the bulk properties of aerosols within a defined particle size range. To determine aerosol size distribution parameters, the measured property for each size range must be divided by the number of particles in that range. Finally, the aerosol property is expressed as the fraction of particles per unit size of the interval. The Probability Density Function (PDF) and the Cumulative Distribution Function (CDF) are two valuable mathematical tools for representing the dispersion characteristics of aerosols.

4.3.1 Rosin-Rammler Distribution

The Rosin-Rammler distribution is commonly utilized in mineral processing to describe particle size distributions. The Rosin-Rammler distribution assumes an exponential relationship between the droplet diameter $\mathrm{d_d}$ and the mass fraction of particles with a diameter greater than $\mathrm{d_d}$. Its probability density function is defined as [14]:

$$\mathrm{F}(\mathrm{d_d};\lambda,n) = 1 - exp\left[-(\frac{\mathrm{d_d}}{\lambda})^{n}\right] \tag{4.17}$$

Here, n >0 and λ >0 are referred to as the shape and scale parameters of the distribution, respectively. The shape parameter n determines the steepness of the cumulative curve, while λ represents a particle diameter such that 36.8% of the particles are larger than this value. A higher n corresponds to a narrower distribution. By rearranging Equation 4.17, the Rosin-Rammler distribution can be expressed in a linearized form [14]:

$$\ln\left[\ln\left(\frac{1}{1-F(\mathrm{d_d})}\right)\right] = \ nln\mathrm{d_d} - nln\lambda \tag{4.18}$$

Equation 18 demonstrates that a linear relationship emerges when $\ln\left[\ln\left(\frac{1}{1-F(\mathrm{d_d})}\right)\right]$ is plotted against $ln\lambda$. From the slope and intercept of this straight line, the shape parameter n and the scale parameter λ can be calculated.

4.3.2 Log-normal Distribution

In practice, most aerosol particle distributions are skewed, exhibiting a long tail at larger sizes. As a result, the normal distribution function is seldom used to characterize aerosol particle size. However, assuming that the logarithms of particle diameters follow a normal distribution, the log-normal distribution effectively represents most polydisperse aerosols. The general form of the Probability Density Function (PDF) for a log-normal distribution is [14]:

$$\mathrm{f}(\mathrm{d_d}; \sigma, \mathrm{\mu}) = \frac{1}{\sqrt{2\pi}\mathrm{d_d}\sigma} exp\left[-\frac{(ln\mathrm{d_d}-\mathrm{\mu})^2}{2\sigma^2}\right] \tag{4.19}$$

In this context, μ and σ represent the natural logarithm of the Count Median Diameter (lnCMD) and the Geometric Standard Deviation (*ln*GSD), respectively. For a log-normal count distribution of spherical particles with uniform density, the geometric mean diameter and CMD are identical, expressed as CMD=$e^{\mathrm{\mu}}$ while the geometric standard deviation is GSD=e^{σ}.

The mode diameter, corresponding to the maximum point of the density function, is $e^{\mathrm{\mu}-\sigma^2}$. The GSD quantifies the spread of the aerodynamic particle size distribution. A key advantage of the log-normal distribution is that the GSD remains consistent across number, surface, and mass distributions. The GSD is typically calculated using the following formula [14]:

$$\mathrm{GSD} = (\frac{d_{84}}{d_{16}})^{1/2} \tag{4.20}$$

Here, d_{84} and d_{16} denote the particle diameters at which 84% and 16% of the aerosol mass, respectively, is contained in diameters smaller than these values. Examples of log-normal distributions with varying μ and σ are illustrated in **Fig 4.2**.

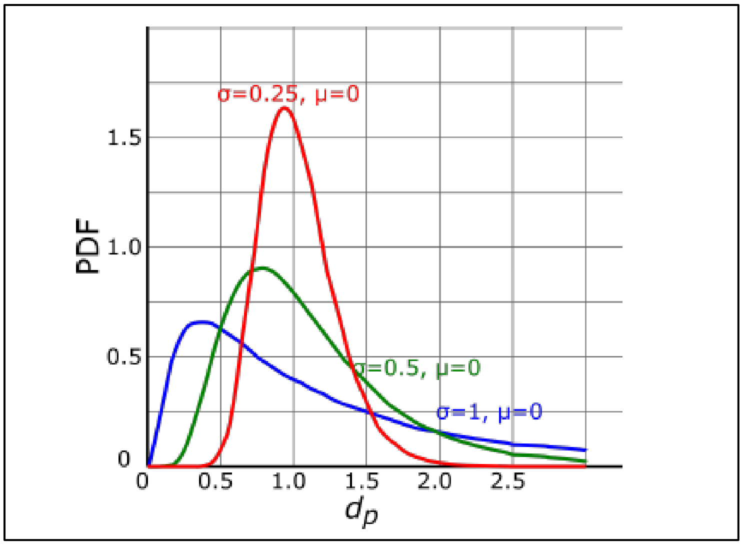

Fig 4.2 Several log-normal density functions with the same location parameter (μ) but differing scale parameters (σ) are depicted, highlighting how variations in σ affect the distribution's spread [15].

Once the parameters of one distribution are known, all related distributions can be determined. For instance, the Mass Median Diameter (MMD) from the mass distribution can be calculated using the CMD from the count distribution as follows:

$$\mathrm{MMD} = \mathrm{CMD}\, \exp(3 ln^2 GSD) \tag{4.21}$$

Fig 4.3 presents sample data collected from an aerosol sampling device, along with three distribution models: normal, log-normal, and Rosin-Rammler.

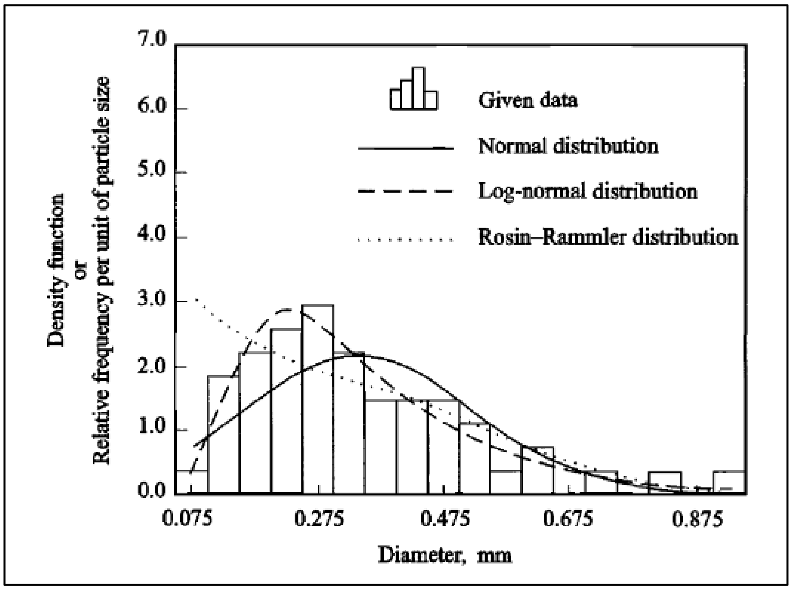

Fig 4.3 Comparisons of the relative frequency distribution are made using the collected data and three density functions [15].

The Lagrangian Discrete Phase Model (DPM) approach was employed to simulate particle motion, capturing the wide range of droplet sizes (0.1–60 μm) produced by the SMI [16]. The trajectory of each particle is calculated by integrating the forces acting on it within a Lagrangian reference frame. Here, the force balance equation equates the particle's inertia to the sum of all forces acting upon it, expressed as [17], [18]:

$$\frac{\partial \mathrm{u}_d}{\partial \mathrm{t}} = \frac{\mathrm{f_D}}{\tau_\mathrm{d}}(\vec{u} - \vec{u}_d) + \vec{g} + \mathrm{f_{i,lift}} \tag{4.22}$$

$$\frac{\mathrm{dx_i}}{\mathrm{dt}} = \vec{u}_d(\mathrm{t}) \tag{4.23}$$

$$\mathrm{f_D} = \frac{\mathrm{C_D Re_d}}{24} \tag{4.24}$$

$$\mathrm{C_D} = \begin{cases} \frac{24}{\mathrm{Re_d}}(1 + 0.15\mathrm{Re_d^{0.687}}) \text{ if } \mathrm{Re_d} \le 1000 \\ 0.44 \qquad\qquad\qquad \text{ if } \mathrm{Re_d} > 1000 \end{cases} \tag{4.25}$$

$$\mathrm{Re_d} = \rho \mid \vec{u} - \vec{u}_d \mid \frac{\mathrm{d_d}}{\mu} \tag{4.26}$$

$$\tau_\mathrm{d} = \frac{\mathrm{C_c \rho_d d_d^2}}{18\mu} \tag{4.27}$$

$$\mathrm{f_{i,lift}} = \frac{5.188\ \mathrm{m_d} \upsilon^{0.5} \rho \mathrm{D_{ij}}}{\rho_\mathrm{d} \mathrm{d_d} (\mathrm{D_{lk} D_{kl}})^{0.25}}(\vec{u} - \vec{u}_d) \tag{4.28}$$

$$\mathrm{D_{ij}} = 0.5\left(\frac{\partial \bar{\mathrm{u}}_\mathrm{i}}{\partial \mathrm{x_j}} + \frac{\partial \bar{\mathrm{u}}_\mathrm{j}}{\partial \mathrm{x_i}}\right) \tag{4.29}$$

In these equations, $\vec{u}_d$ represent the velocity of droplets. $\mathrm{f_D}$ is the drag force, τ_d is the relaxation time of droplets,$\vec{g}$ denotes the gravitational force, and $\mathrm{f_{i,lift}}$ represents the lift force. $\mathrm{C_D}$ is the drag coefficient, $\mathrm{Re_d}$ is the droplet Reynolds number, $\mathrm{C_c}$ is the Cunningham correction factor [17], ρ_d represents droplet density, $\mathrm{m_d}$ is the droplet mass, and $\mathrm{D_{ij}}$ is the deformation tensor.

The discrete random walk model was applied to examine the influence of sudden variations in turbulent air velocity on droplet motion [19]. This model assumes that the air velocity (as defined in Eq. (22)) remains constant while a droplet resides within an eddy. The velocity is expressed as follows in Eq. (30):

$$\vec{u} = \bar{u}_i + u_i' \tag{4.30}$$

Here, u_i' represents the fluctuating component of the instantaneous velocity, which is sampled from a Gaussian distribution with a variance of 2k/3.

4.4 CFD Solver Setting

The Navier-Stokes equations for incompressible fluids are transformed into their integral form, as required by control volume-based CFD solvers. In this study, we used the CFD package ANSYS Fluent v20.2 (ANSYS Inc., Canonsburg, PA). The computational domain is discretized into control volumes, and the governing equations (Equations 4.3, 4.4, 4.11, and 4.12) are reformulated in integral form to facilitate their integration over each control volume within the mesh.

This process generates a set of algebraic equations for dependent variables such as velocity, pressure, and temperature, which are then solved. The segregated solver in Ansys Fluent was utilized, solving the governing equations sequentially (i.e., independently of one another).

Turbulence modelling approaches employed in the study are RANS k-ω and LES. For LES, the unresolved subgrid scales are treated with the kinetic energy transport model. The momentum equations are solved applying the bounded central differencing scheme. The gradients are obtained using the least squares cell method for spatial discretization settings. The pressure, subgrid kinetic energy, energy, and H_2O are all calculated using the second-order upwind scheme. The bounded second order implicit along with the wraped-face gradient correction was used for the transient formulation. For the pressure–velocity coupling, the Semi-Implicit Method for Pressure-Linked Equations Consistent (SIMPLEC) algorithm was used.

For the SST k-ω model, The QUICK (Quadratic Upstream Interpolation for Convective Kinematics) scheme was employed to discretize the non-linear convection terms in the Navier-Stokes equations. For pressure-velocity coupling, the SIMPLE (Semi-Implicit Method for Pressure-Linked Equations) solution method was utilized. The momentum equations were solved using a bounded central differencing scheme, while a second-order upwind scheme was applied to the convective terms to interpolate values from cell centers to nodes. To improve gradient accuracy, a warped-face gradient correction was implemented. Finally, the algebraic multigrid controls were fine-tuned to ensure smoother convergence and avoid divergence during the solution process.

4.5 Nomenclature

Abbreviation

CDF	Cumulative Distribution Function
CFD	Computational Fluid Dynamics
CMD	Count Median Diameter
DPM	Discrete Phase Model
GSD	Geometric Standard Deviation
HRT	Human Respiratory Tract
LRN	Low Reynolds Number
LES	Large Eddy Simulation
MMD	Mass Median Diameter
PDF	Probability Density Function
MP	Mouthpiece
QUICK	Quadratic Upstream Interpolation for Convective Kinematics
RANS	Reynolds Averaged Navier-Stokes
SIMPLE	Semi-Implicit Method for Pressure-Linked Equations
SIMPLEC	Semi-Implicit Method for Pressure-Linked Equations Consistent

Notations

C_c	Cunningham correction factor, -
C_D	drag coefficient, -
$C_k, \mathrm{C}_\varepsilon$	model constants, -
D_{ij}	rate of deformation tensor, 1/s
D	hydraulic diameter, m
$\mathrm{D}_{\mathrm{lk}}, \mathrm{D}_{\mathrm{kl}}$	indices of the rate of deformation tensor, 1/s
d_{16}, d_{84}	particle diameters at which 84% and 16% of the aerosol mass, m
d_d	diameter of droplets, m
F	Rosin-Rammler distribution function, -
$\vec{F}$	body force including gravitational force, N
$f_{i,lift}$	lift force, N

f_D	drag force, N
$\vec{g}$	gravitational acceleration, m/s^2
I	upstream turbulence intensity, -
k	turbulent kinetic energy, m^2/s^2
k_{sgs}	SGS kinetic energy, m^2/s^2
m_d	droplet mass, kg
n	Shape parameter in Rosin-Rammler distribution, -
$\bar{P}$	pressure, N/m^2
Re_d	droplet Reynolds number, -
Re_T	turbulence Reynolds number, -
$\bar{S}_{ij}$	resolved rate of strain tensor, -
t	time, s
$\vec{u}$	velocity of air, m/s
$\vec{u}_{in}$	average velocity magnitude, m/s
$\vec{u}_d$	velocity of droplets, m/s
u_i'	fluctuating component of the instantaneous velocity, m/s
$\bar{u}_i$	resolved velocity field in three Cartesian coordinate directions, m/s

Greek letters

ρ	air density, kg/m^3
β^*, σ_k, α, and β	Equation constants, -
ρ_d	droplet density, kg/m^3
C_μ	equation constant, -
f_μ	turbulence damping function, -
T_{ij}	Reynolds stress tensor, kg/ms^2
τ_{ij}^{sgs}	subgrid scale stress, N/m^2
τ_d	relaxation time of droplets, s
δ_{ij}	Kronecker delta, -
$\bar{\Delta}$	subgrid characteristic length scale, m
σ	standard deviation of the natural logarithm

μ	air dynamic viscosity, kg/ms
μ_{log}	mean of the natural logarithm, -
υ	air kinematic viscosity, m^2/s
υ_t	subgrid scale viscosity, m^2/s
υ_T	kinematic turbulent (eddy) viscosity, m^2/s
ω	specific dissipation rate, 1/s
λ	scale parameter in Rosin Rammler distribution, m

4.6 References

[1] J. Tu, G.-H. Yeoh, and C. Liu, "Governing Equations for CFD: Fundamentals," in *Computational Fluid Dynamics*, Elsevier, 2018, pp. 65–124. doi: 10.1016/b978-0-08-101127-0.00003-9.

[2] B. Ma, V. Ruwet, P. Corieri, R. Theunissen, M. Riethmuller, and C. Darquenne, "CFD simulation and experimental validation of fluid flow and particle transport in a model of alveolated airways," *J Aerosol Sci*, vol. 40, no. 5, pp. 403–414, 2009, doi: 10.1016/j.jaerosci.2009.01.002.

[3] Z. Li, C. Kleinstreuer, and Z. Zhang, "Simulation of airflow fields and microparticle deposition in realistic human lung airway models. Part I: Airflow patterns," *European Journal of Mechanics, B/Fluids*, vol. 26, no. 5, pp. 632–649, Sep. 2007, doi: 10.1016/j.euromechflu.2007.02.003.

[4] P. Worth Longest and M. Hindle, "CFD simulations of enhanced condensational growth (ECG) applied to respiratory drug delivery with comparisons to in vitro data," *J Aerosol Sci*, vol. 41, no. 8, pp. 805–820, 2010, doi: 10.1016/j.jaerosci.2010.04.006.

[5] L. Nicolaou, "Inertial and gravitational effects on aerosol deposition in the conducting airways," *J Aerosol Sci*, vol. 120, pp. 32–51, Jun. 2018, doi: 10.1016/j.jaerosci.2018.03.003.

[6] K. Ekambara, M. T. Dhotre, and J. B. Joshi, "CFD simulations of bubble column reactors: 1D, 2D and 3D approach," *Chem Eng Sci*, vol. 60, no. 23, pp. 6733–6746, 2005, doi: 10.1016/j.ces.2005.05.047.

[7] R. B. Bird, W. E. Stewart, and E. N. Lightfoot, *Transport Phenoma*, Second. John Wiley & Sons, Inc, 2002.

[8] C. Hirsch, *Numerical Computation of Internal and External Flows Fundamentals of Computational Fluid Dynamics*, Second., vol. 1. John Wiley & Sons, Ltd, 2007.

[9] V. Madadi Avargani, S. Zendehboudi, S. Osfouri, and A. Rostami, "Performance evaluation of a solar nano-photocatalytic reactor for wastewater treatment applications: Reaction kinetics, CFD, and scale-up perspectives," *J Clean Prod*, vol. 421, Oct. 2023, doi: 10.1016/j.jclepro.2023.138240.

[10] M. Rahimi-Gorji, O. Pourmehran, M. Gorji-Bandpy, and T. B. Gorji, “CFD simulation of airflow behavior and particle transport and deposition in different breathing conditions through the realistic model of human airways,” *J Mol Liq*, vol. 209, pp. 121–133, May 2015, doi: 10.1016/j.molliq.2015.05.031.

[11] Z. Li, C. Kleinstreuer, and Z. Zhang, “Simulation of airflow fields and microparticle deposition in realistic human lung airway models. Part II: Particle transport and deposition,” *European Journal of Mechanics, B/Fluids*, vol. 26, no. 5, pp. 650–668, Sep. 2007, doi: 10.1016/j.euromechflu.2007.02.004.

[12] D. C. Wilcox, *Turbulence modeling for CFD (Third edition)*. 2006.

[13] K. Inagaki and H. Kobayashi, “Transport and modeling of subgrid-scale turbulent kinetic energy in channel flows,” *AIP Adv*, vol. 12, no. 4, Apr. 2022, doi: 10.1063/5.0083398.

[14] C. H. William, *Aerosol Technology: Properties, Behavior, and Measurement of Airborne Particles*, 2nd ed., vol. 1. New York: John Wiley & Sons Inc, 2012.

[15] W. C. Hinds, *Properties, Behavior, and Measurement of Airborne Particles*, Second., vol. 1. Aerosol Technology, 2012.

[16] P. Worth Longest and M. Hindle, “Evaluation of the respimat soft mist inhaler using a concurrent cfd and in vitro approach,” *J Aerosol Med Pulm Drug Deliv*, vol. 22, no. 2, pp. 99–112, Jun. 2009, doi: 10.1089/jamp.2008.0708.

[17] M. D. Allen and O. G. Raabe, “Slip correction measurements of spherical solid aerosol particles in an improved millikan apparatus,” *Aerosol Science and Technology*, vol. 4, no. 3, pp. 269–286, 1985, doi: 10.1080/02786828508959055.

[18] M. M. Paul and L. Pakzad, “Bubble size distribution and gas holdup in bubble columns employing non-Newtonian liquids: A CFD study,” *Canadian Journal of Chemical Engineering*, vol. 100, no. 10, pp. 3030–3046, Oct. 2022, doi: 10.1002/cjce.24352.

[19] C. Xu, X. Zheng, and S. Shen, “A numerical study of the effect of breathing mode and exposure conditions on the particle inhalation and deposition,” *Inhal Toxicol*, vol. 32, no. 13–14, pp. 456–467, 2020, doi: 10.1080/08958378.2020.1840679.

Chapter 5- Evaluation of Soft Mist Inhaler Aerosol Velocity, Size, and Deposition Inside the Mouth -A CFD Study

5.1 Abstract

Respiratory diseases debilitate more than 250 million people around the world. Among available inhalation devices, the soft mist inhaler (SMI) is the most efficient at delivering drugs to ease respiratory disease symptoms. In this study, we analyzed the SMI performance in terms of the aerosol's velocity profiles, flow pattern, size distribution, and deposition by employing computational fluid dynamics (CFD) simulations. We modeled two different simplified mouth geometries, idealized mouth (IM) and standard mouth (SM). Three different locations (x= 0, x= 5, and x= 10 mm) for the SMI nozzle orifice were chosen along the mouth cavity centerlines, followed by two different SMI nozzle angles (10° and 20°) for IM geometry. A flow rate of 30 l/min was applied. The simulation results were evaluated against experimental data. It was found that the SMI could be simulated successfully with a level of error of less than 5%. The inhalation flow rate significantly impacted the aerosol's velocity profile and deposition efficiency on both the IM and SM walls. The lowest particle deposition on the mouth wall occurred when a fixed flow rate (30 l/min) was applied inside both geometries, and the SMI nozzle position moved forward to x= 10 mm from the IM and SM inlets. An increase in the SMI nozzle angle increased particle deposition and decreased the deposition fraction for particles with a diameter above 5 µm inside the IM.

5.2 Introduction

Despite substantial research on drug delivery to the human respiratory tract for treating asthma and chronic obstructive pulmonary disease, inhaler device efficiency is still under study. The geometric design of inhaler devices and the inaccuracy in coordination between the actuation and inhalation play significant roles in drug wastage [1]. Pharmaceutical aerosol delivery to human lungs is inefficient due to about a 40% drug loss in the extra-thoracic region and approximately 22-27% in the device mouthpiece [2-4]. This amount varies for different inhaler devices. Pressurized metered dose inhalers (pMDIs), which deliver drug droplets under liquid propellant pressure, and dry powder inhalers (DPIs) that deliver drug particles by the act of a patient's inspiratory effort result in 10-20% lung deposition [8]. Soft mist inhalers (SMIs), which were made commercially available in 2003 [7], atomize the drug solution through a tiny nozzle into small droplets [5,6]—these inhalers result in almost 40% drug deposition into the lungs. This enhanced drug delivery is attributed to the patient's inhalation dependency reduction, improved usability, and the SMIs' propellant-free nature [7]. These advantages have enabled many researchers to investigate and perform further experimental and CFD studies using SMI [9-11].

For in vivo functionality, inhalers must produce fine aerosols of a suitable size (typically 5 μm in diameter) [12]. Converting a drug solution to appropriately sized droplets involves using electrical energy to generate mechanical energy in the form of vibration [13]. New SMIs generate fine aerosol droplets and deliver a metered dose of the drug solution to the target site of action by mechanical energy derived from a metal spring located at the device's base. Twisting the base of the SMI about 180° compresses the spring, simultaneously withdrawing a predefined dose of liquid inhalation solution from the reservoir into the capillary tube [12]. The drug solution is then forced through two converging (at an angle of approximately 90°), 10 μm-diameter microchannels, generating two high-speed liquid streams. The streams then collide downstream of the precisely engineered nozzle system (uniblock) to form a slow-moving, inhalable aerosol plume [14]. The high pressure (hundreds of atmospheres) at the orifice nozzle [15] and the resulting fine droplets lead to a longer generation time and lower velocity. This high-pressure stream results in more drug droplets reaching the lungs rather than being wasted in the oral cavity, pharynx, and larynx, as is the case with traditional inhalers [16,17].

Among pharmaceutical inhalers' variables, the drug aerosol's diameter and velocity are the two most important factors in drug deposition in the human respiratory tract [18,19]. These factors themselves depend on environment temperature, relative humidity, coordination of inhalation, and the patient's respiratory tract [20].

Drug aerosol diameters range from nanometers to micrometers [11], but generally, droplets with a diameter range of 2-5 μm can reach and deposit in the lungs; thus, understanding the respirable size range is necessary [8]. Aerosol droplets bigger than 5 μm are deposited before entering the trachea on the oropharynx, mouth-throat, and upper tracheobronchial region due to inertial impact along their path to the lungs. In comparison, droplets smaller than 2 μm have a great potential to be exhaled from the body [19].

A number of studies have evaluated the effect of independent parameters, such as the SMI nozzle angle and position [29,30] as well as the inhalation flow rate [31], on the drug particles' velocity and diameter. Wasted medication at the back of the throat can be reduced by optimizing the nozzle's position [32]. A flow rate of 75 l/min results in the lowest and highest mouth-throat drug deposition for DPI and MDI at the nozzle angle of +10° and -20° (relative to the horizontal axis), respectively [33]. Drug deposition in the human respiratory tract by a pMDI can vary with the angle of the actuator nozzle. Using a CFD approach, the best angle of the pMDI actuator nozzle was found to be 120°, leading to a higher particle velocity and a greater possibility of the drug reaching the alveoli [30]. Ocular and facial drug deposition can occur due to misuse, as when a patient holds a Respimat SMI at an angle, causing unwanted side effects from drug deposition of less than 1% of a dose deposited in the ocular area [29]. The aerosol plume's entrance angle strongly affects drug droplet penetration efficiency through a human oral airway. The aerosol penetration efficiency monotonically increases with a range of 0° to 20° of the plume's entrance angle, with maximum efficiency occurring at 20° [34].

Though the SMI nozzle produces drug droplets in the diameter range of 100 nm to 60 µm, the distribution is polydisperse [4]. This uneven drug particle distribution [21,22] is attributed to several factors: aerosol evaporation and condensation, relative humidity inside the mouth-throat, and drug deposition at the inhaler's mouthpiece. Droplet evaporation leads to finer particle sizes, while droplet condensation results in greater aerosol diameter [2].

The term aerodynamic diameter is commonly used by the pharmaceutical industry. It refers to the diameter of a spherical particle with a constant density of 1000 kg/m^3, which has the same vertical velocity in the air as the particle of interest [23]. The aerodynamic diameter can be calculated using Eq. (5.1):

$$Aerodynamic\ diameter = Geometric\ diameter \times (\frac{\rho_p}{\rho_0 x'})^{1/2} \tag{5.1}$$

where ρ_p and ρ_0 are the particle and unit densities, respectively, and x' is the dynamic shape factor [24]. Earlier research has reported that SMI can generate aerosol drug droplets with a fine particle fraction of > 60%, which can be defined as the mass fraction of particle size less than 5 µm; and mass median aerodynamic diameter of <5 µm, which means that 50% of particles have an aerodynamic diameter greater than 5 µm and 50% of the particles have an aerodynamic diameter less than 5 µm (D50) [25,26]. Several in vitro, in vivo, and in silico research studies have been conducted to assess the effect of different parameters on aerodynamic particle size distribution through the human respiratory tract [27,28].

The inhalation flow rate is one of the most critical parameters affecting aerosol velocity, diameter, and, consequently, aerosol deposition. A steady inhalation rate results in an approximately 20% improvement in aerosol drug deposition in a patient's lungs when the flow rate increases from 15 to 60 l/min; a flow rate increase also causes a higher (16%) throat deposition [35]. This result was confirmed by Ciciliani *et al.*, who showed that a higher inhalation flow rate increases the inertial impaction of aerosol particles at bifurcations in the oropharynx in large central airways [1]. Mehri *et al.* showed that with an increase in the flow rate from 45 to 60 l/min, the total dose recovered using a mechanical ventilator increased by almost 16% (at constant relative humidity) [36]. The importance of the flow rate was better demonstrated in an in vitro study by Wei *et al.*, showing that the mean mouth-throat particle deposition increased from 9.8 to 14.2 µg for flow rates of 15 to 45 l/min (representing weak to strong flow rates, respectively) [37]. They also showed that the impact of the mouth-throat geometry compared to the inhalation flow rates was higher for the MDI and SMI, but much less critical than inhalation strength for the DPI [37].

Aerosol interaction with the continuous phase can change the spray plume formation, affecting particle deposition inside the human respiratory tract. Gavtash *et al.* explored the effects of hydrofluoroalkane MDI spray injection into a stabilized airflow field inside a mouth-throat geometry on an aerosol plume [38]. They showed that a shield-like particle-embedded configuration formed at the early stages of the plume's spatial development. This formation happened due to the existence of an extremely high drag force. As the mass loading of the droplets was low at the initial stages of actuation, an upward trend of the plume was observed that resulted in the formation of recirculation regions inside the mouth-throat.

Although designing an appropriate experimental setup to evaluate drug deposition in mouth-throat is essential, testing processes and developing new SMI nozzles at different positions cost time and material resources. CFD can make the analysis and simulation of multiphase flow faster by avoiding the need for real-time experiments [39-41]. In a CFD study by Ma and Lutchen, total particle deposition was evaluated based on different flow rates and particle sizes in human airways [42]. As expected, the deposition fraction increased with an increase in flow rate. However, deposition efficiency was found to be more sensitive to particle diameter than to flow rate, showing the importance of aerodynamic particle size distribution through the human respiratory tract. Bass and Longest went further and examined the effect of airflow conditions on particle deposition in the mouth-throat path [43]. They found that higher flow rates and a consequently higher Reynolds number increased the sensitivity of the fine aerosols' deposition [43]. This result was also confirmed by Ahookhosh *et al.*, who used pMDI in a CFD study to evaluate the deposition fraction of particles in mouth-throat at four constant inhalation flow rates [44]. The significant increase in deposition fraction at higher flow rates was attributed to a higher turbulence level and particle inertia. However, Yousefi *et al.* studied the effects of flow rates (15, 30, and 60 l/min) on the particle deposition rate by a pMDI, and the optimum deposition rate in the lung was acquired at 30 l/min [22].

It's apparent from the literature mentioned earlier that very few studies have examined the effect of the nozzle angle on aerosol deposition inside the human mouth. This is paramount because it can frequently occur when an SMI is misused. Furthermore, although a few studies shed light on spray performance, there is a significant lack of research that helps understand the effects of flow rate and nozzle position on respiratory aerosol delivery. In the current study, we used CFD to explore the impact of flow rate, SMI nozzle position, and the angle on the aerosol's velocity, size distribution, and deposition inside the mouth. Two mouth geometries, i.e., the idealized mouth (IM) and standard mouth (SM), were modeled in our study.

5.3 CFD Model Development

5.3.1 Geometry Design and Mesh

The 3-dimensional geometries of simplified mouth cavities based on both IM and SM were created using the geometry module available in the ANSYS workbench [45]. **Fig 5.1(a)** shows the mouth cavity portion of IM as described by Zhang *et al.,* and **Fig 5.1(b)** shows the midplane view of the Andersen cascade impactor induction port (only horizontal section) representing the SM [46]. As seen in **Fig 5.1**, we considered three locations for the SMI nozzle near the mouth inlet along the x-axis (i.e., x_0, x_1, and x_2) and two SMI nozzle angles (10° and 20°). The SMI nozzle was located at the inlet (x_0) due to the SMI insertion through the mouthpiece connector. The mouthpiece connector was excluded from the mesh and did not affect the results of this study.

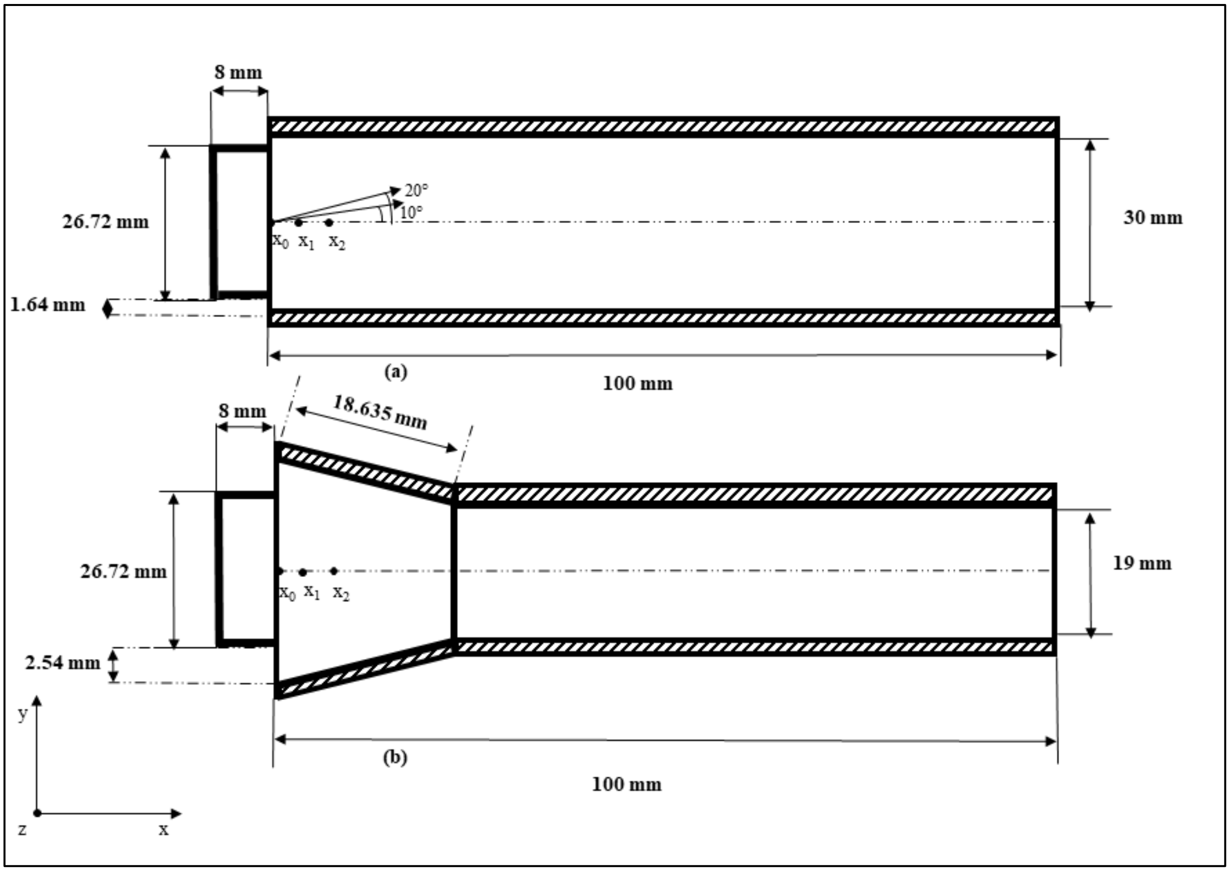

Fig 5.1 Geometry schematics (side views) of **(a)** IM, and **(b)** SM, with defined x_0, x_1, and x_2 as nozzle positions at 0, 5, and 10 mm, respectively, and nozzle angles of 10° and 20°.

A hexahedral structured mapped mesh was applied to both IM and SM geometries to ensure a high-quality computational solution. **Fig 5.2(a)** and **Fig 5.2(b)**, respectively, show the front and side views of the meshed IM and SM geometries. Both the average skewness and orthogonal quality measurements were ensured to be in an acceptable range (see [47] for more information). Additionally, in both models with 162k and 158k cells, an inflation layer meshing with a maximum of 15 layers and a growth rate of 1.2 was adopted to capture the effect of velocity fluctuations near the wall.

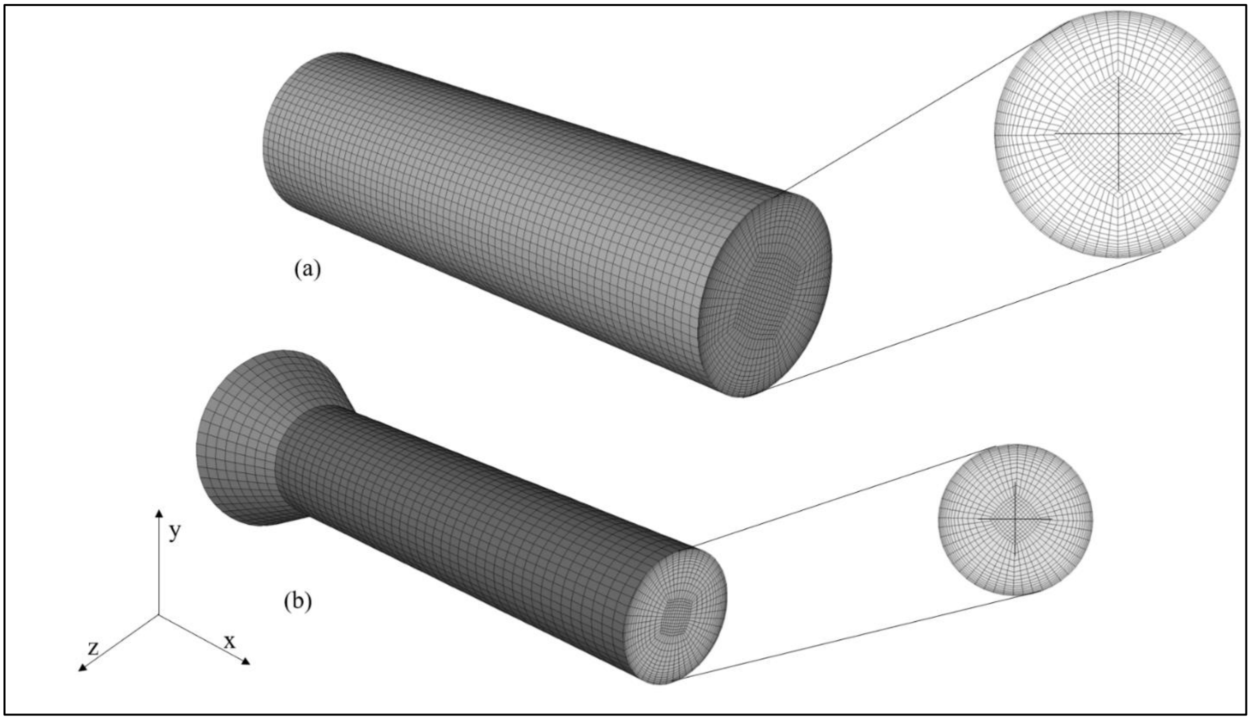

Fig 5.2 Geometries mesh views (side and front views) of **(a)** IM, and **(b)** SM, including vertical (y-direction) and horizontal (z-direction) lines on front views.

5.3.2 Transport Equations and Methods

The commercial code ANSYS Fluent v19.1 was employed to solve the continuity and momentum equations. The multiphase flow involves a continuous phase (air) and aerosol particles. The multiphase volume of the fluid method was adopted to simulate the liquid injection and atomization process from an SMI nozzle. This method is a well-established Eulerian numerical approach based on the solution of transport equations by tracking the volume fraction of the target fluid in the grid unit [48]. The key feature of the volume of fluid method is its ability to capture the effect of surface tension and the interphase's behavior [49].

The flow inside the geometries is laminar to turbulent and also highly vortical (300<Re<2050). By considering the velocity at a single point as a sum of the mean ($\bar{\mathrm{U}}_{\mathrm{i}}$) and the fluctuating ($\mathrm{u}'_{\mathrm{i}}$) component in the three coordinates' directions (i.e., i = 1, 2, and 3), the momentum equation can be expressed as follows:

$$\vec{u} = \bar{\mathrm{U}}_{\mathrm{i}} + \mathrm{u}'_{\mathrm{i}} \quad (5.2)$$

Equally, the continuity equation accounting for mass conservation can be expressed as below:

$$\frac{\partial \rho_{air}}{\partial t} + \frac{\partial \rho_{air} \bar{U}_i}{\partial x_i} = 0 \tag{5.3}$$

where ρ_{air} is the continuous phase density, and t is the time [50].

Physical properties of the continuous phase and aerosol used in this simulation include air density ρ_{air} =1.225 kg/m^3, air dynamic viscosity μ =1.789×10^{-5} kg/m.s, aerosol density ρ_p =998.2 kg/m^3, and aerosol viscosity μ_p=0.00103 kg/m.s [51]. The continuous phase flow is solved using an unsteady Reynolds averaged Navier-Stokes (URANS) two-equation turbulent model. The URANS equations are highly functional in simulating aerosol spray behavior due to their time-efficient particle trajectories and flow field calculations [3,14]. One of the most popular URANS turbulence models is the low Reynolds number k-ω shear stress transport approximation employed in this study to simulate turbulent effects. The k-ω turbulence model has been widely used in models of multiple bifurcations and oral airways [1,52]. This is due to its advantages in predicting velocity profile, pressure drop, and shear stress for turbulent and transitional flows. The required equations are presented below [50]:

$$\begin{aligned} &\frac{\partial(\rho_{air}\bar{U}_i)}{\partial t} + \frac{\partial(\rho_{air}\bar{U}_i\bar{U}_j)}{\partial x_i} \\ &\quad = -\frac{\partial P}{\partial x_j} + \frac{\partial}{\partial x_j}(\mu\,(\frac{\partial \bar{U}_i}{\partial x_j} + \frac{\partial \bar{U}_j}{\partial x_i})) + \rho_{air}\vec{g} - \frac{\partial}{\partial x_j}(\rho_{air}\overline{u_i' u_j'}) \end{aligned} \tag{5.4}$$

where P is the time-average pressure, $\vec{g}$ is the component of gravitational acceleration in the x_i-axis direction, and the last term, $\rho_{air}\overline{u_i' u_j'}$ is known as Reynolds stress.

The k-ω model was used to increase accuracy based on using both the near wall region calculation of the k-ω model and the free stream calculation of k-ε model [53, 54]. In the k-ω model, an extended Boussinesq relationship has been used to relate the Reynolds stress term in URANS equations to the velocity gradient in the flow as presented below [50]:

$$-\rho_{air}\overline{u_i' u_j'} = v_t\left(\frac{\partial \bar{U}_i}{\partial x_j} + \frac{\partial \bar{U}_j}{\partial x_i}\right) - \frac{2}{3}\rho_{air}k\delta_{ij} \tag{5.5}$$

where v_t is the turbulent viscosity term, k is the turbulent kinetic energy per unit mass, and δ_{ij} is

Kronecker delta constant (in three coordinate directions, i.e., i, j=1, 2, and 3). The corresponding equations are read as:

$$\nu_t = C_u \rho_{air} \frac{k^2}{\varepsilon} \tag{5.6}$$

$$k = \frac{1}{2}(\bar{U}_i^2) \tag{5.7}$$

$$\begin{aligned} \delta_{ij} &= 1, \text{when } i = j \\ \delta_{ij} &= 0, \text{when } i \neq j \end{aligned} \tag{5.8}$$

where C_u is a model constant, and ε is the dissipation rate calculated using Eq. (9) [50]:

$$\varepsilon = \nu \frac{\partial \bar{U}_i}{\partial x_i} \frac{\partial \bar{U}_j}{\partial x_j} \tag{5.9}$$

From the above equation, ν is the kinematic eddy viscosity. The governing transport equations for the k-ω turbulence model are as follows:

$$\frac{\partial k}{\partial t} + \bar{u}_j \frac{\partial k}{\partial x_j} = \tau_{ij} \frac{\partial u_i}{\partial x_j} - \beta^* k\omega + \frac{\partial}{\partial x_j}\left((\nu + \sigma_k \nu_t)(\frac{\partial k}{\partial x_j}) \right) \tag{5.10}$$

$$\frac{\partial \omega}{\partial t} + \bar{u}_j \frac{\partial \omega}{\partial x_j} = \alpha \frac{\omega}{k} \tau_{ij} \frac{\partial u_i}{\partial x_j} - \beta \omega^2 + \frac{\partial}{\partial x_j}\left((\nu + \sigma_k \nu_t)(\frac{\partial \omega}{\partial x_j}) \right) \tag{5.11}$$

where ω is the specific rate of dissipation, τ_{ij} is the Reynolds stress tensor, and the other shear stress transport equation coefficients are β^*=0.9, β=0.075, α_k=0.31, σ_ω=0.5, and σ_k=0.85 [52].

During spray atomization, the density of air (ρ_{air} =1.225 kg/m^3) and aerosol particles (ρ_p=998.2 kg/m^3) remain- almost unchanged. This is because of the low density of the continuous phase and sufficiently small mass flow rate of aerosol particles (1×10^{-5} kg/s) that keeps the total volume of phases almost constant. Also, continuous phase compressibility has a negligible effect on the spraying process, making the model incompressible. Although droplet evaporation at a relative humidity below 90% is low, the small aerosol droplet size in SMI makes droplet evaporation inevitable [4]. Droplet evaporation can affect relative humidity, temperature, and continuous field properties inside an IM and SM. To put evaporation into effect, a species transport model (Eq.

(5.12, 5.13)) with mass transfer between the water vapor (relative humidity) and the air was employed:

$$\frac{\partial Y_V}{\partial t}+\frac{\partial (u_j Y_V)}{\partial x_j}=\frac{\partial}{\partial x_j}\left((D_V+\frac{v_t}{Sc_T})(\frac{\partial Y_V}{\partial x_j})\right)+S_V \tag{5.12}$$

where Y_V is the mass fraction of water vapor in the mixture (air and water vapor); D_V is the diffusion coefficient of water vapor in the mixture; Sc_T is the turbulent Schmidt number (Sc_T=0.9); and S_V is the water vapor (mass) source term, which is to account for the increase or decrease in water vapor mass fraction in the mixture from evaporating or condensing aerosols. A thermal energy equation is also needed to determine the temperature field inside the geometries, which is expressed as:

$$\rho C_P(\frac{\partial T}{\partial t}+\frac{\partial u_j T}{\partial x_j}) = \frac{\partial}{\partial x_j}\left(\left(k_g+\frac{\rho C_P v_t}{Pr_T}\right)\left(\frac{\partial T}{\partial x_j}\right)+\sum_s h_s\,(\rho D_V+\frac{\rho v_t}{Sc_T})\frac{\partial Y_s}{\partial x_j}\right) + S_e \tag{5.13}$$

In this equation, ρ is the mixture density; C_P is constant specific heat; k_g is air conductivity; Pr_T is turbulent Prandtl number (Pr_T=0.9); h_s is the enthalpy of each species (air and aerosol); and finally, S_e is air energy source term due to the presence of a discrete phase. The first term on the right-hand side of Eq. (13) accounts for conductive transport due to turbulent mechanism, and the second term represents energy transport due to species diffusion. The presence of mass and energy source terms in Eq. (12) and Eq. (13) is due to evaporation and condensation at the aerosol surface (for more information, see [3]).

5.3.3 Discrete Phase Model (DPM)

The aerosol particles were considered as the discrete phase since the volume fraction of the liquid is small (<10%). The SMI nozzle atomizes aerosols in a wide range of diameters (100 nm to 60 µm), and nozzle actuation in different positions results in varied particle trajectories [55]. To address this broad range of particle paths, the unsteady Lagrangian particle tracking method was employed [56].

A random walk method was also implemented to consider the effect of random velocities on particle trajectories [54]. However, this model does not account for reduced turbulent fluctuations in the wall-normal direction, which affect particle deposition. An anisotropic turbulence correction can be applied to better approximate the effects of turbulence on particle deposition. Therefore, near-wall fluctuating velocities are calculated from the following equations:

$$\mathrm{u'}_{\mathrm{i}} = \digamma\lambda_{\mathrm{i}}\sqrt{\left(\frac{2}{3}\right)\mathrm{k}} \tag{5.14}$$

where $\digamma$ is an anisotropic correction factor which computes as $\digamma = 1\text{-}e^{-0.02n}$ while *n* value ranging from 0 to 60 and λ_i is a normally distributed random number [3]. The effect of aerosol droplets on the continuous phase (air), referred to as two-way coupling [57], was also included. Previous studies showed a noticeable difference when comparing two-way coupling with one-way coupling to predict the particle deposition rate onto the wall [16].

The Lagrangian equation (Eq. 5.15) accounts for the governing forces on the particles. The governing forces that are employed in this study include the drag force, the gravitational force, Brownian motion, and lift force or lift due to shear [58,59]. The virtual mass force, pressure gradient force, and thermophoretic force are excluded from this study due to the very small size of particles, negligible pressure, and temperature differences [3, 60]:

$$\varepsilon\frac{\partial \mathrm{v_i}}{\partial \mathrm{t}} = \mathrm{a}\frac{\mathrm{Du_i}}{\mathrm{Dt}} + \frac{\mathrm{f}}{\tau_{\mathrm{p}}}(\vec{u} - \vec{\mathrm{v}}) + \vec{\mathrm{g}}(1 - \mathrm{a}) + \mathrm{f_{i,Brownian}} + \mathrm{f_{i,lift}}\,, \frac{\mathrm{dx_i}}{\mathrm{dt}} = \vec{\mathrm{v}}(\mathrm{t}) \tag{5.15}$$

$$\tau_{\mathrm{p}} = \frac{\mathrm{C_c}\rho_{\mathrm{p}}\mathrm{d_p^2}}{18\mu} \tag{5.16}$$

where $\vec{v}$ is the component of the particle velocity, $\vec{u}$ is the component of local continuous velocity, a is the ratio of mixture density to droplet density ($a = \rho_{air}/\rho_p \approx 10^{-3}$), τ_p is the particle relaxation time, f is the drag factor, C_c is the Cunningham correction factor, d_p is the particle diameter, and μ is the air dynamic viscosity. Injection characteristics used in this simulation are given in **Table 5.1**.

Table 5.1 Summary of physical characteristics of materials and DPM injection model.

Parameter	Value
Injection duration [60]	1.5 s
Velocity magnitude [2]	17.5 m/s
Cone angle [61]	22.57°
Particle size range [55]	100 nm to 60 µm
Total mass flow rate [3]	1×10^{-5} kg/s
Time step size	1×10^{-5} s

5.3.4 Boundary Conditions and Flow Systems

This study consists of two different configurations for boundary conditions. For the first configuration, while the air flow rate is zero, the pre-specified outlet pressure for the inlet and outlet was assigned for both the IM and SM geometries based on the experimental system and the zero-pressure gradient inside the geometries. For the second configuration, while there is an airflow rate in the system, an inlet velocity was selected at the outlet to account for the effect of flow rate on drug aerosol velocity and deposition. A stationary wall with zero slip shear and a trap DPM condition was considered to capture drug particles while accounting for drug deposition when they hit the mouth wall so that there is no bounce. A constant temperature of 23°C was considered during the simulations with a normal relative humidity level of 50% inside both geometries to meet the experimental procedure [2].

5.3.5 Numerical Controls and Computational Power

For numerical accuracy, a second-order upwind scheme was employed for momentum, k, and ω [49]. In this study, the convergence of the flow field was determined when continuity, k, and ω residuals reached below 1×10^{-5}. To perform computational tasks, the supercomputing facility at Lakehead University was used. This supercomputer was equipped with an Intel Xeon Gold 6148 CPU @ 2.40GHz with 16 cores. In addition, parallel processing was used on Intel Xeon Silver 4214 CPU @ 2.20 and 2.19 GHz processors with 16 cores. The simulation duration varied between 3-7 days.

5.3.6 Mesh Independency Study

Mesh independency studies were carried out for both geometries using a mesh adaptation technique. **Table 5.2** shows four cell sizes and a corresponding number of meshes for both IM and SM geometry.

Table 5.2 Cell sizes and the number of cells for IM and SM.

Geometry	Mesh	Average cell size (mm)	Number of cells	Comparison	NRMSE in X=15 mm (%)	NRMSE in X=30 mm (%)
IM	Mesh A	2.10	37,488	Mesh A&B	3.8	11.1
	Mesh B	1.50	81,472	Mesh B&C	2.3	9.4
	Mesh C	1.10	162,360	Mesh C&D	1.6	3.5
	Mesh D	0.81	320,044			
SM	Mesh E	2.10	42,336	Mesh E&F	12.2	11.3
	Mesh F	1.60	79,040	Mesh F&G	3.5	4.9
	Mesh G	1.15	158,752	Mesh G&H	2.3	3.0
	Mesh H	0.83	312,301			

Fig 5.3 shows the particles' velocity for different meshes (Mesh A to Mesh H, see **Table 5.2**) for both IM and SM geometry on two lines in the y-direction (vertical) at 15 mm and 30 mm from the SMI nozzle on the x-axis. We selected these lines close to the nozzle because of high turbulence and velocity fluctuations in that area. The normalized root mean square error (NRMSE), is defined as:

$$NRMSE(\%) = \frac{\sqrt{(\sum_{i,j=1}^{N}(u_i - u_j)^2)/N}}{\sqrt{(\sum_{i=1}^{N}(u_i)^2)/N}} \times 100 \tag{5.17}$$

Where i, j are the variables, N is the number of data points, which is 7 in this case, and u_i and u_j are two different sets of particles' velocity values, were utilized to quantify the differences among the particles' velocity profiles [62]. All the measured velocity in this study is velocity magnitude. **Table 5.2** shows the NRMSE between the meshes.

As can be seen in **Fig 5.3(a) and 3(b)** and NRMSEs reported in **Table 5.2**, at both distances from the SMI nozzle (15 mm and 30 mm, respectively), particles' velocity changes significantly between Mesh A and Mesh B, and Meshes B and C. However, for the third refinement (from Mesh C to Mesh D), increasing the number of cells two times (162k to 320k) resulted in the NRMSEs =1.6 and 3.5 % for lines at x= 15 *mm* and x= 30 *mm*, respectively (see **Table 5.2**). For the SM geometry, shown in **Fig 5.3(c)** and **Fig 5.3(d),** the NRMSEs reported in **Table 5.2** were 2.3 and 3.0 % between Mesh G and Mesh H for x= 15 *mm* and x= 30 *mm* distance from the SMI nozzle, respectively. Therefore, the IM and SM mesh contained 162k cells (Mesh C) and 158k cells (Mesh G), respectively.

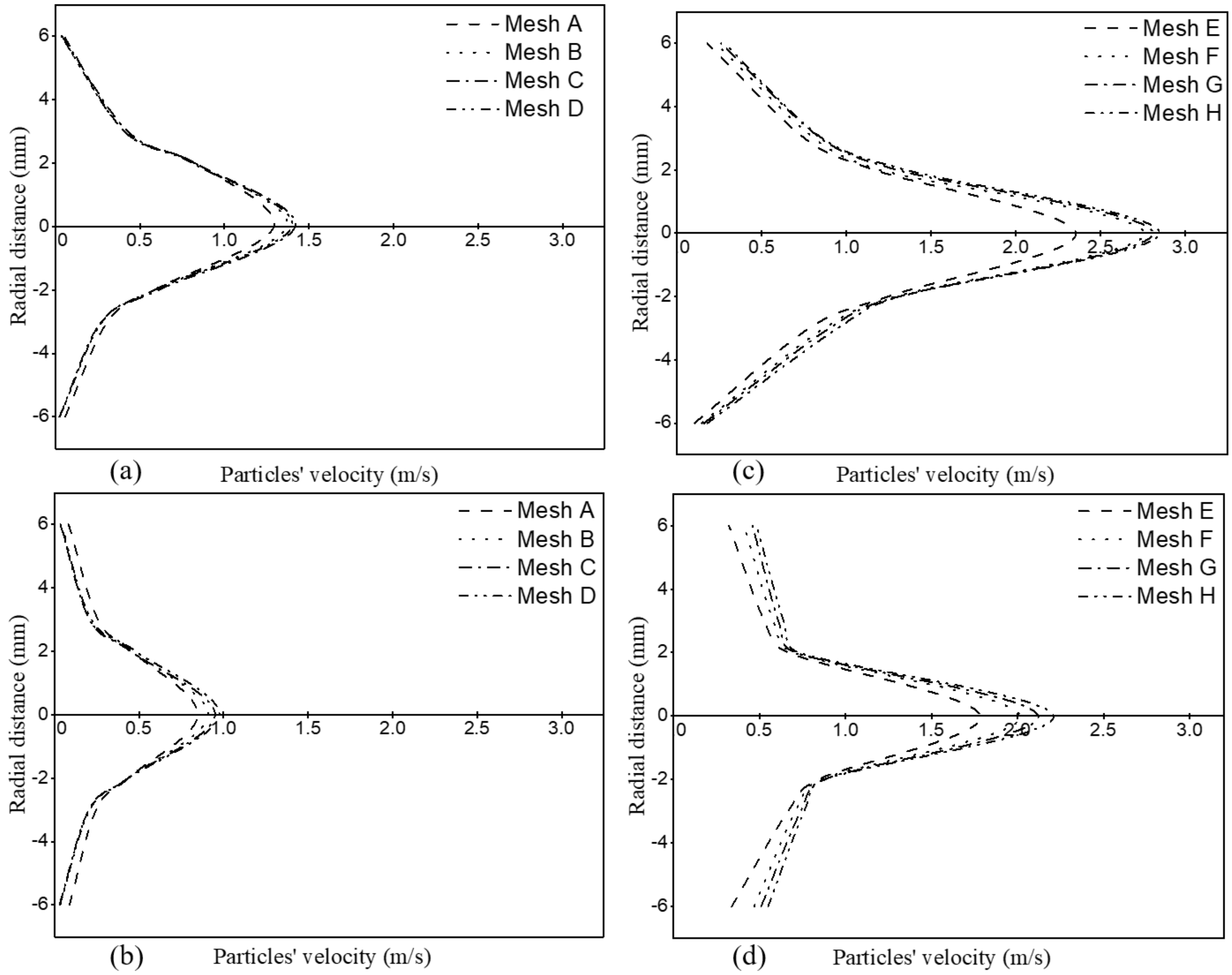

Fig 5.3 Particles' velocity for different meshes in IM for **(a)** vertical (y-direction) at 15 mm, **(b)** vertical (y-direction) at 30 mm; Particles' velocity for different meshes in SM for **(c)** vertical (y-direction) at 15 mm, and **(d)** vertical (y-direction) at 30 mm. (legend shows the number of cells).

5.4 Results and Discussion

The numerical results of particles' velocity at the outlets of both the IM and SM geometries when the nozzle position was at $x_{0,}$ and the flow rate was 0 l/min were compared with the previous experimental data [2]. The experimental particles' magnitude velocities were measured at the outlets of IM and SM at seven radial distances (i.e., 6, 3, 2, 0, -2, -3, and -6 mm) in the vertical and horizontal directions, that is, y and z, respectively.

Fig 5.4 shows a good agreement between CFD and experimental results of (2) at the outlets of both geometries at the zero-flux of air and nozzle position of x0. The maximum NRMSEs calculated were 6.5 and 9.6 %for both CFD and experimental particles' velocity for the IM and SM geometries, respectively. The discrepancy between experimental results and the simulations can be attributed to imperfect replications of determining locations in simulations and/or experimental uncertainties at the outlet related to particles' velocity and distributions.

A fixed flow rate of 30 l/min was applied to both IM and SM to investigate the effect of the flow rate. **Fig 5.5** shows that with a flow rate of 30 l/min, vertical and horizontal (y and z) particle velocities increased at both geometries' outlets. The addition of flow rate to the system helped drug particles to accelerate. Since the SMI nozzle was located along the centerline of the mouth geometry, the average velocity at the center of the profile was higher. However, the velocity increment was more significant (almost two times higher than IM) in the presence of the flow rate of 30 l/min for the SM geometry, as shown in **Fig 5.5(c)** and **5(d).** This is mainly due to the geometry of the SM, in which the outlet diameter is narrower by 11 mm than that of the IM geometry, thus enhancing the impact of the flow rate. The axial velocity increment associated with geometry constriction was consistent with the previous CFD study of Xi and Longest in a constant inhalation rate [63]. They also related the aerosol axial velocity to the drug deposition at the back of the throat. Their study showed that as a result of higher aerosol velocity, a more significant number of particles passed through the mouth (outlet of IM and SM) and were deposited on the back of the throat [63].

Slightly different vertical and horizontal velocity profiles are observed when comparing **Fig 5.5(a, b)** and **Fig 5.5 (c,d)**. This is because the particles' velocity was reduced due to evaporation and loss of inertia as the particles traveled downstream. However, the asymmetrical velocity profile in vertical and horizontal directions can be attributed to the gravitational effect.

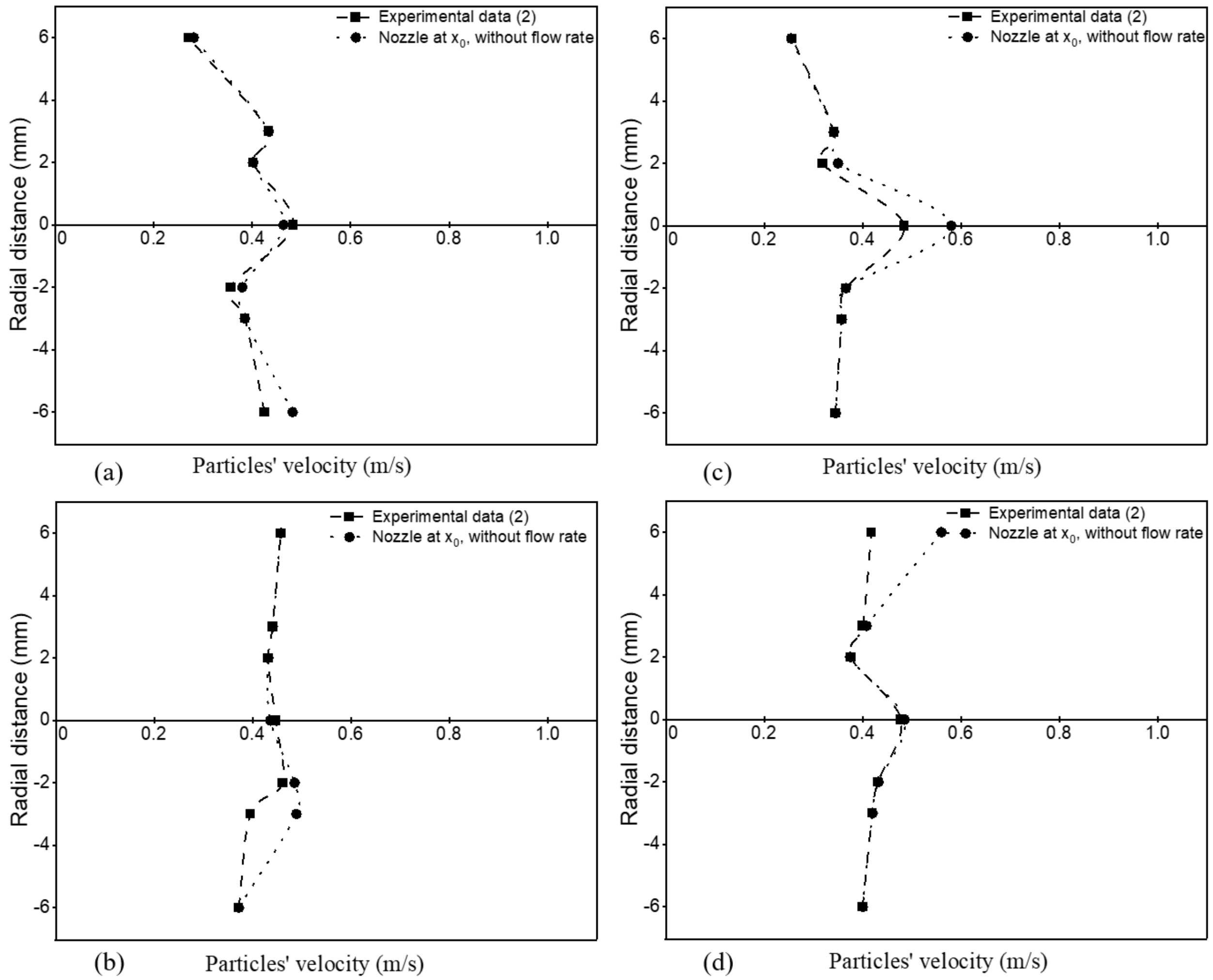

Fig 5.4 Model validation for particles' velocity at zero-flux of air and nozzle position of x_0 at the outlet of IM geometry for **(a)** vertical (y-direction), and **(b)** horizontal (z-direction); and model validation for particles' velocity at zero-flux of air and nozzle position of x_0 at the outlet of SM geometry for **(c)** vertical (y-direction), and **(d)** horizontal (z-direction).

Fig 5.6 represents vertical velocity vector plots along the mouth pathway, that is, in x direction, for the IM and SM**.** This figure also confirms higher velocity profiles for the SM geometry. As the plume travels along the mouth, uniform profiles were observed in the presence of the flow rate (see **Fig 5.6(b,d)**), which is more significant in **Fig 5.6(d)** for SM geometry. However, in both IM and SM, velocities along the centerline decreased more rapidly for the case with no flow rate (see **Fig 5.6(a,c)**) in comparison with near-the-wall locations that are more dominant in **Fig 5.6(a)** for the IM geometry. In fact, the particles' trajectory is influenced by the drag force, which is caused by the surrounding flow field and results in a decrease in the particles' velocity. This effect is more significant at the center of the velocity profile, where the particles have the highest velocity, and when there is no flow rate inside the geometry. In fact, in the absence of a constant flow rate in the system, the aerosol plume is not well formed and developed. Previously, Longest and Hindle also showed that SMI creates an uneven aerosol plume in an open-air environment during the actuation in a zero-flux of air atmosphere [4].

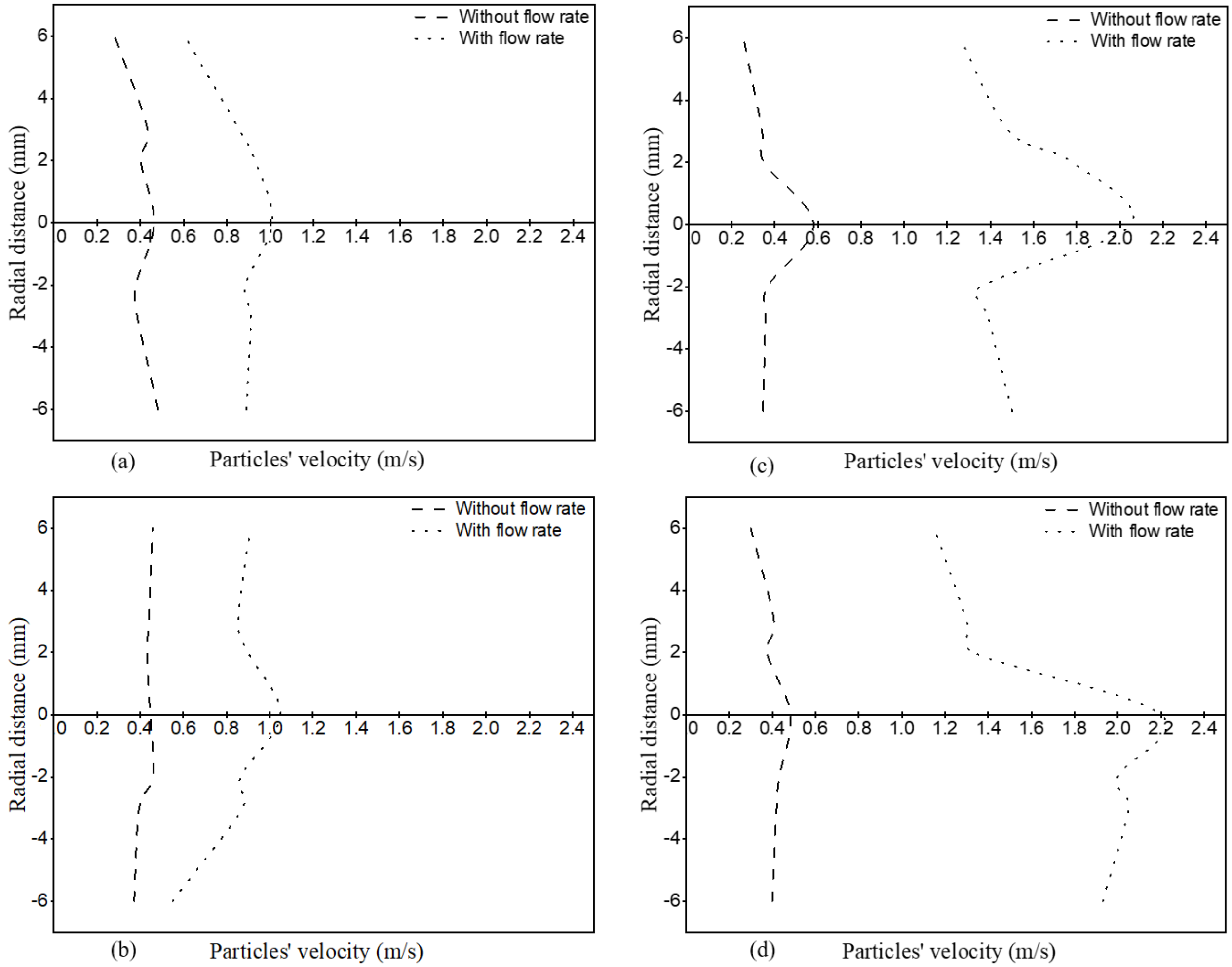

Fig 5.5 Particles' velocity at the outlet of IM for **(a)** vertical (y-direction), and **(b)** horizontal (z-direction); velocity profiles at the outlet of SM for **(c)** vertical (y-direction), and **(d)** horizontal (z-direction), for nozzle position at x_0.

Table 5.3 presents the mouth deposition for both IM and SM geometries as a function of the flow rate (either 0 or 30 l/min) and nozzle position (x_0, x_1, and x_2: see **Fig 5.1**). This table shows an almost 15-fold and 40-fold decrease in mouth wall deposition in the IM and SM geometries, respectively, in the presence of the flow rate. With a fixed flow rate of 30 l/min inside both IM and SM, the particles had less residence time, and consequently, the possibility of deposition on the mouth wall was dramatically reduced. According to Longest *et al.*, a higher inhalation rate resulted in lower particle residence time in the human respiratory tract [3]. Thus, a lack of inhalation results in an increase in drug deposition (a waste of drugs inside the mouth region, which leads to increased side effects) [3].

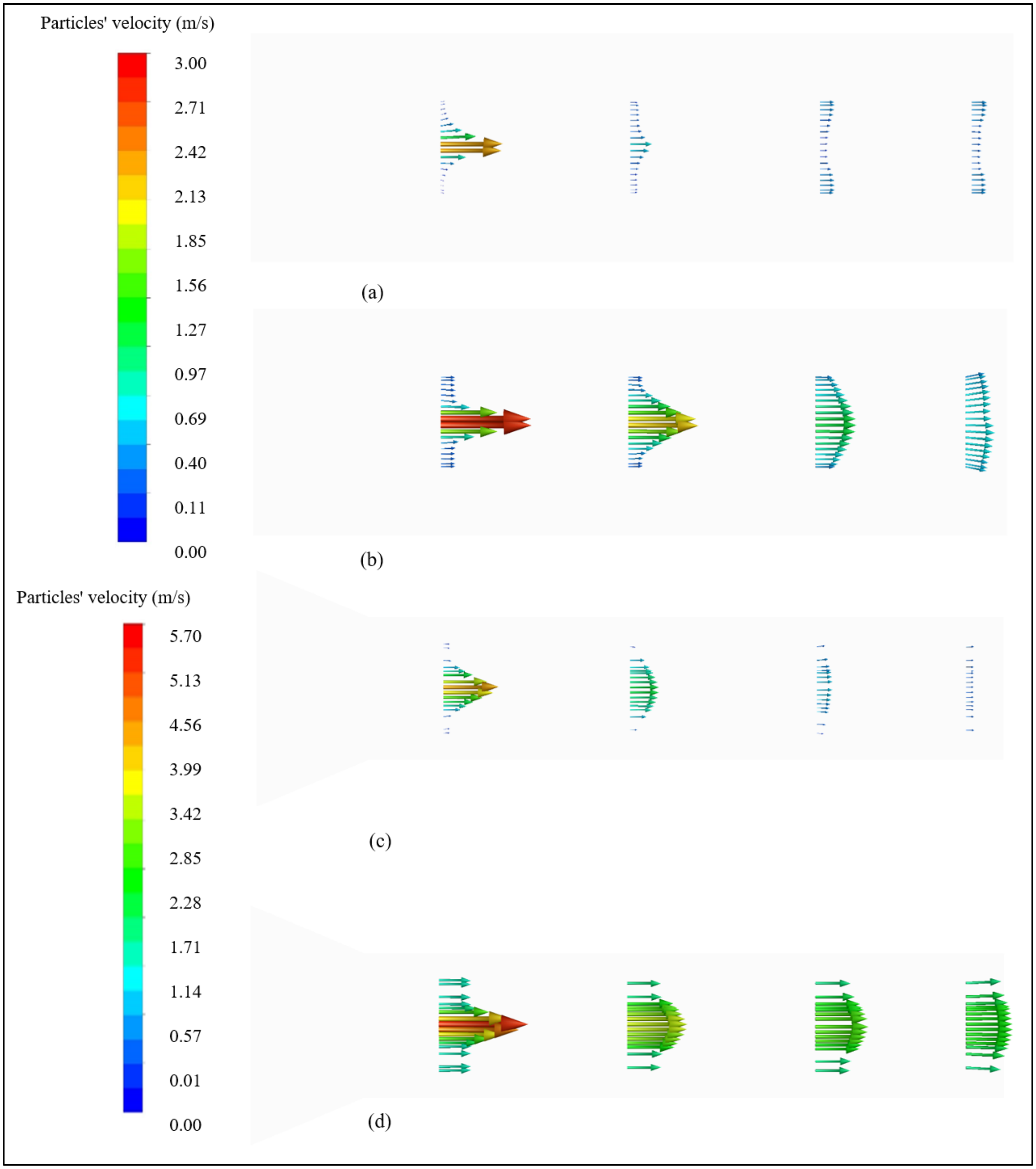

Fig 5.6 Particles' velocity vectors inside IM: **(a)** without flow rate, and **(b)** with a flow rate of 30 l/min; and inside SM: **(c)** without flow rate, and **(d)** with a flow rate of 30 l/min; at nozzle position of x_0.

Table 5.3 Particle deposition data for both IM and SM

Geometry	Flow rate (l/min)	Nozzle position on x-axis	Mouth wall deposition (kg)	Deposition fraction of particles with diameter >5 µm on mouth wall (%)
IM	0	x_0	1.27×10^{-7}	97
	30	x_0	6.82×10^{-11}	100
	0	x_1	3.97×10^{-7}	97.3
	30	x_1	2.75×10^{-11}	100
	0	x_2	5.12×10^{-7}	99
	30	x_2	2.23×10^{-11}	100
SM	0	x_0	3.93×10^{-7}	64.5
	30	x_0	1.5×10^{-8}	100
	0	x_1	7.96×10^{-7}	75.11
	30	x_1	6.97×10^{-9}	100
	0	x_2	8.19×10^{-7}	76.1
	30	x_2	2.08×10^{-9}	98.9

Fig 5.7(a-d) shows velocity path lines inside IM and SM geometries. Recirculation regions were formed inside both geometries (see **Fig 5.7(a)** for IM and **Fig 5.7(c)** for SM) near the SMI nozzle when there was no flow rate. The presence of recirculation flows was also discussed in other studies as one of the leading causes of an increase in particle deposition inside the human respiratory tract [63,64]. In a CFD study by Koullapis *et al.*, recirculation zones are found near the mouth wall due to the geometry curvature [65]. However, no studies showed strong recirculation regions around the nozzle when moving the nozzle position further along the x-axis, forcing particles to flow backward toward the inlet. As demonstrated in **Fig 5.7(b, d)**, the flow rate in the system removed recirculation regions inside both the IM and SM geometries, resulting in lower particle deposition, as reported in **Table 5.3**.

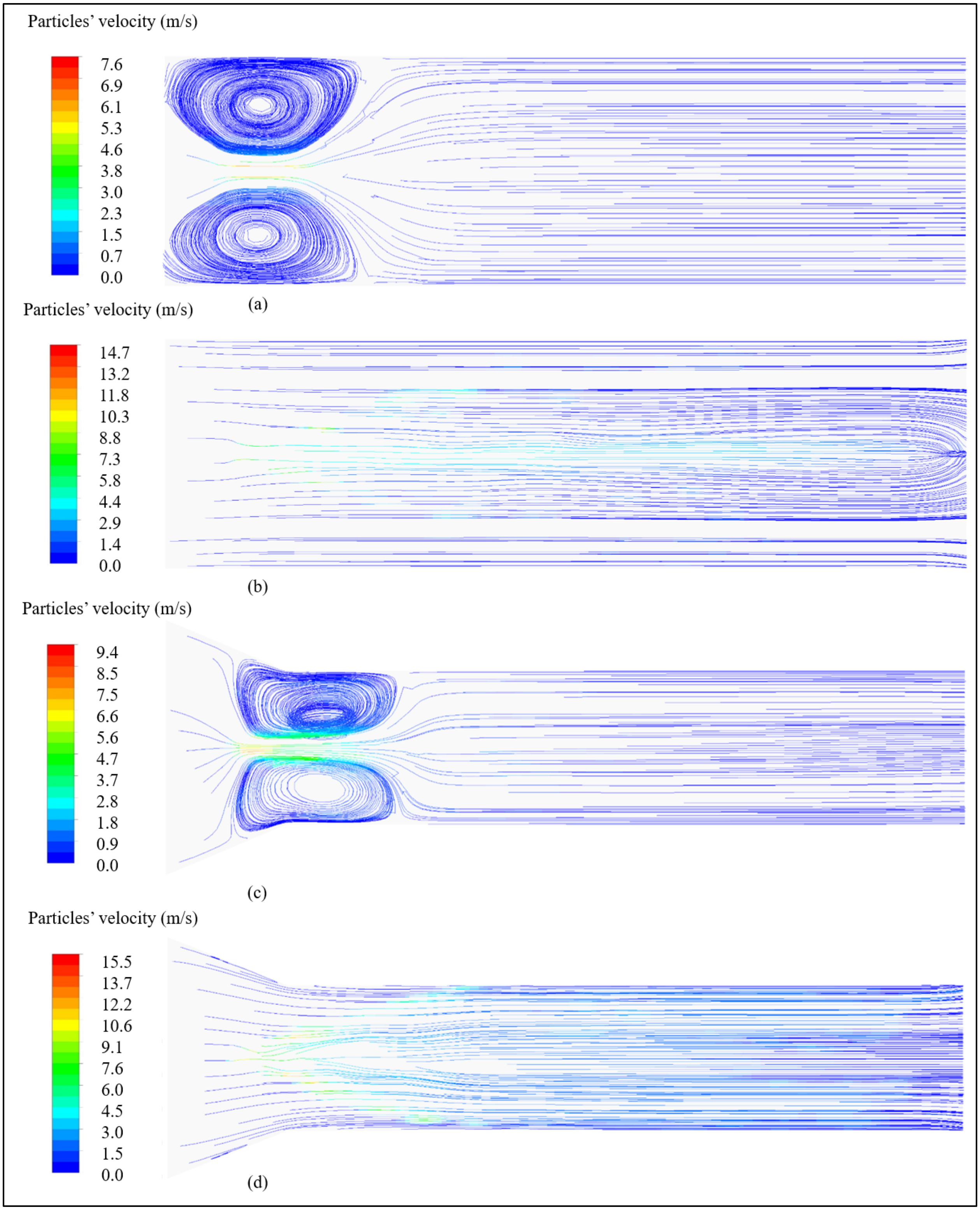

Fig 5.7 Particles' velocity path line at 0.03s for IM: **(a)** without flow rate, and **(b)** with a flow rate of 30 l/min; and for SM: **(c)** without flow rate, and **(d)** with a flow rate of 30 l/min, at the nozzle position of x_2.

Table 5.3 also shows that particle deposition on the mouth wall for both IM and SM was increased when the nozzle position was changed from x_0 to x_1 and x_2 within the mouth on the x-axis. Despite the shorter distance of the inhaler device's nozzle from the outlet in the x_1 and x_2 positions, particle deposition on the walls of IM and SM increased when there was no flow rate. This is due to a number of particles traveling in the opposite direction (toward the inlet), which can be called the "backflow" of an aerosol plume. The plume backflow was caused by the interaction of the high-speed aerosol plume exiting from the nozzle and zero-flux of air inside the mouth geometry that forms recirculation flows around the nozzle. During the recirculation, larger particles (higher mass) are likelier to travel in a straight line rather than follow the recirculation trajectory due to their higher inertia, leading them to leave the recirculation region and deposit on the mouth wall. As seen in **Fig 5.8(a)**, recirculation flow increases the particles' residence time in the system, which, in turn, leads to higher particle deposition on the wall of IM and SM. Milenkovic *et al.*, through a CFD approach using DPI devices, reported that a slow flow field is developed by recirculation flow that results in a higher residence time for drug particles inside the mouth area [66]. The presence of backflow is evident from **Fig 5.8(b)** at the beginning of actuation (0.03 s). However, with a fixed flow rate in the system, that backflow field significantly disappeared (see **Fig 5.7(b)**).

Table 5.3 shows that moving the nozzle position from x_0 to x_1 and x_2 in both geometries, especially in the SM geometry, increases deposition on the mouth area for particles with diameters higher than 5 μm. Despite the nozzle position, with a fixed flow rate (30 l/min) in both geometries, an increase in deposition fraction for particles with a diameter greater than 5 μm was observed. This observation is consistent with the result of previous CFD analyses. For example, Longest and Hindle showed that particles with a diameter >5 μm primarily reside at the exterior edge of the SMI plume due to their greater inertia [4]. The flow rate adds to their inertia, and consequently, their chance of deposition increases. In fact, particles with a diameter >5 μm have a reduced possibility of deposition in the lower airways [4]. This table also demonstrates that a greater number of fine particles, that is <5 μm, traveled from IM and SM geometry outlets to human lungs. Smaller particles, with a diameter of approximately 3-5 μm, have a better chance of deposition in the lungs due to their good lung penetration efficiency and less loss from exhalation in adults [61].

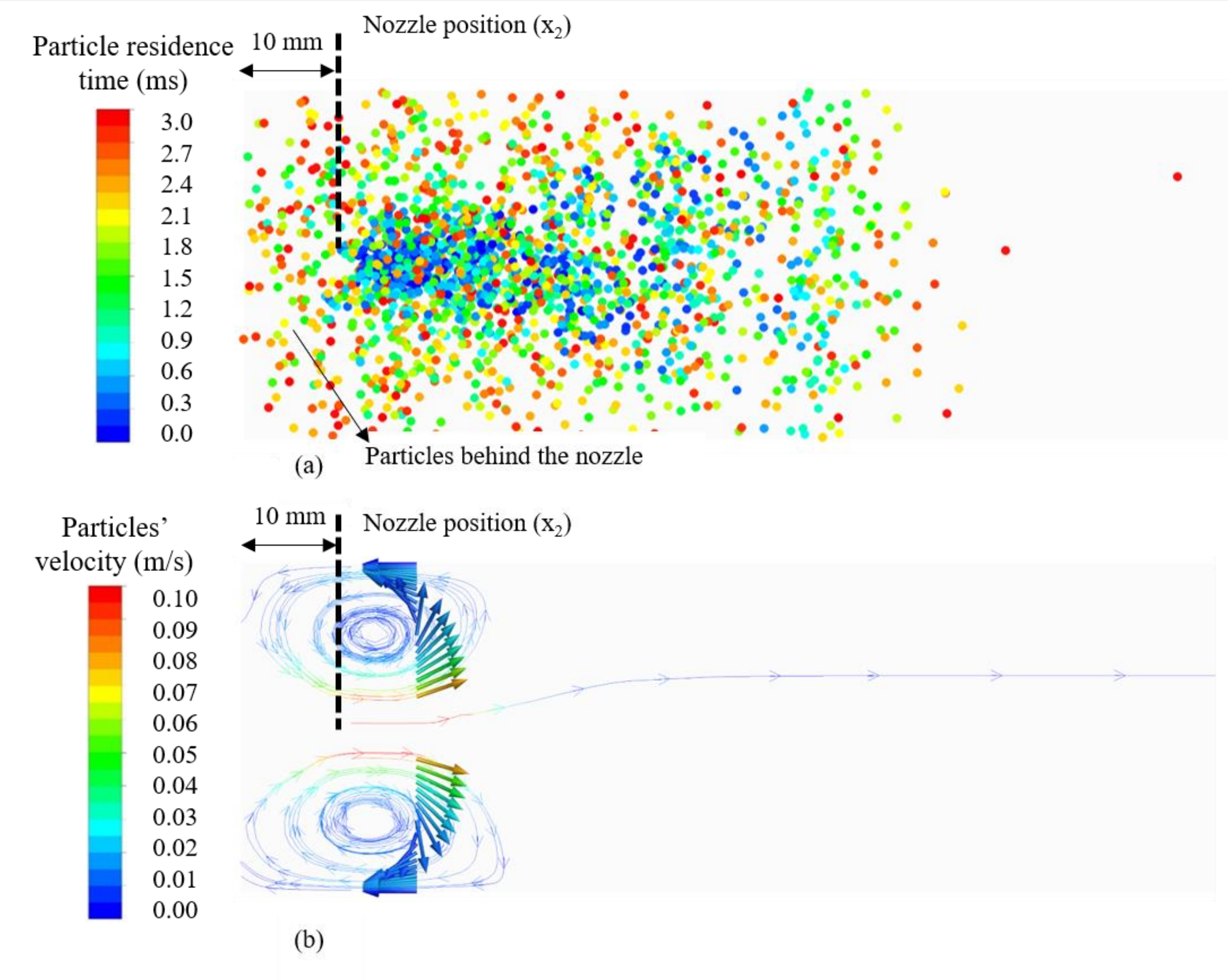

Fig 5.8 (a) Particle residence time at the beginning of actuation inside IM; and **(b)** Particles' velocity for the backflow near the SMI nozzle inside IM; at nozzle position of x_2 for zero-flux of air.

Fig 5.9 shows the effect of different SMI nozzle angles on particle deposition with no flow rate inside the IM. Increasing the SMI nozzle angle from 0° to 10° and 20° increased particle deposition in the mouth area, and this increment was more significant while the nozzle was positioned at x_2. It was found that stronger recirculation regions increased particle residence time and backflow effect. This resulted in higher deposition rates inside the IM geometry. In contrast, particle deposition on the mouth wall decreased when a fixed flow rate of 30 l/min was applied in the IM. This shows that the flow rate helped particles to pass the outlet. Histograms in **Fig 5.9** also show that the flow rate was more influential than the nozzle position.

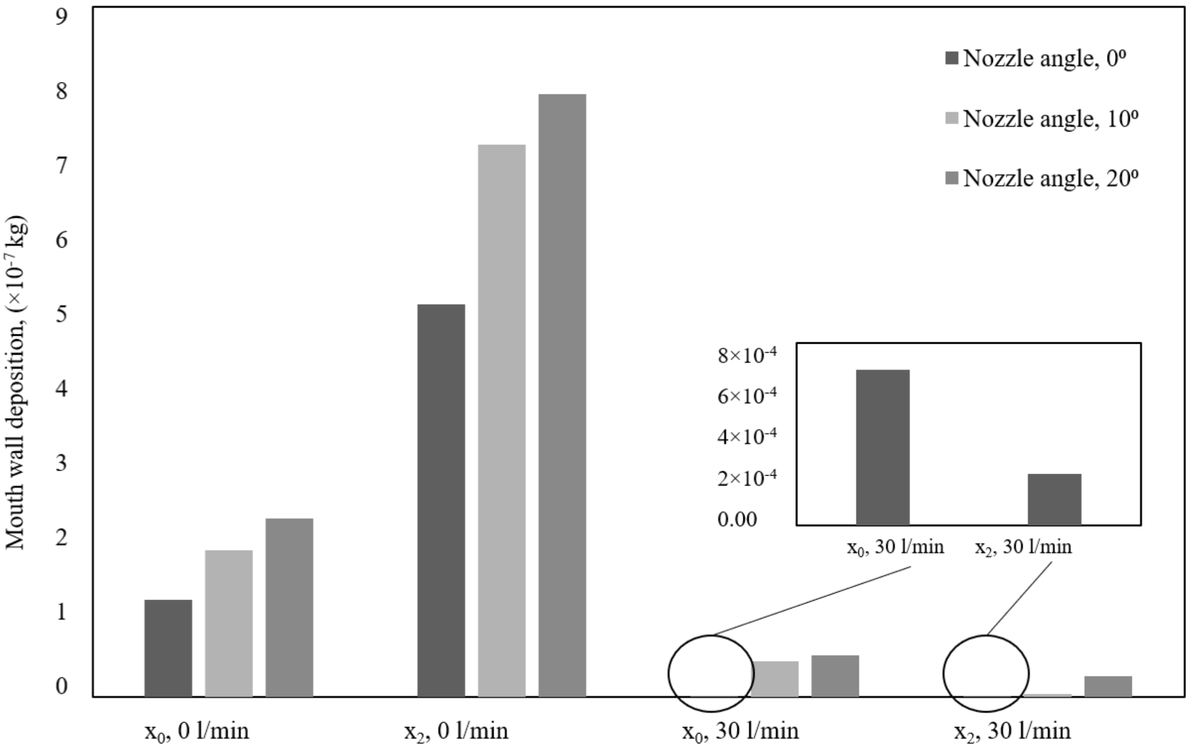

Fig 5.9 Comparison of mouth wall deposition inside IM at x_0 and x_2 for different SMI nozzle angles with and without a flow rate of 30 l/min.

Table 5.4 presents the particle deposition mass and fraction on the mouth wall and for particles that passed the outlet of IM as a function of nozzle angle (10° and 20°), nozzle position (x_0 and x_2), and flow rate (either 0 or 30 l/min). Considering the total mass flow rate (1.5×10^{-5} kg in 1.5 s), when the nozzle angle is 20°, and the SMI nozzle is at x_0 for a case of 0 l/min (i.e., no flow rate), a total mass of 0.44×10^{-5} kg/s is lost in the human mouth. Moving the nozzle position as well as applying a fixed flow rate of 30 l/min allowed more particles to exit the IM geometry. In contrast, increasing the SMI nozzle's angle decreased the number of particles leaving the mouth outlet. The deposition fraction of particles with a diameter >5 µm on the wall and the mass fraction of particles that passed the outlet of the IM decreased when the nozzle angle increased to 20°. The decrease in the deposition fraction for particles with a diameter >5 µm when changing the SMI angle to 20° is attributed to the reduced chance of particle impact on the IM wall for the lower side of the aerosol plume. However, an upward trend was still observed in the total mass deposition for particles with a diameter >5 µm on the mouth wall and the mass of particles with the same diameter range that passed the outlet of IM. This shows that moving the SMI nozzle forward along the x-axis and applying a fixed flow rate of 30 l/min has a more substantial effect on particle deposition than increasing the SMI nozzle angle.

Table 5.4 Data for particles that pass the outlet for different SMI nozzle angles inside IM

Flow rate (l/min)	**Nozzle position on x-axis**	**SMI nozzle angle**	**Mass of particles that passed the outlet (kg)**	**Mass fraction of particles that passed the outlet with a diameter >5 µm (%)**	**Deposition fraction of particles with diameter >5 µm on mouth wall (%)**
0	x_0	10°	1.13×10^{-5}	36	92
0	x_0	20°	1.06×10^{-5}	34.5	89
0	x_2	10°	1.39×10^{-5}	36.1	99
0	x_2	20°	1.32×10^{-5}	35.6	92
30	x_0	10°	1.43×10^{-5}	37.1	26
30	x_0	20°	1.42×10^{-5}	37	23
30	x_2	10°	1.46×10^{-5}	36.9	58
30	x_2	20°	1.45×10^{-5}	36.8	54

Fig 5.10 shows the effect of nozzle angle on the particle size distribution with a flow rate of 30 l/min inside the IM. **Fig 5.10(a)** shows that when the SMI nozzle angle is 0° (the inhaler mouthpiece is positioned correctly in the mouth), particles with a diameter >5 µm primarily reside at the upper and lower sides of the aerosol plume. When the SMI nozzle angle increased to 20°, see **Fig 5.10(b)**, particles with a diameter >5 µm residing at the upper side of the plume deposited on the IM wall. However, particles with a diameter >5 µm residing at the lower side of the aerosol plume exit the IM outlet toward the throat. This explains the decrease in the deposition fraction of particles with a diameter >5 µm at the SMI nozzle angle of 20° reported in **Table 5.4**.

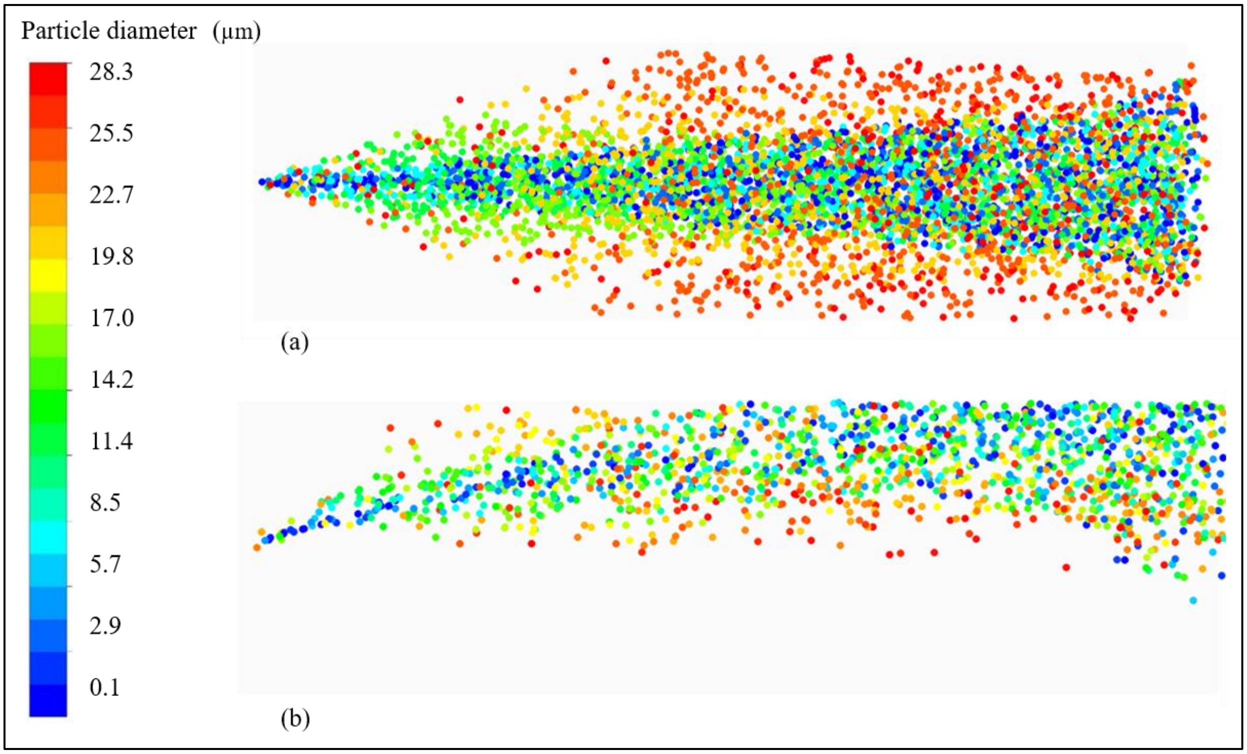

Fig 5.10 Particle size distribution inside IM at x_0 and with a constant flow rate of 30 l/min at **(a)** SMI nozzle angle of 0°, and **(b)** SMI nozzle angle of 20°.

Fig 5.11 shows that by changing the SMI nozzle position in the mouth along the x-axis from x_0 to x_1 and x_2, the average velocity of drug particles at the IM and SM outlet increased. **Fig 5.11(a, b)** show that the drug particles' average velocity at the outlet for IM increased from 0.173 m/s to 0.390 m/s as the nozzle's position changed from x_0 to x_1, respectively. Moving the nozzle further forward from the mouth inlet along the x-axis to x_2 increased the outlet drug particles' average velocity to 0.519 m/s due to fewer interactions of the drug particles with air. However, the velocity increment when the nozzle moved from x_0 to x_1 was more than twice that of when the nozzle moved from x_1 to x_2. As shown in **Fig 5.8(b)**, the backflow of the drug particles noticeably affected the sensitivity of the velocity increment in IM.

Fig 5.11(c,d) show that the average velocity of drug particles at the outlet of the SM increased from 0.190 m/s at the nozzle position of x_0 to 0.660 m/s at the nozzle position of x_2. The aerosol particles' velocity decreased nonlinearly along the x-axis due to their entry into a stabilized atmosphere that imparts a drag force onto each aerosol. We also observed that at the beginning of the actuation, due to the zero-flow rate of the continuous phase in the mouth, some of the drug particles flowed in the opposite direction (along the negative x-axis). When the SMI nozzle is positioned further inside the mouth (x_1 or x_2), the system tracks more drug particles flowing backward (see **Fig 5.8(a, b)**), and consequently, the sensitivity of the velocity increment is reduced. While comparing the aerosols' horizontal (z-direction) and vertical (y-direction) velocity profiles at the outlets, no noticeable change was observed along the centerline. The horizontal velocity profile, however, showed a slightly higher aerosol velocity near the mouth wall. This asymmetric velocity profile in the y- and z-direction was not unexpected due to the turbulent flow inside the system. Applying a constant flow rate when moving the SMI nozzle to x_1 and x_2 removed backward flow and increased the particles' average velocity at both IM and SM outlets. This increment was more noticeable for SM due to its narrower diameter. The comparison of vertical and horizontal velocity profiles did not show any significant difference between IM and SM.

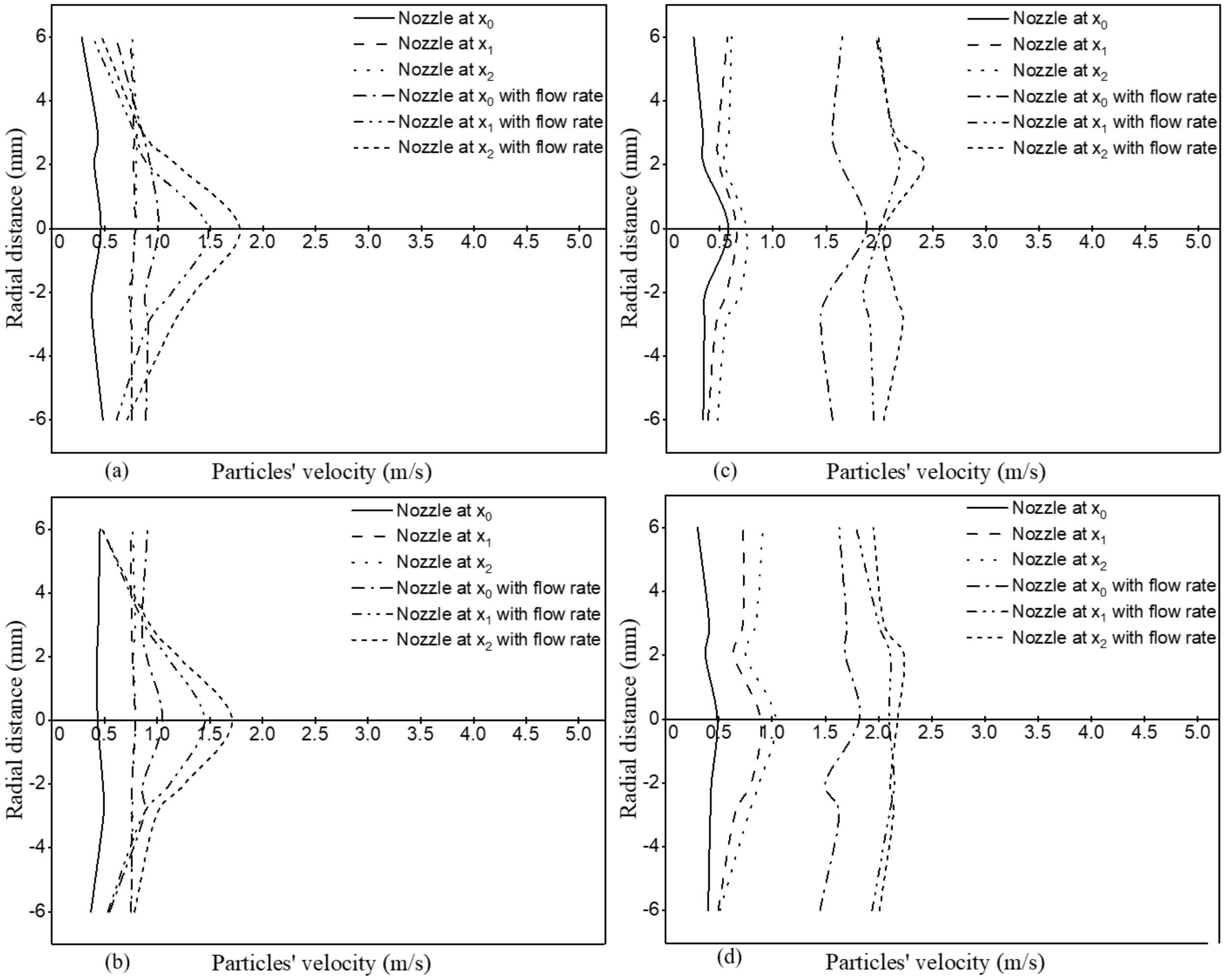

Fig 5.11 Particles' velocity at the outlet of IM for **(a)** vertical (y-direction), and **(b)** horizontal (z-direction); Particles' velocity at the outlet of SM for **(c)** vertical (y-direction), and **(d)** horizontal (z-direction), for different nozzle positions with and without flow rate of 30 l/min.

5.5 Conclusions

A CFD study investigated the effects of flow rate and SMI nozzle position and angle on the particles' velocity profile, size distribution, and deposition in the mouth area. We modeled the simple mouth geometries and did not consider the throat region in our study to mimic the geometries employed in the available experimental study. The CFD results were first validated against experimental data and showed that the CFD model could simulate aerosol particle transport and deposition inside the mouth. Our results showed that mouth geometry (IM and SM) significantly affects the velocity of aerosol particles and particle deposition on the mouth wall. With a fixed flow rate of 30 l/min, the aerosol velocity at the outlet of both geometries increased while the mouth wall deposition decreased. The deposition fraction of larger particles that is >5 μm, increased with a fixed flow rate of 30 l/min. We found that recirculation regions and backward flow were the main reasons for the increase in the particles' residence time, leading to higher particle deposition in the absence of the flow rate. By moving the SMI nozzle further forward in the mouth along the center line (x-axis), the velocity at the outlet of both IM and SM increased, and this increment was more significant for SM geometry. Particle deposition on the mouth wall increased by moving the nozzle position to x_1 and x_2. The flow rate inside the IM geometry decreased particle deposition significantly. This shows that flow rate is a more effective parameter on particle deposition than the nozzle's position. Also, wrongly positioning the SMI by changing the SMI's nozzle angle inside the human mouth increased the particle deposition in the mouth and, consequently, decreased the mass of particles that passed the outlet of the IM geometry. However, a sufficient flow rate of 30 l/min as an inhalation rate can make the effect of the SMI's nozzle angle less significant. Although the geometries modeled in this study were simple and limited only to the mouth area, the results can be used to design a new add-on (such as a sensor or a mouthpiece) that can notify patients (primarily children or the elderly) when they use an SMI inhaler in the wrong position.

5.6 Nomenclature

Abbreviations

CFD	Computational Fluid Dynamic
DPI	Dry Powder Inhaler
DPM	Discrete Phase Model

IM	Idealized Mouth
NRMSE	Normalized Root Mean Square Error
pMDI	Pressurized Metered Dose Inhaler
SM	Standard Mouth
SMI	Soft Mist Inhaler
URANS	Unsteady Reynolds Averaged Navier-Stokes

Notations

C_u	model constant, -
C_p	specific heat constant, J/kg.K
d_p	particle diameter, μm
D_V	diffusion coefficient, m^2/s
$\vec{g}$	gravitational acceleration, m/s^2
h_s	enthalpy of species, J
k	turbulent kinetic energy, m^2/s^2
k_g	air conductivity, W/m.K
N	Number of data points, -
P	time-average pressure, Pa
Pr_T	turbulent Prandtl number, -
Sc_T	turbulent Schmidt number, -
S_e	air energy source term, W/m^3
S_V	water vapor source term, kg/m^3
t	time, s
$\vec{u}$	velocity at a single point, m/s
$\bar{U}_i$	mean velocity, m/s
u'_i	fluctuating velocity, m/s
$\vec{v}$	Component of particle velocity, m/s
x'	dynamic shape factor, -
Y_V	mass fraction of water vapor in the mixture, -

Greek letters

$\alpha_k, \beta^*, \beta, \sigma_k, \sigma_\omega$	coefficients of shear stress transport model, -
δij	Kronecker delta, -
ε	dissipation rate, m^2/s^3
F	anisotropic correction factor, -
λ_i	normally distributed random number. -
μ	air dynamic viscosity, kg/m.s
ρ	mixture density, kg/m^3
ρ_{air}	air density, kg/m^3
ρ_0	unit density, kg/m^3
ρ_p	particle density, kg/m^3
ν	kinematic eddy viscosity, kg/m.s
ν_t	turbulent viscosity, kg/m.s
τ_{ij}	Reynold stress tensor, m^2/s^2
ω	turbulent frequency, s^{-1}

5.7 References

[1] A. M. Ciciliani, M. Denny, P. Langguth, T. Voshaar, and H. Wachtel, "Lung Deposition Using the Respimat® Soft Mist^{TM} Inhaler Mono and Fixed-Dose Combination Therapies: An In Vitro/In Silico Analysis," COPD: Journal of Chronic Obstructive Pulmonary Disease, vol. 18, no. 1, pp. 91–100, 2020, doi: 10.1080/15412555.2020.1853091.

[2] A. Alatrash, R. Mehri, N. Ogrodnik, E. Matida, and F. Fiorenza, "Experimental Study of Spiriva Respimat Soft Mist Inhaler Spray Characterization: Size Distributions and Velocity," J Aerosol Med Pulm Drug Deliv, vol. 32, no. 5, pp. 293–302, 2019, doi: 10.1089/jamp.2018.1501.

[3] P. W. Longest, G. Tian, X. Li, Y. J. Son, and M. Hindle, "Performance of combination drug and hygroscopic excipient submicrometer particles from a softmist inhaler in a characteristic model of the airways.," Ann Biomed Eng, vol. 40, no. 12, pp. 2596–2610, 2012, doi: 10.1007/s10439-012-0616-2.

[4] P. Worth Longest and M. Hindle, "Evaluation of the respimat soft mist inhaler using a concurrent cfd and in vitro approach," J Aerosol Med Pulm Drug Deliv, vol. 22, no. 2, pp. 99–112, Jun. 2009, doi: 10.1089/jamp.2008.0708.

[5] F. Dastoorian, L. Pakzad, J. Kozinski, and E. Behzadfar, "A CFD Investigation on the Aerosol Drug Delivery in the Mouth–Throat Airway Using a Pressurized Metered-Dose Inhaler Device," Processes, vol. 10, no. 7, Jul. 2022, doi: 10.3390/pr10071230.

[6] T. Iwanaga, Y. Tohda, S. Nakamura, and Y. Suga, “The Respimat® Soft Mist Inhaler: Implications of Drug Delivery Characteristics for Patients,” Nov. 01, 2019, Springer International Publishing. doi: 10.1007/s40261-019-00835-z.

[7] A. H. de Boer, P. Hagedoorn, M. Hoppentocht, F. Buttini, F. Grasmeijer, and H. W. Frijlink, “Dry powder inhalation: past, present and future,” Expert Opin Drug Deliv, vol. 14, no. 4, pp. 499–512, 2017, doi: 10.1080/17425247.2016.1224846.

[8] M. Saeedipour, “Atomization of two colliding micro liquid jets in a respiratory inhaler: A computational study,” ILASS–Europe 2019, 29th Conference on Liquid Atomization and Spray Systems, 2-4 September 2019, Paris, France, no. September, 2019.

[9] K. J. Brown, W. Kalata, and R. J. Schick, “Experimental and Computational Study of a Spray at Multiple Injection Angles Impact Study of a Clean in Place Tank Wash System,” Analysis, no. May, pp. 2010–2010, 2010.

[10] W. Longest, B. Spence, and M. Hindle, “Devices for Improved Delivery of Nebulized Pharmaceutical Aerosols to the Lungs,” J Aerosol Med Pulm Drug Deliv, vol. 32, no. 5, pp. 317–339, Oct. 2019, doi: 10.1089/jamp.2018.1508.

[11] P. W. Longest and C. Kleinstreuer, “Computational models for simulating multicomponent aerosol evaporation in the upper respiratory airways,” Aerosol Science and Technology, vol. 39, no. 2, pp. 124–138, Feb. 2005, doi: 10.1080/027868290908786.

[12] B. Zierenberg, “The Respimat, a new inhalation system based on the piezoelectric effect,” Biopharm sci, vol. 3, pp. 85–90, 1992.

[13] B. Zierenberg, “Optimizing the in Vitro Performance of Respimat,” Mary Ann Liebert, Inc. Pp. S, 1999. [Online]. Available: www.liebertpub.com

[14] S. K. Aggarwal, Review of “Handbook of Atomization and Spray: Theory and Applications,” vol. 50, no. 3. 2012. doi: 10.2514/1.j051310.

[15] A. R. Martin and W. H. Finlay, “Nebulizers for drug delivery to the lungs,” Expert Opin Drug Deliv, vol. 12, no. 6, pp. 889–900, 2015, doi: 10.1517/17425247.2015.995087.

[16] P. W. Longest and M. Hindle, “Condensational growth of combination drug-excipient submicrometer particles for targeted high efficiency pulmonary delivery: Comparison of CFD predictions with experimental results,” Pharm Res, vol. 29, no. 3, pp. 707–721, Mar. 2012, doi: 10.1007/s11095-011-0596-1.

[17] E. A. Matida, W. H. Finlay, C. F. Lange, and B. Grgic, “Improved numerical simulation of aerosol deposition in an idealized mouth-throat,” J Aerosol Sci, vol. 35, no. 1, pp. 1–19, 2004, doi: 10.1016/S0021-8502(03)00381-1.

[18] M. G. Cochrane, M. V. Bala, K. E. Downs, J. Mauskopf, and R. H. Ben-Joseph, “Inhaled corticosteroids for asthma therapy: Patient compliance, devices, and inhalation technique,” 2000, American College of Chest Physicians. doi: 10.1378/chest.117.2.542.

[19] W. R. Ke et al., “In vitro evaluation of aerosol performance and delivery efficiency during mechanical ventilation between soft mist inhaler and pressurized metered-dose inhaler,” Respir Care, vol. 65, no. 7, pp. 1001–1010, Jul. 2020, doi: 10.4187/respcare.06993.

[20] P. Demoly, P. Hagedoorn, A. H. De Boer, and H. W. Frijlink, “The clinical relevance of dry powder inhaler performance for drug delivery,” Respir Med, vol. 108, no. 8, pp. 1195–1203, 2014, doi: 10.1016/j.rmed.2014.05.009.

[21] S. P. Newman, K. P. Steed, S. J. Reader, D. Pavia, and A. K. Sohal, “An in vitro study to assess facial and ocular deposition from Respimat® Soft Mist™ inhaler,” Journal of Aerosol Medicine: Deposition, Clearance, and Effects in the Lung, vol. 20, no. 1, pp. 7–12, 2007, doi: 10.1089/jam.2006.0563.

[22] M. F. A. Rahman, N. Z. Asmuin, I. Taib, M. N. H. Mat, and R. Khairulfuaad, “Influence of actuator nozzle angle on the flow characteristics in pressurized-metered dose inhaler using cfd,” CFD Letters, vol. 12, no. 6, pp. 67–79, 2020, doi: 10.37934/cfdl.12.6.6779.

[23] D. Hira et al., “Assessment of inhalation flow patterns of soft mist inhaler co-prescribed with dry powder inhaler using inspiratory flow meter for multi inhalation devices,” PLoS One, vol. 13, no. 2, Feb. 2018, doi: 10.1371/journal.pone.0193082.

[24] Ronald Dahl, “Systemic side effects of inhaled corticosteroids in patients with asthma,” pp. 1307–1317, 2006, doi: 10.1016/j.rmed.2005.11.020.

[25] R. R. Delvadia, P. Worth Longest, M. Hindle, and P. R. Byron, “In vitro tests for aerosol deposition. III: Effect of inhaler insertion angle on aerosol deposition,” J Aerosol Med Pulm Drug Deliv, vol. 26, no. 3, pp. 145–156, Jun. 2013, doi: 10.1089/jamp.2012.0989.

[26] A. Fadl, J. Wang, Z. Zhang, and Y. Sung, “Effects of MDI spray angle on aerosol penetration efficiency through an oral airway cast,” vol. 38, pp. 853–864, 2007, doi: 10.1016/j.jaerosci.2007.06.002.

[27] R. Dutta, B. Spence, X. Wei, S. Dhapare, M. Hindle, and P. W. Longest, “CFD Guided Optimization of Nose-to-Lung Aerosol Delivery in Adults: Effects of Inhalation Waveforms and Synchronized Aerosol Delivery,” Pharm Res, vol. 37, no. 10, 2020, doi: 10.1007/s11095-020-02923-8.

[28] M. Yousefi, K. Inthavong, and J. Tu, “Effect of Pressurized Metered Dose Inhaler Spray Characteristics and Particle Size Distribution on Drug Delivery Efficiency,” J Aerosol Med Pulm Drug Deliv, vol. 30, no. 5, pp. 359–372, Oct. 2017, doi: 10.1089/jamp.2016.1299.

[29] W. H. Finlay and C. Darquenne, “Particle Size Distributions,” J Aerosol Med Pulm Drug Deliv, vol. 33, no. 4, pp. 178–180, 2020, doi: 10.1089/jamp.2020.29028.whf.

[30] K. Miyamoto, H. Taga, T. Akita, and C. Yamashita, “Simple method to measure the aerodynamic size distribution of porous particles generated on lyophilizate for dry powder inhalation,” Pharmaceutics, vol. 12, no. 10, pp. 1–14, 2020, doi: 10.3390/pharmaceutics12100976.

[31] R. Mehri, K. L. Slew, A. Alatrash, E. Matida, and F. Fiorenza, “Aerosol Deposition Measurements with ODAPT Mask Adapter,” vol. 13, no. 2, pp. 10–14, 2018.

[32] G. Pitcairn, S. Reader, D. Pavia, and S. Newman, “Deposition of Corticosteroid Aerosol in the Human Lung by Respimat ® Soft Mist^{TM} Inhaler Compared to Deposition by Metered Dose Inhaler or by Turbuhaler ® Dry Powder Inhaler,” 2005. [Online]. Available: www.liebertpub.com

[33] M. Hindle and P. W. Longest, “Evaluation of Enhanced Condensational Growth (ECG) for controlled respiratory drug delivery in a mouth-throat and upper tracheobronchial model,” Pharm Res, vol. 27, no. 9, pp. 1800–1811, 2010, doi: 10.1007/s11095-010-0165-z.

[34] P. Worth Longest and M. Hindle, “CFD simulations of enhanced condensational growth (ECG) applied to respiratory drug delivery with comparisons to in vitro data,” J Aerosol Sci, vol. 41, no. 8, pp. 805–820, 2010, doi: 10.1016/j.jaerosci.2010.04.006.

[35] P. Brand, B. Hederer, G. Austen, H. Dewberry, and T. Meyer, “Higher lung deposition with Respimat ® Soft Mist^{TM} Inhaler than HFA-MDI in COPD patients with poor technique,” 2008.

[36] R. Mehri, A. Alatrash, N. Ogrodnik, E. A. Matida, and F. Fiorenza, “In Vitro Measurements of Spiriva Respimat Dose Delivery in Mechanically Ventilated Tracheostomy Patients,” J Aerosol Med Pulm Drug Deliv, vol. 34, no. 4, pp. 242–250, Aug. 2021, doi: 10.1089/jamp.2019.1570.

[37] X. Wei et al., “In vitro tests for aerosol deposition. VI: Realistic testing with different mouth-throat models and in vitro - In vivo correlations for a dry powder inhaler, metered dose inhaler, and soft mist inhaler,” J Aerosol Med Pulm Drug Deliv, vol. 31, no. 6, pp. 358–371, Dec. 2018, doi: 10.1089/jamp.2018.1454.

[38] B. Gavtash et al., “Multi-physics theoretical approach to predict PMDI spray charactersitics [Abstract],” Drug Delivey to the Lungs 27, pp. 4–8, 2017.

[39] H. Mortazavi and L. Pakzad, “The hydrodynamics and mixing performance in a moving baffle oscillatory baffled reactor through computational fluid dynamics (CFD),” Processes, vol. 8, no. 10, pp. 1–30, 2020, doi: 10.3390/pr8101236.

[40] S. Agahzamin and L. Pakzad, “CFD investigation of the gas dispersion and liquid mixing in bubble columns with dense vertical internals,” Chem Eng Sci, vol. 203, pp. 425–438, 2019, doi: 10.1016/j.ces.2019.03.048.

[41] K. Sutherland, L. Pakzad, and P. Fatehi, “CFD population balance modeling and dimensionless group analysis of a multiphase oscillatory baffled column (OBC) using moving overset meshes,” Chem Eng Sci, vol. 199, pp. 552–570, May 2019, doi: 10.1016/j.ces.2019.01.005.

[42] B. Ma and K. R. Lutchen, “CFD simulation of aerosol deposition in an anatomically based human large-medium airway model,” Ann Biomed Eng, vol. 37, no. 2, pp. 271–285, 2009, doi: 10.1007/s10439-008-9620-y.

[43] K. Bass and P. Worth Longest, “Recommendations for simulating microparticle deposition at conditions similar to the upper airways with two-equation turbulence models,” J Aerosol Sci, vol. 119, pp. 31–50, May 2018, doi: 10.1016/j.jaerosci.2018.02.007.

[44] K. Ahookhosh et al., “Flow Structure and Particle Deposition Analyses for Optimization of a Pressurized Metered Dose Inhaler (pMDI) in a Model of Tracheobronchial Airway,” European Journal of Pharmaceutical Sciences, vol. 164, no. June, p. 105911, 2021, doi: 10.1016/j.ejps.2021.105911.

[45] F. ANSYS, ANSYS, FLUENT, 19.3 Theory Guide. Canonsburg, PA., 2019.

[46] Y. Zhang, W. H. Finlay, and E. A. Matida, “Particle deposition measurements and numerical simulation in a highly idealized mouth-throat,” J Aerosol Sci, vol. 35, no. 7, pp. 789–803, 2004, doi: 10.1016/j.jaerosci.2003.12.006.

[47] S. Sarkar, S. P. Peri, and B. Chaudhuri, “Investigation of multiphase multicomponent aerosol flow dictating pMDI-spacer interactions,” Int J Pharm, vol. 529, no. 1–2, pp. 264–274, 2017, doi: 10.1016/j.ijpharm.2017.07.005.

[48] C. Paz, E. Suárez, J. Vence, and A. Cabarcos, “Engineering Analysis of the volume of fluid (VOF) method for the simulation of the mucus clearance process with CFD,” Comput Methods Biomech Biomed Engin, vol. 22, no. 5, pp. 547–566, 2019, doi: 10.1080/10255842.2019.1569637.

[49] X. Yin, I. Zarikos, N. K. Karadimitriou, A. Raoof, and S. M. Hassanizadeh, “Direct simulations of two-phase flow experiments of different geometry complexities using Volume-of-Fluid (VOF) method,” Chem Eng Sci, vol. 195, pp. 820–827, 2019, doi: 10.1016/j.ces.2018.10.029.

[50] H. Versteeg and W. Malalasekera, An introduction to computional fluid dynamics: The finite volume method. 2007.

[51] Y. Ge, Z. Tong, R. Li, F. Huang, and J. Yu, “Numerical and experimental investigation on key parameters of the respimat® spray inhaler,” Processes, vol. 9, no. 1, pp. 1–17, Jan. 2021, doi: 10.3390/pr9010044.

[52] P. Das, E. Nof, I. Amirav, S. C. Kassinos, and J. Sznitman, “Targeting inhaled aerosol delivery to upper airways in children: Insight from computational fluid dynamics (CFD),” PLoS One, vol. 13, no. 11, Nov. 2018, doi: 10.1371/journal.pone.0207711.

[53] R. L. Walenga, G. Tian, and P. Worth Longest, “Development of characteristic upper tracheobronchial airway models for testing pharmaceutical aerosol delivery,” J Biomech Eng, vol. 135, no. 9, 2013, doi: 10.1115/1.4024630.

[54] D. C. Wilcox, Turbulence modeling for CFD (Third edition). 2006.

[55] P. W. Longest, M. Hindle, S. Das Choudhuri, and J. Xi, “Comparison of ambient and spray aerosol deposition in a standard induction port and more realistic mouth-throat geometry,” J Aerosol Sci, vol. 39, no. 7, pp. 572–591, 2008, doi: 10.1016/j.jaerosci.2008.03.008.

[56] F. R. Menter, "Two-equation eddy-viscosity turbulence models for engineering applications," AIAA Journal, vol. 32, no. 8, pp. 1598–1605, 1994, doi: 10.2514/3.12149.

[57] R. V. A. O. W. S. J. Uijttewaal, "Particle dispersion and deposition in direct numerical and large eddy simulations of vertical pipe flows," physics of fluids, vol. 2590, no. June 1996, 1998.

[58] K. Inthavong, "From indoor exposure to inhaled particle deposition: A multiphase journey of inhaled particles," Jun. 01, 2020, Tsinghua University Press. doi: 10.1007/s42757-019-0046-6.

[59] M. M. Paul and L. Pakzad, "Bubble size distribution and gas holdup in bubble columns employing non-Newtonian liquids: A CFD study," Canadian Journal of Chemical Engineering, vol. 100, no. 10, pp. 3030–3046, Oct. 2022, doi: 10.1002/cjce.24352.

[60] S. Agahzamin and L. Pakzad, "A comprehensive CFD study on the effect of dense vertical internals on the hydrodynamics and population balance model in bubble columns," Chem Eng Sci, vol. 193, pp. 421–435, Jan. 2019, doi: 10.1016/j.ces.2018.08.052.

[61] W. Kamin, M. Frank, S. Kattenbeck, P. Moroni-Zentgraf, H. Wachtel, and S. Zielen, "A Handling Study to Assess Use of the Respimat® Soft Mist^{TM} Inhaler in Children under 5 Years Old," J Aerosol Med Pulm Drug Deliv, vol. 28, no. 5, pp. 372–381, Oct. 2015, doi: 10.1089/jamp.2014.1159.

[62] M. Gholamzadehdevin and L. Pakzad, "Hydrodynamic characteristics of an activated sludge bubble column through computational fluid dynamics (CFD) and response surface methodology (RSM)," Canadian Journal of Chemical Engineering, vol. 97, no. 4, pp. 967–982, Apr. 2019, doi: 10.1002/cjce.23335.

[63] J. Xi and P. W. Longest, "Effects of oral airway geometry characteristics on the diffusional deposition of inhaled nanoparticles," J Biomech Eng, vol. 130, no. 1, Jan. 2008, doi: 10.1115/1.2838039.

[64] R. Mehri, A. Alatrash, N. Ogrodnik, K. Lee Slew, and E. A. Matida, "Comparison of tiotropium delivery with the ODAPT adapter and a valved holding chamber," Canadian Journal of Respiratory, Critical Care, and Sleep Medicine, vol. 0, no. 0, pp. 1–7, 2020, doi: 10.1080/24745332.2020.1787112.

[65] P. G. Koullapis, L. Nicolaou, and S. C. Kassinos, "In silico assessment of mouth-throat effects on regional deposition in the upper tracheobronchial airways," J Aerosol Sci, vol. 117, pp. 164–188, Mar. 2018, doi: 10.1016/j.jaerosci.2017.12.001.

[66] J. Milenkovic, A. H. Alexopoulos, and C. Kiparissides, "Deposition and fine particle production during dynamic flow in a dry powder inhaler: A CFD approach," Int J Pharm, vol. 461, no. 1–2, pp. 129–136, 2014, doi: 10.1016/j.ijpharm.2013.11.047.

Chapter 6- Effect of Nasal Inhalation on Drug Particle Deposition and Size Distribution in the Upper Airway- with Soft Mist Inhalers

6.1 Abstract

Delivery of drugs to the lungs is commonly achieved using nasal and/or oral breathing-assisted techniques. The route of inhalation can substantially change the fate of inhaled droplets. The Respimat® Soft Mist™ Inhaler (SMI) is a commercially available efficient inhaler with 40-60% effectiveness. In the present study, we used computational fluid dynamics (CFD) with a custom setup to investigate the effect of a combined oral/nasal inhalation route on the SMI's regional droplet deposition, size distribution, and flow field. Our setup used a modified induction port (MIP) to mimic nasal inhalation inside the human respiratory tract. Six different oral/nasal flow rate ratios inside the MIP were applied (total flow rate of 30 l/min). Overall, a good agreement was achieved between simulation outcomes and in-vitro results. Our results confirmed that the combined inhalation route affects the flow field, altering the MIP's droplet deposition and size distribution. The lowest depositional loss, mainly in the mouth area, was observed at oral/nasal flow rate ratios of O/N=1 and O/N=2 with 3% and 7.7% values, respectively. Droplets with a 2-5 µm diameter range showed the highest droplet mass inside the MIP at all combined flow rates. We observed less intense vortexes followed by a lower level of turbulent kinetic energy at the oral/nasal ratio of 1. Increasing the relative humidity (RH) at oral/nasal flow rate ratios of 0.07, 1, and 14 led to an increase in droplet deposition at the outlet of the MIP.

Keywords: SMI, CFD, combined oral and nasal inhalation, droplet diameter, deposition efficiency, relative humidity.

6.2 Introduction

Inhalation therapy is the most common treatment for pulmonary infections and incurable and debilitating respiratory diseases like asthma, chronic obstructive pulmonary disease, and cystic fibrosis [1]. Various administration methods, such as oral and nasal inhalation, are employed to deliver the medication directly to the lungs via the pulmonary route [1]. To achieve targeted delivery and minimize unwanted systemic side effects, it is essential to finetune the deposition site of the drug-aerosol within the human lower respiratory tract [2]. Drug deposition in the mouth-throat region wastes medication (hence decreasing its effectiveness) and increases intersubject variability and side effects [3–5]. Several factors affect mouth-throat deposition and subsequent lung deposition, including the inhaler device, inhalation flow rate, and breathing pattern [6–8]. Therefore, understanding the impact of these factors on drug deposition in the human respiratory tract is crucial to optimizing drug delivery and improving therapeutic outcomes.

Inhalers, including pressurized metered-dose inhalers, dry powder inhalers, and soft mist inhalers (SMIs), cause significant drug loss in the mouthpiece and mouth-throat region. Among inhaler types, SMIs demonstrate the highest efficiency, with about 40-60% drug deposition in the lungs, compared to only 10-20% for pressurized metered-dose and dry powder inhalers [3,9]. This higher efficiency of SMIs is attributed to their optimized droplet size and velocity, ease of use, and reduced dependency on patient inhalation [10]. Additionally, the long-lasting, slow-moving aerosol plume of an SMI contains a large fine-particle (<5 μm) fraction, enabling more efficient drug delivery to the lungs [11]. Generally, droplets with a diameter range of 2-5 μm have a higher chance of reaching and depositing in the lungs [12]. Aerosol droplets bigger than 5 μm are normally deposited before entering the trachea on the oropharynx and upper tracheobronchial region [13]. In comparison, droplets smaller than 2 μm have a great potential to be exhaled from the mouth [13].

Table 6.1 outlines research studies investigating the impact of inhalation rates and routes on localized droplet deposition patterns within the human respiratory tract. Overall, these investigations revealed that high inhalation flow rates could significantly change localized droplet deposition patterns, deposition fraction, and deposition efficiency of inhaled droplets based on the inhalation route. Regardless of the inhalation pathway, the incremental deposition rate in the lower human respiratory tract is slower for higher inhalation flow rates.

Breathing patterns in children, especially infants and toddlers, differ significantly from those of adults. In babies (<20 months), nasal inhalation is more prevalent than oral inhalation; nasal and oral breathing become equivalent at 20 months [14]. This is due to babies' varying developmental stages of nasal and oral cavities. In addition, nasal inhalation is more common than oral inhalation among small children under sleeping and rest conditions [15].

Individuals of different races exhibit diverse breathing patterns. Bennett and Zeman [16] compared the deposition of fine particles (1 and 2 μm carnauba wax particles) in the nasal airways of North and African American adults for nasal inhalation. These authors discovered that African-American adults have less elliptical nostrils and lower nasal resistance, thereby decreasing nasal deposition efficiency [16].

Table 6.1 Selected experimental and numerical studies comparing the effect of different inhalation rates on particle deposition.

Reference	**Inhalation route**	**Range of inhalation flow rate (l/min)**	**Findings**
Sadeghi *et al.* [17]	Oral airway	0-30	Droplet deposition on the mouth wall decreased by increasing the flow rate.
Ciciliani *et al.* [18]	Oral airway	27.5-82.5	Particle deposition on the lower respiratory tract increased at higher flow rates.
Mehri *et al.* [19]	Mechanical ventilator	28.3-60	Higher medication loss was observed in the ODAPT adapter, mask, and face at 40-50% of RH at higher flow rates.
Zhang and Kleinstreuer [20]	Nasal airway	30-60	The relative variation of segmental and regional deposition fraction was decreased at higher flow rates.
Brand *et al.* [9]	Oral airway	15-60	Drug deposition in the lungs increased at higher flow rates.
Longest and Xi [7]	Oral airway	15-60	Deposition efficiency in the oral cavity decreased for fine particles ranging from 1 to 120 nm at higher flow rates.
Zwartz and Guilmette [21]	Nasal airway	10-40	Particle deposition in the nasal cavity increased at higher flow rates.
Heyder *et al.* [22]	Nasal airway	30-60	Higher nasal cavity deposition was observed at higher flow rates.
Dong *et al.* [23]	Oral and nasal airways	18-50	Higher nasal and oral cavity deposition efficiency was observed for 5-100 nm particles at higher flow rates.
Tiwari *et al.* [24]	Oral airway	15-60	Drug particle accumulation was higher in the oral cavity at higher flow rates.
Ou *et al.* [25]	Oral and nasal airways	3-60	Higher deposition on the lower respiratory tract was observed for larger particles (10 μm) at higher flow rates.

Airway health/physical status also plays a significant role in determining the efficiency of the inhalation route. People have different preferences for oral, nasal, or combined inhalation routes when nasal passages are temporarily or permanently unavailable (i.e., suffering from colds/flu and small nostril size) [6]. Additionally, people usually rely on oral inhalation during peak exercise but use both oral and nasal inhalation during light activity [26]. Particle delivery to the lungs is significantly better in infants when delivered via the nasal airway than the mouth-throat airway at a constant flow rate and particle size due to different development stages of nasal and oral cavities in the early ages [27]. The research conducted by Zhang and Kleinstreuer [20] revealed that the ratio of oral to nasal flow rate substantially influences the deposition of particles within the pharynx, larynx, and trachea regions.

Furthermore, the airflow RH significantly impacts the trajectory of drug particles within the respiratory tract. Elevated humidity levels within human airways can induce hygroscopic growth of drug particles upon reaching the lungs [4]. An increase in RH from 30-45% to 90% led to a higher volume distribution percentage of particles when employing various jet nebulizers [28]. Specific characteristics of the drug solution being administered can heavily influence the behavior of particles at different RHs [29]. When employing the drug solution hydrofluoroalkane (HFA)135a in the RH range below 35%, there were minimal differences in throat deposition and lung dose fraction, regardless of airflow or temperature. However, within the RH range of 35-80%, throat deposition increased while lung dose fraction decreased. Notably, no significant effects of RH on throat deposition and lung dose fraction were observed when using drug solution HFA227 [29].

CFD modeling approaches are often used to predict aerosol transport and flow field and investigate the effect of any variable that is difficult to learn experimentally. Due to poor resolution, experimental procedures can only measure averaged data sets for regional droplet deposition. Nevertheless, validated CFD models can provide accurate localized deposition data sets for inhaled aerosols and flow distributions within nasal and oral airways [20,30]. While CFD studies can have high computational costs, the precision of the results cannot be disregarded [31]. As a result, the CFD technique (also referred to as an in-silico tool for upper oral and nasal airways) has been used in numerous studies [32,33].

Although CFD studies can give a detailed understanding of flow behavior and particle size distribution, they still need to be validated with in-vitro results. Only a few published studies compare factors influencing aerosol transport models on particle deposition in oral and nasal airways [2,6,34,35]. However, these studies have not considered the potential variations in flow fields created by different types of inhalers, nor have they explored the potential impact of varying oral/nasal flow rate ratios on the deposition patterns within the human respiratory tract. Thus, we created a modified induction port (MIP), a simplified version of the nasal airway, paired with a next-generation impactor (NGI) to generate in vitro results that we used to validate the CFD simulation. Using experimental and mathematical approaches, we determined the effect of nasal airflow on droplet deposition and size distribution inside the MIP. In order to simulate diverse breathing patterns and account for the significant impact of oral/nasal flow rate ratios on droplet deposition, various ratios were examined at a total flow rate of 30 l/min as a reasonable representative of the inspiratory flow rate of adults [36]. Finally, the impact of different airflow-RHs on droplet size distribution was investigated.

6.3 Experimental Methods

6.3.1 Experimental Setup

Fig 6.1 shows our experimental setup. The United States Pharmacopeia has specified using an induction port for aerosol deposition by an SMI. It remains the standard apparatus, along with an impactor used by the pharmaceutical industry to estimate the droplet deposition fraction in the human respiratory tract [37,38]. We modified an induction port to create a simplified nasopharynx cavity on the port's top end section (representing the nasopharynx and oropharynx intersection) to simulate the effect of nasal flow rate on drug droplet deposition and flow pattern inside the mouth-throat. We then 3-dimensionally (3D) printed (Ultimaker S3, Lakehead University) our MIP, which we used with an SMI and flow meter to measure droplet size distribution inside an NGI (Copley Scientific Ltd, Nottingham, UK) consisting of eight cups with cut-off size values of 0.4-11.72 µm, a breath actuation control, and a vacuum pump. A cooler was used to prevent solvent loss, which could produce artificially low droplet size measurements and compromise the integrity of the resulting data. The flow meter monitored the flow rate at the mouth and nasal inlets.

6.3.2 Experimental Procedure

Following the manufacturer's instruction, we actuated the SMI (Boehringer Ingelheim, Germany) device five times to prime it and to have a steady aerosol plume before connecting it to the experimental setup. The cooler was maintained at 5°C for 15 minutes, and the breath actuation control was calibrated before each test by connecting its outlet to a calibrated reference flow meter. The breath actuation control is set to specific flow rates (e.g., 5, 15, and 30 L/min), and its readings are compared against the reference meter. Any discrepancies are corrected using the breath actuation control’s adjustment interface or software. The vacuum pump drew air flow into the NGI at a temperature of 23±1°C and a relative humidity level of 40-50%. The flow meter monitored the flow rate at both mouth and nasal inlets after applying a 30 l/min flow rate by the vacuum pump, i.e., the measured oral/nasal flow rate ratio was O/N=14, equal to 28 l/min and 2 l/min flow rates in oral and nasal cavities, respectively. Following preliminary tests, thirty actuations with 30-second intervals between each actuation were sprayed to ensure sufficient drug deposition on all the impactor cups and a measurable quantity of medication reaching the filter via the HPLC, thereby facilitating an accurate evaluation of medication delivery [39]. The vacuum pump was left running for an additional 60 seconds after the last actuation to facilitate proper drug deposition at each stage of the NGI. The entire experiment was repeated three times to ensure the data was reproducible.

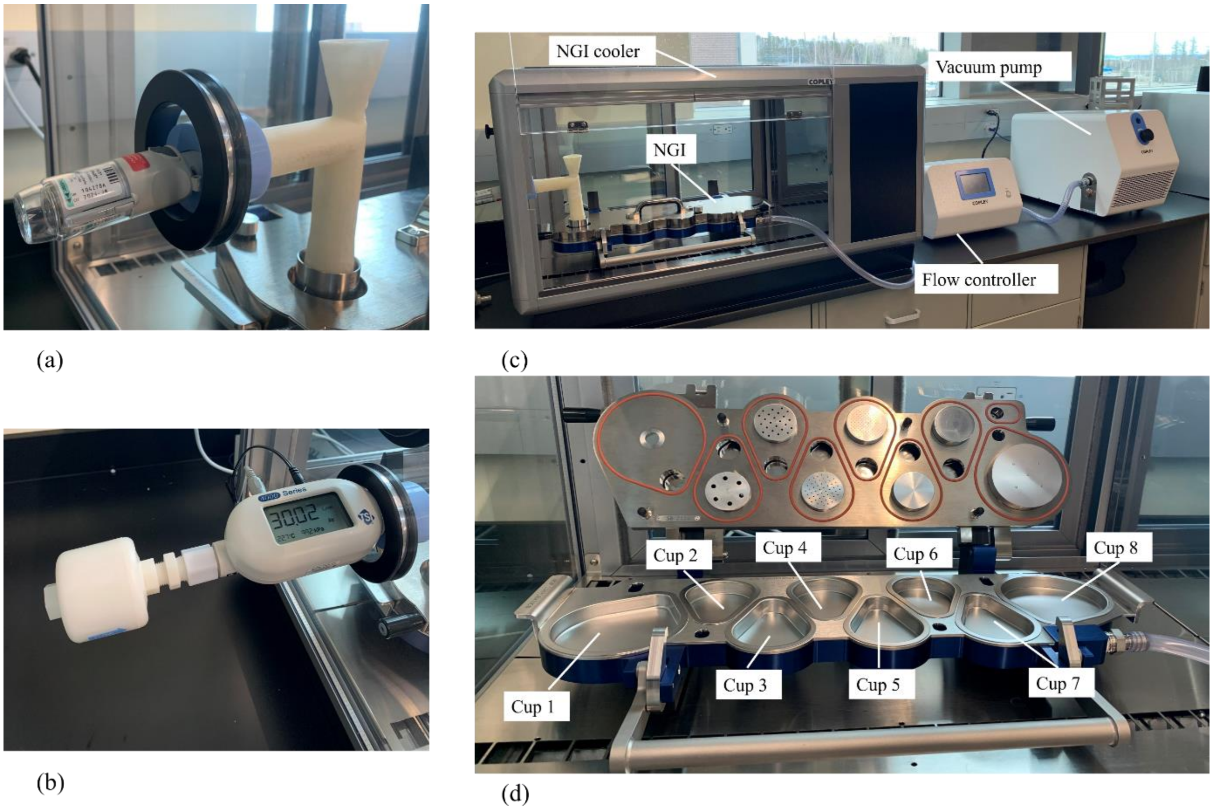

Fig 6.1 Experimental setup: **(a)** SMI and MIP, **(b)** Flow meter, **(c)** NGI, NGI cooler, flow controller, and vacuum pump, and **(d)** NGI cups with various cut-off sizes.

At the end of each experimental attempt, the SMI mouthpiece (MP), MIP, and NGI cups were disassembled, and each part was washed using 15 ml of 0.1% formic acid (v/v%) HPLC water solution to quantify the amount of deposited drug. Each piece held the solution individually while being slowly shaken for 1 minute. A stock solution of 1 mg of pure tiotropium bromide and 100 ml of 0.1% formic acid (v/v%) HPLC water solution was prepared and diluted to create the calibration curve. The drug deposition of each sample was then determined via HPLC. The absorption wavelength of tiotropium bromide was found at 237 nm.

Table 6.2 shows different combinations of the oral and nasal flow rates inside the MIP, which were considered to numerically evaluate the impact of oral and nasal breathing. These oral and nasal flow rates were selected to address the broad range of breathing patterns (2-28 l/min), inspired by the study of Lizal *et al.* [6]

In the current MIP model, the droplet deposition fraction for polydisperse droplets with diameters ranging from 0.1-60 µm was measured at various oral/nasal flow rate ratios, with a total flow rate of 30 l/min.

Table 6.2 Combination of flow rates used in the present study.

Oral and nasal flow rate ratio, O/N (-)	Oral flow rate (l/min)	Nasal flow rate (l/min)
0.07	2	28
0.2	5	25
0.5	10	20
1	15	15
2	20	10
5	25	5
14	28	2

6.4 CFD Model Development

6.4.1 Geometry and Mesh

Fig 6.2(a) shows the dimensional geometry of the SMI inhaler attached to the MIP by a mouthpiece with defined walls, each of which was used to evaluate droplet deposition and size distribution inside the MIP. The SMI body was excluded to avoid extra mesh and unnecessary computational costs.

Polyhedral and hex-dominant elements were used to discretize the MIP geometry. To accurately model the turbulent flow, the grid resolution close to the walls was refined; the first layer thickness of 0.1 mm was taken into account in our calculations. Also, a mesh refinement was done near the

SMI air vents and SMI nozzle to capture the flow behavior, especially during actuation (see **Fig 6. 2(b)**). To track droplet size distribution, six different planes were considered inside the MIP (**Fig 6. 2(c)**). These planes were chosen before or after a change in the diameter of the MIP geometry at 0, 18, 36.024, and 97 mm on the x-axis and 68.424 and 105 mm on the y-axis.

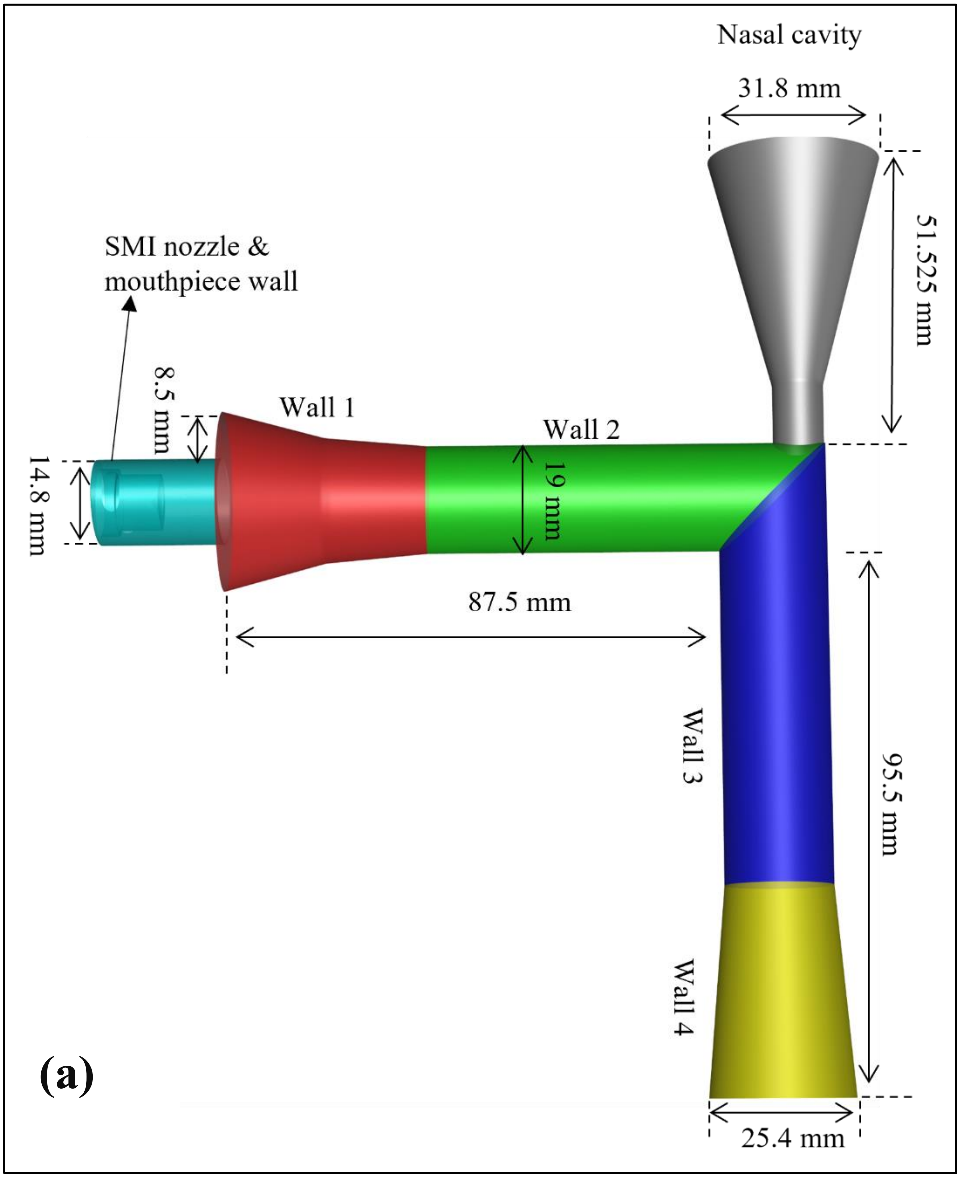

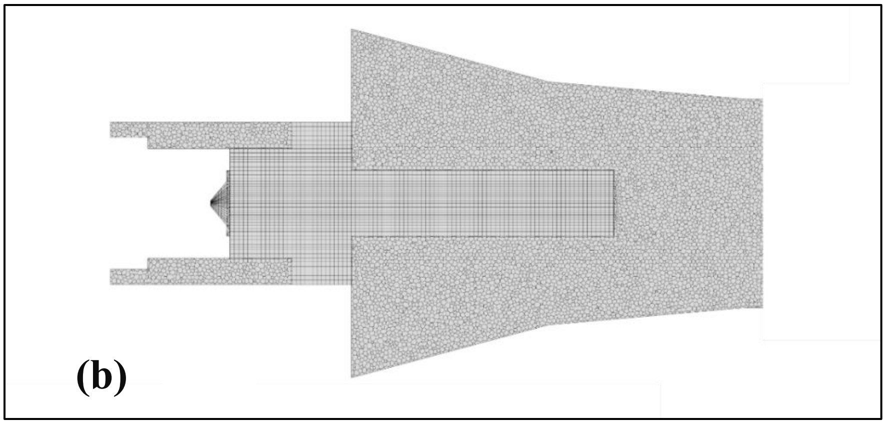

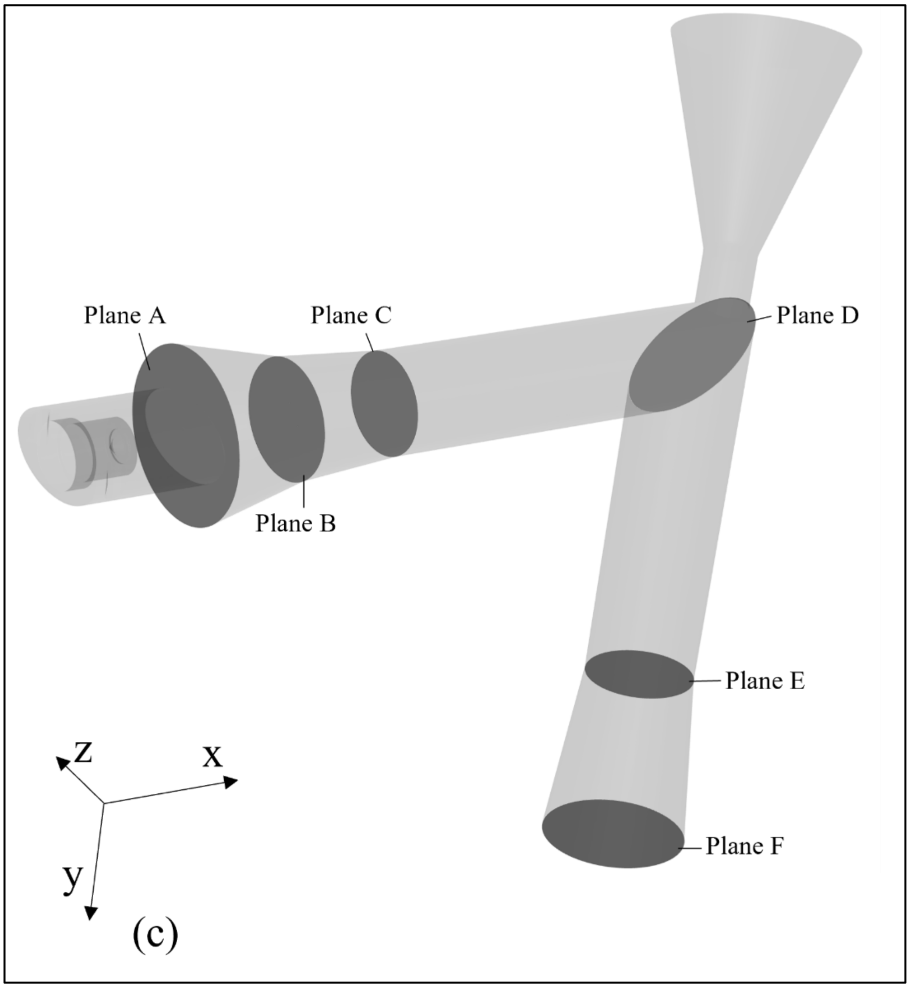

Fig 6.2 (a) MIP geometry (side view) including AB line at the MIP 90-degree bend for mesh independence purposes and colored walls to evaluate regional particle deposition and size distribution, and **(b)** Sample of mesh at the midplane near the mouth inlet (side view), and (c) Cross-sectional planes inside the MIP.

6.4.2 Mesh Sensitivity Analysis

Four mesh arrangements were established, from coarse to ultrafine, with elements numbering around 600,000, 1,200,000, 2,400,000, and 4,800,000. Air velocity magnitude was attained on lines AA (r) and AC (r) near the inlet and outlet of the MIP, respectively. As the droplets have rotational motion and swirl along the pipe, tangential air velocity was captured on the line AB (r) at the MIP 90-degree bend where the oral and nasal inhalation mixes, at O/N= 14 (**Fig 6.3**). The profiles were observed at 0.2 s of actuation and when the aerosol plume reached the MIP outlet. The root-mean-square error expressed the deviation between air velocity magnitude (for lines AA and AC, and air tangential velocity values (for line AB) on different element numbers [40]. Increasing the mesh resolution from 2,400,000 to 4,800,000 elements changed the root-mean-square error from 0.120 to 0.031 at line AA, 0.044 to 0.018 at line AB, and 0.056 to 0.014 at line AC. Therefore, the MIP geometry with a mesh of 2,400,000 elements was selected for this study.

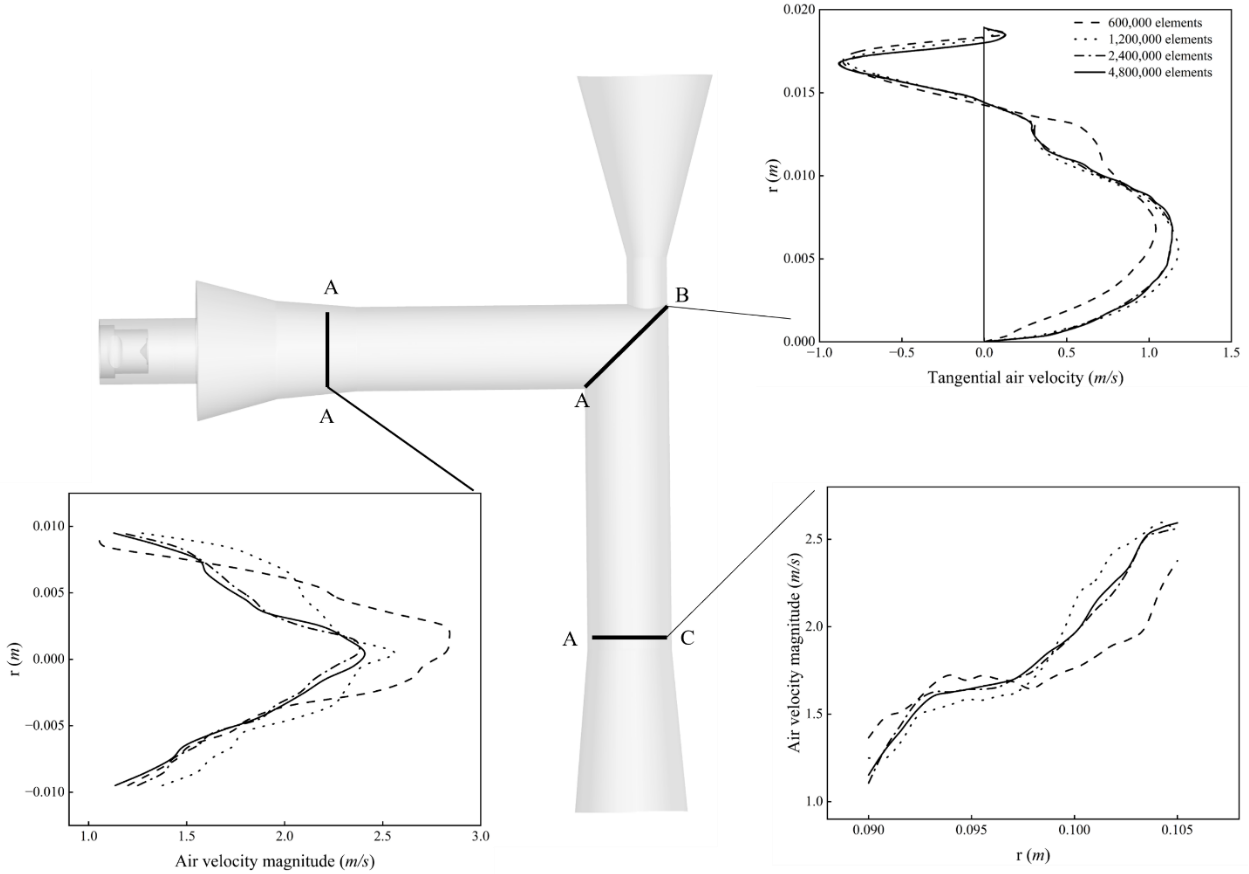

Fig 6.3 Mesh independence study: comparison of air velocity magnitude on lines AA (r) and AC (r) near the MIP inlet and MIP outlet, respectively, and tangential air velocity on the line AB (r) at the 90-degree bend.

6.4.3 Boundary Conditions

The representative magnitude velocity at the SMI air vents and nasal inlet ranged from 0.64-8.96 m/s and 0.04-0.63 m/s, respectively, to address all oral/nasal flow rate ratios. The geometric outlet was selected as a pressure outlet with constant atmospheric pressure. The temperature of 37°C at the geometry walls represented human body temperature. The trap boundary condition was set on all walls, and droplets were deposited upon wall contact. **Table 6.3** shows the detailed physical properties and model settings used in the current study in ANSYS Fluent.

Table 6.3 Summary of physical parameters and injection properties for numerical simulation.

Parameter	**Value**
Mass of each actuation (μg)	1.5
Aerosol generation time (s)	1.5
Droplet size diameter range (μm)	0.1-60
Velocity magnitude (m/s)	17.5
Cone angle (°)	11.28
Total flow rate (kg/s)	1×10^{-5}
Time step size (s)	1×10^{-4}
Air density (kg/m^3)	1.225
Air dynamic viscosity (kg/m.s)	1.789×10^{-5}
Droplet density (kg/m^3)	998.2
Droplet viscosity (kg/m.s)	0.00103

6.4.4 Mathematical Model and Simulation Scheme

Continuity and momentum equations were applied as follows [41,42]:

$$\frac{\partial \bar{u}_i}{\partial x_i} = 0 \tag{6.1}$$

$$\frac{\partial \bar{u}_i}{\partial t} + \bar{u}_j \frac{\partial \bar{u}_i}{\partial x_j} = -\frac{1}{\rho}\frac{\partial p}{\partial x_i} + \frac{\partial}{\partial x_j}\left[(\upsilon + \upsilon_T)\left(\frac{\partial \bar{u}_i}{\partial x_j} + \frac{\partial \bar{u}_j}{\partial x_i}\right)\right] + \vec{g} \tag{6.2}$$

where $\bar{u}_i$ is the mean air velocity component in three Cartesian coordinate directions, i.e., i = 1, 2 and 3, ρ is the air density, υ is the air kinematic viscosity, and υ_T is the kinematic turbulent (eddy) viscosity and $\vec{g}$ is the gravitational acceleration.

To capture the structure of airflow in the transition of laminar to turbulent flow regimes within the Reynolds number range of 870 to 2,700, the transition shear-stress transport model was selected for the simulation [32]. The shear stress transport turbulence model is obtained by:

$$\Omega_3 = F_1\Omega_1 + (1 - F_1)\Omega_2 \qquad (6.3)$$

where, Ω_1 is the standard $k - \omega$ model, and Ω_2 is the developed $k - \varepsilon$ model [43,44]. F_1 and (1-F_1) are the blending functions which are critical for the succession of the method and are dependent on the viscosity, density, and kinetic energy of the flow:

$$F_1 = \tanh(T_1^4) \qquad (6.4)$$

$$T_1 = \min\left(\max\left(\frac{\sqrt{k}}{0.09\omega y}, \frac{500\mu}{\rho y^2 \omega}\right), \frac{3.424\rho k}{£ y^2}\right) \qquad (6.5)$$

$$£ = \max\left(1.712\rho\frac{1}{\omega}\frac{\partial k}{\partial x_j}\frac{\partial \omega}{\partial x_j}, 1 \times 10^{-10}\right) \qquad (6.6)$$

$$\upsilon_T = \frac{k\rho}{\omega.\max\left(1, \frac{3.22SF_2}{\omega}\right)} \qquad (6.7)$$

$$F_2 = \tanh\,(T_2^2) \qquad (6.8)$$

$$T_2 = \max\,(\frac{2\sqrt{k}}{0.09\omega y}, \frac{500\mu}{\rho y^2 \omega}) \qquad (6.9)$$

where k is the turbulent kinetic energy per unit mass, ω is the specific dissipation rate, μ is the air dynamic viscosity, S is the strain rate magnitude, and y is the distance to the next surface.

The discrete phase model was employed to monitor and collect droplet data, including details about their size distributions and trajectories. SMI actuation resulted in a wide range of droplet diameters (0.1-60 μm). The effect of random velocities on droplet paths was also considered by implementing a random walk method [45]. The unsteady Lagrangian particle tracking method (Eq. (6.10) was employed to address the broad range of droplet trajectories. The governing forces included in this study are the drag, gravitational, and lift forces [46].

$$\frac{\partial \mathrm{v_i}}{\partial \mathrm{t}} = \mathrm{a}\frac{\mathrm{Du_i}}{\mathrm{Dt}} + \frac{\mathrm{f_D}}{\tau_\mathrm{d}}(\vec{u} - \vec{\mathrm{v}}) + \vec{g}(1 - \mathrm{a}) + \mathrm{f_{i,lift}} \tag{6.10}$$

$$\frac{\mathrm{dx_i}}{\mathrm{dt}} = \vec{\mathrm{v}}(\mathrm{t}) \tag{6.11}$$

$$\mathrm{a} = \rho/\rho_\mathrm{d} \approx 10^{-3} \tag{6.12}$$

$$\tau_\mathrm{d} = \frac{\mathrm{C_c}\rho_\mathrm{d}\mathrm{d_d^2}}{18\mu} \tag{6.13}$$

where, $\mathrm{u_i}$ and $\mathrm{v_i}$ are the components of mean air and droplet velocities, a is the mixture density to droplet density ratio, $\mathrm{f_D}$ is the drag factor, and τ_d is the droplet relaxation time, $\mathrm{C_c}$ is the Cunningham correction factor [47], $\mathrm{d_d}$ is the droplet diameter, and μ is the air dynamic viscosity.

In order to simulate how turbulent fluctuations influence droplet paths, a random walk model was employed. This approach operates under the assumption that the air velocity referenced in Eq. (6.10) remains consistent while a droplet is within an eddy, and this velocity is represented as [48]:

$$\vec{u} = \bar{\mathrm{u}}_\mathrm{i} + \mathrm{u}'_\mathrm{i} \tag{6.14}$$

where $\mathrm{u_i}$ is the air mean velocity and u'_i is the fluctuating component of the instantaneous velocity selected from a Gaussian distribution with a variance of $\frac{2k}{3}$.

The drag factor $\mathrm{f_D}$, denoting the ratio of the drag coefficient to Stokes drag, is derived from the formulation presented by Morsi and Alexander in 1972 [49].

$$\mathrm{f_D} = \frac{\mathrm{C_D Re_d}}{24} \tag{6.15}$$

$$\mathrm{C_D} = \begin{cases} \frac{24}{\mathrm{Re_d}}(1 + 0.15\mathrm{Re_d^{0.687}}) & \text{if } \mathrm{Re_d} \le 1000 \\ 0.44 & \text{if } \mathrm{Re_d} > 1000 \end{cases} \tag{6.16}$$

where $\mathrm{C_D}$ is the drag coefficient, and droplet Reynolds number is $\mathrm{Re_d} = \rho \mid \vec{\mathrm{u}} - \vec{\mathrm{v}} \mid \mathrm{d_d}/\mu$. The lift force $\mathrm{f_{i,lift}}$ was derived by Saffman in 1995 [50] and is given by:

$$\mathrm{f_{i,lift}} = \frac{5.188\ \mathrm{m_d}\upsilon^{0.5}\rho\mathrm{D_{ij}}}{\rho_\mathrm{d}\mathrm{d_d}(\mathrm{D_{lk}D_{kl}})^{0.25}}(\vec{u} - \vec{\mathrm{v}}) \tag{6.17}$$

where $\mathrm{m_d}$ is the mass of the droplet and $\mathrm{D_{ij}}$ is deformation tensor expressed as:

$$\mathrm{D_{ij}} = 0.5\left(\frac{\partial \mathrm{u_i}}{\partial \mathrm{x_j}} + \frac{\partial \mathrm{u_j}}{\partial \mathrm{x_i}}\right) \tag{6.18}$$

The two-way coupling method was also considered as the aerosol droplets of the liquid phase affected the continuous phase and approximated the effective initial aerosol and jet velocities. Also, the RH of the airflow could impact the droplet size distribution through condensation and evaporation at the droplet surface. A noticeable difference was observed from previous studies when comparing the effect of two-way and one-way coupling on droplet deposition fraction onto the walls of the human respiratory tract [51].

The numerical simulations were performed with Ansys Fluent v20.2 (ANSYS Inc., Canonsburg, PA). The QUICK (Quadratic Upstream Interpolation for Convective Kinematics) scheme was used to discretize the Navier-Stokes equation's non-linear convection terms. At the same time, the pressure-velocity coupling was solved using the SIMPLE (Semi-Implicit Method for Pressure-linked Linked Equations) solution method. The momentum equations were computed, employing a bounded central differencing scheme. A second-order upwind scheme was applied for convective terms to interpolate values from cell centers to nodes. Warped-face gradient correction was also implemented to enhance gradient accuracy, particularly in the 90° bend's high aspect ratio mesh cells. Finally, the algebraic multigrid controls were optimized to ensure smoother convergence and prevent divergence.

The simulations were conducted on the Lakehead University supercomputer, consisting of an Intel Xeon Gold 6148 CPU @ 2.40 GHz with 16 cores. In addition, parallel processing was performed on 2 Intel Xeon Silver 4214 CPUs @ 2.20 GHz and 2.19 GHz (2 processors). Each computational task comprised 2,400,000 elements and required approximately 168 hours to run.

6.4.5 Model Validation

Fig 6.4(a) compares our CFD results for the cumulative mass fraction versus cut-off diameters on plane F (the throat outlet) of MIP with our in vitro results at the oral/nasal flow rate ratio of O/N=14 (same condition). Data were collected from plane F by dividing the droplet diameter range (0.1-60 μm) into different diameter cut-off sizes. The numerical prediction agrees well with the in vitro result of the current study with a root-mean-square error of 0.142. This figure also presents previous in vitro studies of Ke *et al.* [52] and Spallek *et al.* [53], which are aligned with our results. The observed discrepancies can be attributed to our different airway geometry (MIP), which creates a different flow pattern due to its nasal cavity mimic.

Fig 6.4(b) compares the current in vitro results of droplet depositions versus the cut-off diameters of the in vitro results of Mehri *et al.* [39], Wachtel *et al.* [54] and the numerical results of the current study. Droplet diameter cut-off size ranges for each cup of the NGI can be found in [55]. This figure shows that the trend of droplet deposition matched despite some differences in previous studies' experimental setups and conditions. We also notice discrepancies in the cut-off diameters, particularly in the measured droplet deposition at the MIP and cup 8, which can be attributed to the differences in experimental setups. It should be noted that Mehri *et al.* [39] used the Andersen cascade impactor with no mouthpiece (MP) at a flow rate of 28.3 l/min, while Wachtel *et al.* [54] employed a valved holding chamber and a shutter for 1–5-year-old children in their experimental setups.

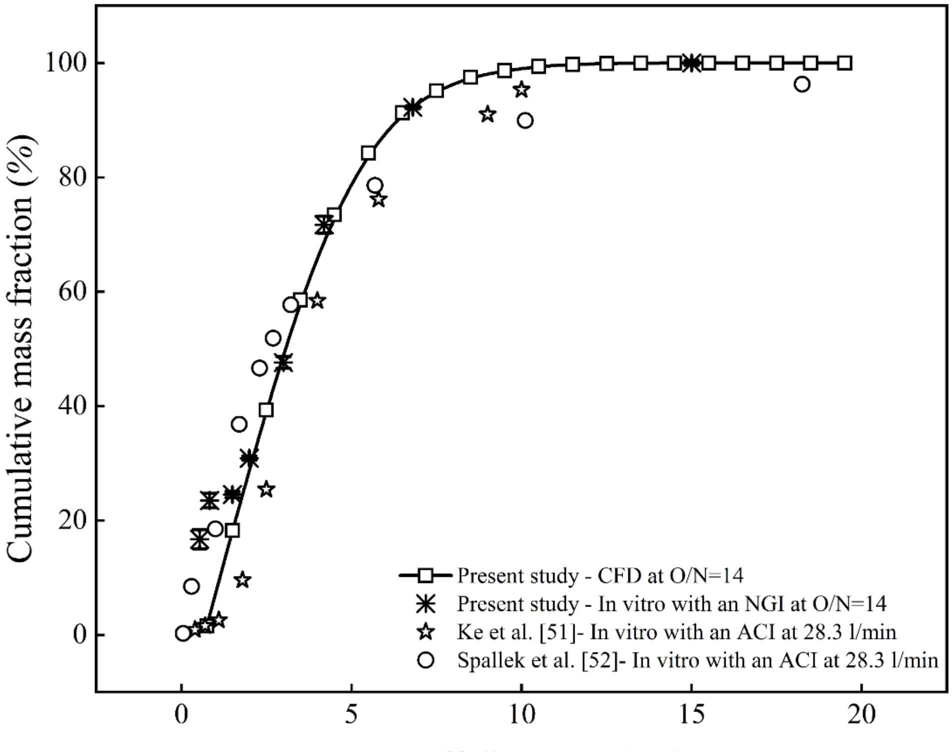

(a)

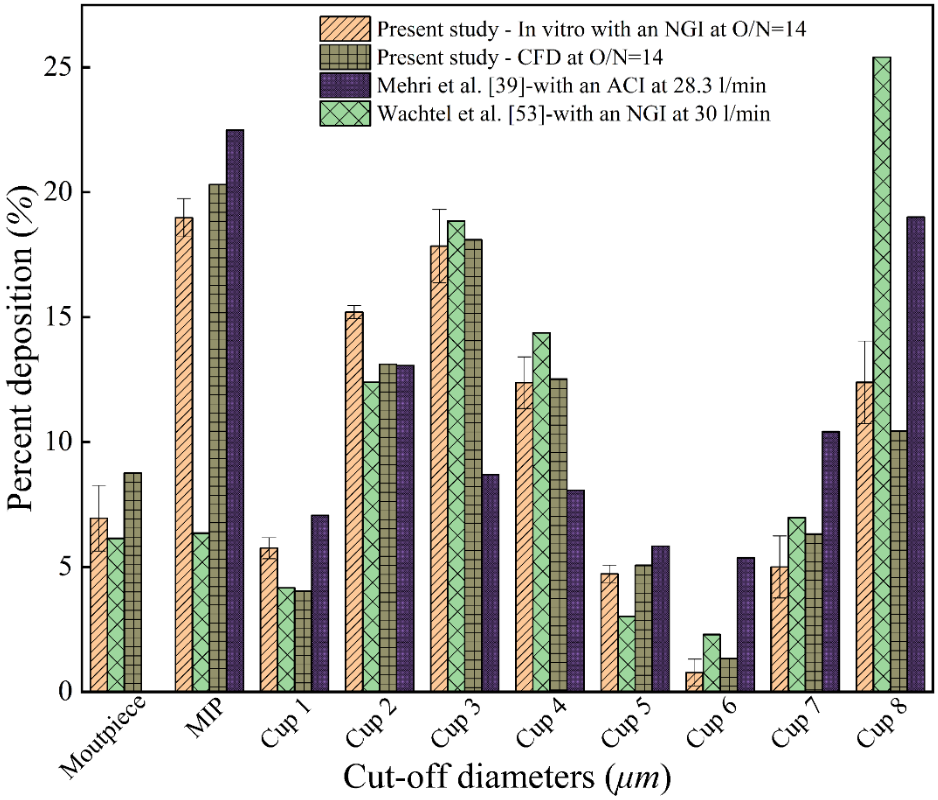

(b)

Fig 6.4 Comparison of: **(a)** Numerical cumulative mass fraction of drug, and **(b)** Drug deposition in SMI mouthpiece, MIP, and NGI at O/N=14, with in vitro results of current and previous studies. Error bars are standard deviation.

6.5 Results and Discussion

Fig 6. 5 displays the numerical results of the droplet deposition fraction at different locations inside the MIP (see **Fig 6. 2(a)**) in a histogram. We didn't notice any droplet deposition on Wall 5; thus, we excluded this wall from the analysis. The droplet deposition fraction on the SMI nozzle and mouthpiece wall increased from 1% to 44% as the oral-nasal flow rate ratio increased from O/N=0.07 to 14. These findings are consistent with Wei *et al.* [56], who also reported a higher drug deposition fraction inside inhalers. This increase in droplet deposition was attributed to most of the flow passing through the small air vents of the SMI, leading to increased droplet interaction when the airstreams encountered the aerosol plume. The nasal and mouth flow combination and higher droplet interaction at the MIP bend allowed for higher droplet deposition on Walls 2 and 3. The lowest droplet deposition fraction inside the MIP was observed for oral/nasal flow rate ratios of O/N=1 and 2. Droplet deposition fraction on wall 2 inside the MIP was 3% and 7.7%, and on wall 3 was 11% and 10.5% for O/N=1 and O/N=2, respectively. This suggests a moderate nasal flow rate can reduce drug droplet deposition through the mouth-throat airways.

Fig 6. 5(b) shows the average droplet deposition fraction across all flow rates inside the MIP. Walls 4 and 1 had the lowest droplet deposition fraction (almost 11% of total deposition). In comparison, droplet deposition on the SMI nozzle and MIP wall (Walls 2 and 3) was approximately 89% of total droplet deposition.

Table 6. 4 presents droplet deposition fraction with diameters ranging from 0.1-60 µm on plane F (MIP outlet) at different oral/nasal flow rate ratios. We chose plane F since droplets (with a specific diameter) passing this plane are more likely to be deposited on the lower human respiratory tract. The deposition fraction of droplets in the size ranges of 0.1-2 µm and 2-5 µm increased with increasing O/N ratio until O/N=1, followed by a downward trend at higher O/N ratios. In contrast, this trend was reversed for droplets with a diameter greater than 5 µm. These droplets had greater inertia, and consequently, the inertial impaction was more effective, especially at higher oral or nasal flow rates. The deposition fraction for droplets with diameters of 2-5 µm, which have a higher chance of depositing in human lungs, increased to 55.78% at O/N=1. This represents a significant increase of 0.95% and 0.89% compared to droplet deposition fractions at O/N=0.07 and O/N=14, respectively. This result supports the notion that a combination of mouth and nasal flow rates, particularly at mid-range oral/nasal flow rate ratios, results in less droplet deposition on the MIPs' walls and a higher number of droplets with diameters between 2-5 µm at plane F of the MIP, which have the highest chance of deposition in the human lung.

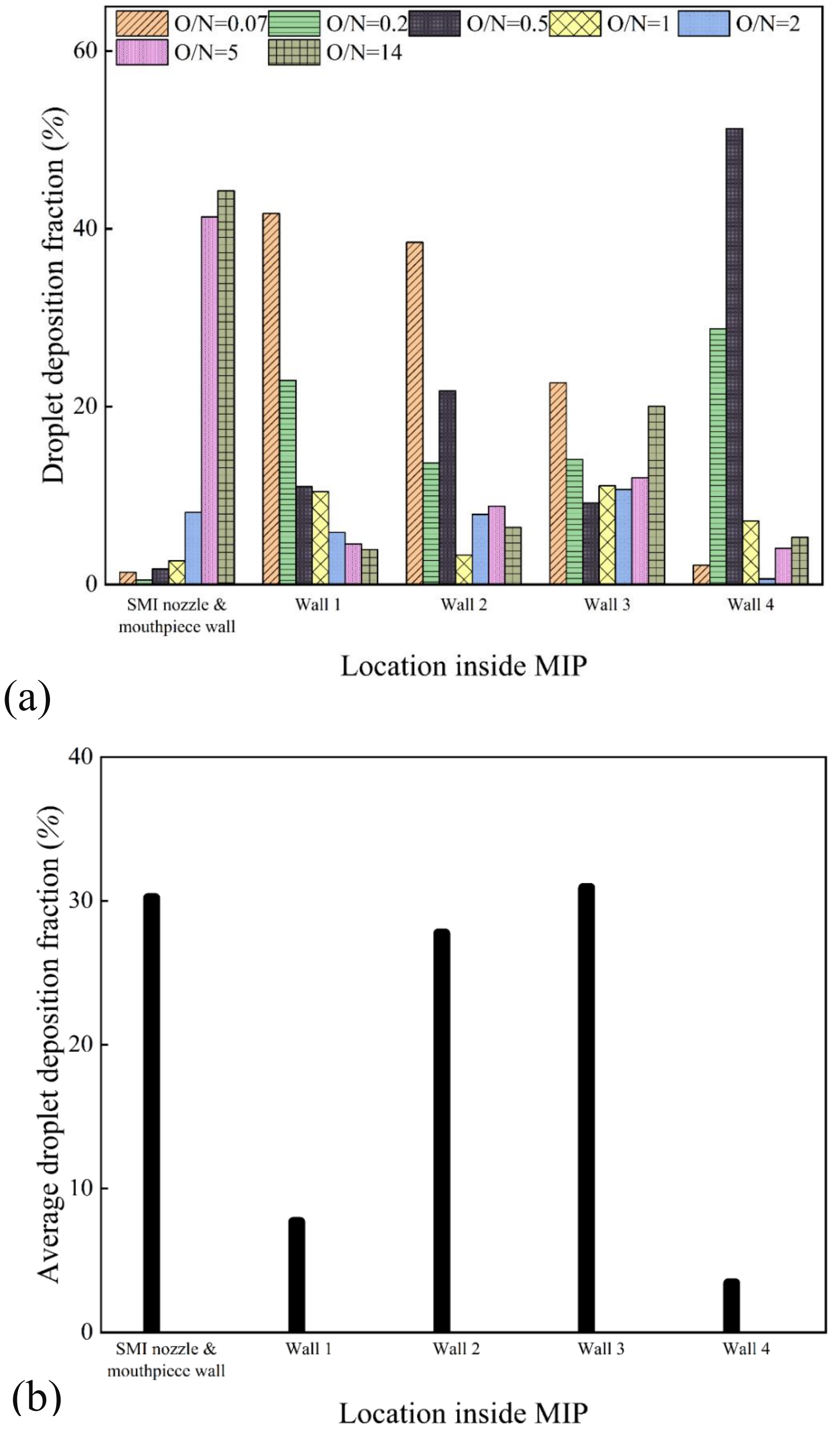

Fig 6.5 Numerical results of the droplet deposition in different locations inside the MIP at various flow rates. **(a)** Droplet deposition fraction for different oral/nasal flow rate ratios, and **(b)** Average droplet deposition fraction across all oral/nasal flow rate ratios.

Table 6.4 Numerical droplet deposition fraction values on plane F at various oral/nasal flow rate ratios for droplet diameter groups.

Flow rate ratio (-) / **Droplet diameter (μm)**	**O/N=0.07**	**O/N=0.2**	**O/N=0.5**	**O/N=1**	**O/N=2**	**O/N=5**	**O/N=14**
	Deposition fraction (%)						
0.1-2	18.00	18.17	18.7	18.94	18.2	18.47	18.29
2 – 5	54.83	55.21	55.25	55.78	55.19	54.91	54.89
> 5	27.17	26.62	26.05	25.28	26.61	26.62	26.82

Fig 6.6 displays the size distribution of droplets in three diameter groups: 0.1-2 µm, 2-5 µm, and droplets above 5 µm. The mass of droplets decreased in all three diameter groups, indicating that droplets deposited on the walls of the MIPs, with a higher reduction rate observed for droplets in the diameter range of 2-5 µm. The highest droplet mass was found in droplets with 2-5 µm diameters across all oral/nasal flow rate ratios and in all planes. This was followed by droplets with diameters above 5 µm and droplets with diameters between 0.1-2 µm. In the three diameter groups, a substantial reduction in droplet mass was observed for O/N=0.07 from plane C to plane F. The mass reduction can be attributed to the rapid airflow originating from the nasal cavity, which interacts with the airflow from the mouth at a 90° bend, impeding the easy passage of droplets.

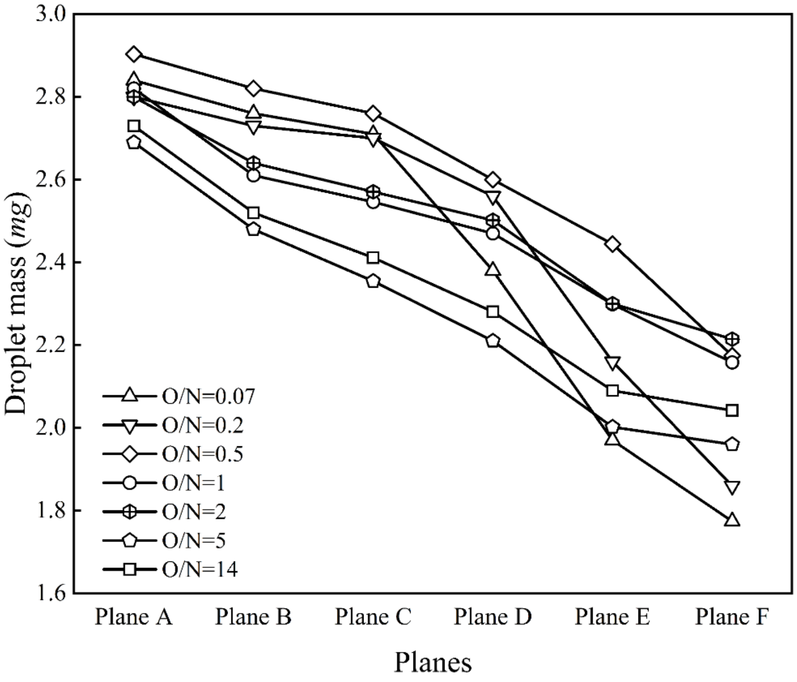
3.0
2.8
2.6
2.4
2.2
2.0
1.8
1.6
Droplet mass (*mg*)
O/N=0.07
O/N=0.2
O/N=0.5
O/N=1
O/N=2
O/N=5
O/N=14
Plane A
Plane B
Plane C
Plane D
Plane E
Plane F
Planes

(a)

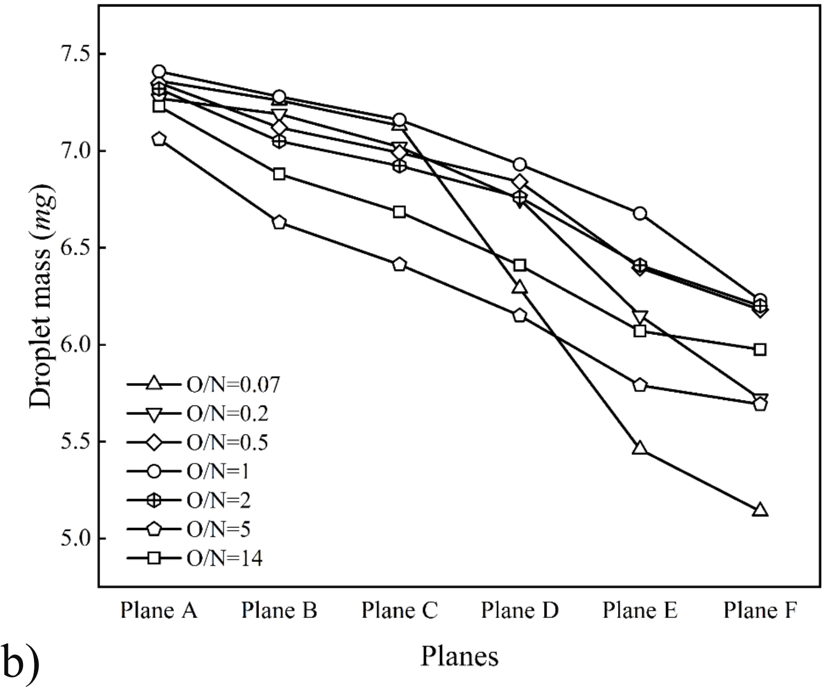
7.5
7.0
6.5
6.0
5.5
5.0
Droplet mass (*mg*)
O/N=0.07
O/N=0.2
O/N=0.5
O/N=1
O/N=2
O/N=5
O/N=14
Plane A
Plane B
Plane C
Plane D
Plane E
Plane F
Planes

(b)

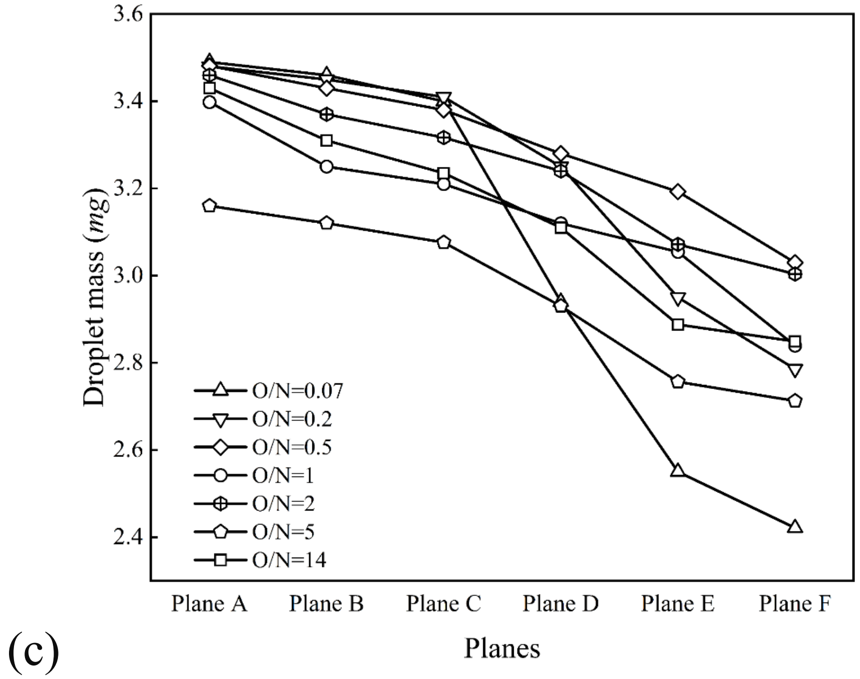

Fig 6.6 Droplet size distribution inside the MIP for droplets with a diameter of **(a)** 0.1-2 µm, **(b)** 2-5 µm, and **(c)** above 5 µm.

Fig 6.7 (a, b, and c) depicts the impact of the combined flow rate on the distribution of droplet sizes within the MIP for three different O/N ratios: 0.07, 1, and 14. Droplet diameters are represented by their size growth and color-coded according to their velocity. A greater concentration of droplets was observed within the SMI mouthpiece and Wall 1 for O/N ratios of 0.07 and 14, indicating a higher fraction of droplet deposition in these regions compared to O/N=1. At an O/N ratio of 0.07, droplets with lower velocities were predominantly found in the upper MIP, consistent with the higher deposition fraction observed in this area (**Fig 6. 5(a)**). The high-speed nasal airflow at this ratio prevents these droplets from entering the lower MIP. This phenomenon explains the significant decrease in droplet mass observed after plane D inside the MIP, as shown in **Fig 6.6** for an O/N ratio of 0.07.

Furthermore, it was observed that larger droplets tend to primarily occupy the outer edge of the plume due to their greater inertia, allowing them to maintain their initial angled trajectories over a longer distance. This behavior of larger droplets aligns with results published by Longest and Hindle [57]. Additionally, when comparing the volume of droplets passing through the outlet, a slightly higher quantity of droplets with larger diameters, indicating greater droplet mass, was observed around the MIP outlet. This phenomenon enhances the potential for drug delivery to the lungs, particularly at an O/N ratio of 1.

Fig 6.7 (d, e, and f) shows the MIP flow field by magnitude velocity streamline patterns for O/N=0.07, 1 and 14, respectively. As the airflow enters the SMI mouthpiece from the two small air vents on the SMI side wall, it separates while merging with the aerosol plume close to the SMI nozzle. This air mixture forms small vortexes close to the SMI nozzle and two vortexes in the anterior upper and lower part of Wall 1, creating recirculation areas. According to Longest and Hindle, these areas, especially near the SMI nozzle and mouthpiece wall, are the main reason for the high deposition rate in the SMI nozzle and mouthpiece wall[57]. Aside from small recirculation regions (due to the acceleration of flow rate caused by SMI injection) formed close to outer Wall 1, a single streamline pattern was observed inside the MIP at O/N=1. This unified flow field reduced droplet deposition inside the MIP, improving droplet deposition in human lungs. However, larger recirculation areas were observed for O/N=0.07 and 14 as the flow moved along the MIP geometry. These recirculation regions, mainly at O/N=0.07, changed the droplets' behavior and intensified aerosol dispersion and mixing, increasing the potential for droplet impaction with the wall (see **Fig 6.5**). The high-speed airflow from the nasal cavity at O/N=0.07 acts like a shield wall, narrowing the airway and promoting recirculation regions. Any droplet that enters these vortical regions due to turbulent dispersion or angled spray trajectories is directed toward the surface of the MIP wall, increasing the chance of deposition loss in these regions. This is in line with the findings of Lizal *et al.* [6] regarding the effect of the inhalation route on droplet deposition. In a total flow rate of 30 l/min and aerodynamic diameter of 2.82 µm, they found that droplet deposition is higher in lower human airways when combined inhalation was used rather than oral or nasal inhalation only. Delvadia *et al.* [57] and Talaat *et al.* [58] discussed the importance of the recirculation regions' effect on droplet deposition.

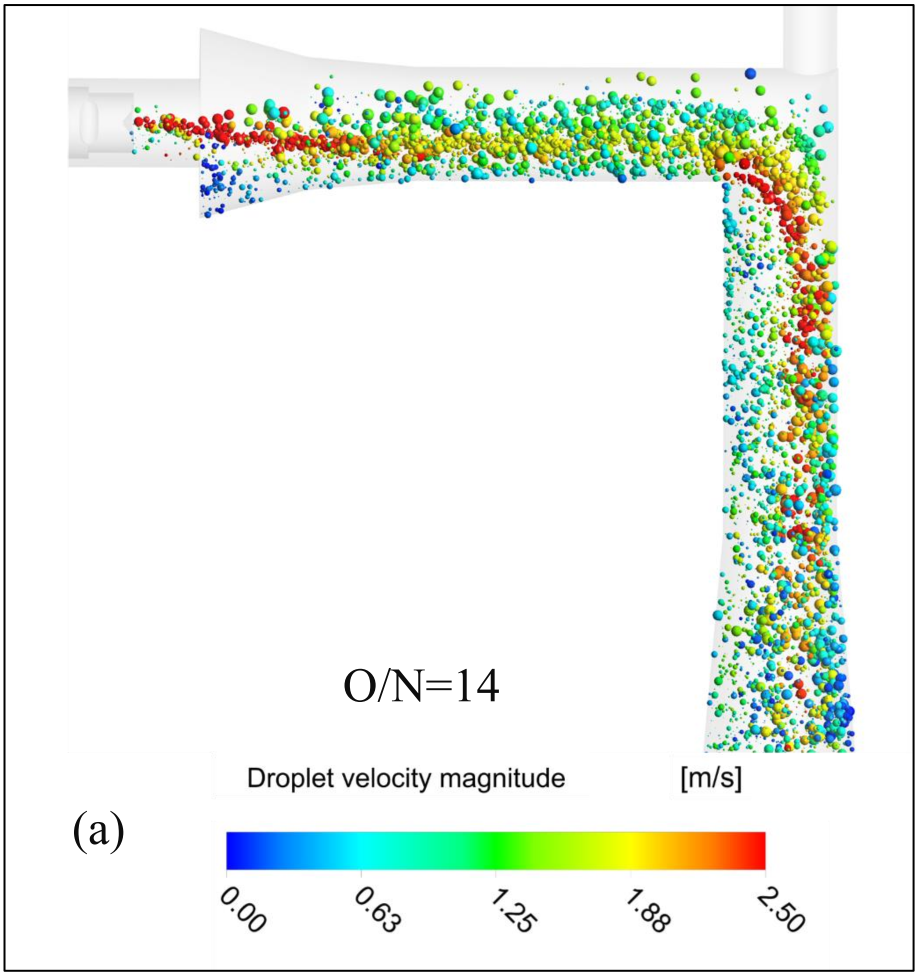
O/N=14
Droplet velocity magnitude
[m/s]
(a)
0.00
0.63
1.25
1.88
2.50

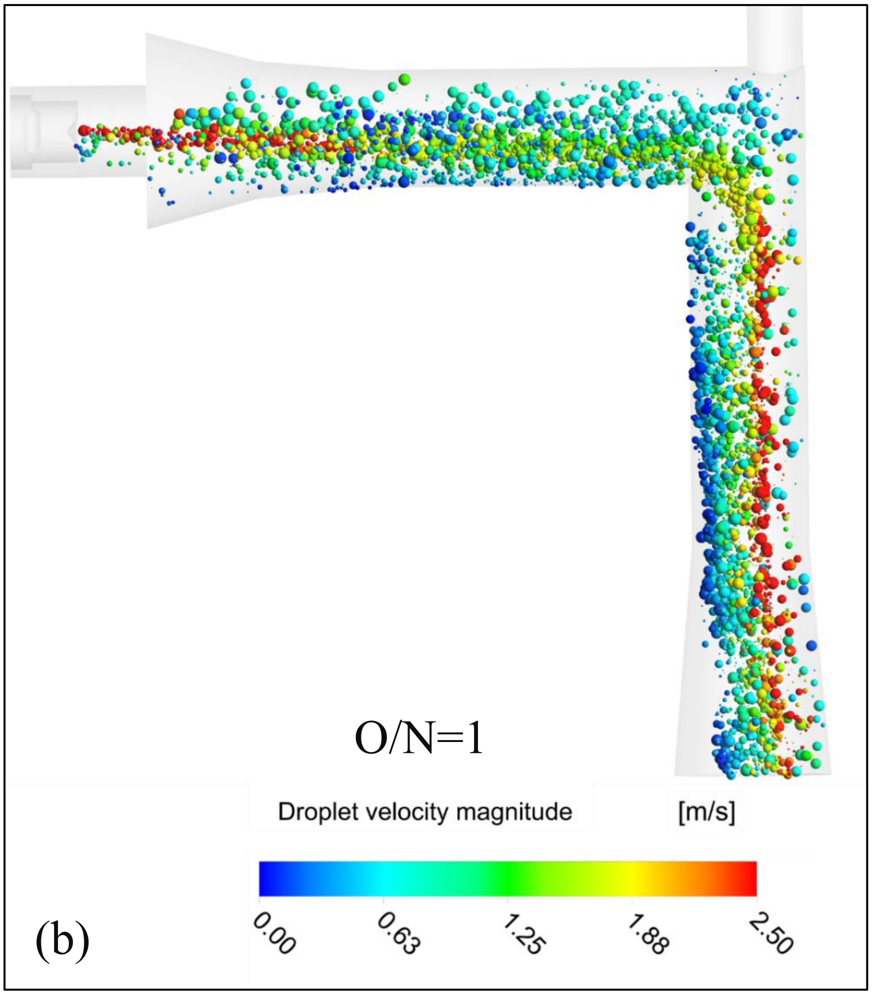
O/N=1
Droplet velocity magnitude
[m/s]
0.00
0.63
1.25
1.88
2.50
(b)

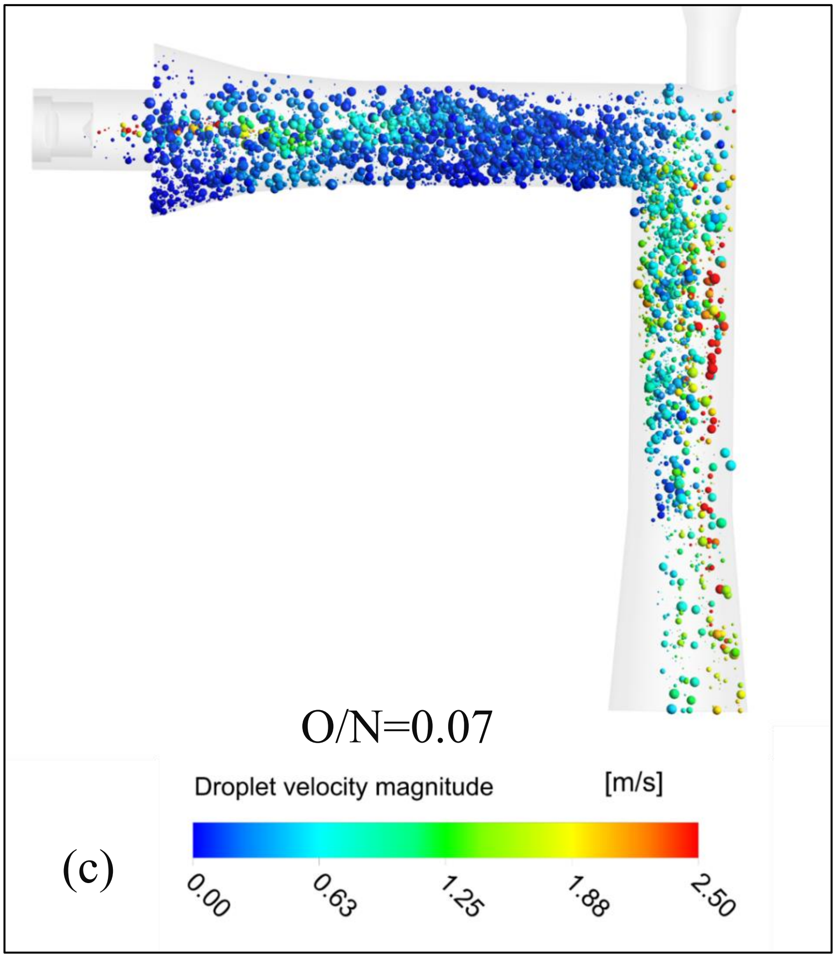
O/N=0.07
Droplet velocity magnitude
[m/s]
0.00
0.63
1.25
1.88
2.50
(c)

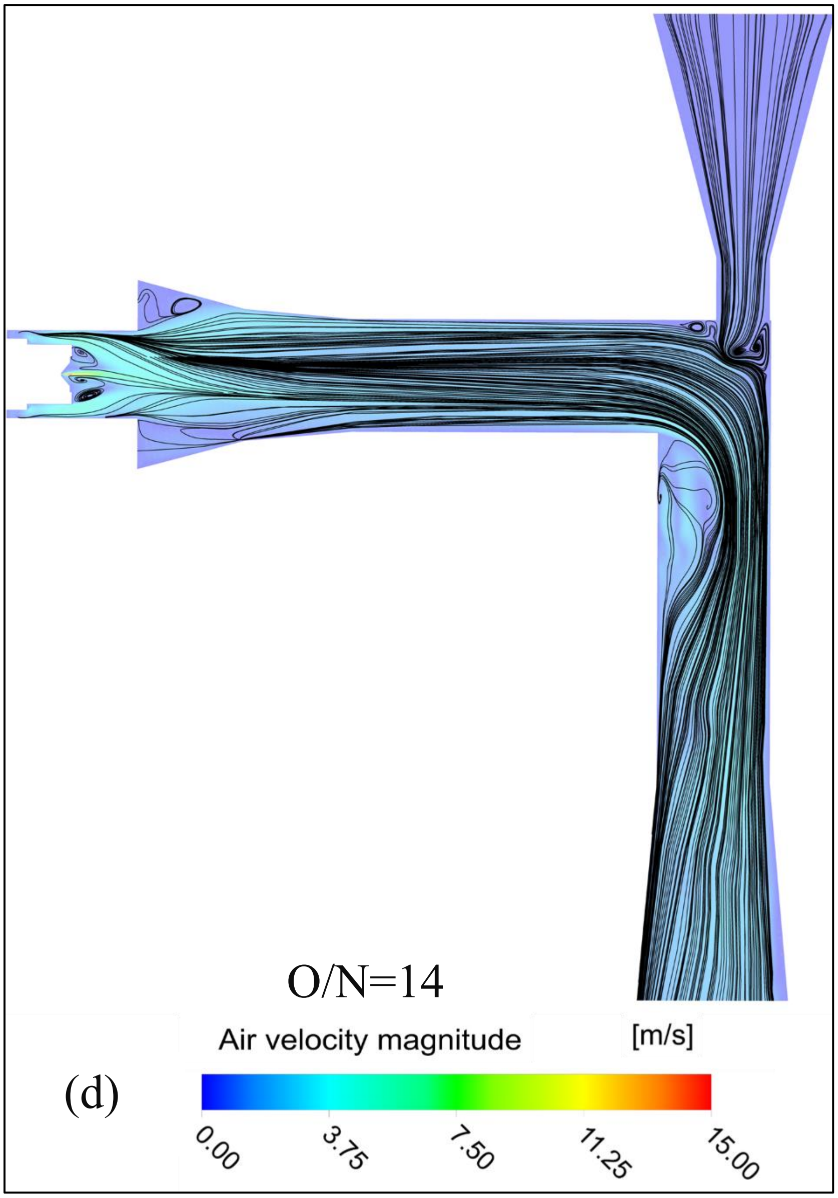
O/N=14
Air velocity magnitude
[m/s]
(d)
0.00
3.75
7.50
11.25
15.00

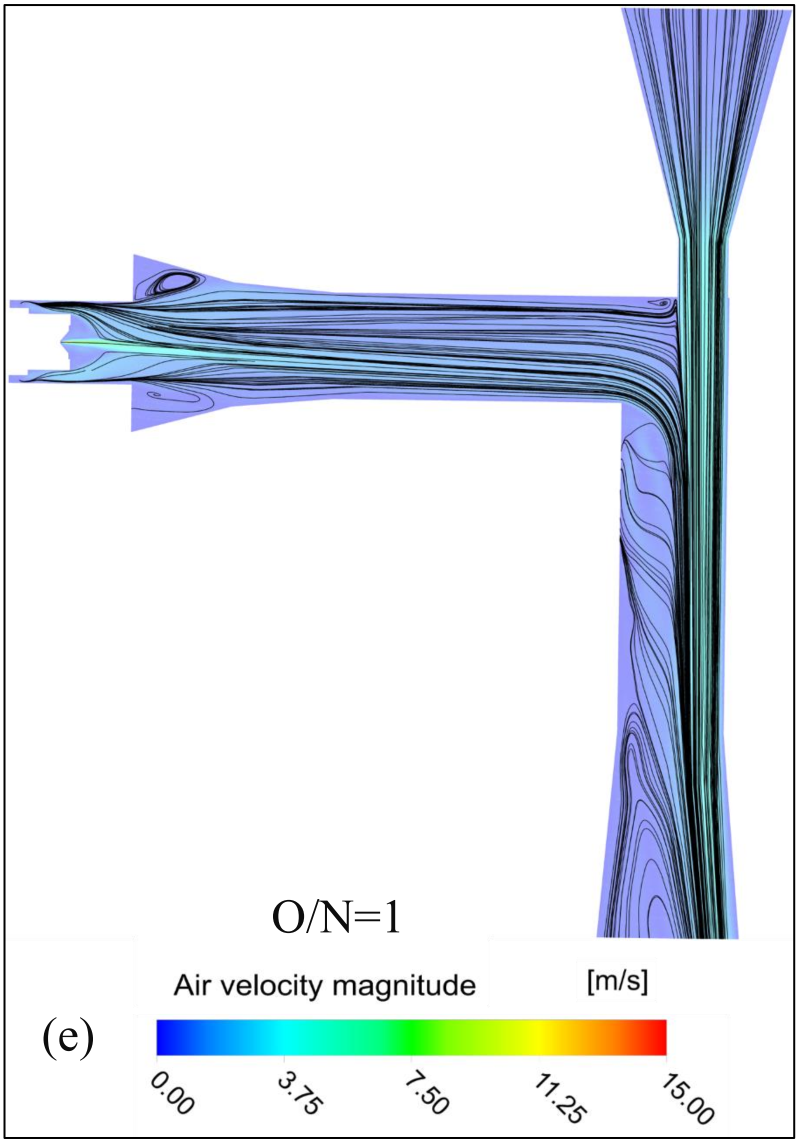
O/N=1
Air velocity magnitude
[m/s]
(e)
0.00
3.75
7.50
11.25
15.00

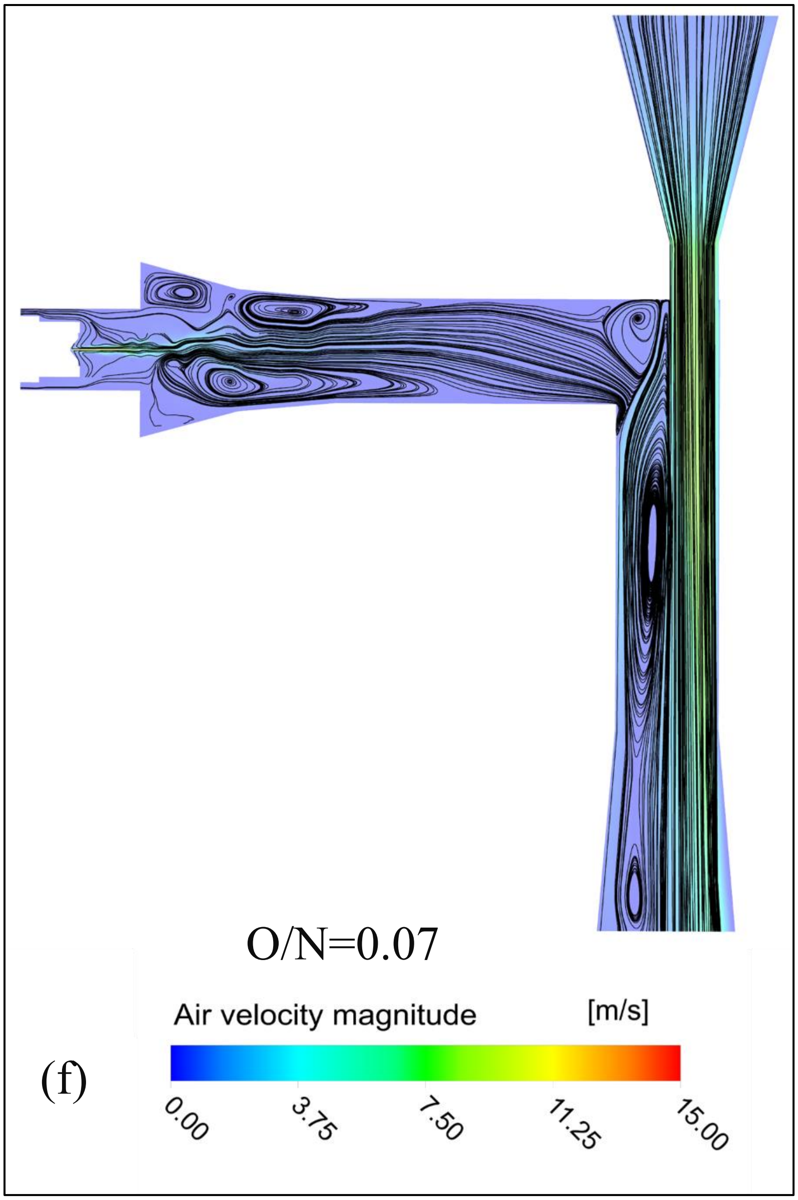

Fig 6.7 Droplet size distribution and flow streamline inside the MIP for different oral/nasal flow rate ratios. **(a)** droplet size distribution for three diameter groups (0.1-2 µm, 2-5 µm, and >5 µm) at O/N=14, **(b)** droplet size distribution for three diameter groups at O/N=1, **(c)** droplet size distribution for three diameter groups at O/N=0.07, **(d)** Flow streamlines at O/N=14, **(e)** Flow streamlines at O/N=1, and **(f)** Flow streamlines at O/N=0.07.

Variations in the size and quantity of recirculation regions examined by the turbulent kinetic energy levels for different oral/nasal flow rate ratios are shown in **Fig 6.8**. This Figure shows the normalized turbulent kinetic energy (k/U^2) along the x and y axes, where U is the magnitude velocity. The higher value of k was recorded near the SMI nozzle and mouthpiece area for O/N=1 and 14. This confirms the persistence of recirculation in these regions. The highest level of turbulent kinetic energy was observed at 15 mm from the mouthpiece wall at O/N=0.07, consistent with the droplet deposition in this area reported in **Fig 6.5**. This can be attributed to the reduction of cross-sectional area in the Wall 1 region. While the k level steadily dropped for O/N=1 and 14 in the Wall 2 part and reached a plateau, it fluctuated for O/N=0.07, showing the number of recirculation regions along the x-axis of the MIP. Similar observations were reported in the study by Koullapis *et al.* [2] with a detailed explanation of the flow pattern in the human respiratory tract geometry. In **Fig 6.8(b)**, the flow field at O/N=0.07 showed the highest k, followed by O/N=1 and 14. The level of k then remained almost constant at O/N=1 and O/N=14 while slightly increasing at O/N=0.07 after a sudden drop around -20 mm on the y-axis (right after the flow disturbances at MIP 90° bend region) as the flow developed.

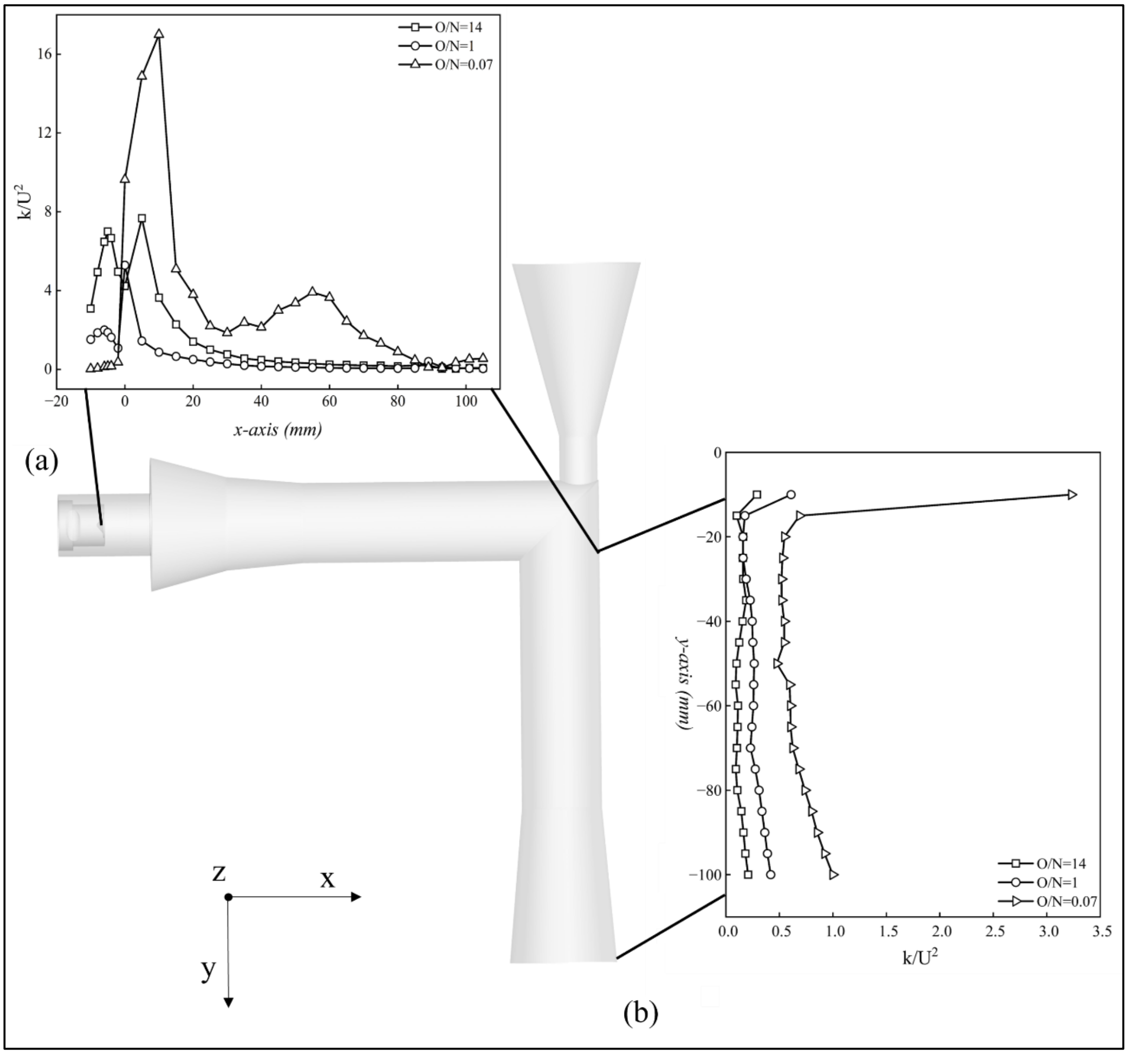

Fig 6.8 Normalized turbulent kinetic energy (k/U^2) at O/N=14, 1, and 0.07 along the **(a)** x-axis and **(b)** y-axis of the MIP geometry.

Fig 6.9 shows the simulation results for droplet size distribution on plane F for RHs of 75% and 95%, using oral/nasal flow rate ratios of O/N=0.07, O/N=1, and O/N=14. It was observed that an increase in RH led to higher total droplet deposition across all droplet diameter groups and O/N flow rate ratios. These findings align with previous studies [39,58], which also demonstrated an increase in deposition rate with rising RH. Among the three oral/nasal flow rate ratios, O/N=1 exhibited the highest droplet deposition, followed by O/N=14 and O/N=0.07, respectively. Notably, aerosolized droplets ranging from 0.1-2 µm displayed the most significant increment in deposition rate (19.36%) at RH of 75%. In humid air inhalations, drug-aerosolized droplets collide with water droplets inside the air. In other words, when aerosolized droplets come into contact with humid air, they have the capacity to absorb water molecules from their surroundings, becoming larger and heavier [59]. This process is known as hygroscopic growth [60]. As droplets grow, they are more likely to deposit in the respiratory tract due to increased inertial impaction of aerosolized droplets [59].

These observations were also discussed in a previous study by Mehri *et al.* [19] that highlighted an increase in the fine particle fraction (particles with a diameter < 5 µm) with increasing RH from 30-50% to 100%. The particle size remained relatively unchanged between RHs of 75% and 95%, indicating size stability at RH > 75.

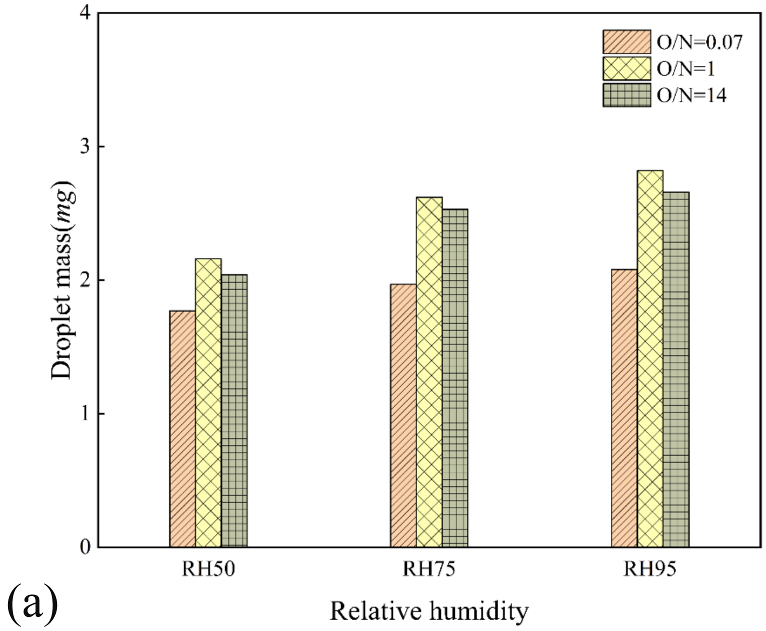

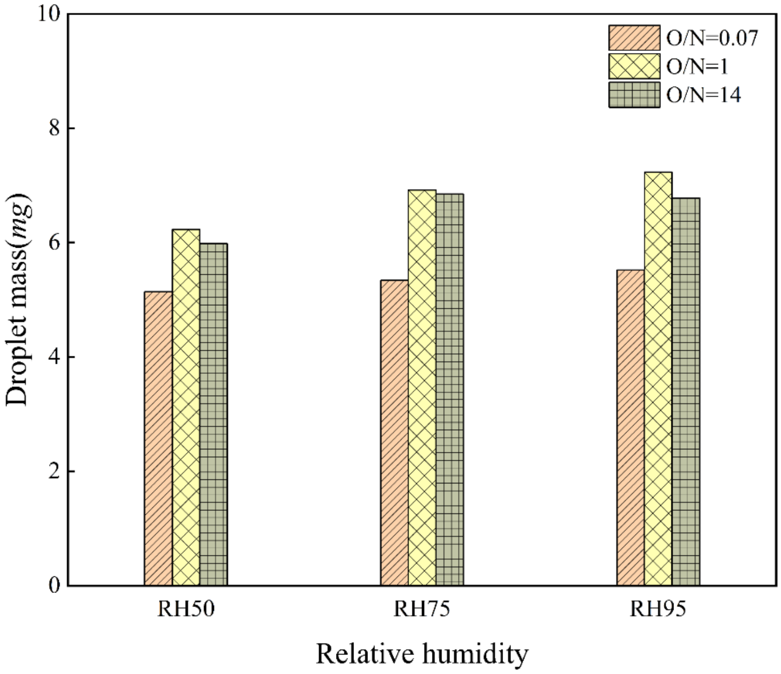

(b)

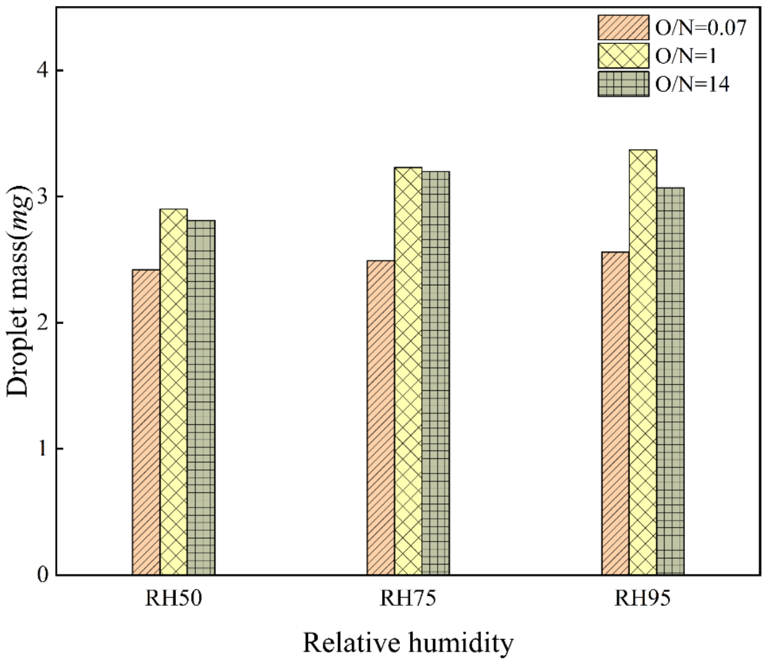

(c)

Fig 6.9 Droplet size distribution on plane F at relative humidities of 75% and 95% for droplets with a diameter of **(a)** 0.1-2 µm, **(b)** 2-5 µm, and **(c)** above 5 µm at O/N=14, 1, and 0.07.

6.6. Conclusions

The present study quantified the effect of the combination of flow rate from the nasal and oral cavity on flow pattern, regional deposition, and size distribution of an SMI fitted to a custom MIP. Our induction port was modified to capture the effect of the airflow coming from the nasal cavity into the MIP. It was not intended to show the actual behavior of the human oral pharynx but rather to include adequate geometric features to enable a valid comparison. The droplet transport and airflow were simulated using shear stress transport $\mathrm{k}-\omega$ at a steady flow rate for different oral/nasal flow rate ratios. The 3D-printed MIP was used to validate the CFD results of the current study and other numerical studies under comparable test conditions.

Results show that simultaneous oral and nasal breathing could significantly affect the flow field, regional deposition, and size distribution inside the MIP. At O/N=1 and 2, the lowest droplet deposition fraction inside the MIP was observed, suggesting that those particular flow rate combinations can lower the deposition loss inside MIP. Droplet size distribution was investigated in three diameter range groups at the outlet of the MIP (plane F). The highest deposition fraction was observed for droplets with a diameter of 2-5 µm, followed by droplets with a diameter of 0.1-2 µm. In comparison, the droplets with a diameter above 5 µm showed the lowest deposition fraction at equal oral and nasal flow rates (O/N=1). Droplets with a 2-5 µm diameter were the most dominant type of droplet mass along the MIP at O/N=1. Fewer vortexes, recirculation regions, and consecutively lower turbulent kinetic energy levels were found in the flow field caused at O/N=1. We found that moderate oral and nasal inhalation simultaneously unifies the air streams inside the MIP and reduces recirculation, lowering the deposition loss in MIP.

Additionally, as the RH increased, there was a rise in drug droplets passing the outlet of the MIP (i.e., the throat outlet towards the lower respiratory tract). This increase was observed across oral/nasal flow rate ratios of 0.07, 1, and 14, with the highest growth occurring at a ratio of 1. Notably, droplets ranging from 0.1 to 2 µm in diameter exhibited the most significant response to changes in RH. This study demonstrates that the combined oral and nasal inhalation method significantly affected the delivery of droplets with a diameter of 2-5 µm, which have a higher chance of deposition on the lower respiratory tract. The results of this study can be applied to in vivo studies. Combining oral and nasal inhalation (with an O/N=1 ratio suggested) while using SMI helps to lower the drug deposition inside patients' mouth-throat airways.

The current study's limitations include using MIP, which is not a realistic human upper respiratory tract geometry. Droplet coalescence and collision were not considered in the modelling. Additionally, local validation for sub-micrometer droplets could have been more aligned with experimental results due to the HPLC device's inability to accurately determine low concentrations of sub-micrometer droplets. Future studies will address these limitations to develop more physically realistic droplet deposition models in the human respiratory tract. Additionally, investigating how airway geometric characteristics can influence drug droplet flow patterns within the human respiratory tract will provide valuable insights into designing different airways. Also, it is essential to consider the influence of airflow temperature in developing soft mist inhalers. This is particularly relevant when aiming to minimize the impact of environmental temperature and subsequent changes in RH on drug delivery to the lung.

6.6. Nomenclature

Abbreviations

CFD	Computational Fluid Dynamic
HFA	Hydrofluoroalkane
HPLC	High-Performance Liquid Chromatography
MIP	Modified Induction Port
NGI	Next Generation Impactor
RH	Relative Humidity
SMI	Soft Mist Inhaler
3D	Three-Dimensional

Notations

a	mixture density ratio, -
C_c	Cunningham correction factor, -
C_D	drag coefficient, -
d_d	droplet diameter, m

D_{ij}	deformation tensor, -
F_1, F_2	blending functions, -
$\vec{g}$	gravitational acceleration in the x -axis direction, m/s^2
k	turbulent kinetic energy, m^2/s^2
m_d	mass of the droplet, kg
r	radial distance, m
Re	Reynold's number, -
Re_d	droplet Reynold's number, -
S	strain rate magnitude, 1/s
t	time, s
$\vec{u}$	mean air velocity component, m/s
$\bar{u}_i$	time-averaged air velocity, m/s
u_i'	fluctuating component of instantaneous velocity, m/s
U	magnitude velocity, m/s
$\vec{v}$	droplet velocity component, m/s
y	distance to the next surface, m

Greek letters

f_D	drag factor, -
μ	air dynamic viscosity, kg/m.s
υ	air kinematic viscosity, m^2/s
υ_T	air kinematic turbulent (eddy) viscosity, m^2/s
ρ	air density, kg/m^3
ρ_d	droplet density, kg/m^3
τ_d	droplet relaxation time, s
Ω_1	standard $k - \omega$ model, -
Ω_2	developed $k - \varepsilon$ model, -
ω	specific dissipation rate, 1/s

6.7 References

[1]H. D. C. Smyth and A. J. Hickey, *Controlled Pulmonary Drug Delivery*, 1st ed. New York, NY: Springer New York, 2011. doi: 10.1007/978-1-4419-9745-6.

[2]P. G. Koullapis, L. Nicolaou, and S. C. Kassinos, “In silico assessment of mouth-throat effects on regional deposition in the upper tracheobronchial airways,” *J Aerosol Sci*, vol. 117, pp. 164–188, Mar. 2018, doi: 10.1016/j.jaerosci.2017.12.001.

[3]R. Dalby, M. Spallek, and T. Voshaar, “A review of the development of Respimat® Soft Mist^{TM} Inhaler,” *Int J Pharm*, vol. 283, no. 1–2, pp. 1–9, Sep. 2004, doi: 10.1016/j.ijpharm.2004.06.018.

[4]P. W. Longest and M. Hindle, “Condensational growth of combination drug-excipient submicrometer particles for targeted high efficiency pulmonary delivery: Comparison of CFD predictions with experimental results,” *Pharm Res*, vol. 29, no. 3, pp. 707–721, Mar. 2012, doi: 10.1007/s11095-011-0596-1.

[5]S. P. Newman, K. P. Steed, S. J. Reader, D. Pavia, and A. K. Sohal, “An in vitro study to assess facial and ocular deposition from Respimat® Soft Mist^{TM} inhaler,” *Journal of Aerosol Medicine: Deposition, Clearance, and Effects in the Lung*, vol. 20, no. 1, pp. 7–12, 2007, doi: 10.1089/jam.2006.0563.

[6]F. Lizal *et al.*, “The effect of oral and nasal breathing on the deposition of inhaled particles in upper and tracheobronchial airways,” *J Aerosol Sci*, vol. 150, p. 105649, Dec. 2020, doi: 10.1016/j.jaerosci.2020.105649.

[7]P. W. Longest and J. Xi, “Effectiveness of direct Lagrangian tracking models for simulating nanoparticle deposition in the upper airways,” *Aerosol Science and Technology*, vol. 41, no. 4, pp. 380–397, Apr. 2007, doi: 10.1080/02786820701203223.

[8]G. Pitcairn, S. Reader, D. Pavia, and S. Newman, “Deposition of corticosteroid aerosol in the human lung by Respimat Soft Mist inhaler compared to deposition by metered dose inhaler or by Turbuhaler dry powder inhaler.,” *J Aerosol Med*, vol. 18, no. 3, pp. 264–72, Sep. 2005, doi: 10.1089/jam.2005.18.264.

[9]P. Brand, B. Hederer, G. Austen, H. Dewberry, and T. Meyer, “Higher lung deposition with Respimat Soft Mist inhaler than HFA-MDI in COPD patients with poor technique.,” *Int J Chron Obstruct Pulmon Dis*, vol. 3, no. 4, pp. 763–70, 2008.

[10]T. Iwanaga, Y. Tohda, S. Nakamura, and Y. Suga, “The Respimat® Soft Mist Inhaler: Implications of Drug Delivery Characteristics for Patients,” *Clin Drug Investig*, vol. 39, no. 11, pp. 1021–1030, Nov. 2019, doi: 10.1007/s40261-019-00835-z.

[11]W. Kamin, M. Frank, S. Kattenbeck, P. Moroni-Zentgraf, H. Wachtel, and S. Zielen, “A Handling Study to Assess Use of the Respimat® Soft Mist^{TM} Inhaler in Children under 5 Years Old,” *J Aerosol Med Pulm Drug Deliv*, vol. 28, no. 5, pp. 372–381, Oct. 2015, doi: 10.1089/jamp.2014.1159.

[12]R. Dalby, M. Spallek, and T. Voshaar, “A review of the development of Respimat® Soft Mist^{TM} Inhaler,” *Int J Pharm*, vol. 283, no. 1–2, pp. 1–9, 2004, doi: 10.1016/j.ijpharm.2004.06.018.

[13]W. R. Ke *et al.*, “In Vitro Evaluation of Aerosol Performance and Delivery Efficiency During Mechanical Ventilation Between Soft Mist Inhaler and Pressurized Metered-Dose Inhaler,” *Respir Care*, vol. 65, no. 7, pp. 1001–1010, 2020, doi: 10.4187/respcare.06993.

[14]I. Amirav, A. A. T. Borojeni, A. Halamish, M. T. Newhouse, and L. Golshahi, “Nasal versus oral aerosol delivery to the ‘lungs’ in infants and toddlers,” *Pediatr Pulmonol*, vol. 50, no. 3, pp. 276–283, Mar. 2015, doi: 10.1002/ppul.22999.

[15]G. Tian, M. Hindle, and P. W. Longest, “Targeted lung delivery of nasally administered aerosols,” *Aerosol Science and Technology*, vol. 48, no. 4, pp. 434–449, 2014, doi: 10.1080/02786826.2014.887829.

[16]W. D. Bennett and K. L. Zeman, “Effect of race on fine particle deposition for oral and nasal breathing,” *Inhal Toxicol*, vol. 17, no. 12, pp. 641–648, Nov. 2005, doi: 10.1080/08958370500188984.

[17]T. Sadeghi, L. Pakzad, and P. Fatehi, “Evaluation of Soft Mist Inhaler Aerosol Velocity, Size, and Deposition Inside the Mouth—A Computational Fluid Dynamics Study,” *J Biomech Eng*, vol. 145, no. 6, Mar. 2023, doi: 10.1115/1.4056967.

[18]A. M. Ciciliani, M. Denny, P. Langguth, T. Voshaar, and H. Wachtel, “Lung Deposition Using the Respimat® Soft Mist^{TM} Inhaler Mono and Fixed-Dose Combination Therapies: An In Vitro/In Silico Analysis,” *COPD: Journal of Chronic Obstructive Pulmonary Disease*, vol. 18, no. 1, pp. 91–100, 2020, doi: 10.1080/15412555.2020.1853091.

[19]R. Mehri, A. Alatrash, E. A. Matida, and F. Fiorenza, “Respimat soft mist inhaler (SMI) in-vitro aerosol delivery with the ODAPT adapter and facemask,” *Canadian Journal of Respiratory, Critical Care, and Sleep Medicine*, vol. 5, no. 1, pp. 3–12, 2021, doi: 10.1080/24745332.2019.1598309.

[20]Z. Zhang and C. Kleinstreuer, “Computational analysis of airflow and nanoparticle deposition in a combined nasal-oral-tracheobronchial airway model,” *J Aerosol Sci*, vol. 42, no. 3, pp. 174–194, 2011, doi: 10.1016/j.jaerosci.2011.01.001.

[21]G. J. Zwartz and R. A. Guilmette, “Effect of flow rate on particle deposition in a replica of a human nasal airway.,” *Inhal Toxicol*, vol. 13, no. 2, pp. 109–27, Feb. 2001, doi: 10.1080/089583701300001050.

[22]J. Heyder, L. Armbruster, J. Gebhart, E. Grein, and W. Stahlhofen, “Total deposition of aerosol particles in the human respiratory tract for nose and mouth breathing,” *J Aerosol Sci*, vol. 6, no. 5, pp. 311–328, 1975, doi: 10.1016/0021-8502(75)90020-8.

[23]J. Dong, Y. Shang, L. Tian, K. Inthavong, D. Qiu, and J. Tu, “Ultrafine particle deposition in a realistic human airway at multiple inhalation scenarios,” *Int J Numer Method Biomed Eng*, vol. 35, no. 7, pp. 1–15, 2019, doi: 10.1002/cnm.3215.

[24]A. Tiwari, A. Jain, A. R. Paul, and S. C. Saha, “Computational evaluation of drug delivery in human respiratory tract under realistic inhalation,” *Physics of Fluids*, vol. 33, no. 8, 2021, doi: 10.1063/5.0053980.

[25]C. Ou, J. Hang, and Q. Deng, “Particle deposition in human lung airways: Effects of airflow, particle size, and mechanisms,” *Aerosol Air Qual Res*, vol. 20, no. 12, pp. 2846–2858, Dec. 2020, doi: 10.4209/aaqr.2020.02.0067.

[26]K. H. Cheng and D. L. Swift, “Calculation of total deposition fraction of ultrafine aerosols in human extrathoracic and intrathoracic regions,” *Aerosol Science and Technology*, vol. 22, no. 2, pp. 194–201, Jan. 1995, doi: 10.1080/02786829509508887.

[27]K. H. Cheng *et al.*, “In vivo measurements of nasal airway dimensions and ultrafine aerosol deposition in the human nasal and oral airways,” *J Aerosol Sci*, vol. 27, no. 5, pp. 785–801, 1996, doi: 10.1016/0021-8502(96)00029-8.

[28]X. Song, J. Hu, S. Zhan, R. Zhang, and W. Tan, “Effects of Temperature and Humidity on Laser Diffraction Measurements to Jet Nebulizer and Comparison with NGI,” *AAPS PharmSciTech*, vol. 17, no. 2, pp. 380–388, Apr. 2016, doi: 10.1208/s12249-015-0346-5.

[29]F. M. Shemirani, S. Hoe, D. Lewis, T. Church, R. Vehring, and W. H. Finlay, “In Vitro Investigation of the Effect of Ambient Humidity on Regional Delivered Dose with Solution and Suspension MDIs,” *J Aerosol Med Pulm Drug Deliv*, vol. 26, no. 4, pp. 215–222, Aug. 2013, doi: 10.1089/jamp.2012.0991.

[30]N. L. Phuong and K. Ito, “Investigation of flow pattern in upper human airway including oral and nasal inhalation by PIV and CFD,” *Build Environ*, vol. 94, pp. 504–515, Dec. 2015, doi: 10.1016/j.buildenv.2015.10.002.

[31]A. V. Kolanjiyil, S. Hosseini, A. Alfaifi, M. Hindle, L. Golshahi, and P. W. Longest, “Importance of cloud motion and two-way momentum coupling in the transport of pharmaceutical nasal sprays,” *J Aerosol Sci*, vol. 156, p. 105770, Aug. 2021, doi: 10.1016/j.jaerosci.2021.105770.

[32]F. Dastoorian, L. Pakzad, J. Kozinski, and E. Behzadfar, “A CFD Investigation on the Aerosol Drug Delivery in the Mouth–Throat Airway Using a Pressurized Metered-Dose Inhaler Device,” *Processes*, vol. 10, no. 7, p. 1230, Jun. 2022, doi: 10.3390/pr10071230.

[33]R. Sarangapani, “Modeling Particle Deposition in Extrathoracic Airways,” *Aerosol Science and Technology*, vol. 32, no. 1, pp. 72–89, Jan. 2000, doi: 10.1080/027868200303948.

[34]M. Talaat, X. Si, and J. Xi, “Effect of MDI Actuation Timing on Inhalation Dosimetry in a Human Respiratory Tract Model,” *Pharmaceuticals*, vol. 15, no. 1, Jan. 2022, doi: 10.3390/ph15010061.

[35]J. Elcner, F. Lizal, J. Jedelsky, J. Tuhovcak, and M. Jicha, “Laminar-turbulent transition in a constricted tube: Comparison of Reynolds-averaged Navier–Stokes turbulence models and large eddy simulation with experiments,” *Advances in Mechanical Engineering*, vol. 11, no. 5, 2019, doi: 10.1177/1687814019852261.

[36] H. Wachtel, M. Nagel, M. Engel, G. El Azzi, A. Sharma, and J. Suggett, “In vitro and clinical characterization of the valved holding chamber AeroChamber Plus® Flow-Vu® for administrating tiotropium Respimat® in 1–5-year-old children with persistent asthmatic symptoms,” *Respir Med*, vol. 137, pp. 181–190, Apr. 2018, doi: 10.1016/j.rmed.2018.03.010.

[37] P. Worth Longest and M. Hindle, “Evaluation of the respimat soft mist inhaler using a concurrent cfd and in vitro approach,” *J Aerosol Med Pulm Drug Deliv*, vol. 22, no. 2, pp. 99–112, 2009, doi: 10.1089/jamp.2008.0708.

[38] Y. S. Cheng, Y. Zhou, and W. C. Su, “Deposition of particles in human mouth-throat replicas and a USP induction port,” *J Aerosol Med Pulm Drug Deliv*, vol. 28, no. 3, pp. 147–155, Jun. 2015, doi: 10.1089/jamp.2013.1105.

[39] R. Mehri, A. Alatrash, N. Ogrodnik, E. A. Matida, and F. Fiorenza, “In Vitro Measurements of Spiriva Respimat Dose Delivery in Mechanically Ventilated Tracheostomy Patients,” *J Aerosol Med Pulm Drug Deliv*, vol. 34, no. 4, pp. 242–250, Aug. 2021, doi: 10.1089/jamp.2019.1570.

[40] H. Mortazavi and L. Pakzad, “The hydrodynamics and mixing performance in a moving baffle oscillatory baffled reactor through computational fluid dynamics (CFD),” *Processes*, vol. 8, no. 10, pp. 1–30, 2020, doi: 10.3390/pr8101236.

[41] M. Rahimi-Gorji, O. Pourmehran, M. Gorji-Bandpy, and T. B. Gorji, “CFD simulation of airflow behavior and particle transport and deposition in different breathing conditions through the realistic model of human airways,” *J Mol Liq*, vol. 209, pp. 121–133, May 2015, doi: 10.1016/j.molliq.2015.05.031.

[42] K. Kadota *et al.*, “In silico evaluation of particle transport and deposition in the airways of individual patients with chronic obstructive pulmonary disease,” *European Journal of Pharmaceutics and Biopharmaceutics*, vol. 174, pp. 10–19, May 2022, doi: 10.1016/j.ejpb.2022.03.010.

[43] O. Pourmehran, B. Cazzolato, Z. Tian, and M. Arjomandi, “The effect of inlet flow profile and nozzle diameter on drug delivery to the maxillary sinus,” *Biomech Model Mechanobiol*, vol. 21, no. 3, pp. 849–870, Jun. 2022, doi: 10.1007/s10237-022-01563-8.

[44] F. R. Menter, “Two-equation eddy-viscosity turbulence models for engineering applications,” *AIAA Journal*, vol. 32, no. 8, pp. 1598–1605, 1994, doi: 10.2514/3.12149.

[45] P. W. Longest, M. Hindle, S. Das Choudhuri, and J. Xi, “Comparison of ambient and spray aerosol deposition in a standard induction port and more realistic mouth-throat geometry,” *J Aerosol Sci*, vol. 39, no. 7, pp. 572–591, 2008, doi: 10.1016/j.jaerosci.2008.03.008.

[46] M. M. Paul and L. Pakzad, “Bubble size distribution and gas holdup in bubble columns employing non-Newtonian liquids: A CFD study,” *Canadian Journal of Chemical Engineering*, vol. 100, no. 10, pp. 3030–3046, Oct. 2022, doi: 10.1002/cjce.24352.

[47] M. D. Allen and O. G. Raabe, “Slip correction measurements of spherical solid aerosol particles in an improved millikan apparatus,” *Aerosol Science and Technology*, vol. 4, no. 3, pp. 269–286, 1985, doi: 10.1080/02786828508959055.

[48] P. W. Longest, S. Vinchurkar, and T. Martonen, “Transport and deposition of respiratory aerosols in models of childhood asthma,” *J Aerosol Sci*, vol. 37, no. 10, pp. 1234–1257, 2006, doi: 10.1016/j.jaerosci.2006.01.011.

[49] S. A. Morsi and A. J. Alexander, “An investigation of particle trajectories in two-phase flow systems,” *J Fluid Mech*, vol. 55, no. 2, pp. 193–208, 1972, doi: 10.1017/S0022112072001806.

[50] P. G. Saffman, “The lift on a small sphere in a slow shear flow,” 1965.

[51] P. W. Longest, G. Tian, X. Li, Y. J. Son, and M. Hindle, “Performance of combination drug and hygroscopic excipient submicrometer particles from a softmist inhaler in a characteristic model of the airways.,” *Ann Biomed Eng*, vol. 40, no. 12, pp. 2596–2610, 2012, doi: 10.1007/s10439-012-0616-2.

[52] W. R. Ke *et al.*, “In vitro evaluation of aerosol performance and delivery efficiency during mechanical ventilation between soft mist inhaler and pressurized metered-dose inhaler,” *Respir Care*, vol. 65, no. 7, pp. 1001–1010, Jul. 2020, doi: 10.4187/respcare.06993.

[53] M. W. Spallek, D. Hochrainer, and H. Wachtel, “Optimizing nozzles for soft mist inhalers,” *Respiratory Drug Delivery VIII*, vol. 2, no. 2, pp. 375–378, 2002.

[54] H. Wachtel, M. Nagel, M. Engel, G. El Azzi, A. Sharma, and J. Suggett, “In vitro and clinical characterization of the valved holding chamber AeroChamber Plus ® Flow-Vu ® for administrating tiotropium Respimat ® in 1–5-year-old children with persistent asthmatic symptoms,” *Respir Med*, vol. 137, no. March, pp. 181–190, Apr. 2018, doi: 10.1016/j.rmed.2018.03.010.

[55] V. A. Marple, B. A. Olson, K. Santhanakrishnan, J. P. Mitchell, S. C. Murray, and B. L. Hudson-Curtis, “Next Generation Pharmaceutical Impactor (a new impactor for pharmaceutical inhaler testing). Part II: Archival calibration,” *Journal of Aerosol Medicine: Deposition, Clearance, and Effects in the Lung*, vol. 16, no. 3, pp. 301–324, 2003, doi: 10.1089/089426803769017668.

[56] X. Wei *et al.*, “In vitro tests for aerosol deposition. VI: Realistic testing with different mouth-throat models and in vitro - In vivo correlations for a dry powder inhaler, metered dose inhaler, and soft mist inhaler,” *J Aerosol Med Pulm Drug Deliv*, vol. 31, no. 6, pp. 358–371, Dec. 2018, doi: 10.1089/jamp.2018.1454.

[57] P. W. Longest and M. Hindle, “Evaluation of the respimat soft mist inhaler using a concurrent cfd and in vitro approach,” *J Aerosol Med Pulm Drug Deliv*, vol. 22, no. 2, pp. 99–112, Jun. 2009, doi: 10.1089/jamp.2008.0708.

[58] J. Ziegler and H. Wachtel, “Comparison of Cascade Impaction and Laser Diffraction for Particle Size Distribution Measurements,” *Journal of Aerosol Medicine*, vol. 18, no. 3, pp. 311–324, Sep. 2005, doi: 10.1089/jam.2005.18.311.

[59] J. Xi, J. Kim, X. A. Si, and Y. Zhou, “Hygroscopic aerosol deposition in the human upper respiratory tract under various thermo-humidity conditions,” *J Environ Sci Health A Tox Hazard Subst Environ Eng*, vol. 48, no. 14, pp. 1790–1805, Dec. 2013, doi: 10.1080/10934529.2013.823333.

[60] P. W. Longest and M. Hindle, “Condensational growth of combination drug-excipient submicrometer particles for targeted high efficiency pulmonary delivery: Comparison of CFD predictions with experimental results,” *Pharm Res*, vol. 29, no. 3, pp. 707–721, Mar. 2012, doi: 10.1007/s11095-011-0596-1.

Chapter 7- Effect of Tongue Position on Droplet Deposition and Airflow Pattern in the Mouth-throat Pediatric Airway at Varying Inhalation Profiles- with Soft Mist Inhalers

7.1 Abstract

Respiratory diseases, such as chronic obstructive pulmonary disease (COPD) and asthma, impact children all over the world, making it essential to accurately assess aerosol delivery. This underscores the importance of accurately assessing aerosol delivery in children. This study integrates computational fluid dynamics (CFD) and in-vitro experiments to analyze drug delivery and deposition patterns from a soft mist inhaler (SMI) within a detailed anatomical model of a pediatric mouth-throat (MT) airway.

Using large eddy simulation (LES) modeling in ANSYS Fluent, we studied the effects of inhalation profile and tongue positioning on drug droplet size distribution and deposition efficiency. The numerical results for drug deposition closely matched in-vitro data from the next-generation impactor (NGI), with a root mean square error (RMSE) of 0.061.

The findings showed that drug deposition in the pediatric MT was more than double that of adults at a flow rate of 30 l/min with the tongue in its normal position. However, lowering the tongue position decreased deposition on both the mouth and SMI mouthpiece, while increasing it on the throat's outlet and walls. Increasing the flow rate from 7.5 to 30 l/min enhanced the retention of small droplets (0.1-2 μm) within the pediatric MT geometry. Additionally, simulating realistic COPD conditions along with a two-step pulsatile inhalation profile significantly improved small droplets retention while decreasing the number of large droplets (5-60 μm). This notably reduced mouth deposition while increasing drug deposition on the SMI mouthpiece. Moreover, we established a correlation to predict mouth deposition percentages across varying flow rates for Stokes (St) numbers greater than 0.02. Under realistic conditions for COPD and using a two-step pulsatile flow, we observed that the drug droplets deposited more unevenly inside the SMI device mouthpiece and mouth region. Specifically, there was a higher deposition on the tongue with the two-step profile and more on the palate wall in the COPD profile. In contrast, no deposition occurred on the outer wall of the device when constant flow rates were used. At a low flow rate of

7.5 l/min, deposition was confined to the tongue and back wall of the mouth. In contrast, increasing the flow rate to 30 l/min resulted in deposition extending to the lumen teeth-cheek region, palate wall, and upper lip region.

7.2 Introduction

Respiratory health issues like chronic obstructive pulmonary disease and asthma have affected 14 % of children worldwide, with rising prevalence [1]. It is crucial to accurately measure inhaled aerosols to assess the delivery of respiratory medications. A number of factors, including airflow and breathing patterns, drug droplet characteristics such as size distribution and electrostatic charge, as well as airway geometry, influence the transport and deposition of drug droplets in the human respiratory tract [2–4]. While studies have explored the effects of breathing conditions and droplet characteristics [5–9], research on the impacts of airway geometry and breathing patterns in children is limited compared to adults. This is due in part to restrictions on medical images of human airways, technical challenges in constructing human airway geometry, and variations in breathing patterns [10,11]. Assessing drug delivery within the respiratory tract heavily relies on oropharyngeal geometry, which can be reconstructed using high-resolution medical imaging data, such as computed tomography (CT) or magnetic resonance imaging (MRI) scans [12].

The United States Pharmacopeia induction port (USP-IP) geometry is one of the first models used for analyzing the size of pharmaceutical aerosols [13]. Although it does not accurately represent the shape of the mouth and throat, the USP-IP, which features a sharp 90° bend, is widely recognized as the standard for sampling pharmaceutical aerosols [14,15]. Utilization of simplified oropharyngeal geometries has been common due to limited access to CT or MRI scans and to reduce computational expenses for numerical studies [16,17]. However, when simplified geometries are compared to more realistic ones, the results are often found to be inadequate, as shown by various assessments [18,19]. Cheng *et al.* [20] introduced a well-established oropharyngeal model, frequently referenced in numerous studies [21–24]. This model was developed using a dental mold taken from the mouth of an adult human volunteer, while the throat portion was obtained from a deceased donor [25]. They measured approximately equal deposition fractions of monodispersed droplets inside the main oral cavity and laryngeal-tracheal section for both inhalation and exhalation at the flow rate range of 7.5-30 l/min. Longest and Hindle [26] compared Respimat aerosol deposition in a USP-IP and a realistic adult mouth-throat (MT) geometry. They observed significant drug wastage in the soft mist inhaler (SMI) device mouthpiece and increased deposition in the realistic MT area by 80% (compared with the USP-IP), primarily due to recirculating flow patterns within the mouthpiece and the complex airflow dynamics in the realistic geometry. Wei *et al.* [27] investigated the potential of using adult realistic MT geometries to predict lung deposition. The study found that using more realistic MT geometries led to a stronger correlation between in-vitro and in-vivo results. In another study, Musante *et al.* [28] compared the whole lung deposition rates between pediatric and adult subjects. They discovered that 7-month-old infants exhibited a deposition fraction rate approximately twice that of adults. This was primarily attributed to variances in lung anatomy development and subsequent differences in flow patterns within the lung geometry.

Along with studies on the impact of airway geometry using both numerical simulations and in-vitro approaches [29–32], researchers have also investigated the effects of other factors on the delivery of drug aerosols [27–30]. For example, a study by Xi *et al.* [33] examined the impact of the periodic movement of the glottis on airflow within a model of an adult human upper airway. The results showed that changes in the glottis shape have a greater impact on secondary airflow patterns than changes in inhalation type (constant or sinusoidal), particularly associated with swirling flows in a transverse direction. Haghnegahdar *et al.* [34] investigated how varying nasal hair thickness affects airflow patterns and inhaled droplet dynamics in an adult human nasal cavity. They observed that nasal hairs enhanced the filtering of small droplets, increasing filtration efficiency by more than 20% for droplet size ranges corresponding to impaction parameter values between 3e+3 to 2e+4 $\mu m^2 cm^3/s$.

The effectiveness of drug delivery is not only influenced by the shape of the airways but also by the breathing pattern [35]. It is challenging to fully replicate all aspects of the respiratory process in a single study due to its complexity. Therefore, many numerical studies rely on simplified assumptions to reduce computational costs, allowing for a focused examination of specific aspects of respiration [8,36–38]. However, it is important to simulate inhalation flow profiles in order to accurately understand respiratory dynamics and replicate in-vivo conditions [33] William *et al.* [39] investigated how droplets from inhalers deposit in the lungs of individuals with healthy and impaired breathing patterns. It was found that healthy inhalation led to 35% higher drug deposition in the lower to upper lobes of the lungs compared to impaired breathing. Xu *et al.* [40] focused on the effect of the breathing method on droplet deposition and inhalation in adult human airways during steady inhalation using computational methods. They found that nasal inhalation caused the acceleration of airflow after the glottis due to nasal passage narrowing, while oral inhalation resulted in a 'glottal jet' phenomenon, where the airflow velocity was 2.3 times higher than the inlet velocity. Tiwari *et al.* [41] examined the impact of breathing conditions on drug delivery and found that faster inhalation led to greater deposition of larger droplets in the adult oral cavity, with approximately 38% deposition efficiency for 10 µm drug droplets compared to 25% for 1 µm droplets.

Additionally, a number of studies highlighted the importance of mobile geometric features within the human respiratory tract in influencing the behavior of inhaled droplets [42–45]. The human tongue, with its eight movable muscles, can move in various directions within the oropharyngeal region owing to its intrinsic and extrinsic muscles [46]. The literature has underscored the impact of tongue positions and movements on drug administration [47–49]. Nagel and Mitchell [50] investigated how tongue positioning affects aerosol delivery from a pressurized metered dose inhaler (pMDI) and valve-holding chamber in two adult oropharyngeal airways. They found a notable difference in the amount of drug deposited in the oropharyngeal airways when the tongue was removed from the geometric model. Yokoi *et al.* [51] conducted a study on the impact of lowering the tongue in one direction in an adult mouth on the amount of drug droplets released from dry powder inhalers (DPI) and pMDIs. They showed how changing the position of the tongue can alter the cross-sectional area of the oropharynx, leading to modifications in aerosol transport.

Our literature review indicates that further research is necessary to understand the behavior and deposition of inhaled droplets in children compared to adults. Pediatric patients have distinct airway structures that can influence the distribution and deposition of drug aerosols. Harless *et al.* [52]found that young children have a relatively larger tongue size compared to adults, which can significantly impact drug deposition and distribution in pediatric airways. Previous computational fluid dynamic (CFD) studies have not considered the position of the tongue in the pediatric oropharyngeal area and its effects on drug delivery using an SMI device.

This study investigates the impact of tongue orientation and breathing conditions on drug deposition, size distribution, and airflow dynamics in the pediatric MT airway [53] using an SMI device. We employed both in-vitro experiments and computational modeling approaches. We validated our CFD modeling study by measuring deposition fractions at the outlet of a three-dimensional (3D) printed pediatric airway model using a next-generation impactor (NGI) at a flow rate of 30 l/min. The CFD study employed large eddy simulation (LES) using ANSYS Fluent v20.2 (ANSYS Inc., Canonsburg, PA) to model a two-way-coupled aerosol plume and found it effective in accurately predicting transient behaviors in a realistic pediatric MT geometry. We examined three constant flow rates of 7.5, 15, and 30 l/min, in addition to realistic COPD and two pulsative inhalation flow rates across five tongue positions.

7.3 Methodology

In **Fig 7.1**, a commercially available SMI (Respimat®) from Boehringer Ingelheim, Germany, was connected to a pediatric MT geometry [53] using a mouthpiece connector at a horizontal angle (0°). A laboratory clamp was used to keep it in a fixed position during the experiments. From the other end, the airway geometry was connected via another connector to the impactor of the NGI system.

The pediatric MT geometry was constructed using a 3D printer (Ultimaker S5, Confederation College) and tough plastic (polylactic acid filament with standard finish). The model featured the tongue in a normal position and was divided into two separate components (mouth and throat) to measure local droplet deposition. This model was initially developed in the Pharmaceutical Physics Laboratory of Boehringer Ingelheim Pharma GmbH & Co. KG by Bickmann *et al.* [53]. It is a representative mouth-throat geometry of a 5-year-old child that has a volume of 37.21 cm^3 and a surface area of 127.53 cm^2. The model was featured in Respiratory Drug Delivery online. The pediatric mouth inlet was designed with a circular base to ensure a secure seal when connected to the device mouthpiece. This design maintains the integrity of the geometry, as air flows exclusively through the two SMI air vents. A Hyper Tough rotary tool was used to eliminate surface imperfections and uneven areas. Following this, the internal walls of the airway geometry were polished with cotton swabs soaked in acetonitrile to refine and smooth the internal surface, while ensuring that the internal volume remained constant due to acetonitrile's low solubility with polylactic acid [54].

The droplet deposition efficiency (DE) was measured using the NGI device and chromatography system. The regional spray delivery percentages were calculated as the fraction of the aerosol mass deposited in specific regions (mouth and throat and droplets that escaped from the airway outlet) divided by the total deposited and escaped aerosol mass in the entire geometry, expressed as a percentage (×100).

As illustrated in **Fig 7.1**, the MT airway geometry and the impactor were placed in a cooler box and maintained at 5°C throughout the test. A vacuum pump (HCP5, Copley Scientific, UK) was connected to the NGI via a flow controller (TPK 2000, Copley Scientific, UK) to maintain a constant flow rate of 30 l/min, which corresponds to moderate activity levels in children under 7 years old under laboratory conditions (23 ± 1°C and 50 ± 5% relative humidity) [55]. The constant flow rate was recorded using a digital flow meter (TSI model 4043, USA).

Prior to each experiment, the SMI device was primed with five actuations as per the manufacturer's instructions to ensure a stable aerosol plume. For each experiment, the SMI was actuated 30 times to ensure that enough drug concentration was achieved on each part of the geometry and NGI cups. There was a 10-second gap between each actuation, and after the final actuation, the pump operated for 60 seconds to ensure that all droplets were deposited within the airway geometry or NGI cups. To ensure reproducibility, the experiment was repeated three times. The drug amount deposited within the SMI mouthpiece (SMI and connector), MT airway geometry (mouth and throat), and NGI eight cups was quantified using high-performance liquid chromatography (HPLC) (XSelect CSH Prep C18 5 μm OBD 19 × 150 mm column, at 40°C, 1525 Binary HPLC pump, and 2489 Ultraviolet/Visible detector) from Waters, US. After each experiment, the SMI mouthpiece, airway geometry parts, and NGI cups were disassembled and rinsed with 10 mL, 10 mL, and 5 mL of 0.1% formic acid (v/v%) HPLC-grade water solution, respectively, to accurately determine the amount of deposited drug. The concentration of the deposited drug was measured using a tiotropium bromide and 0.1% formic acid (v/v%) HPLC water solution calibration curve with $R^2 = 0.999$ and a limit of quantification of 1.8 μg/ml.

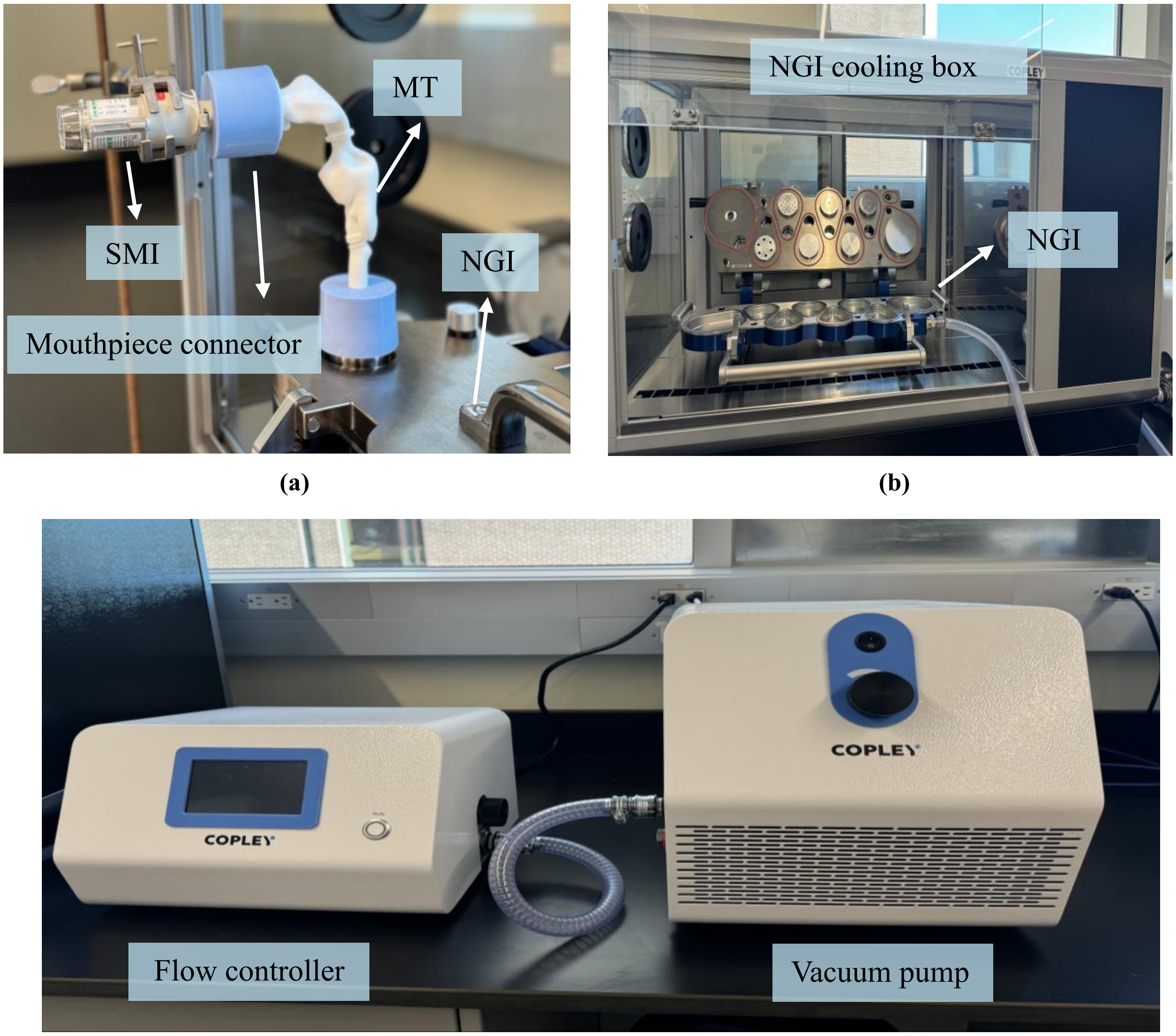

(a) **(b)**

(c)

Fig 7.1 (a) Close-up of the SMI attached to the pediatric MT airway geometry [51] connected to the NGI, **(b)** Opened NGI located inside a cooling box, and **(c)** Flow controller and vacuum pump.

7.4 CFD Model Development

7.4.1 Geometry and Mesh

The reconstructed geometry and mesh, along with different views of the tongue in varied directions, are shown in **Fig 7.2**. In our numerical study, we used the realistic pediatric MT model developed by Bickmann *et al.* [53] to assess various tongue positions. It is worth noting that we also 3D printed the same pediatric MT airway with the tongue in a normal position for an in-vitro study, as detailed in the preceding section.

We utilized two primary methods to develop our models with different tongue positions: refinement and segmentation, along with surface and volume reconstruction. We employed SolidWorks software to integrate the SMI mouthpiece into the model and refine the inner surface of the structure. The geometry was divided into three regions - the SMI mouthpiece, mouth, and throat - as shown in **Fig 7.2(a)**, to calculate regional drug depositions. Finally, the model was exported from SolidWorks, in stereolithography file format, which is compatible with CFD mesh generation tools.

The tongue is situated at the base of the mouth, and its movements can significantly impact the shape of the mouth. Children have a relatively larger tongue surface area [52], so any changes in tongue position can greatly affect the delivery of aerosol droplets. The human tongue is an incredibly flexible organ capable of contorting into various shapes and positions [56]. In accordance with the research of Xi and Yang [24], we chose the central tongue position to represent variations in height to replicate tongue movements within the mouth. The central part of the tongue was divided into multiple sections, and handles were specified at the boundary of each section using CATIA-V5. Four different positions of the central part of the tongue were obtained by moving its handles in controlled and quantitative manners: C+4, C+2, C-2, and C-4. These positions indicate changes in the central height measured in millimetres from the standard position. For instance, in C+4, the central part of the tongue is raised 4 mm above its normal position. The dimensions of the mouth's surface area and volume for various oropharyngeal models are listed in **Table 7.1.**

The computational domains, including SMI mouthpiece, mouth, and throat, were discretized by using the Ansys Fluent Meshing Toolkit (ANSYS Inc., Canonsburg, PA). A polyhedral mesh [57] was created, along with five prismatic layers **(**refer to **Fig 7. 2(b)**), starting at 0.1 mm thickness and growing with a growth ratio of 1.2 within the boundary layer near the walls. These layers were designed to capture turbulence near walls, impacting droplet deposition.

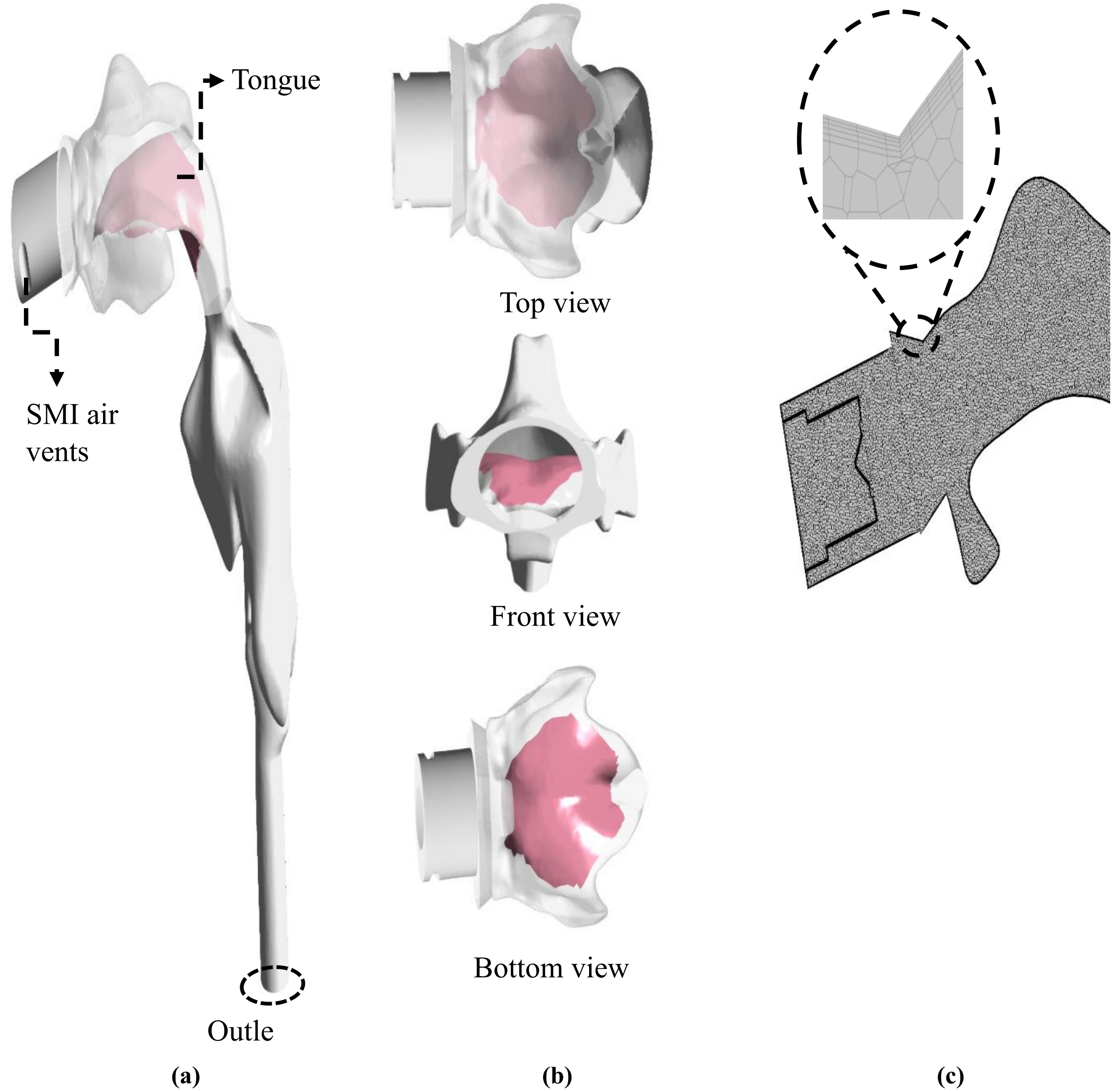

Fig 7.2 (a) Pediatric MT airway geometry [51] with tongue at its normal position, **(b)** Different views of SMI mouthpiece and mouth including tongue, and **(c)** Sample of polyhedral mesh with fine layers near the wall.

Table 7.1 Volume and surface area for pediatric MT models with different tongue positions.

Parameter	**C+4**	**C+2**	**C0**	**C-2**	**C-4**
Volume (cm^3)	33.49	35.54	37.21	39.65	41.71
Surface area (cm^2)	131.32	129.02	127.53	126.12	124.22

7.4.2 Governing Equations

The CFD package ANSYS Fluent v20.2 (ANSYS Inc., Canonsburg, PA) was used in this study to simulate the flow field inside a pediatric MT airway for inspiratory inhalation rates of 7.5, 15, and 30 l/min, as well as for a realistic COPD inhalation rate and pulsative inhalation profiles. These flow rates correspond to minimum and maximum Reynolds numbers ranging from 703 to 12,500, indicating a laminar to a turbulent airflow regime. We also modeled a realistic COPD inhalation profile and two pulsative inhalation profiles. The Reynolds-averaged Navier Stokes (RANS) method is effective for fully developed turbulence [58]. However, it may not be the best choice for simulating droplet transport in complex geometries, such as the respiratory tract, as it oversimplifies their flow behaviour[59]. For this reason, the large eddy simulation (LES) method was used in this study to simulate the airflow and droplet deposition in the pediatric MT airway. It is important to note that the computational cost of LES is significantly higher than that of RANS modeling. However, LES preserves a substantially larger portion of the underlying turbulence physics [60]. The LES method can capture transient flow features as well as laminar to turbulent transitions. The kinetic energy transport subgrid-scale (SGS) model was used to compute smaller eddies and unsteady flow in the pediatric MT airway geometry. The incompressible large-eddy velocity fields can be formally described by the filtered incompressible Navier-Stokes equations [61]:

$$\frac{\partial \bar{u}_i}{\partial x_i} = 0 \tag{7.1}$$

$$\frac{\partial \bar{u}_i}{\partial t} + \frac{\partial}{\partial x_j}\left(\bar{u}_i \bar{u}_j\right) = -\frac{1}{\rho}\frac{\partial \bar{P}}{\partial x_i} - \frac{\partial}{\partial x_j}\tau_{ij}^{sgs} + \frac{\partial}{\partial x_j}(2\upsilon \bar{S}_{ij}) + \vec{F} \tag{7.2}$$

where $\bar{u}_i(x_i, t)$ is the resolved velocity field in three cartesian coordinate directions, i.e., i =1, 2 and 3, ρ is the air density, $\bar{P}$ is pressure, υ is the air kinematic viscosity, $\vec{F}$ represents body forces acting on the flow, including the gravitational force, and τ_{ij}^{sgs} is the subgrid scale stress defined by:

$$\tau_{ij}^{sgs} = \overline{u_i u_j} - \bar{u}_i \bar{u}_j \tag{7.3}$$

The resolved rate of strain tensor, $\bar{S}_{ij}$, is computed as:

$$\bar{S}_{ij} = \frac{1}{2}\left(\frac{\partial \bar{u}_i}{\partial x_j} + \frac{\partial \bar{u}_j}{\partial x_i}\right) \tag{7.4}$$

The SGS turbulent stress resulting from the filtering operation in Eq. (7.3) is unknown and needs a closure model. The eddy-viscosity assumption model yields [62]:

$$\tau_{ij} = \frac{2}{3}k_{sgs}\delta_{ij} - 2\upsilon_t\bar{S}_{ij} \tag{7.5}$$

where δ_{ij} is the Kronecker delta, υ_t(= $C_k k_{sgs}^{1/2}\bar{\Delta}$) is the subgrid-scale viscosity, and the model based on isotropic eddy-viscosity computes SGS kinetic energy from the transport equation, which is given as:

$$\frac{\partial k_{sgs}}{\partial t} + \frac{\partial}{\partial x_j}\left(k_{sgs}\bar{u}_j\right) = \frac{\partial}{\partial x_j}\left(\frac{\upsilon_t}{\sigma_k}\frac{\partial k_{sgs}}{\partial x_j}\right) - C_\varepsilon\frac{k_{sgs}^{3/2}}{\bar{\Delta}} - \frac{\partial \bar{u}_i}{\partial x_j}\tau_{ij} \tag{7.6}$$

where C_k , σ_k, C_ε, are the model constants which define the relationship between the turbulent kinetic energy, eddy viscosity, and energy dissipation [63], and $\bar{\Delta}$ is the subgrid characteristic length scale. The three terms on the right-hand-side of Eq. (7.6) represent, respectively, the transport rate of k_{sgs}, the dissipation rate, and the production rate [63].

The discrete phase model (DPM) was implemented to simulate the movement of aerosolized droplets within the pediatric MT airway. The Lagrangian droplet tracking method (Eq. (7.7)) was used to track the movement of drug droplets ranging from 0.1 to 60 μm [26], diameters emitted from an SMI:

$$\frac{\partial u_d}{\partial t} = \frac{f_D}{\tau_d}(\vec{u} - \vec{u}_d) + \vec{g} + f_{i,lift} \tag{7.7}$$

$$\frac{dx_i}{dt} = \vec{u}_d(t) \tag{7.8}$$

$$f_D = \frac{C_D Re_d}{24} \tag{7.9}$$

$$C_D = \begin{cases} \frac{24}{Re_d}\left(1 + 0.15Re_d^{0.687}\right) & \text{if } Re_d \leq 1000 \\ 0.44 & \text{if } Re_d > 1000 \end{cases} \tag{7.10}$$

$$Re_d = \rho \mid \vec{u} - \vec{u}_d \mid \frac{d_d}{\mu} \tag{7.11}$$

$$\tau_d = \frac{C_c\rho_d d_d^2}{18\mu} \tag{7.12}$$

$$f_{i,\mathrm{lift}} = \frac{5.188\, m_d \upsilon^{0.5} \rho D_{ij}}{\rho_d d_d (D_{lk} D_{kl})^{0.25}} (\vec{u} - \vec{u}_d) \tag{7.13}$$

$$D_{ij} = 0.5\left(\frac{\partial \bar{u}_i}{\partial x_j} + \frac{\partial \bar{u}_j}{\partial x_i}\right) \tag{7.14}$$

In these equations, $\vec{u}$ and $\vec{u}_d$ represent the velocities of air and droplets, respectively, f_D is the drag force, τ_d denotes the relaxation time of droplets, $\vec{g}$ is the gravitational force, $f_{i,\mathrm{lift}}$ is the lift force, C_D is the drag coefficient, Re_d is the droplet Reynolds number, d_d indicates the diameter of droplets, μ represents the air dynamic viscosity, C_c stands for the Cunningham correction factor [64], ρ_d is the droplet density, m_d is defined as droplet mass, and D_{ij} is the deformation tensor.

The discrete random walk model was used to analyze the impact of sudden changes in turbulent air velocity on the movement of droplets [65]. This model operates under the assumption that the air velocity (in Eq. (7.7)) remains constant while a droplet is inside an eddy. The velocity is represented as Eq. (7.15):

$$\vec{u} = \bar{u}_i + u_i' \tag{7.15}$$

where u_i' is the fluctuating component of the instantaneous velocity selected from a Gaussian distribution with a variance of $\frac{2k}{3}$ [66].

Droplet deposition fraction (DF) is defined as the mass of deposited droplets in the region of interest divided by the total mass of injected droplets via SMI [67].

$$\mathrm{DF} = \frac{\text{Deposited droplet mass}}{\text{Total injected droplet mass}} \times 100 \tag{7.16}$$

7.4.3 Boundary Conditions and Simulation Scheme

It is well recognized that actual inhalation profiles, particularly in clinical or patient-specific scenarios, are inherently unsteady. However, most initial simulations and experimental tests of inhaler performance and aerosol deposition are conducted under steady flow conditions for several reasons. First, steady flow assumptions simplify the numerical or experimental setup, reducing computational cost and complexity while allowing researchers to isolate key geometric and flow-related parameters. Second, steady flow simulations are part of widely accepted standardized testing protocols in the pharmaceutical industry, enabling easier cross-comparisons and regulatory approval. Third, many fundamental flow characteristics and deposition trends can still be reliably observed under steady flow, providing a baseline before investigating more complex transient effects [68,69]. The study considered three different breathing conditions: resting (7.5 l/min), light (15 l/min), and moderate (30 l/min) [70]. We also used a realistic COPD inhalation profile for a 4-year-old boy, based on experiments conducted by Lindert *et al.* [71]. The inhalation profile includes a maximum peak inspiratory flow rate of 31 l/min at 0.5 seconds and an average flow rate of 15 l/min over 2 seconds of inhalation. Additionally, a 2-step pulsatile inhalation profile was introduced and compared with other inhalation profiles at the normal tongue position, as shown in **Fig 7.3(a) and (b)**. The airflow pattern is incorporated into the computational model through transient tabular data at the air vents of the SMI mouthpiece.

The mass flow rate boundary condition was applied at the SMI air vents. A pressure outlet boundary condition was chosen for the throat outlet. Additionally, the no-slip boundary condition was applied on airway walls for airflow, and a trap condition was applied to prevent droplets from bouncing when they come into contact with the airway wall. The two-way coupling method was used to account for the impact of droplets on the continuous phase. More details are presented in **Fig 7.3**.

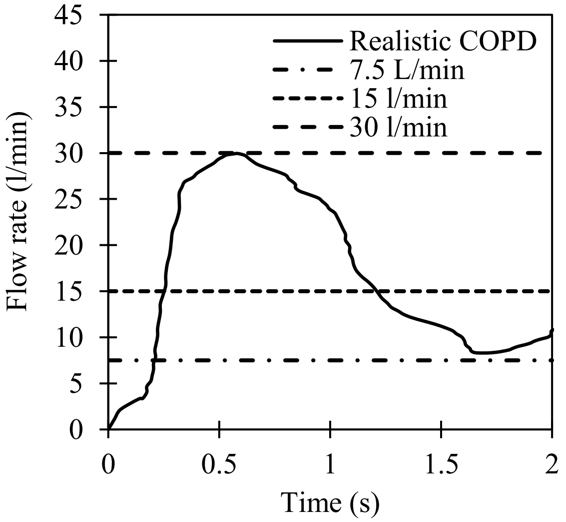

(a)

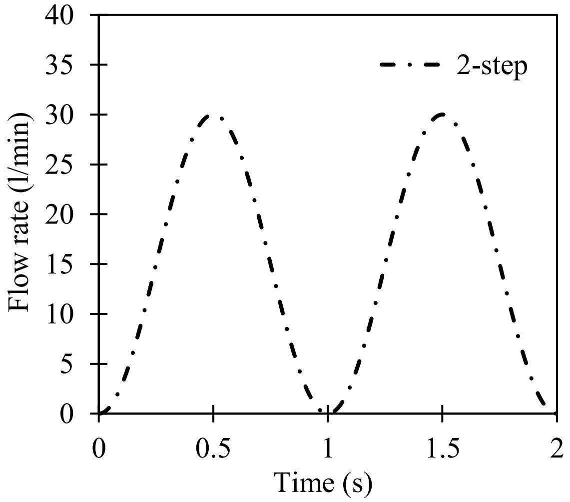

(b)

Injection properties		**Properties of droplets**		**Properties of fluid**	
Total mass flow rate (kg/s)	1e-5	Viscosity (kg/m.s)	0.001	Viscosity (kg/m.s)	1.789e-5
Cone half angle	11.28	Density	998.2	Density (kg/m^3)	1.225

(°)		(kg/m^3)			
Spread parameter (-)	1.48	Surface tension (N/m)	0.072	Temperature (K)	296

(c)

Fig 7.3 Flow profiles for **(a)** constant and realistic COPD flow rates, **(b)** 2-step pulsatile inhalation profile, and **(c)** model parameters used [72].

The software ANSYS Fluent v20.2 (ANSYS Inc., Canonsburg, PA) was employed to solve the continuity and momentum equations for both the fluid and discrete phases. The equations were discretized using bounded central differencing, with a second-order scheme applied for pressure, subgrid kinetic energy, and energy. The SIMPLEC (Semi-Implicit Method for Pressure-Linked Equations Consistent) algorithm was employed to evaluate pressure-velocity coupling. For transient simulation, a bounded second-order implicit method was used, with a time step size of 0.0001 s. The flow field solution was considered converged when the residuals dropped below 10^{-4}. Simulations were conducted on the Narval cluster, using 40 Intel Cascade Lake cores at 2.5 GHz, featuring 64-core processors and 20 GiB/202 GB RAM per node. On average, each simulation took approximately 30 days to complete on the Narval cluster.

7.4.4 Grid Refinement Results

In **Fig 7.4**, velocity profiles for different mesh configurations are displayed along with an air velocity contour. We compared the air velocity magnitude along lines AA´ and BB´, representing highly turbulent regions within our model at 30 l/min. We analyzed four different mesh configurations: 1,000,000, 1,500,000, 2,700,000, and 4,100,000 elements. Increasing the mesh resolution from 2,700,000 to 4,100,000 elements reduced the root-mean-square error (RMSE) [29] at line AA´ to 0.031 and at line BB´ to 0.031, both remaining below five percent error. As a result, the grid with 2,700,000 elements was found to be sufficient and did not require further refinement.

7.5 CFD Model Validation

Fig 7.5(a) shows the cumulative distributions of drug droplet sizes at the outlet of the MT, measured at a flow rate of 30 l/min from our in-vitro and CFD study. Additionally, this data is compared with the in-vitro results published by Wachtel *et al.* [73]. This figure shows that our CFD data collected at the outlet boundary of the throat geometry aligns well with our in-vitro measurements with an RMSE of 0.061. We determined the in-vitro distribution by collecting the drugs deposited in the NGI cups, which passed through the throat outlet, based on their aerodynamic droplet sizes. However, we observe a discrepancy when compared to the findings of Wachtel *et al.* [73]. It is important to note that their study utilized a highly simplified airway geometry that did not consider complex airway features. Consequently, their model could not effectively capture droplets, especially those with larger diameters.

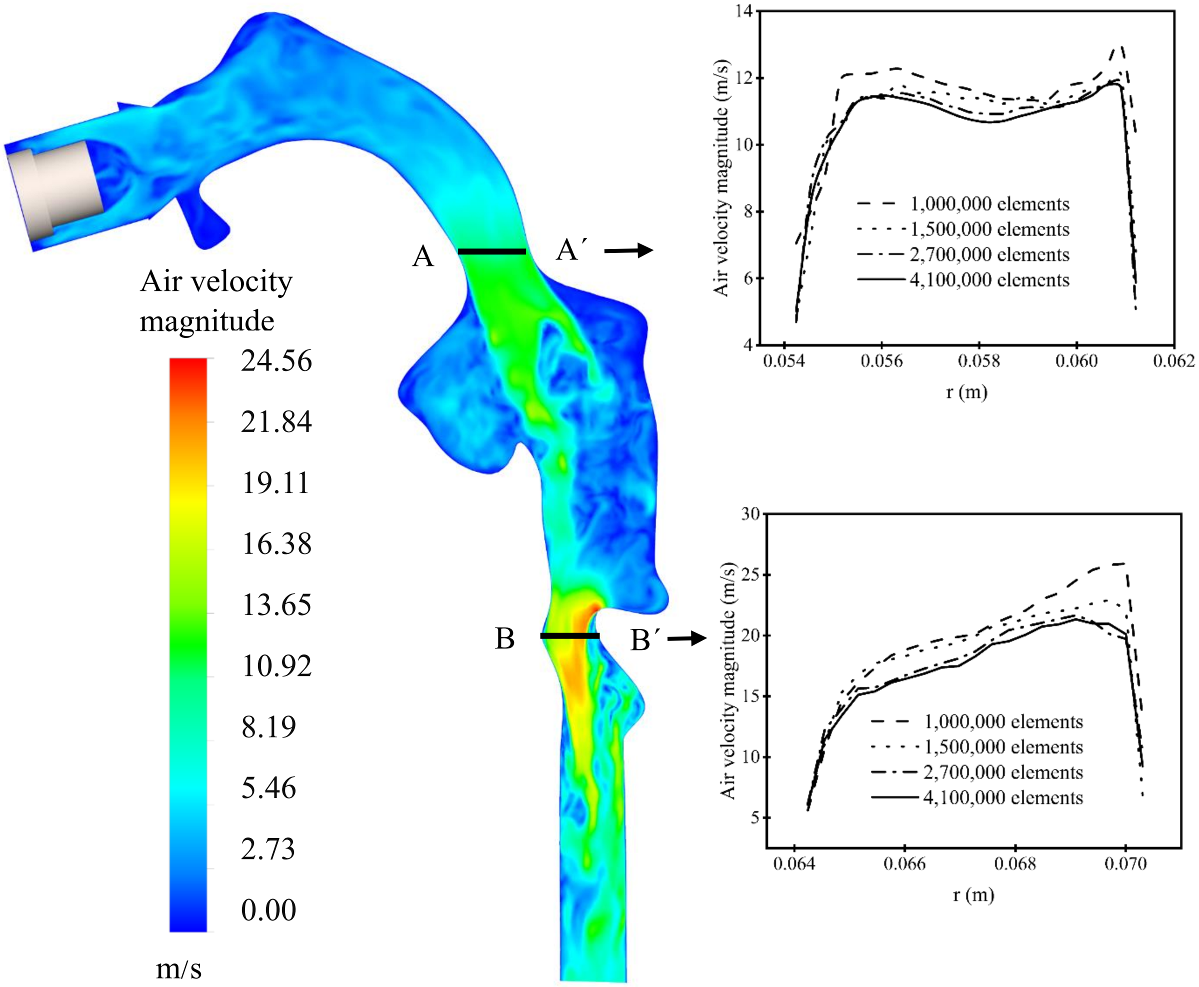

Line AA′		Line BB′	
Number of elements (million)	RMSE	Number of elements (million)	RMSE
1 and 1.5	0.110	1 and 1.5	0.104
1.5 and 2.7	0.052	1.5 and 2.7	0.089
2.7 and 4.1	0.031	2.7 and 4.1	0.031

Fig 7.4 Mesh independence study: comparison of air velocity magnitude on lines AA´ and BB´ (r) along with the contour showing air velocity magnitude at 30 l/min.

In **Fig 7.5(b)**, droplet deposition at a flow rate of 30 l/min was studied within the SMI mouthpiece, MT airway geometry, and NGI cups. Our CFD predictions for the MT and NGI cups closely match the in-vitro results of this study, both in terms of deposition patterns and quantities, with an RMSE of 0.20. However, there is a noticeable difference in the drug deposition of the device's mouthpiece. It is important to highlight that the DPM used in our numerical simulations inject droplets from a single point, at an angle of 22.56° and with a constant velocity of 17.5 m/s, refer to **Fig 7.3(c)**. In contrast, the SMI generates sprays from two impinging jets, which leads to the formation of soft mist clouds near the mouthpiece. As a result, our in-vitro study found a higher drug deposition within the mouthpiece of the device.

Fig 7.5(b) also compares our results (both CFD and in-vitro) with the in-vitro findings of Wachtel *et al.* [73] and [74]. Notably, Wachtel *et al.* [73] reported significantly lower drug depositions within the MT region due to their use of a simplified airway geometry. They utilized a sample inlet port instead of a realistic pediatric MT geometry, which resulted in reduced deposition within the MT and correspondingly increased deposition on the NGI cups, particularly in cups 6, 7, and 8. This emphasizes the importance of considering realistic airway structures in studies, especially for children. However, our CFD results for the mouthpiece and MT depositions align with the findings of Wachtel *et al.* [74], who employed a more realistic pediatric geometry. The slightly higher MT deposition observed in our study is likely due to the inclusion of more realistic anatomical features, such as dental impressions and epiglottis. The agreement between our CFD results and in-vitro data confirms the reliability of our CFD model in simulating aerosol deposition.

The results of the MT airway deposition from a previous in-vitro study for children [74] and CFD predictions for adults [26,75,76] are shown in **Fig 7.5(c).** This figure compares deposition in pediatric and adult airways, with the tongue in a normal position at a flow rate of 30 l/min. Overall, MT deposition in pediatric airways is significantly higher than in adult airways. Notably, in the studies by Longest *et al.* [26] and Wang *et al.* [76], adult deposition is more than double that observed in pediatric airways. This increase can be attributed to the greater geometric complexity and narrower airway structures found in children.

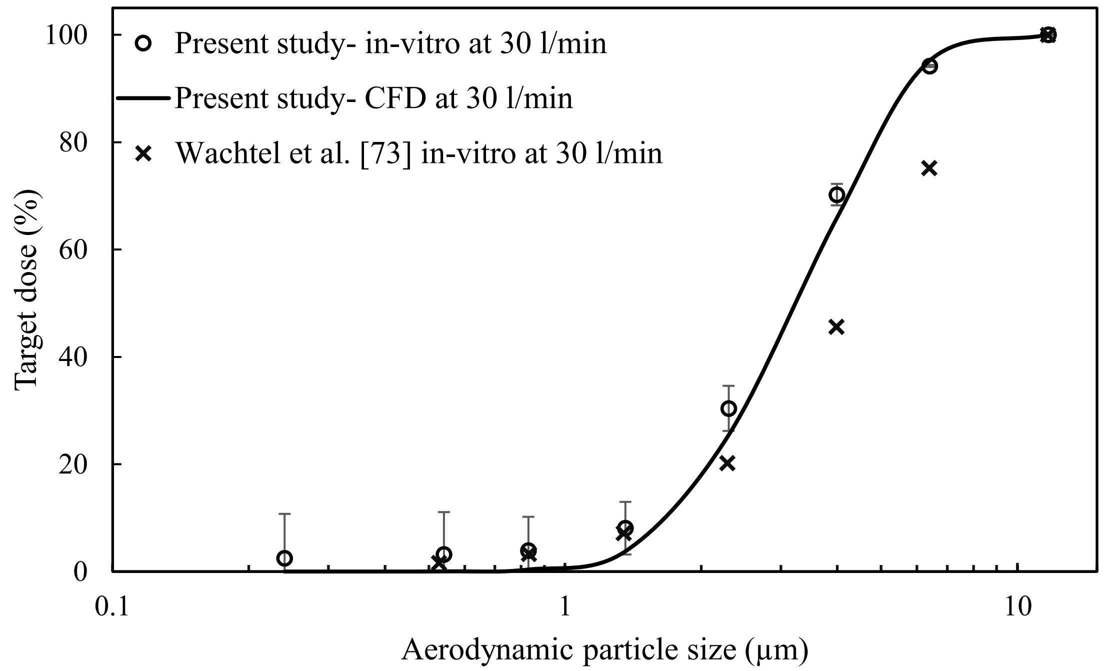
Present study- in-vitro at 30 l/min
Present study- CFD at 30 l/min
Wachtel et al. [73] in-vitro at 30 l/min
Target dose (%)
0
20
40
60
80
100
0.1
1
10
Aerodynamic particle size (μm)

(a)

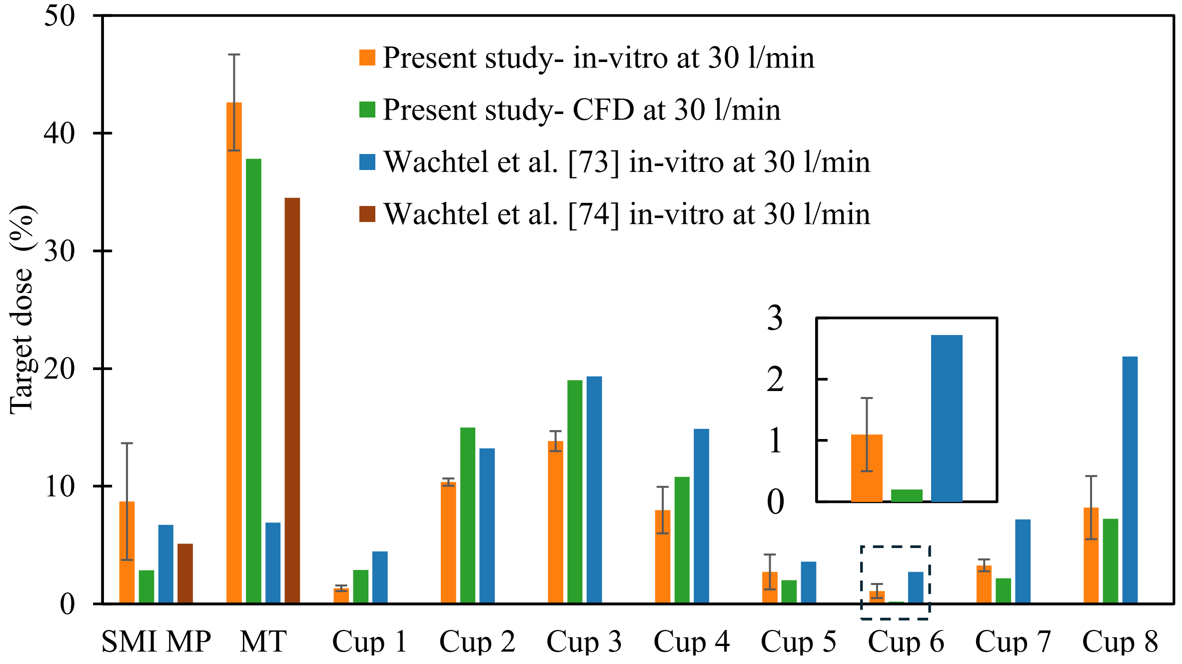
Present study- in-vitro at 30 l/min
Present study- CFD at 30 l/min
Wachtel et al. [73] in-vitro at 30 l/min
Wachtel et al. [74] in-vitro at 30 l/min
Target dose (%)
0
10
20
30
40
50
3
2
1
0
SMI MP
MT
Cup 1
Cup 2
Cup 3
Cup 4
Cup 5
Cup 6
Cup 7
Cup 8

(b)

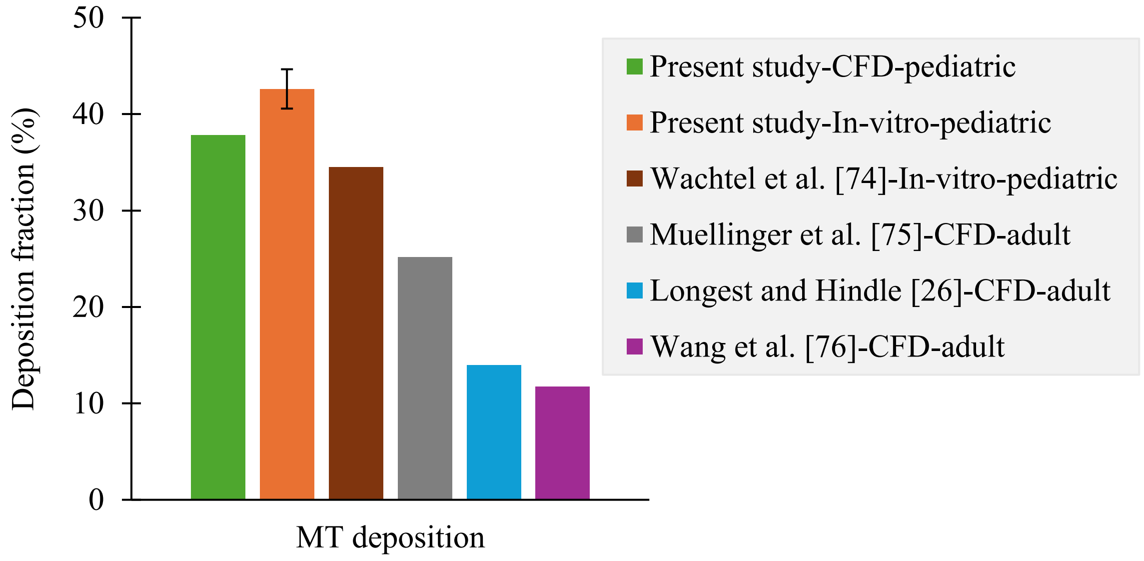

(c)

Fig 7.5 Comparison of CFD results with in-vitro data at 30 l/min, and normal position of tongue (C0): **(a)** cumulative droplet size distribution, **(b)** droplet deposition fraction in SMI mouthpiece, MT airway geometry, and NGI cups, and **(c)** comparison of MT deposition in pediatric and adult airways. CFD data were measured based on the NGI cut-off size at the outlet of pediatric MT geometry.

7.6 Results and Discussion

Fig 7.6 illustrates how mouth deposition, calculated using Eq. (7.17), varies with the Stokes (St) number (defined by Eq. (7.18)) at different flow rates of 7.5, 15, and 30 l/min, as well as under a realistic COPD inhalation flow rate. The figure also displays the impact of various tongue positions within the mouth. Each plot includes fitted lines on a logarithmic scale for St > 0.02, which emphasizes the curve slopes and highlights the relationship between the mouth deposition and St number at different tongue positions and airflow rates [18,19].

$$\text{mouth deposition (\%)} = \frac{\text{Number of droplets deposited in a specific region}}{\text{Total number of droplets entering that region}} \times 100 \qquad (7.17)$$

$$\mathrm{St} = \frac{\rho_d d_d^2 \vec{u}}{18\mu D} \qquad (7.18)$$

where D represents the hydraulic diameter (refer to Eq. (7.19)) of the mouth area at the tongue centerline, a crucial parameter reflecting the varying geometry of the mouth as the tongue position changes.

$$D = \frac{4A}{P} \tag{7.19}$$

where A is the mouth cross-sectional area, and P is the perimeter at the central tongue position. This characteristic diameter was selected because it significantly influences airflow patterns, particularly at the onset of inhalation.

Fig 7.6(a) presents that as the tongue moves from its highest position (C+4) to its lowest position (C-4), there is a noticeable change in mouth deposition for an inhalation flow rate of 7.5 l/min. For instance, at St = 0.05, mouth deposition decreases from 25% at C+4 to 7.4% at C-4. When the tongue is at its highest position, the mouth volume and cross-section area decrease, which leads to increased droplet velocity and, consequently, higher mouth deposition. This increase is particularly noticeable at lower St numbers, as indicated in the highlighted box on the figure, due to greater impaction and turbulence within the airway. This trend becomes even more pronounced at higher flow rates of 15 and 30 l/min, as shown in **Fig 7.6(b)** and **6(c)**. At these flowrates, the smaller mouth volume at C+4 resulted in increased velocity, leading to higher mouth deposition at the same St numbers. The decreased mouth volume allows for less uniform dispersion of droplets, thereby increasing the likelihood of deposition.

The St number (as shown in Eq. (7.18)) is influenced by the size and velocity of the droplets, as well as the properties of the fluid. Turbulence decreases at a low airflow rate of 7.5 l/min, compared to 15 and 30 l/min. This results in droplet deposition being more significantly influenced by the gravitational force [43]. At lower airflow rates, smaller droplets with low inertia—reflected by a smaller St number—tend to settle more easily because the weaker airflow is less effective at keeping them suspended. This suggests that, at these lower flow rates, the behavior of small droplets is influenced more by gravitational forces than by airflow dynamics or inertial effects[77]. Furthermore, we observed a stronger correlation between mouth deposition and the St number at lower flow rates, as shown in **Fig 7.6(a)**, within a specific range of St numbers. Even small changes in the St number, which represents droplet size and inertia, can lead to significant variations in droplet deposition efficiency.

On the other hand, in conditions with higher flow rates, as shown in **Fig 7.6(b)** and **6(c)**, inertial impaction becomes a more significant factor in the settling of droplets, particularly for larger droplets [78]. However, as the flow rate increases, the higher momentum of the airflow enhances the ability of droplets, particularly those with moderate St numbers, to follow the main flow. This is because the increased flow velocity results in a stronger drag force on the droplets, counteracting their inertia more effectively and aligning their motion with the airflow, thereby improving their adherence to the flow direction. This phenomenon leads to a decrease in the steepness of the settling efficiency curves for flow rates of 15 and 30 l/min due to smoother relationship between Stokes number and mouth deposition. A correlation (Eq. (7.20)) was established between the fitted lines for the tongue in its normal position at various flow rates. Initially, the data was linearized using a logarithmic transformation, followed by regression analysis employing an inverse model. The correlation was developed as follows:

$$\text{mouth deposition } (\%) = \mathrm{a}\ln(\mathrm{St}) + \mathrm{b} \quad (\mathrm{St} > 0.02) \text{ and}$$
$$\begin{cases} \mathrm{a} = \frac{430}{\mathrm{Q}} + 18 \\ \mathrm{b} = \frac{1203}{\mathrm{Q}} + 86 \end{cases} \tag{7.20}$$

Here, a and b represent the equation coefficients, and Q is the flow rate (l/min).

Fig 7.6(d) shows the mouth deposition (%) versus St number for the realistic COPD inhalation rate (illustrated in **Fig 7.3(a)**) at the tongue in three positions: C+4 (highest central tongue position), C0 (normal central tongue position), and C-4 (lowest central tongue position) within the pediatric MT geometry. In comparison with the constant flow rates, the COPD inhalation profile resulted in less scattered data across varied tongue positions. The transient nature of COPD airflow, with its dynamic fluctuations, enables more efficient droplet transport, particularly for droplets with moderate to low Stokes numbers. This leads to better alignment of deposition data, as the transient forces promote more uniform droplet movement and deposition. In contrast, constant flow rates offer fewer opportunities for such dynamic coupling, resulting in greater variability and more scattered data. An average inhalation rate of 15 l/min was employed to generate a fitted line using Eq (7.20). The data points align closely with the fitted line, exhibiting an RMSE of 0.014.

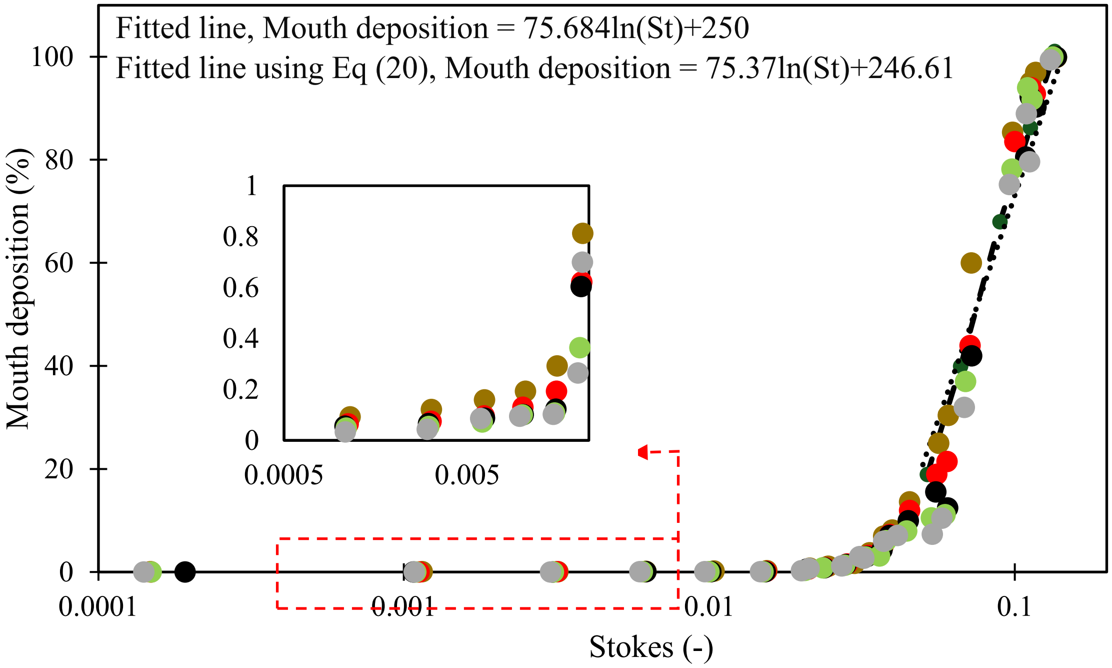
Fitted line, Mouth deposition = 75.684ln(St)+250
Fitted line using Eq (20), Mouth deposition = 75.37ln(St)+246.61
Mouth deposition (%)
100
80
60
40
20
0
0.0001
0.001
0.01
0.1
Stokes (-)
1
0.8
0.6
0.4
0.2
0
0.0005
0.005

(a)

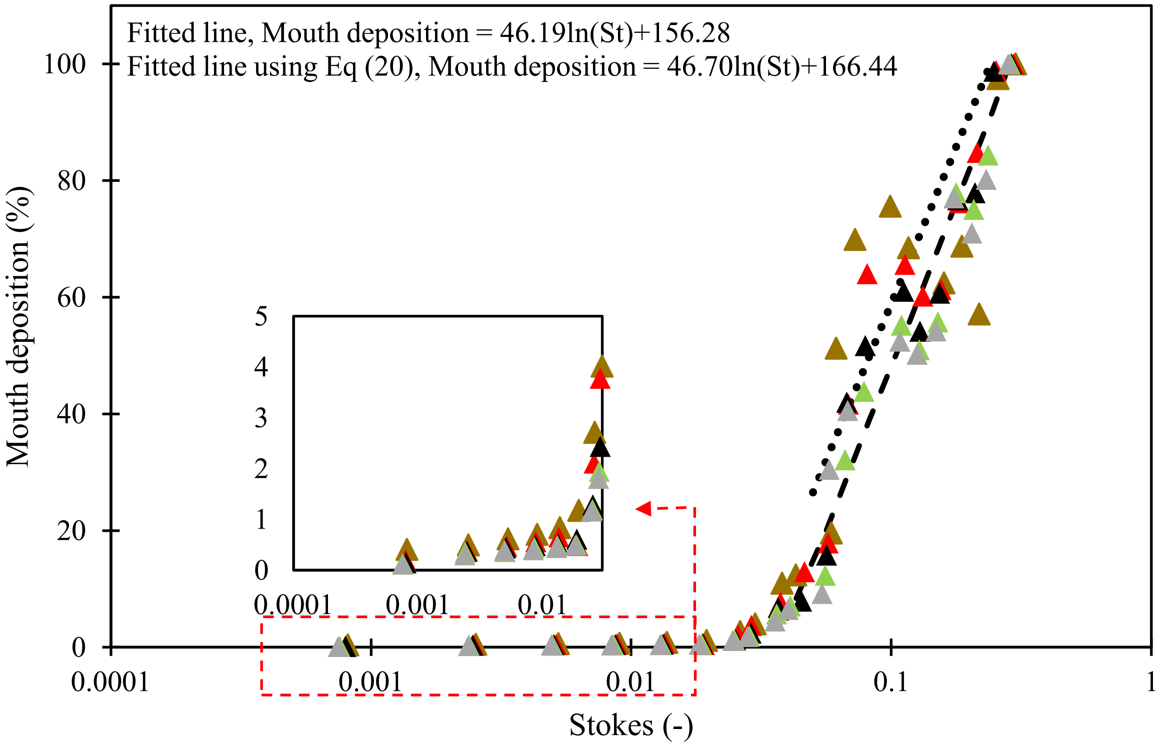
Fitted line, Mouth deposition = 46.19ln(St)+156.28
Fitted line using Eq (20), Mouth deposition = 46.70ln(St)+166.44
Mouth deposition (%)
100
80
60
40
20
0
0.0001
0.001
0.01
0.1
1
Stokes (-)
5
4
3
2
1
0
0.0001
0.001
0.01

(b)

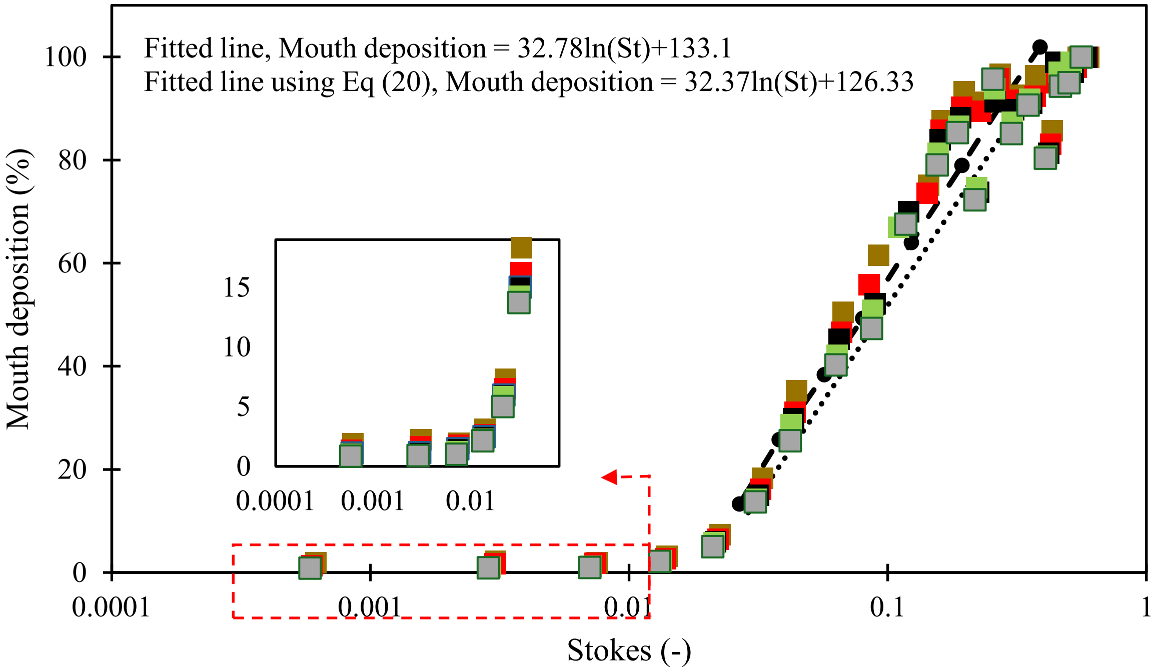
Fitted line, Mouth deposition = 32.78ln(St)+133.1
Fitted line using Eq (20), Mouth deposition = 32.37ln(St)+126.33
Mouth deposition (%)
0
20
40
60
80
100
0.0001
0.001
0.01
0.1
1
Stokes (-)
0
5
10
15
0.0001
0.001
0.01

(c)

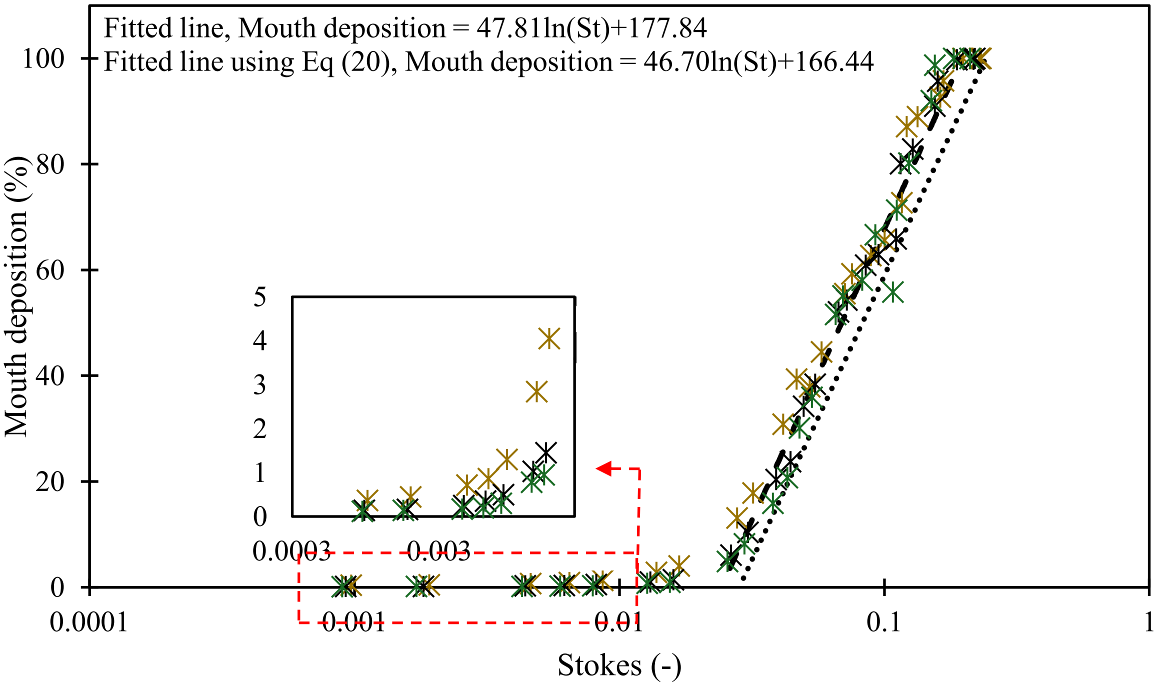
Fitted line, Mouth deposition = 47.81ln(St)+177.84
Fitted line using Eq (20), Mouth deposition = 46.70ln(St)+166.44
Mouth deposition (%)
0
20
40
60
80
100
0.0001
0.001
0.01
0.1
1
Stokes (-)
0
1
2
3
4
5
0.0003
0.003

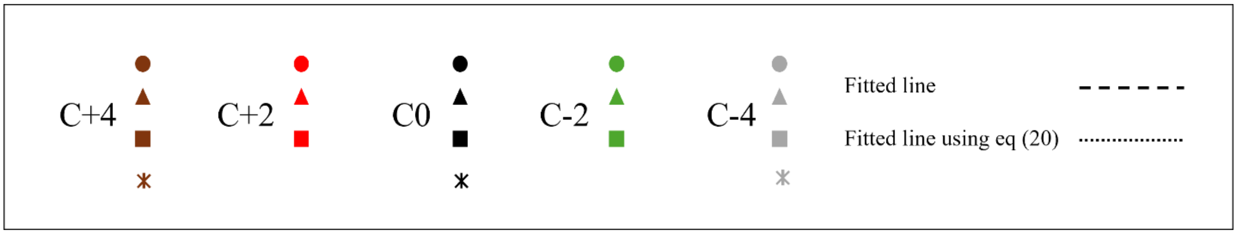

(d)

Fig 7.6 Mouth deposition as a function of Stokes number at varying tongue positions of C+4, C+2, C0, C-2, and C-4 for flow rates of **(a)** 7.5 l/min (circle), **(b)** 15 l/min (triangle), **(c)** 30 l/min (square), and **(d)** realistic COPD inhalation flow rate (star).

Fig 7.7 illustrates the mouth deposition (%) in the mouth as a function of the St number at a flow rate of 30 l/min, with the tongue positioned normally as part of **Fig 7.6(c)**. This data demonstrates that the proposed correlation (Eq. (7.20)) can successfully predict mouth drug deposition based on the St number, with a maximum RMSE of 0.1. Additionally, for a flow rate of 7.5 l/min, the maximum RMSE between the fitted and predicted lines using Eq (7.20) was 0.038, as shown in **Fig 7.6(a)**. For a flow rate of 15 l/min, the maximum RMSE was 0.09, as presented in **Fig 7.6(b)**. This demonstrates that equation (7.20) accurately predicts mouth drug deposition as a function of the St number.

Furthermore, **Fig 7.7** shows that the predicted line aligns well with the findings of Cheng *et al.*, Gregic *et al.*, and Xu *et al.* [79–81] for the same flow rate of 30 l/min, where the maximum RMSE is 0.18. All data points are contained within the shaded region, further supporting the robustness and validity of the current results and proposed collection.

Fig 7.8 illustrates the deposition fraction within the pediatric MT airway geometry at three primary tongue positions: C+4 (highest), C0 (normal), and C-4 (lowest). This analysis considers various constant flow rates, a realistic COPD inhalation flow rate, and a two-step inhalation profile. As discussed in **Fig 7.6**, this figure shows that as the flow rate increases from 7.5 to 30 l/min, there is a clear trend of increased droplet deposition in the mouth region (illustrated in yellow). This trend is consistent across all tongue positions. However, throat deposition decreases as the flow rate increases for all tongue positions referred to as green regions. Additionally, MT deposition (yellow and green together) shows a slight increase as the flow rate rises from 7.5 to 30 l/min. This indicates that fewer drug droplets pass through the pediatric MT airway at higher flow rates across all tongue positions.

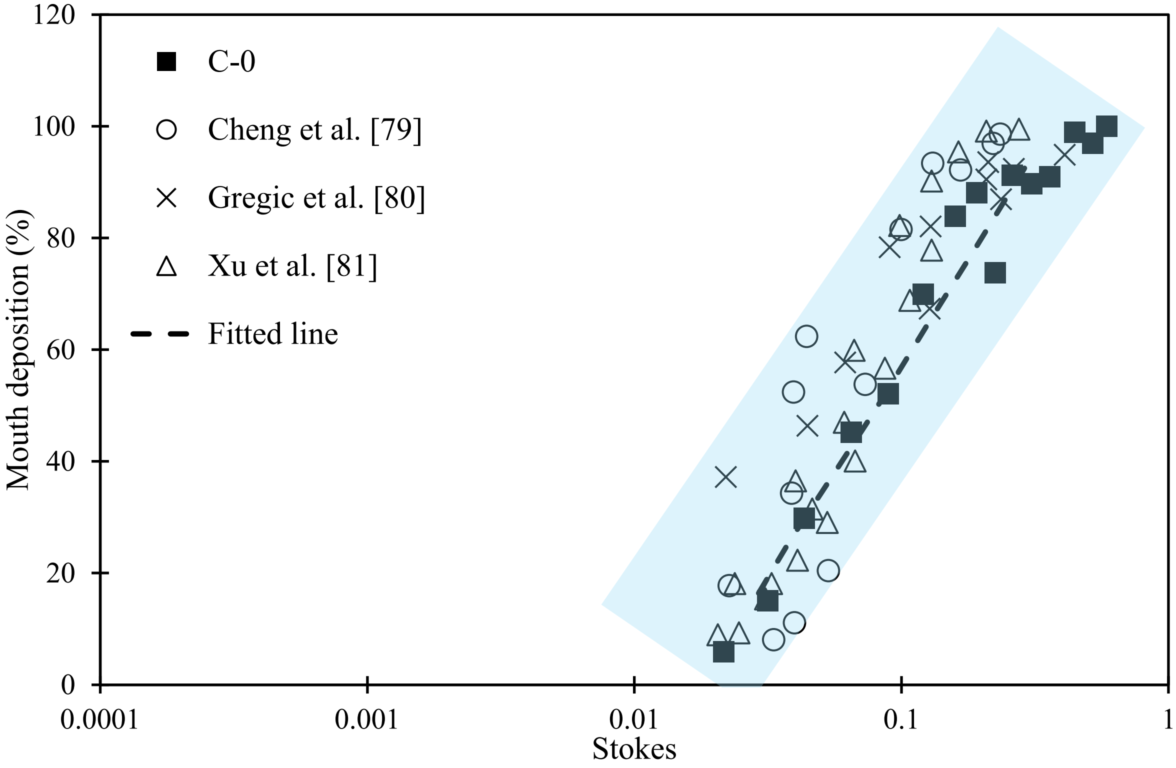

Fig 7.7 Validation of correlation equation with previous studies at normal tongue position and at 30 l/min.

Additionally, **Fig 7.8** illustrates that the highest deposition of MT droplets occurred at the tongue position (C+4) across all constant flow rates, peaking at 40.05% with a flow rate of 30 l/min. At this rate, 54.75% of droplets passed through the throat outlet. The narrow diameter of the oral airway, resulting from the elevated tongue position, restricted airflow and increased the likelihood of droplet-wall interactions, which led to greater droplet impaction within the MT. When the tongue was positioned at a normal level (C0), the deposition on the MT airway wall and the throat outlet at a flow rate of 30 l/min was measured at 37.84% and 59.31%, respectively. In contrast, at the lowest tongue position (C-4) with a flow rate of 30 l/min, a greater percentage of droplets (61.75%) passed through the outlet, reducing deposition on the pediatric MT walls, which was only 32.44%. Furthermore, **Fig 7.8** indicates that, regardless of tongue position and flow rates (ranging from 7.5 to 30 l/min), there was minimal deposition on the SMI mouthpiece. As the flow rate increased from 7.5 to 30 l/min at the highest tongue position, the deposition on the SMI mouthpiece rose from 1.35% to a maximum of 5.18%.

Fig 7.8 also illustrates that the realistic COPD inhalation profile leads to reduced deposition of drug droplets on the pediatric MT airway across all tongue positions. For the normal tongue position, total deposition on the MT wall reached approximately 31%, consistent with previous pediatric MT deposition by Wachtel *et al.* [74]. This effect is primarily due to the transient nature of realistic inhalation, which prevents drug droplets from gaining sufficient momentum during the slower phases of the inhalation cycle to impact the MT walls. For example, the average droplet velocity was measured 0.55 m/s before reaching the peak inhalation flow at 0.5 seconds, compared to 0.67 m/s at the lowest constant flow rate of 7.5 l/min. As inhalation flow peaks, drug droplets tend to bypass the mouth and throat regions, following the airflow toward the throat outlet. This results in lower deposition of droplets on the MT walls.

The deposition of droplets at the outlet is similar but slightly lower than what is observed at constant flow rates. This indicates that even with irregular airflow, a significant portion of droplets still travel through the airway and reach the lower respiratory tract. The reduced droplet deposition at the outlet for the COPD inhalation profile supports the findings of Williams *et al.* [82], who noted that drug delivery to the lower respiratory tract was greater with a healthy inhalation profile compared to one with impaired inhalation. Notably, deposition on the SMI mouthpiece significantly increases during realistic COPD inhalation, peaking at 15.76% at the C+4 tongue position. This increase is attributed to the slower phases of inhalation, which allow more time for droplets to settle and impact the mouthpiece surface before being carried into the airway. The combination of slower airflow and varying droplet momentum during these phases enhances the likelihood of droplets depositing on the mouthpiece.

Fig 7.8 illustrates that the 2-step inhalation profile (see **Fig 7.3(b)**) with the tongue at the normal position results in the lowest deposition of droplets in the mouth and throat compared to all other inhalation conditions, with values of 5.04% and 12.54%, respectively. This reduction occurs despite the higher average droplet velocity during the 2-step inhalation (0.57 m/s) compared to the COPD inhalation (0.26 m/s). The reason for this difference lies in the intermittent nature of the 2-step flow, which includes periods of near-zero airflow between the peaks. During these slower phases, droplets have less momentum, limiting their ability to impact and deposit on the mouth and throat walls. In contrast, the realistic COPD inhalation profile exhibits a smoother and more sustained velocity pattern, with a gradual rise and fall in airflow. This continuous flow allows droplets to maintain consistent contact with the airway walls for a longer duration, resulting in higher deposition on the mouth and throat surfaces, with values of 9.56% and 20.61%, respectively. The continuous nature of the COPD profile increases the likelihood that the droplets will interact with the airway surfaces, even though its average velocity is lower than that of the 2-step profile.

Fig 7.8 indicates that the 2-step inhalation profile leads to the highest deposition on the SMI mouthpiece, recording a value of 20.03%. This is significantly greater than the 12.92% observed during realistic COPD inhalation and 2.85% at a constant flow rate of 30 l/min. The increased deposition can be attributed to the variability in airflow seen in the 2-step profile. During the low flow phases between peaks, the airflow slows down, allowing droplets to settle more easily on the mouthpiece surface. Then, during the following faster flow phase, these droplets are carried further into the airway. Since the SMI mouthpiece is the first surface that droplets encounter, the slower airflow phases increase the chances of droplets adhering to this upstream region.

Additionally, **Fig 7.8** shows the deposition percentages at the throat outlet for a normally positioned tongue across various inhalation flow rates. The deposition values are as follows: 64.07% at 7.5 l/min, 62.08% at 15 l/min, 59.31% at 30 l/min, 57.91% for COPD inhalation, and 62.40% for the two-step inhalation flow rates. It is evident that drugs do not effectively reach the throat outlet at different inhalation flow rates, with deposition rates ranging from 36% to 43%. Additionally, this figure confirms some of this drug loss occurs at the device's mouthpiece, which may actually benefit patients by reducing side effects. In our in-vitro experiment using a flow rate of 30 l/min, we reported an average mouthpiece drug deposition of 8.7% (see **Fig 7.5(b)**). Importantly, the outlet deposition during the 2-step inhalation flow rate is higher than what is observed with realistic COPD inhalation. This indicates that droplets can travel through the airway more effectively during the rapid phases of the 2-step cycle. Consequently, droplets can reach the outlet while bypassing the airway walls more efficiently than under the steadier conditions experienced during realistic COPD inhalation.

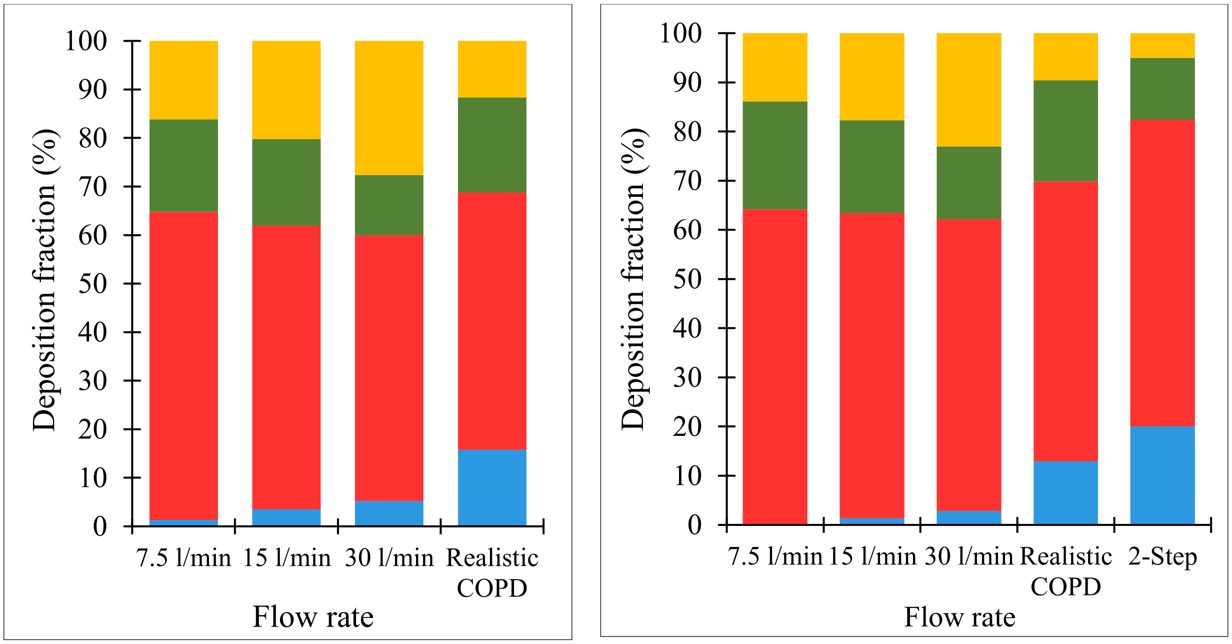

(a) C+4 Tongue position **(b)** C0 Tongue position

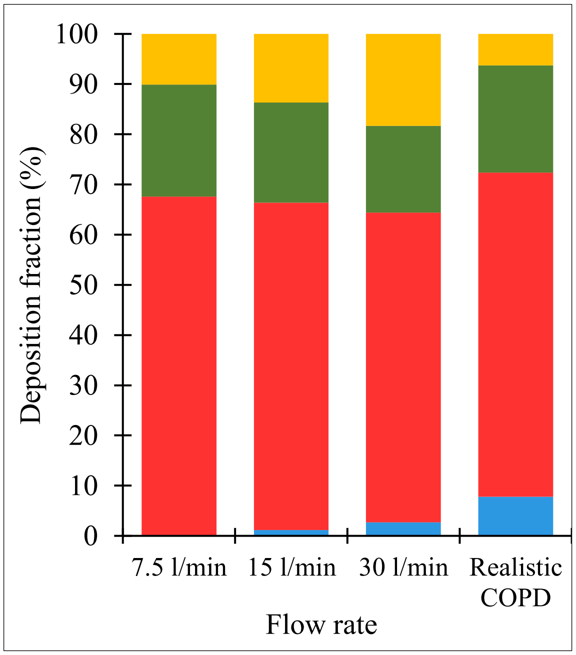

(c) C-4 Tongue position

Mouth wall 🟨 Throat wall 🟩 Outlet 🟥 SMI mouthpiece 🟦

Fig 7.8 Deposition fraction (%) of droplets at different regions (mouth, throat, SMI mouthpiece, and throat outlet) at different flowrates for three tongue positions: **(a)** C+4, **(b)** C0, and **(c)** C-4.

Fig 7.9 shows the drug droplet depositions on the SMI metal mouthpiece for three inhalation profiles: a constant flow rate of 30 l/min, a realistic COPD inhalation rate, and a 2-step pulsatile inhalation profile at the normal tongue position (C0). The highest droplet deposition is observed with the 2-step pulsatile inhalation profile, followed by the realistic COPD inhalation flow rate and, lastly, the constant flow rate of 30 l/min. Droplet deposition is most concentrated near the SMI micro nozzle, which can be attributed to the cone-shaped design of the device's nozzle, which enhances local deposition. As shown in **Fig 7.9(b)**, no deposition is observed on the outer wall of the SMI mouthpiece. In contrast, **Fig 7.9(c)** and **9(d)** show droplet deposition on the outer wall surface of the SMI mouthpiece, indicating that time-dependent flow rates introduce fluctuations in the flow pattern, particularly around the mouthpiece. Since the mouthpiece is the initial contact region for the drug droplets, these fluctuations lead to a more dispersed droplet pattern compared to patterns formed by constant flow rates. Additionally, droplet deposition is greater in the lower half of the SMI mouthpiece, a factor influenced by gravity, which was accounted for in this study.

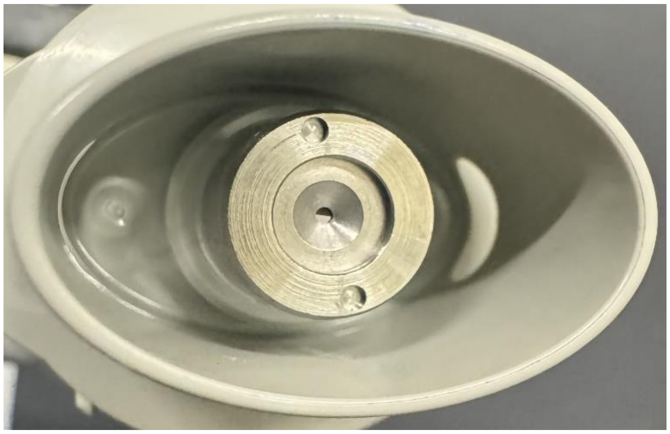

(a) SMI mouthpiece

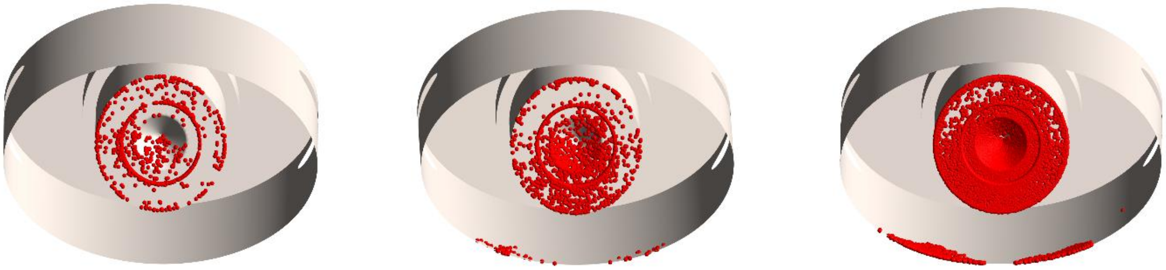

(b) Flow rate of 30 l/min **(c) COPD inhalation** **(d) 2-step pulsatile**

Fig 7.9 Drug deposition pattern on the **(a)** SMI mouthpiece wall for three inhalation profiles of **(b)** constant flow rate of 30 l/min, **(c)** realistic COPD inhalation rate, and **(d)** 2-step pulsatile inhalation profile at normal tongue position (C0).

Table 7.2. presents the droplet fraction at the outlet of the pediatric MT for different tongue positions at various flow rates. Three droplet size categories were analyzed: droplets with diameters between 0.1 and 2 µm, droplets between 2 and 5 µm, and droplets between 5 and 60 µm. These size ranges were selected because they influence how droplets behave within the pediatric airway and their ability to reach different areas. The results indicate that the highest proportion of droplets occurs in the 2 to 5 µm range, with a maximum fraction of 54.63% at the C-4 tongue position and a flow rate of 30 l/min. In contrast, the smallest fraction of droplets is within the 5 to 60 µm size range at the C+4 tongue position. Larger droplets have greater mass and higher inertia, making them less capable of following the airflow path, which increases their likelihood of deposition within the pediatric airway.

The table indicates that larger droplets, ranging from 5 to 60 µm, show a weaker correlation with changes in the constant inhalation flow rate compared to smaller droplets. As the flow rate increased, we observed a decrease in the percentage of drug droplets in the 0.1 to 2 µm range that were deposited at the throat outlet. In contrast, the percentage of droplets in the 2 to 5 µm and 5 to 60 µm size ranges increased. This suggests that higher flow rates result in a greater likelihood of smaller droplets being deposited in the mouth and throat regions of the pediatric airway. This can be attributed to the expansion of recirculation regions and the heightened turbulence due to higher flow rates, as demonstrated in **Fig 7.10**.

Furthermore, **Table 7.2.** shows that under realistic COPD inhalation flowrates, similar patterns appeared among different droplet size groups across the three primary tongue positions. The percentage of droplets in the 2 to 5 µm range remained relatively constant for all tongue positions, it decreased by more than 10% for the 0.1 to 2 µm droplet group and increased by over 10% for the 5 to 60 µm droplet group. Small droplets have lower inertia, allowing them to remain suspended in the airflow, especially in the recirculation regions of the mouth and throat. In contrast, larger droplets, which possess higher inertia, are more likely to bypass the airway walls and exit through the outlet during the peak inhalation phase of a realistic COPD inhalation. The slower initial airflow helps these larger droplets stay suspended, while the peak flow provides the momentum needed for them to exit through the outlet.

Also, the 2-step inhalation profile at the C0 tongue position results in a more balanced deposition pattern across various droplet size ranges, as presented in **Table 7.2.** Smaller droplets (0.1 to 2 µm) exhibit a slightly reduced outlet fraction compared to steady flow conditions, as they tend to interact more with the airway walls during slower flow phases. Nevertheless, these smaller droplets still exit in higher proportions than what is observed in a typical COPD profile. Droplets sized between 2 to 5 µm remain stable across different flow conditions, showing minimal variability. In contrast, droplets ranging from 5 to 60 µm benefit from peak flow phases in the 2-step profile compared to constant flow rates. However, their outlet fraction is still lower than in a realistic COPD profile, where continuous fluctuating airflow provides better conditions for larger droplets to reach the outlet.

Table 7.2 Droplet fraction (%) at the outlet of pediatric MT at different tongue positions and droplet size ranges for flow rates of 7.5 1/min, 15 l/min, 30 l/min, and realistic COPD inhalation profile.

Tongue position	**Droplet size range (µm)**	**Droplet deposition (%) at the pediatric MT airway outlet**				
		7.5 l/min	**15 l/min**	**30 l/min**	**Realistic COPD inhalation flowrate**	**2-step inhalation profile**
C+4	[0.1, 2)	45.26	41.76	36.4	26.30	-
	[2, 5)	47.05	49.78	54.37	51.99	-
	[5, 60]	7.63	8.46	9.215	21.69	-
C0	[0.1, 2)	43.11	41.02	36.15	24.57	33.38
	[2, 5)	48.91	50.4	54.51	52.86	49.55
	[5, 60]	7.97	8.57	9.35	22.55	17.05
C-4	[0.1, 2)	42.45	39.34	34.79	22.02	-
	[2, 5)	49.47	50.92	54.63	54.90	-
	[5, 60]	8.00	9.69	10.56	23.06	-

Fig 7.10 shows the contours of turbulent intensity and velocity streamlines for three primary tongue positions (C+4, C0, and C-4) at two different flow rates: 7.5 l/min and 30 l/min. The variations in cross-sectional areas and flow directions generate complex velocity patterns that

appear as coherent vortex structures within the velocity field. As the flow rate increases from 7.5 l/min to 30 l/min, there are significant fluctuations in the flow field, resulting in an increase in turbulent intensity. Deflections in the flow streamline near the mouth inlet, the posterior area of the mandible, the palate wall, and the pharynx create co-rotating vortices, which result in recirculation regions. These recirculation zones display varying velocities between their inner and outer areas. As the flow rate increases from 7.5 to 30 l/min, the difference in velocity becomes more pronounced. This increased disparity leads to a higher deposition of smaller droplets (i.e., 0 to 2 μm) in the mouth and throat regions.

As shown in **Fig 7.10**, As the tongue moves from its highest position (C+4) to its lowest position (C-4), the airflow experiences reduced acceleration and separation, which results in a decrease in the size of the recirculation zone. This observation aligns with the lower drug deposition in the mouth at the C-4 tongue position. This finding is consistent with the research of Xi and Yang [24], who investigated single-sized particle deposition in an adult airway and reported that elevated tongue positions lead to increased deposition in the mouth.

We can notice in **Fig 7.10** that these recirculating regions gradually diminish as the airflow transitions from the palate wall to the upper pharynx. However, new recirculation zones form in the pharynx due to abrupt changes in cross-sectional areas, which increase turbulent intensity. Although the number of recirculating regions in the pharynx increases as the flow rate rises from 7.5 to 30 l/min, these regions are still not strong enough to capture and retain small droplets. Instead, the high-speed jet from the larynx propels the droplets further down into the trachea and out of the mouth.

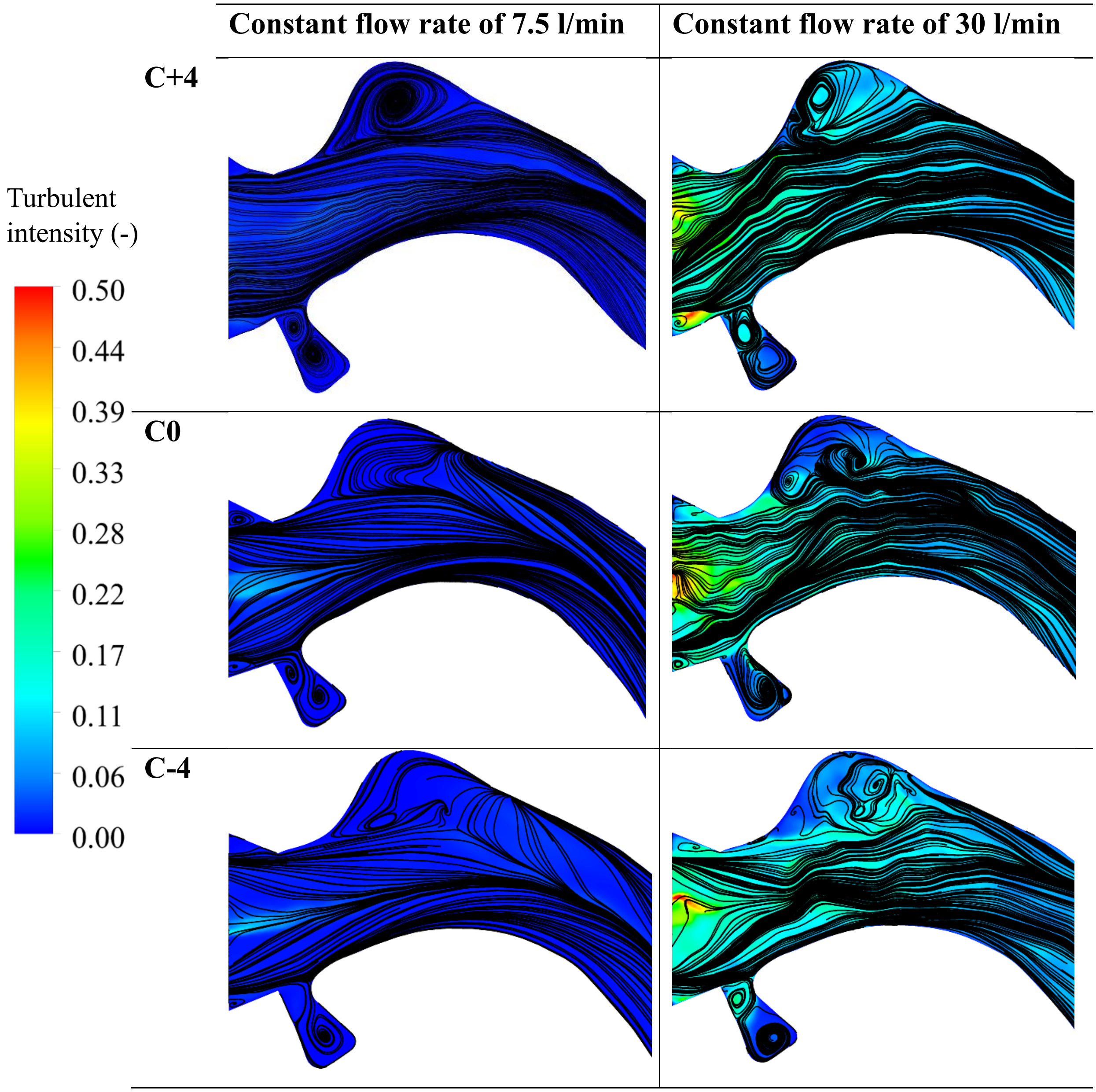

(a) Mouth region

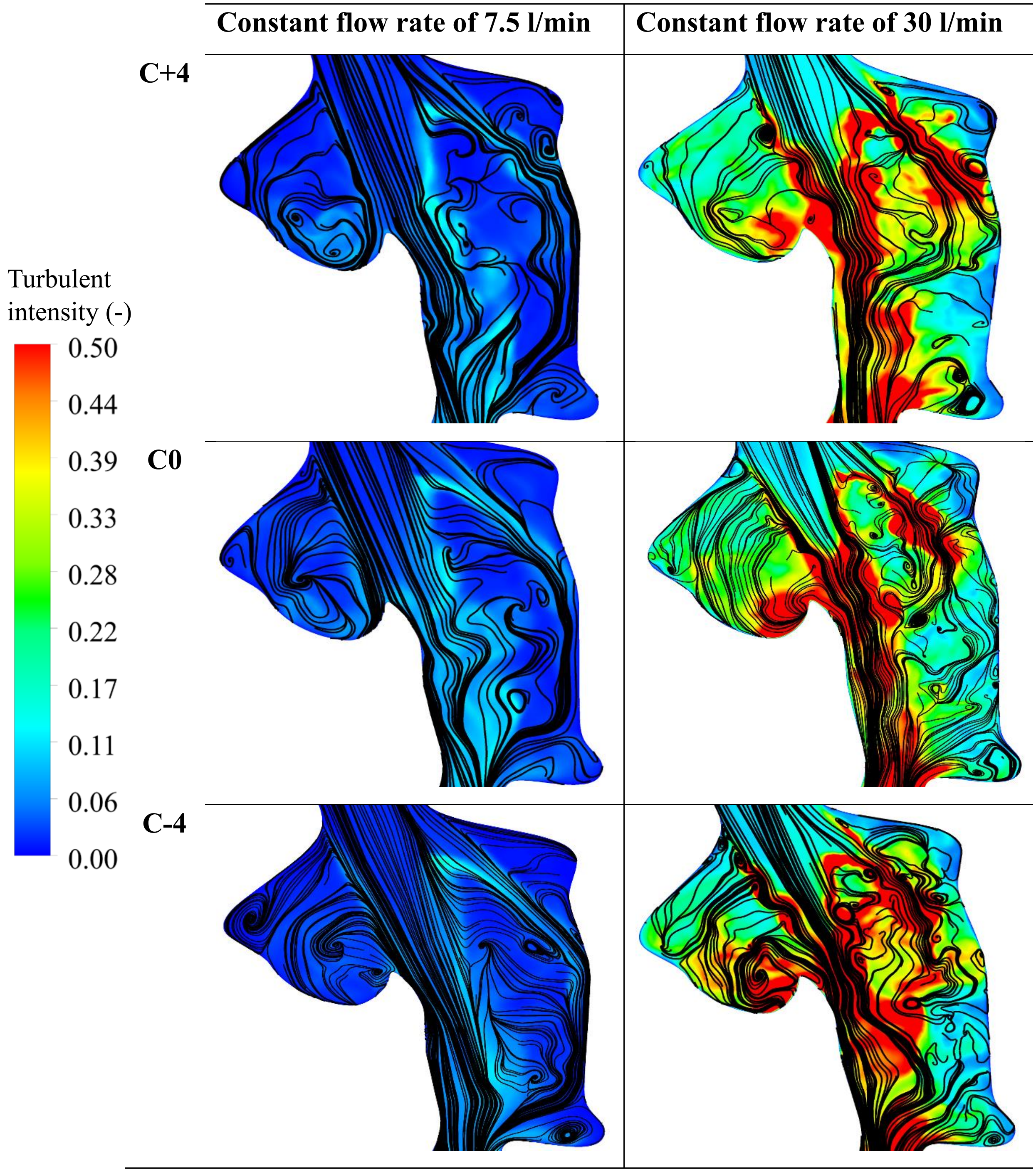

(b) Throat region

Fig 7.10 Contour of turbulent intensity and streamlines at flow rates of 7.5 and 30 l/min in **(a)** pediatric mouth region and **(b)** throat region for three main tongue positions: C+4, C0, and C-4.

Fig 7.11 shows the drug distribution pattern inside the pediatric MT airway for three primary tongue positions (C+4, C0, and C-4) at two constant flow rates, 7.5 l/min and 30 l/min. Three view orientations—side, lateral, and tongue front—are presented to provide a comprehensive 3D mapping of deposition patterns. Despite the complexity and heterogeneity of each model, unique deposition patterns can be observed that reflect the specific airway morphologies.

As shown in **Fig 7.11**, increasing the flow rate from 7.5 l/min to 30 l/min leads to greater deposition in the mouth and reduced deposition in the throat region, regardless of tongue position. At the lower flow rate of 7.5 l/min, droplets are primarily concentrated on the tongue, the exterior wall of pharynx and the lower larynx (indicated by the black dashed line circle), and This distribution pattern is primarily driven by abrupt changes in flow direction and inertial impaction, which are the dominant mechanisms for deposition. At the higher flow rate of 30 l/min, the distribution of droplets expands, with droplets also observed on the side walls of the teeth-cheek lumen, the palate wall, and the upper lip regions (highlighted by the blue dashed line circle). This broader distribution occurs due to flow deviation into side lumens, particularly in more constricted geometries (e.g., C+4), as well as increased turbulence at 30 l/min. This phenomenon corresponds to the stronger and more numerous recirculation regions illustrated in **Fig 7.10** at the 30 l/min flow rate.

The highest droplet deposition is observed in **Fig 7.11(a)**, where the tongue is at its maximum position (C+4). This position results in greater interactions between the droplets and the tongue. As the tongue moves down to C-4 (see **Fig 7.11(c)**), the amount of deposition on both the tongue and pharyngeal wall decreases, while deposition in the throat increases. This change indicates a reduction in airway obstruction, allowing droplets to travel further downstream to the throat and ultimately reach the lungs.

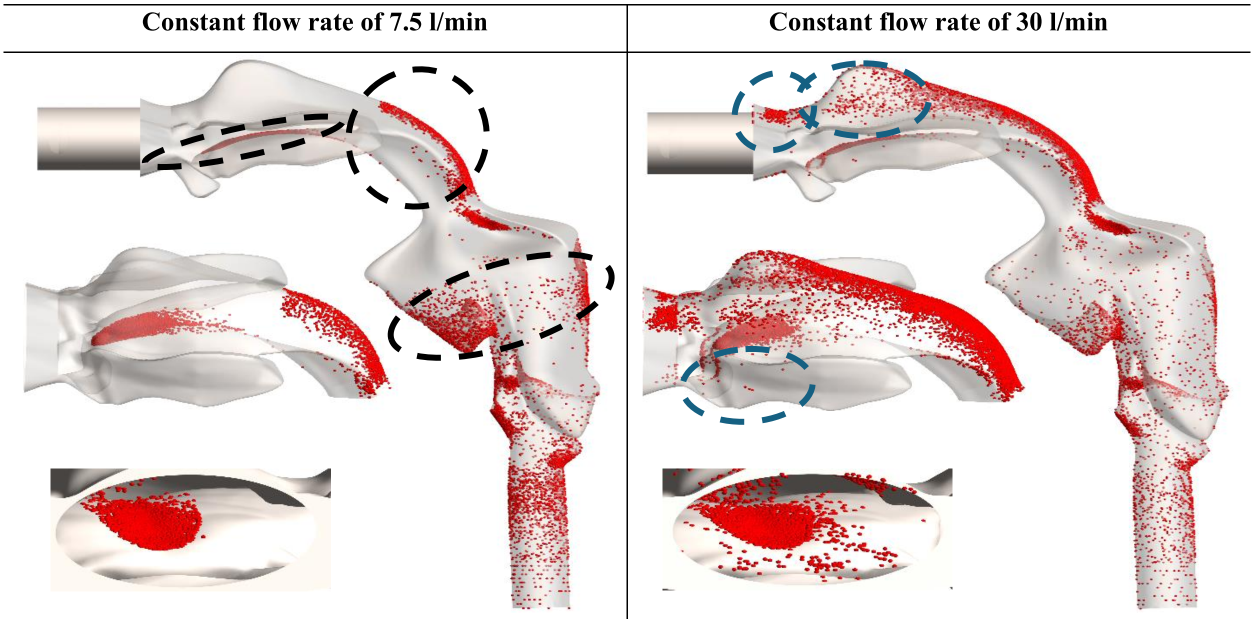

(a) C+4 tongue position

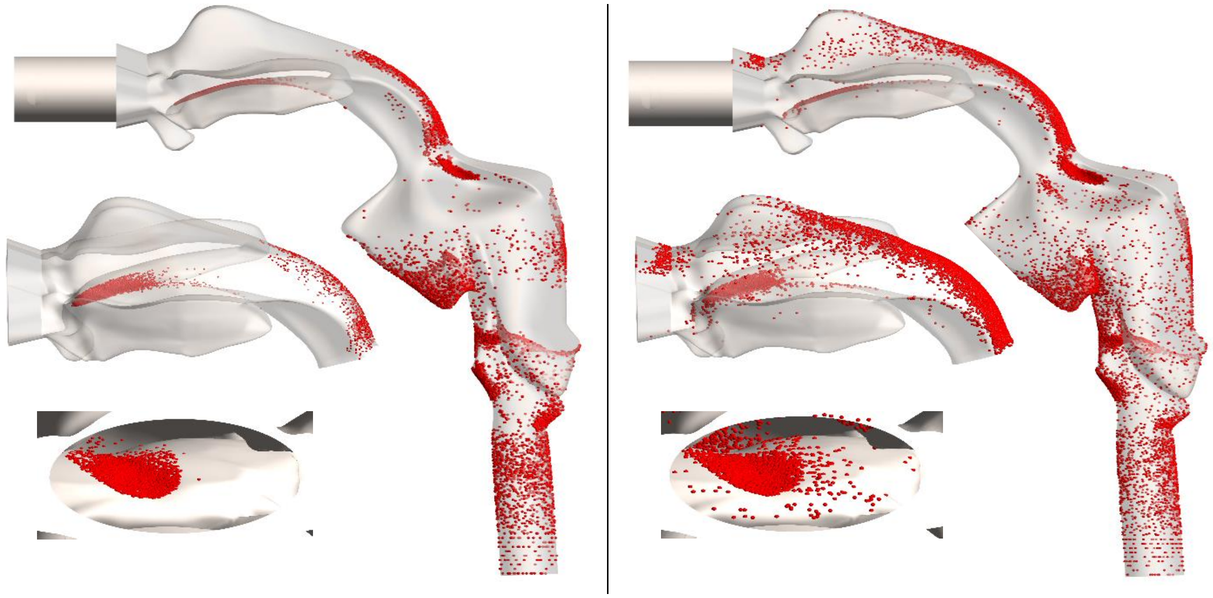

(b) C0 tongue position

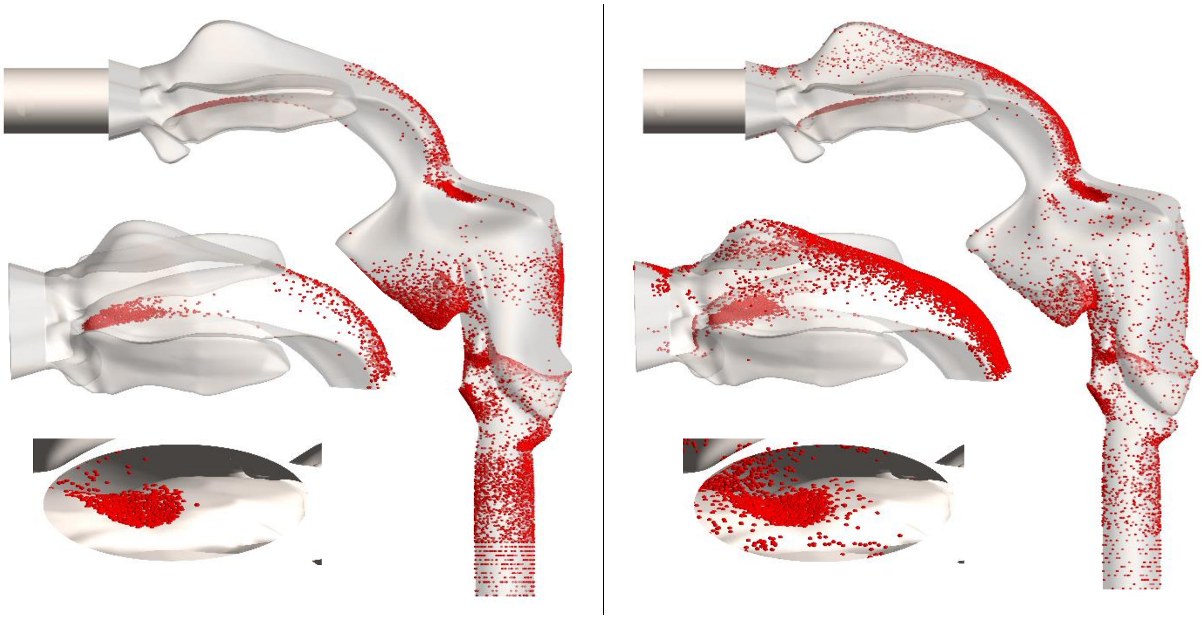

(c) C-4 tongue position

Fig 7.11 Drug distribution inside the pediatric MT airway for three main tongue positions of **(a)** C+4, **(b)** C0, and **(c)** at two constant flow rates of 7.5 l/min and 30 l/min.

The drug distribution inside the pediatric MT for realistic COPD and 2-step inhalation profiles at the tongue in the normal position (C0) is shown in **Fig 7.12**. Overall, the deposition inside the mouth region is significantly lower than mouth deposition at constant flow rates. It is observed that compared to a constant flow rate of 7.5 l/min, the distribution is more scattered, and droplets can be found on the side walls of the teeth-cheek lumen, the palate wall, and the upper lip regions. For the realistic inhalation profile, the deposition on the palate wall was higher than the 2-step inhalation profile, while the tongue deposition was found to be critically lower. The realistic COPD profile features a smoother, more consistent flow with lower turbulence intensity (1.87 vs. 4.66 in the 2-step profile), as shown in **Fig 7.13**. The steady airflow in the COPD profile reduces the likelihood of droplet impaction on the tongue, as the increased recirculation within the mouth region keeps droplets circulating near the palate wall surfaces rather than directing them downward toward the tongue. In the 2-step profile, rapid fluctuations and high turbulence lead to flow deviations that divert droplets away from the palate wall region and into side areas, including the teeth-cheek lumen and lower mouth.

Higher deposition was observed in the throat region at the realistic COPD inhalation profile, which could be attributed to the steady flow in the COPD profile, which allows droplets to travel further down the airway and reach the throat region. With less turbulence, these droplets maintain a more linear trajectory, enhancing deposition in the throat before they exit. However, while the recirculation regions are more numerous in the 2-step inhalation profile, the rapid fluctuations between high and low flow rates could not give droplets enough time to be deposited on the throat wall and make them re-entrained in the flow. The velocity vectors inside the mouth for both realistic COPD and 2-step inhalation profiles are also shown in **Fig 7.13**. In the COPD profile, the vector direction predominantly points toward the palate wall. This upward orientation indicates a steady, continuous airflow pathway that directs droplets toward the upper regions of the mouth rather than downward toward the tongue, which is consistent with the findings in **Fig 7.12**. In contrast, in the 2-step profile, the vector direction points more toward the tongue. This suggests that the fluctuating flow rates and higher turbulence in the 2-step profile cause the airflow to deviate downward, bringing droplets closer to the tongue surface.

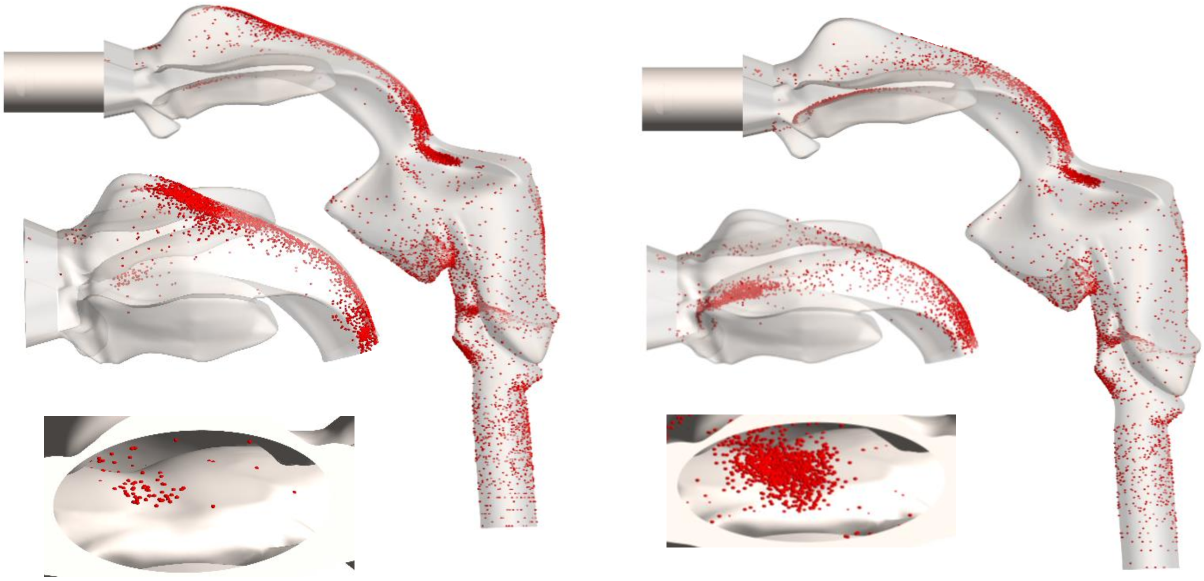

(a) Realistic COPD inhalation profile **(b) 2-step inhalation profile**

Fig 7.12 Drug distribution inside the pediatric MT airway for normal tongue position (C0) at **(a)** Realistic COPD inhalation profile, and **(b)** 2-step inhalation profile.

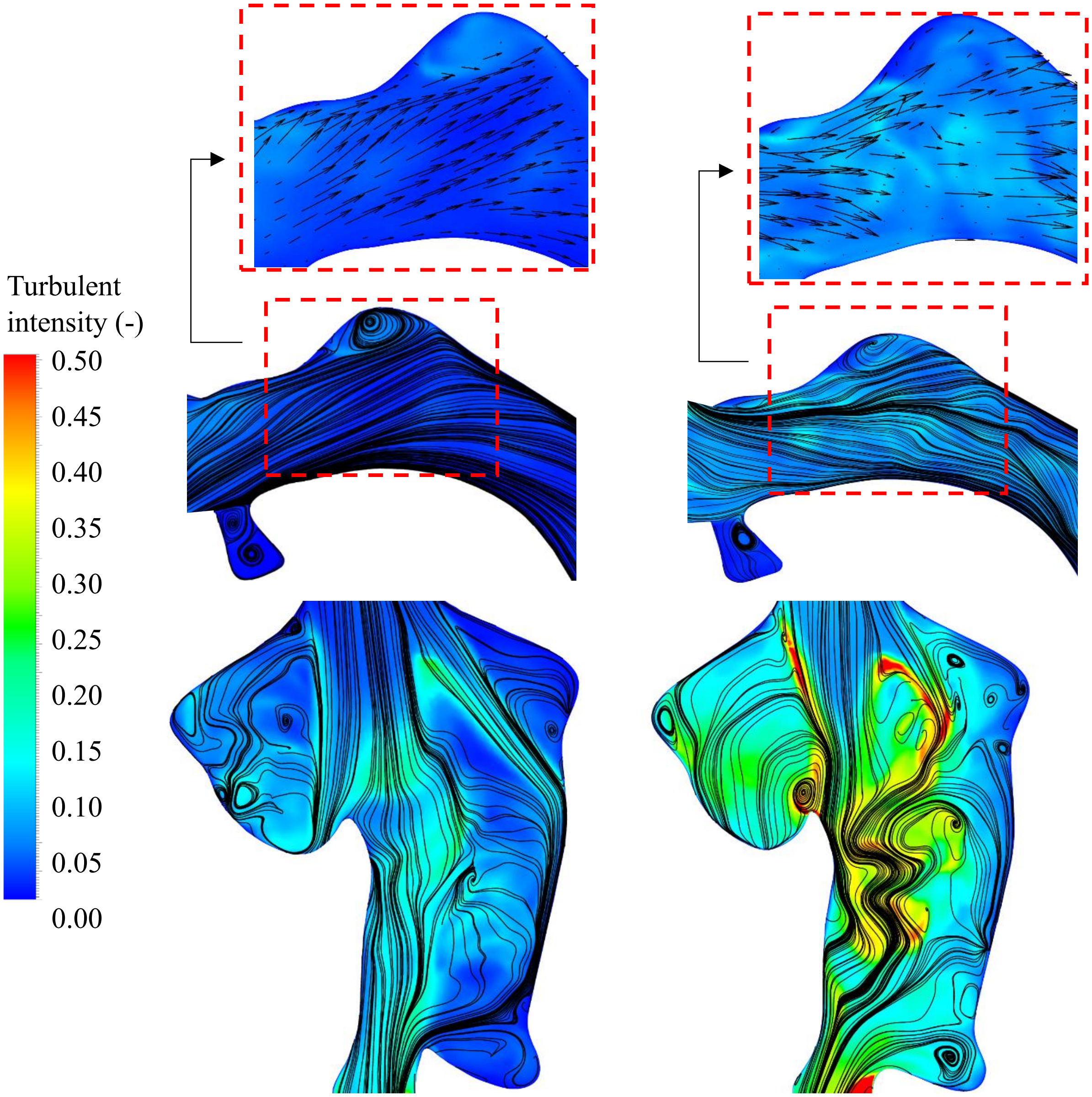

(a) Realistic COPD inhalation **(b) 2-step inhalation**

Fig 7.13 Contour of turbulent intensity and streamlines at normal tongue position (C0) for **(a)** realistic COPD inhalation profile, and **(b)** 2-step inhalation profile.

7.7 Conclusions

In conclusion, our CFD/in-vitro study provides a comprehensive analysis of drug droplet deposition and size distribution patterns within pediatric airway geometries. Understanding these factors in children's airways is crucial due to their unique anatomical and physiological characteristics, which differ significantly from those of adults. These differences affect how droplets interact with the airway surfaces, ultimately influencing drug delivery efficiency, deposition patterns, and potential therapeutic outcomes for pediatric populations.

Treating children can often be more challenging than treating adults, particularly in the area of respiratory drug delivery. Children need to follow specific procedures when taking their medications, but factors such as inhalation flow rates and tongue position can be difficult for them to manage. Unlike adults, children may struggle to accurately follow the ideal medication administration method. This study was conducted using a range of constant flow rates (7.5, 15, and 30 l/min) and a realistic COPD inhalation. It also utilized a two-step pulsatile inhalation profile while examining various tongue positions: C+4, C+2, C0, C-2, and C-4. In this context, C+4 indicates that the central tongue position has been moved 4 mm upward.

By using validated LES modeling alongside a detailed in-vitro approach, we observed significant variations in deposition influenced by airway structures and inhalation profiles. Our analysis identified a correlation that allows for the prediction of mouth deposition (%) for St > 0.02 across different flow rates, achieving a maximum RMSE of 0.18 when compared to previously published data. We also found that pediatric mouth-throat (MT) deposition was significantly higher than that of adults.

The highest mouth drug deposition (27.60%) was observed when the tongue was in its highest position (C+4) at a 30 l/min flow rate. Conversely, the highest throat deposition (22.32%) occurred at a flow rate of 7.5 l/min with the tongue in its lowest position (C-4), which was attributed to increased airway restriction and inertial impaction. As the tongue moved from C+4 to C-4, we noted a decrease in mouth deposition, while both throat and outlet deposition increased. Additionally, raising the flow rate from 7.5 to 30 l/min resulted in more than a 10% increase in mouth deposition, whereas throat and outlet deposition decreased by less than 7% and 9%, respectively. When incorporating realistic COPD flow rates and the 2-step pulsatile inhalation profile, we observed a significant reduction in drug deposition in the mouth, while deposition on the SMI mouthpiece increased. Minimal changes were noted in deposition patterns within the throat and outlet under these inhalation profiles.

Droplet size distribution analysis showed that the largest proportion of exiting droplets from the outlet had a diameter range of 2 to 5 μm (medium size), followed by smaller droplets (0.1 to 2 μm) and larger droplets (5 to 60 μm). Our results indicate that increased flow rates led to heightened turbulence and more recirculation zones within the pediatric MT, which explains the greater retention of smaller droplets at higher flow rates. The inclusion of realistic COPD inhalation and the 2-step pulsatile profile, with the tongue in a neutral position (C0), did not significantly affect the proportion of medium-sized droplets but reduced the proportion of small droplets and increased the proportion of larger droplets. This discrepancy was attributed to the transient nature of COPD and pulsatile inhalation profiles, along with the increased drag forces acting on larger droplets. These factors provide enough force to influence droplet trajectories based on size. Moreover, we observed that realistic COPD inhalation created a distinct deposition pattern compared to constant flow rates, while the 2-step pulsatile profile decreased drug deposition in the pediatric MT but enhanced deposition in the SMI mouthpiece, ultimately improving delivery to the lower airways. Additionally, deposition within the pediatric mouth was more scattered for both the realistic COPD and 2-step inhalation profiles compared to the constant flow rate of 7.5 l/min. The 2-step pulsatile inhalation profile led to increased deposition on the tongue and decreased deposition on the palate wall relative to the COPD inhalation profile. This effect could potentially reduce drug side effects and minimize variability among pediatric patients.

With continued validation, we propose that the results of this study could be integrated into clinical protocols to help optimize inhalation techniques and device settings tailored to patient needs, thereby improving the safety and efficacy of aerosol therapies. For future research, we recommend expanding this study to include individualized airway geometries based on imaging data to support personalized predictions and the development of patient-specific inhalation therapies, especially for individuals with unique anatomical or respiratory conditions. Additionally, considering potential interactions between droplets, such as collision and coalescence—particularly for higher-density aerosolized medications—could further clarify deposition patterns and improve the predictive accuracy of drug distribution within the airway.

7.8 Nomenclature

Abbreviations

CT	Computed Tomography
COPD	Chronic Obstructive Pulmonary Disease
CFD	Computational Fluid Dynamics

DE	Deposition Efficiency
DF	Droplet Deposition Fraction
DPI	Dry Powder Inhaler
DPM	Discrete Phase Model
HPLC	High-Performance Liquid Chromatography
LES	Large Eddy Simulation
MRI	Magnetic Resonance Imaging
MT	Mouth-Throat
NGI	Next Generation Impactor
pMDI	Pressurized Metered Dose Inhaler
RANS	Reynolds-Averaged Navier-Stokes
RMSE	Root-Mean-Square-Error
SGS	Subgrid-Scale
SMI	Soft Mist Inhaler
SIMPLEC	Semi-Implicit Method for Pressure-Linked Equations Consistent
USP-IP	United States Pharmacopeia Induction Port
3D	Three-Dimensional

Notations

a, b	equation coefficients
$\bar{u}_i$	resolved velocity field in three Cartesian coordinate directions, m/s
D_{ij}	rate of deformation tensor, 1/s
D_{lk}, D_{kl}	indices of the rate of deformation tensor, 1/s
$\overline{P}$	pressure, N/m^2
$\vec{F}$	body force including gravitational force, N
$\bar{S}_{ij}$	resolved rate of strain tensor, -
k_{sgs}	SGS kinetic energy, m^2/s^2
C_k, C_ε	model constants, -
C_D	drag coefficient, -
Re_d	droplet Reynolds number, -
$\vec{g}$	gravitational acceleration, m/s^2

k	turbulent kinetic energy, m^2/s^2
d_d	diameter of droplets, m
C_c	Cunningham correction factor, -
m_d	droplet mass, kg
St	Stokes number, -
$\vec{u}$	velocity of air, m/s
$\vec{u}_d$	velocity of droplets, m/s
u_i'	fluctuating component of the instantaneous velocity, m/s
$f_{i,lift}$	lift force, N
f_D	
D	hydraulic diameter, m
A	mouth cross-sectional area, m^2
P	mouth cross-sectional perimeter, m
Q	flow rate, l/min

Greek letters

ρ	air density, kg/m^3
ρ_d	droplet density, kg/m^3
τ_{ij}^{sgs}	subgrid scale stress, N/m^2
τ_d	relaxation time of droplets, s
δ_{ij}	Kronecker delta, -
$\overline{\Delta}$	subgrid characteristic length scale, m
σ_k	Model constant, -
μ	air dynamic viscosity, kg/ms
υ	air kinematic viscosity, m^2/s
υ_t	subgrid scale viscosity, m^2/s

7.9 References

[1] Pearce N., Aït-Khaled N., Beasley R., Mallol J., Keil U., Mitchell EA., Robertson C., Anderson HR., Asher MI., Björkstén B., et al. Worldwide trends in the prevalence of asthma symptoms: Phase III of the International Study of Asthma and Allergies in Childhood (ISAAC). *Thorax* .2007; https://doi.org/10.1136/thx.2006.070169.

[2] Heyder J., Gebhart J., Rudolf G., Schiller CF., Stahlhofen W. Deposition of particles in the human respiratory tract in the size range 0.005–15 μm. *J Aerosol Sci* .1986; https://doi.org/10.1016/0021-8502(86)90035-2.

[3] Hofmann W. Modelling inhaled particle deposition in the human lung-A review. *J Aerosol Sci* .2011; https://doi.org/10.1016/j.jaerosci.2011.05.007.

[4] Martonen TB. Mathematical Model for the Selective Deposition of Inhaled Pharmaceuticals. *J Pharm Sci* .1993; https://doi.org/10.1002/jps.2600821202.

[5] Mahler DA. The role of inspiratory flow in selection and use of inhaled therapy for patients with chronic obstructive pulmonary disease. *Respir Med* .2020; https://doi.org/10.1016/j.rmed.2019.105857.

[6] Talaat M., Si X., Xi J. Effect of MDI Actuation Timing on Inhalation Dosimetry in a Human Respiratory Tract Model. *Pharmaceuticals* .2022; https://doi.org/10.3390/ph15010061.

[7] Baloira A., Abad A., Fuster A., Rivero JLG., García-Sidro P., Márquez-Martín E., Palop M., Soler N., Velasco JL., González-Torralba F. Lung deposition and inspiratory flow rate in patients with chronic obstructive pulmonary disease using different inhalation devices: A systematic literature review and expert opinion. *International Journal of COPD* .2021; https://doi.org/10.2147/COPD.S297980.

[8] Arsalanloo A., Abbasalizadeh M., Khalilian M., Saniee Y., Ramezanpour A., Islam MS. A computational approach to understand the breathing dynamics and pharmaceutical aerosol transport in a realistic airways. *Advanced Powder Technology* .2022; https://doi.org/10.1016/j.apt.2022.103635.

[9] Zhou Y., Sun J., Cheng YS. Comparison of deposition in the USP and physical mouth-throat models with solid and liquid particles. *J Aerosol Med Pulm Drug Deliv* .2011; https://doi.org/10.1089/jamp.2011.0882.

[10] Faizal WM., Ghazali NNN., Khor CY., Badruddin IA., Zainon MZ., Yazid AA., Ibrahim NB., Razi RM. Computational fluid dynamics modelling of human upper airway: A review. *Comput Methods Programs Biomed* .2020; https://doi.org/10.1016/j.cmpb.2020.105627.

[11] Ahookhosh K., Pourmehran O., Aminfar H., Mohammadpourfard M., Sarafraz MM., Hamishehkar H. Development of human respiratory airway models: A review. *European Journal of Pharmaceutical Sciences* .2020; https://doi.org/10.1016/j.ejps.2020.105233.

[12] Asgharian B., Price OT. Airflow Distribution in the Human Lung and its Influence on Particle Deposition. *Inhal Toxicol* .2006; https://doi.org/10.1080/08958370600748687.

[13] LeBelle MJ., Graham SJ., Ormsby ED., Duhaime RM., Lawrence RC., Pike RK. Metered-dose inhalers. II. Particle size measurement variation. *Int J Pharm* .1997; https://doi.org/10.1016/S0378-5173(97)04905-3.

[14] Cheng YS., Zhou Y., Su WC. Deposition of particles in human mouth-throat replicas and a USP induction port. *J Aerosol Med Pulm Drug Deliv* .2015; https://doi.org/10.1089/jamp.2013.1105.

[15] Roberts DL., Chambers F., Copley M., Mitchell JP. Internal Volumes of Pharmaceutical Compendial Induction Port, Next-Generation Impactor with and without Its Pre-separator, and Several Configurations of the Andersen Cascade Impactor with and without Pre-separator. *J Aerosol Med Pulm Drug Deliv* .2020; https://doi.org/10.1089/jamp.2019.1590.

[16] Byron PR., Hindle M., Lange CF., Longest PW., McRobbie D., Oldham MJ., Olsson B., Thiel CG., Wachtel H., Finlay WH. In vivo-in vitro correlations: Predicting pulmonary drug deposition from pharmaceutical aerosols. *J Aerosol Med Pulm Drug Deliv* .2010; https://doi.org/10.1089/jamp.2010.0846.

[17] Kolanjiyil A V., Hosseini S., Alfaifi A., Farkas D., Walenga R., Babiskin A., Hindle M., Golshahi L., Longest PW. Validating CFD predictions of nasal spray deposition: Inclusion of cloud motion effects for two spray pump designs. *Aerosol Science and Technology* .2022; https://doi.org/10.1080/02786826.2021.2011830.

[18] Lizal F., Elcner J., Jedelsky J., Maly M., Jicha M., Farkas Á., Belka M., Rehak Z., Adam J., Brinek A., et al. The effect of oral and nasal breathing on the deposition of inhaled particles in upper and tracheobronchial airways. *J Aerosol Sci* .2020; https://doi.org/10.1016/j.jaerosci.2020.105649.

[19] Bass K., Worth Longest P. Recommendations for simulating microparticle deposition at conditions similar to the upper airways with two-equation turbulence models. *J Aerosol Sci* .2018; https://doi.org/10.1016/j.jaerosci.2018.02.007.

[20] Cheng K-H., Cheng Y-S., Yeh H-C., Swift DL. An Experimental Method for Measuring Aerosol Deposition Efficiency in the Human Oral Airway. *Am Ind Hyg Assoc J* .1997; https://doi.org/10.1080/15428119791012856.

[21] Zhou Y., Sun J., Cheng YS. Comparison of deposition in the USP and physical mouth-throat models with solid and liquid particles. *J Aerosol Med Pulm Drug Deliv* .2011; https://doi.org/10.1089/jamp.2011.0882.

[22] Longest PW., Xi J. Effectiveness of direct Lagrangian tracking models for simulating nanoparticle deposition in the upper airways. *Aerosol Science and Technology* .2007; https://doi.org/10.1080/02786820701203223.

[23] Worth Longest P., Hindle M. Evaluation of the respimat soft mist inhaler using a concurrent cfd and in vitro approach. *J Aerosol Med Pulm Drug Deliv* .2009; https://doi.org/10.1089/jamp.2008.0708.

[24] Xi J., Yang T. Variability in oropharyngeal airflow and aerosol deposition due to changing tongue positions. *J Drug Deliv Sci Technol* .2019; https://doi.org/10.1016/j.jddst.2019.01.006.

[25] Xi J., Yuan JE., Yang M., Si X., Zhou Y., Cheng YS. Parametric study on mouth–throat geometrical factors on deposition of orally inhaled aerosols. *J Aerosol Sci* .2016; https://doi.org/10.1016/j.jaerosci.2016.01.014.

[26] Worth Longest P., Hindle M. Evaluation of the respimat soft mist inhaler using a concurrent cfd and in vitro approach. *J Aerosol Med Pulm Drug Deliv* .2009; https://doi.org/10.1089/jamp.2008.0708.

[27] Wei X., Hindle M., Kaviratna A., Huynh BK., Delvadia RR., Sandell D., Byron PR. In vitro tests for aerosol deposition. VI: Realistic testing with different mouth-throat models and in vitro - In vivo correlations for a dry powder inhaler, metered dose inhaler, and soft mist inhaler. *J Aerosol Med Pulm Drug Deliv* .2018; https://doi.org/10.1089/jamp.2018.1454.

[28] Musante CJ., Martonen TB. Computer simulations of particle deposition in the developing human lung. *J Air Waste Manage Assoc* .2000; https://doi.org/10.1080/10473289.2000.10464176.

[29] Xi J., Longest PW. Transport and deposition of micro-aerosols in realistic and simplified models of the oral airway. *Ann Biomed Eng* .2007; https://doi.org/10.1007/s10439-006-9245-y.

[30] Wedel J., Steinmann P., Štrakl M., Hriberšek M., Cui Y., Ravnik J. Anatomy matters: The role of the subject-specific respiratory tract on aerosol deposition — A CFD study. *Comput Methods Appl Mech Eng* .2022; https://doi.org/10.1016/j.cma.2022.115372.

[31] Asgari M., Lucci F., Bialek J., Dunan B., Andreatta G., Smajda R., Lani S., Blondiaux N., Majeed S., Steiner S., et al. Development of a realistic human respiratory tract cast representing physiological thermal conditions. *Aerosol Science and Technology* .2019; https://doi.org/10.1080/02786826.2019.1612839.

[32] Zhao K., Scherer PW., Hajiloo SA., Dalton P. Effect of anatomy on human nasal air flow and odorant transport patterns: Implications for olfaction. *Chem Senses* .2004; https://doi.org/10.1093/chemse/bjh033.

[33] Xi J., April Si X., Dong H., Zhong H. Effects of glottis motion on airflow and energy expenditure in a human upper airway model. *European Journal of Mechanics, B/Fluids* .2018; https://doi.org/10.1016/j.euromechflu.2018.04.011.

[34] Haghnegahdar A., Bharadwaj R., Feng Y. Exploring the role of nasal hair in inhaled airflow and coarse dust particle dynamics in a nasal cavity: A CFD-DEM study. *Powder Technol* .2023; https://doi.org/10.1016/j.powtec.2023.118710.

[35] O'Neil JA., Villasmil-Urdaneta LA. A path forward in the development of new aerosol drug delivery devices for pediatrics. *Respir Med* .2023; https://doi.org/10.1016/j.rmed.2023.107210.

[36] Zhang Z., Kleinstreuer C. Computational analysis of airflow and nanoparticle deposition in a combined nasal-oral-tracheobronchial airway model. *J Aerosol Sci* .2011; https://doi.org/10.1016/j.jaerosci.2011.01.001.

[37] Rahimi-Gorji M., Pourmehran O., Gorji-Bandpy M., Gorji TB. CFD simulation of airflow behavior and particle transport and deposition in different breathing conditions through the realistic model of human airways. *J Mol Liq* .2015; https://doi.org/10.1016/j.molliq.2015.05.031.

[38] Cheng KH., Swift DL. Calculation of total deposition fraction of ultrafine aerosols in human extrathoracic and intrathoracic regions. *Aerosol Science and Technology* .1995; https://doi.org/10.1080/02786829509508887.

[39] Williams J., Kolehmainen J., Cunningham S., Ozel A., Wolfram U. Effect of patient inhalation profile and airway structure on drug deposition in image-based models with particle-particle interactions. *Int J Pharm* .2022; https://doi.org/10.1016/j.ijpharm.2021.121321.

[40] Xu X., Wu J., Weng W., Fu M. Investigation of inhalation and exhalation flow pattern in a realistic human upper airway model by PIV experiments and CFD simulations. *Biomech Model Mechanobiol* .2020; https://doi.org/10.1007/s10237-020-01299-3.

[41] Tiwari A., Jain A., Paul AR., Saha SC. Computational evaluation of drug delivery in human respiratory tract under realistic inhalation. *Physics of Fluids* .2021; https://doi.org/10.1063/5.0053980.

[42] Lazaridis M. Modelling approaches to particle deposition and clearance in the human respiratory tract. *Air Qual Atmos Health* .2023; https://doi.org/10.1007/s11869-023-01386-1.

[43] Cheng YS. Aerosol deposition in the extrathoracic region. *Aerosol Science and Technology* .2003; https://doi.org/10.1080/02786820300906.

[44] Gunatilaka CC., McKenzie C., Xiao Q., Higano NS., Woods JC., Bates AJ. Effect of airway wall motion on particle deposition and delivery in the neonatal trachea. *J Aerosol Sci* .2024; https://doi.org/10.1016/j.jaerosci.2024.106450.

[45] Mead-Hunter R., King AJC., Larcombe AN., Mullins BJ. The influence of moving walls on respiratory aerosol deposition modelling. *J Aerosol Sci* .2013; https://doi.org/10.1016/j.jaerosci.2013.05.006.

[46] Kajee Y., Pelteret JPV., Reddy BD. The biomechanics of the human tongue. *Int J Numer Method Biomed Eng* .2013; https://doi.org/10.1002/cnm.2531.

[47] Xi J., Yang T. Variability in oropharyngeal airflow and aerosol deposition due to changing tongue positions. *J Drug Deliv Sci Technol* .2019; https://doi.org/10.1016/j.jddst.2019.01.006.

[48] Zhou X., Li Y., Miao H., Zhang Y., Yu A., Huang F., Li R., Tong Z. Numerical study on the effect of the realistic mouth-inhaler positions on orally inhaled drug delivery in pediatric intersubject upper airways. *Powder Technol* .2024; https://doi.org/10.1016/j.powtec.2023.119163.

[49] Martonen TB., Smyth HD., Isaacs KK., Burton RT. Issues in drug delivery: concepts and practice. *Respir Care* .2005;

[50] Nagel M., Mitchell JP., Nagel MW., Suggett JA., Mitchell J. *How does the Tongue Influence Transport of Inhaled Particles from a Pressurized Metered Dose Inhaler (pMDI) and Valved Holding Chamber (VHC)*. vol. 32. n.d.

[51] Yokoi T., Kondo R., Horiguchi T. Residual fluticasone in the oral cavity after inhalation with different tongue positions. *Journal of Allergy and Clinical Immunology: In Practice* .2019; https://doi.org/10.1016/j.jaip.2018.11.032.

[52] Harless J., Ramaiah R., Bhananker S. Pediatric airway management. *Int J Crit Illn Inj Sci* .2014; https://doi.org/10.4103/2229-5151.128015.

[53] Bickmann DWHKRLP. Examining Inhaler Performance Using a Child's Throat Model. *Respiratory Drug Delivery* .2008;

[54] Hughes J., Thomas R., Byun Y., Whiteside S. Improved flexibility of thermally stable poly-lactic acid (PLA). *Carbohydr Polym* .2012; https://doi.org/10.1016/j.carbpol.2011.11.078.

[55] Piglione MC., Fontana D., Vanni M. Simulation of particle deposition in human central airways. *European Journal of Mechanics, B/Fluids* .2012; https://doi.org/10.1016/j.euromechflu.2011.08.003.

[56] Cheng S., Butler JE., Gandevia SC., Bilston LE. Movement of the tongue during normal breathing in awake healthy humans. *Journal of Physiology* .2008; https://doi.org/10.1113/jphysiol.2008.156430.

[57] Ferziger JH., Perić M., Street RL. *Computational Methods for Fluid Dynamics*. Cham: Springer International Publishing; .2020;

[58] Wilcox DC. *Turbulence modeling for CFD (Third edition)*. .2006;

[59] Jing H., Ge H., Wang L., Zhou Q., Chen L., Choi S., Cui X. Large eddy simulation study of the airflow characteristics in a human whole-lung airway model. *Physics of Fluids* .2023; https://doi.org/10.1063/5.0156310.

[60] Koullapis PG., Kassinos SC., Bivolarova MP., Melikov AK. Particle deposition in a realistic geometry of the human conducting airways: Effects of inlet velocity profile, inhalation flowrate and electrostatic charge. *J Biomech* .2016; https://doi.org/10.1016/j.jbiomech.2015.11.029.

[61] Kim W-W., Menon S. A new dynamic one-equation subgrid-scale model for large eddy simulations. *33rd Aerospace Sciences Meeting and Exhibit*. Reston, Virigina: American Institute of Aeronautics and Astronautics; .1995;

[62] Kim W-W., Menon S., Kim W-W., Menon S. Application of the localized dynamic subgrid-scale model to turbulent wall-bounded flows. *35th Aerospace Sciences Meeting and Exhibit*. Reston, Virigina: American Institute of Aeronautics and Astronautics; .1997;

[63] Inagaki K., Kobayashi H. Transport and modeling of subgrid-scale turbulent kinetic energy in channel flows. *AIP Adv* .2022; https://doi.org/10.1063/5.0083398.

[64] Allen MD., Raabe OG. Slip correction measurements of spherical solid aerosol particles in an improved millikan apparatus. *Aerosol Science and Technology* .1985; https://doi.org/10.1080/02786828508959055.

[65] Xu C., Zheng X., Shen S. A numerical study of the effect of breathing mode and exposure conditions on the particle inhalation and deposition. *Inhal Toxicol* .2020; https://doi.org/10.1080/08958378.2020.1840679.

[66] Pope SB. *Turbulent Flows*. Cambridge University Press; .2000;

[67] Haghnegahdar A., Bharadwaj R., Feng Y. Exploring the role of nasal hair in inhaled airflow and coarse dust particle dynamics in a nasal cavity: A CFD-DEM study. *Powder Technol* .2023; https://doi.org/10.1016/j.powtec.2023.118710.

[68] Longest PW., Holbrook LT. In silico models of aerosol delivery to the respiratory tract - Development and applications. *Adv Drug Deliv Rev* .2012; https://doi.org/10.1016/j.addr.2011.05.009.

[69] Finlay WH. *The Mechanics of Inhaled Pharmaceutical Aerosols*. vol. 53. .2019;

[70] Andropoulos DB. Pediatric physiology: How does it differ from adults? *Pediatric Sedation Outside of the Operating Room: A Multispecialty International Collaboration, Second Edition*. Springer New York; .2015; p. 111–23.

[71] Lindert S., Below A., Breitkreutz J. Performance of dry powder inhalers with single dosed capsules in preschool children and adults using improved upper airway models. *Pharmaceutics* .2014; https://doi.org/10.3390/pharmaceutics6010036.

[72] Sadeghi T., Fatehi P., Pakzad L. Effect of Nasal Inhalation on Drug Particle Deposition and Size Distribution in the Upper Airway: With Soft Mist Inhalers. *Ann Biomed Eng* .2024; https://doi.org/10.1007/s10439-023-03423-7.

[73] Wachtel H., Nagel M., Engel M., El Azzi G., Sharma A., Suggett J. In vitro and clinical characterization of the valved holding chamber AeroChamber Plus® Flow-Vu® for administrating tiotropium Respimat® in 1–5-year-old children with persistent asthmatic symptoms. *Respir Med* .2018; https://doi.org/10.1016/j.rmed.2018.03.010.

[74] Wachtel H., Bickmann D., Breitkreutz J., Langguth P. *Respiratory Drug Delivery*. .2010;

[75] Muellinger B., Buchmann N., Bockenstedt D., Mao L., Pant N., de Kruijf W. Effect of inspiratory flow rate on particle size distribution and in silico deposition within the respiratory tract using a soft mist inhaler (SMI). *Respiratory Drug Delivery* .2022;

[76] Wang B., Peng Z., Liu Q., Chen X. Effect of airflow rate on droplet deposition of an impinging-jet inhaler in the human respiratory tract. *Int J Pharm* .2024; https://doi.org/10.1016/j.ijpharm.2024.124408.

[77] Xu Z., Hickey AJ. The Physics of Aerosol Droplet and Particle Generation from Inhalers. In: H.D.C. S, and A.J. H, editors. *Controlled Pulmonary Drug Delivery*. 1st ed. New York, NY: Springer New York; .2011; p. 75–100.

[78] Matijević E. *Fine Particles in Medicine and Pharmacy*. Boston, MA: Springer US; .2012;

[79] Xu C., Zheng X., Shen S. A numerical study of the effect of breathing mode and exposure conditions on the particle inhalation and deposition. *Inhal Toxicol* .2020; https://doi.org/10.1080/08958378.2020.1840679.

[80] Cheng YS., Zhou Y., Chen BT. Particle deposition in a cast of human oral airways. *Aerosol Science and Technology* .1999; https://doi.org/10.1080/027868299304165.

[81] Grgic B., Finlay WH., Burnell PKP., Heenan AF. In vitro intersubject and intrasubject deposition measurements in realistic mouth-throat geometries. *J Aerosol Sci* .2004; https://doi.org/10.1016/j.jaerosci.2004.03.003.

[82] Williams J., Kolehmainen J., Cunningham S., Ozel A., Wolfram U. Effect of patient inhalation profile and airway structure on drug deposition in image-based models with particle-particle interactions. *Int J Pharm* .2022; https://doi.org/10.1016/j.ijpharm.2021.121321.

Chapter 8- Concluding Remarks and Future Recommendations

Over the past five decades, human activities have released numerous harmful gases into the atmosphere, significantly increasing the prevalence of lung diseases. Unlike injected medications, which do not directly target the lungs, inhaling drugs in the form of aerosol particles minimizes side effects, allows for direct absorption into the lungs, and provides rapid relief. Soft Mist Inhalers (SMIs) have been developed to deliver medication to the lungs more efficiently than other inhaler devices; however, their effectiveness remains a topic of debate. This study investigates the factors that affect drug delivery efficiency, including device positioning and angle, inhalation profiles, and human anatomical characteristics. This chapter highlights the key findings and research methods used in the study.

8.1. Effective Use of SMI: Essential for Minimizing Drug Loss in the Mouth

In the first step, a comprehensive analysis of the performance of SMIs using CFD modeling, focusing on aerosol velocity profiles, flow patterns, size distribution, and deposition, is provided. Significant insights into aerosol drug delivery dynamics were achieved by examining two simplified geometries—an idealized mouth and a standard mouth —and testing the effects of nozzle orifice position, nozzle angle, and inhalation flow rates.

The validated CFD model successfully simulated aerosol transport and deposition, with results closely aligning with experimental data. The study revealed that the geometry of the mouth cavity plays a critical role in aerosol velocity and deposition. For both idealized and standard mouth geometries, a fixed flow rate of 30 l/min resulted in increased aerosol velocity at the outlet and decreased particle deposition on the mouth walls. Larger particles (>5 µm) exhibited higher deposition fractions, particularly in regions with recirculation and backward flow, highlighting the influence of residence time.

Furthermore, the positioning and angling of the SMI nozzle had notable effects. Moving the nozzle further forward along the centerline (x-axis) increased aerosol velocity at the outlet and decreased deposition for the standard mouth geometry. However, improper nozzle angles caused higher deposition within the mouth cavity, reducing the mass of particles reaching the outlet. The study demonstrated that the inhalation flow rate (30 l/min) mitigates the impact of nozzle misalignment, emphasizing the importance of proper flow rates in ensuring effective drug delivery.

8.1.1. Future Recommendations

While this study focused on simplified mouth geometries, the findings provide a strong foundation for further research and practical applications. Future studies should incorporate more anatomically accurate geometries, including the throat and upper airway regions, to better understand aerosol particles' entire trajectory and deposition patterns. Developing innovative add-on devices, such as sensors or smart mouthpieces, is also recommended. These devices could provide real-time feedback to patients—particularly children and the elderly—regarding correct SMI positioning and inhalation techniques, ensuring optimal drug delivery. Furthermore, exploring variable flow rates and nozzle configurations across diverse patient demographics could lead to more tailored and effective inhaler designs.

8.2. The Impact of Nasal and Oral Breathing on SMI Aerosol Drug Delivery

This study provided valuable insights into the combined effects of nasal and oral inhalation on airflow patterns, aerosol deposition, and size distribution in the human upper airway using an SMI. Using a modified induction port to simulate nasal airflow, six oral-to-nasal flow rate ratios were investigated, with a total inhalation flow rate of 30 l/min. The results demonstrate that simultaneous oral and nasal inhalation significantly influences the flow field and deposition characteristics, with moderate oral/nasal flow ratios (O/N=1) producing fewer vortices, reduced turbulent kinetic energy, and minimized aerosol deposition loss within the modified induction port.

Droplet size distribution analysis revealed that droplets in the 2–5 μm range exhibited the highest deposition fraction, making them the dominant type of aerosol mass along the modified induction port, especially at O/N=1. Droplets with smaller diameters (0.1–2 μm) showed a more pronounced response to variations in relative humidity, with increased relative humidity enhancing the number of droplets exiting the modified induction port and entering the lower respiratory tract. Notably, combining oral and nasal inhalation at an O/N ratio of 1 unified the airflow streams, reduced recirculation, and lowered drug deposition losses, thereby improving drug delivery efficiency to the lungs. These findings suggest that optimizing oral and nasal inhalation flow rates can enhance the efficacy of SMI-based drug delivery for patients.

8.2.1. Future Recommendations

Future research should incorporate anatomically realistic upper airway geometries to more accurately simulate droplet behavior in human respiratory tracts. Investigating the effects of droplet coalescence, collision, and sub-micrometer droplet dynamics could refine the deposition models further. Additionally, considering airflow temperature is essential to evaluate how environmental factors and relative humidity (RH) affect drug delivery to the lungs. Exploring the influence of varying airway geometric characteristics on aerosol flow patterns can also provide valuable data for optimizing inhaler designs for diverse patient populations.

8.3 Pediatric Airflow Patterns and SMI Drug Delivery: Effects of Tongue Position with Varied Inhalation Profiles

This study offers a detailed investigation into the impact of tongue positioning, airflow dynamics, and inhalation profiles on droplet deposition and size distribution within a realistic pediatric MT geometry using an SMI. Pediatric airways, characterized by distinct anatomical and physiological features compared to adults, present unique challenges in optimizing drug delivery. By employing LES modeling validated with in-vitro experiments, we analyzed various tongue positions (C+4 to C-4), fixed flow rates (7.5, 15, and 30 l/min), and realistic inhalation profiles, including COPD and 2-step pulsatile inhalation patterns.

The findings demonstrate that tongue position and airflow rates significantly influence droplet deposition patterns and size distribution within pediatric airways. Mouth deposition was highest (27.60%) when the tongue was in its highest position (C+4) at a 30 l/min flow rate, whereas throat deposition peaked (22.32%) at a 7.5 l/min flow rate with the tongue in its lowest position (C-4). Additionally, increased flow rates intensified turbulence and recirculation zones, leading to greater retention of smaller droplets and higher deposition in the pediatric MT. A novel correlation was developed to predict mouth deposition (%) for St> 0.02 with a high degree of accuracy (RMSE = 0.18). Notably, pediatric MT deposition was found to be over twice that of adult MT geometries, underscoring the need for tailored inhalation strategies for children.

Inhalation profiles also played a critical role in drug delivery efficiency. The COPD and 2-step pulsatile profiles reduced drug deposition in the mouth while increasing deposition on the SMI mouthpiece, facilitating better delivery to the lower respiratory tract. The pulsatile profile redistributed deposition patterns, reducing palate wall deposition while increasing tongue deposition, which may help mitigate side effects and improve consistency among pediatric patients. Droplet size distribution analysis revealed that medium-sized droplets (2–5 µm) dominated at the outlet, and smaller droplets (0.1–2 µm) were retained in the MT, especially under higher flow rates. These findings emphasize the importance of accounting for pediatric airway characteristics and inhalation behaviors when designing aerosol therapies.

8.3.1. Future Recommendations

To further refine the understanding of pediatric aerosol drug delivery, future research should expand this study to include individualized airway geometries derived from imaging data, enabling personalized predictions and therapies. Investigating the interactions between droplets, such as collision and coalescence, particularly for higher-density medications, could enhance the accuracy of deposition models and clarify distribution patterns. Additionally, incorporating the influence of transient environmental conditions, such as temperature and humidity, may provide deeper insights into the factors affecting aerosol behavior. Exploring the use of adaptive SMI settings tailored to pediatric patients' unique respiratory dynamics will contribute to optimizing safety and efficacy in aerosol therapies. These efforts will be instrumental in advancing patient-specific treatments and improving therapeutic outcomes for children with respiratory conditions.